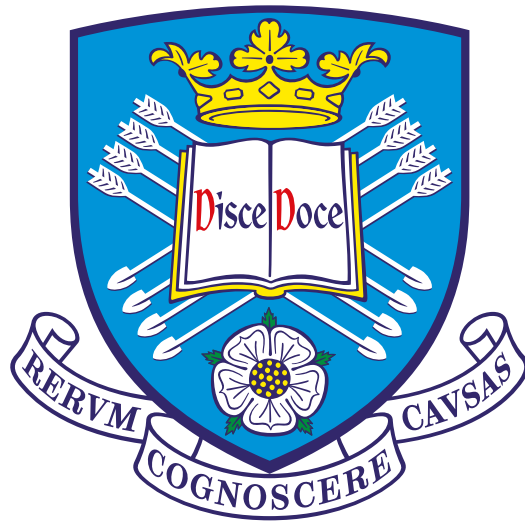


Electron reconstruction and performance studies, search for a heavy Higgs boson decaying to four-leptons using the ATLAS detector, irradiations at the Birmingham Irradiation Facility for the HL-LHC



Kerry Ann Parker

A Thesis Submitted for the Degree of Doctor of Philosophy in Physics

Department of Physics and Astronomy

The University of Sheffield

April 2016

ABSTRACT

This thesis presents electromagnetic (EM) calorimeter performance studies using electrons and photons, a search for a heavy Higgs state using the ATLAS detector at the Large Hadron Collider (LHC) and irradiation work at the Birmingham Irradiation Facility.

A new electron reconstruction algorithm using the ATLAS detector is described, and the performance of these electrons is compared to the current ATLAS algorithm. Multivariate techniques are used to derive calibration weights for the energy response of the EM calorimeter.

This thesis also presents cross-section times branching ratio limits in the search for a heavy Higgs state in the four-lepton channel, using 20.7 fb^{-1} of $\sqrt{s} = 8 \text{ TeV}$ ATLAS data.

The observation of the first $\pi^0 \rightarrow \gamma\gamma$ peak during Run-II using 13 TeV ATLAS data is presented, and $J/\psi \rightarrow e^+e^-$ events at 13 TeV are studied, focusing on background subtraction techniques to compare the EM calorimeter shower variables in data with Monte Carlo simulations.

Finally, irradiations of materials and components to be used at the High Luminosity LHC (HL-LHC) are performed at the Birmingham Irradiation Facility. This thesis describes the commissioning and running of the facility, the irradiation procedure and results of irradiations.

ACKNOWLEDGEMENTS

Firstly, I would like to thank Dr. Stathes Paganis. Through his enthusiasm, knowledge and inspiration both as a researcher and teacher, for his supervision and for opening my eyes to the field of particle physics, leading me to consider this path. I would like to also thank my ‘new’ supervisor, Dr. Christos Anastopoulos for taking over from Stathes and providing me with the help and support to complete my thesis. I am also extremely appreciative of the ShAtlas group, colleagues at CERN and all of the people throughout my studies who have shared their knowledge and have significantly helped me to progress as a researcher. I would particularly like to thank Dimitris, Gary, Tulay and Brais for answering my many questions.

I have thoroughly enjoyed working at the Birmingham Irradiation Facility, on a fascinating project with a brilliant team of people with a notable thank you to Paul D, Paul H, John, Hector and Rich for all of the help, enjoyment and opportunities you have provided me with.

I cannot express how appreciative I am of Dan, his love, patience, and remarkable tea-pouring skills, which have significantly contributed to the making of this thesis and to Helen, for helping me maintain some sanity in coffee discussions, dancing and extremely tasty cakes.

Finally, I am forever thankful for my loving family, I dedicate this work to you, especially to my Mum and Dad for their understanding and for providing me with the support and opportunity which has led me to where I am today.

Contents

Author's Contribution	1
1 Introduction	3
2 Theoretical Background	5
2.1 Introduction	5
2.2 Overview of the Standard Model of Particle Physics	5
2.3 Quantum Electrodynamics (QED)	8
2.4 Quantum Chromodynamics (QCD)	11
2.5 Electroweak Unification	13
2.6 Spontaneous symmetry breaking (SSB)	15
2.7 Electroweak symmetry breaking (EWSB) and the Higgs Mechanism	16
2.8 Limitations of the Standard Model	20
3 The LHC and the ATLAS detector	21
3.1 Introduction	21
3.2 The Large Hadron Collider	21
3.3 The ATLAS Experiment	23
3.3.1 Overview of the ATLAS detector	23
3.3.2 Inner Detector	26
3.3.3 Calorimeter system	29
3.3.4 Magnet System	32
3.3.5 Muon spectrometer	32
3.3.6 Trigger System	33
4 Electron Reconstruction	35
4.1 Introduction	35
4.2 Electron Reconstruction	36
4.2.1 Cluster-track matching	39
4.2.2 Clustering Algorithms	39
4.2.3 Topocluster formation	40
4.3 Superclusters	42
4.3.1 Calibration	44
4.3.2 Performance	50
4.4 Electron Identification	54

4.4.1	Calorimeter information	57
4.4.2	Track information	57
4.4.3	Combined track/calorimeter information	60
4.5	Summary	60
5	Heavy Higgs search in the Higgs to four-lepton channel with 8 TeV data	63
5.1	Introduction	63
5.2	Analysis Overview	66
5.2.1	Event Selection	67
5.2.2	Background Processes and Modelling	71
5.2.3	Signal Modelling	74
5.2.4	Uncertainties	74
5.3	Statistical Interpretation	75
5.3.1	Likelihood Fits	77
5.3.2	Test Statistic	78
5.3.3	Fit Model	78
5.4	Results	79
5.5	Summary	80
6	Calorimeter studies at 13 TeV using $\pi^0 \rightarrow \gamma\gamma$ and $J/\psi \rightarrow e^+e^-$ events	81
6.1	Introduction	81
6.2	Observation of the $\pi^0 \rightarrow \gamma\gamma$ peak	81
6.2.1	Data samples	82
6.2.2	Photon pair selection	82
6.2.3	π^0 mass fit	84
6.3	Background subtraction methods in the $J/\psi \rightarrow e^+e^-$ channel	86
6.3.1	$J/\psi \rightarrow e^+e^-$ selection	87
6.3.2	Background subtraction techniques	88
6.3.3	J/ψ Shower Shapes in data	95
6.4	Summary	95
7	Phase-II ATLAS Upgrades	99
7.1	Introduction	99
7.2	LHC Phase-II Upgrade	99
7.3	Silicon Particle Detectors	104
7.3.1	Semiconductor devices	106
7.3.2	Particle detector operation	108
7.3.3	Signal collected	109
7.4	Radiation Damage	110
7.4.1	Bulk damage	111

7.4.2	Surface damage	111
7.4.3	Annealing	112
7.5	Test Beam Environment	112
7.6	Detector Characterisation	114
7.7	Summary	118
8	Irradiation Facilities	119
8.1	Introduction	119
8.2	The Birmingham Irradiation Facility	119
8.2.1	The University of Birmingham MC40 Cyclotron	121
8.2.2	The scanning system and initial thermal chamber	123
8.2.3	Irradiation Run Procedure	125
8.2.4	Fluence calculation	127
8.2.5	Dosimetry	129
8.3	Birmingham Irradiation Facility Summary	130
8.4	TRIGA Mark III research reactor, Ljubljana	131
8.5	IRRAD, CERN PS	131
8.6	Karlsruhe (KIT)	131
8.7	Los Alamos	132
8.8	CYRIC	132
8.9	Summary	132
9	Results of irradiations and tests performed at the Birmingham Irradiation Facility	135
9.1	Introduction	135
9.2	Initial Results	135
9.3	Development of an improved cooling system	139
9.4	Commissioning of the LN2 system	142
9.4.1	Scan speed	143
9.4.2	Temperature Model	144
9.4.3	Beam current studies	146
9.4.4	Diode studies	146
9.4.5	Energy of cyclotron proton beam	148
9.5	Summary	150
10	Summary	153
	Appendices	154
A	Heavy Higgs search in the Higgs to four-lepton channel Additional Material	155
A.1	Signal Samples for the Heavy Higgs search in the $H \rightarrow ZZ \rightarrow 4\ell$ channel	155
A.2	NWA Limits for the Heavy Higgs search in the $H \rightarrow ZZ \rightarrow 4\ell$ channel	156

List of Tables

2.1	Standard Model fermions and their properties	6
2.2	Standard Model bosons and their properties	6
2.3	Symmetries and conservation laws corresponding to Noether’s Theorem	8
3.1	Resolution requirements of the detector components of the ATLAS detector	25
4.1	Electromagnetic Calorimeter description	37
4.2	Sliding window algorithm parameters used for cluster building	40
4.3	EM Topocluster parameters used for cluster building	41
4.4	Peak and width values of MVA calibrated superclusters and sliding-window electrons	50
4.5	Electron discriminating variables	55
4.6	Electron identification menu variables	56
5.1	Summary of high mass Higgs search in the four-lepton channel event selection	68
5.2	Monte Carlo samples for signal and background for the $H \rightarrow ZZ \rightarrow 4\ell$ analysis	73
6.1	Summary of the event selection requirements applied to $J/\psi \rightarrow e^+e^-$ events using the Tag and Probe Method.	88
7.1	LHC Upgrade programme parameters	102
8.1	MC40 cyclotron beam particles and energies	122
8.2	Overview of the different irradiation facilities	133
9.1	Birmingham irradiation layout configurations	150
A.1	Expected and observed ggF limits on $\sigma \times BR (H \rightarrow ZZ)$ in fb (1/2)	157
A.2	Expected and observed ggF limits on $\sigma \times BR (H \rightarrow ZZ)$ in fb (2/2)	158
A.3	Expected and observed VBF limits on $\sigma \times BR (H \rightarrow ZZ)$ in fb (1/2)	159
A.4	Expected and observed VBF limits on $\sigma \times BR (H \rightarrow ZZ)$ in fb (2/2)	160

List of Figures

2.1	The mexican hat potential of a complex scalar field	17
3.1	The CERN accelerator complex	22
3.2	Peak luminosity versus time for LHC Run-I operation	23
3.3	ATLAS detector and subdetector constituents	24
3.4	ATLAS detector schematic with particle trajectories	25
3.5	ATLAS Inner detector system	27
3.6	Particle traversing the ATLAS Inner detector subdetectors	27
3.7	ATLAS electromagnetic and hadronic Calorimeter systems	29
3.8	Electron resolution curve and its uncertainty	30
3.9	ATLAS electromagnetic calorimeter barrel module	31
3.10	ATLAS toroid and solenoidal magnet system	33
3.11	ATLAS muon spectrometer system	34
4.1	Electromagnetic Calorimeter reconstructed objects: cell, tower and cluster	36
4.2	Material distribution at exit of the ATLAS Inner Detector	37
4.3	ATLAS electron reconstruction and track quality efficiency for 2011 and 2012 data	38
4.4	MVA Calibrated sliding-window single electrons	42
4.5	Supercluster algorithm code flow	43
4.6	ATLAS egamma calibration procedure	45
4.7	Sketch of an MVA algorithm	45
4.8	Uncalibrated accordion energy distribution of superclusters and sliding-window single electrons	47
4.9	Uncalibrated energy response comparing superclusters and sliding-window single electrons	47
4.10	MVA input variable distributions for single electrons	49
4.11	MVA calibrated energy response comparing superclusters and sliding-window single electrons	51
4.12	Uniformity as a function of true E_T and true η for calibrated single electrons	52
4.13	Linearity as a function of true E_T and true η for calibrated single electrons	53
4.14	EM calorimeter discriminating variables for electrons	58
4.15	Inner detector discriminating variables for electrons	59
4.16	Combined track and calorimeter discriminating variables for electrons	61

5.1	95% CL limits on Higgs boson cross-section as set by TeVatron, including limits set by LEP and the LHC	64
5.2	Combined LHC Higgs search results, observation of a 125 GeV Higgs boson	64
5.3	Higgs production cross-sections for pp -collisions at 8 TeV	65
5.4	Feynman diagrams of the Higgs production mechanisms	65
5.5	Cross-section times branching ratio for SM Higgs boson at 8 TeV	66
5.6	Schematic view of the $H \rightarrow ZZ \rightarrow 4\ell$ event categorisation	72
5.7	Combined LEP Higgs search limits, indicating CL_s value	76
5.8	$m_{4\ell}$ distributions for $m_H = 400$ GeV for ggF and VBF categories	79
5.9	95% CL upper limits for $\sigma \times BR (H \rightarrow ZZ)$ in the NWA for ggF production and VBF production	80
6.1	f_1 distribution of photons in π^0 MC events	83
6.2	Kinematic distributions of photon candidates in π^0 events	84
6.3	Invariant mass of diphoton candidates in π^0 events in MC and data	85
6.4	Fit to the invariant mass distribution of diphoton candidates in π^0 events	86
6.5	J/ψ mass distribution comparing MC and pseudo-data indicating the signal region and sideband regions	89
6.6	EM calorimeter shower shapes of electron <i>probes</i> within the signal region	90
6.7	Fitted signal and background components of the J/ψ mass distribution to the pseudo-data	91
6.8	EM calorimeter shower shapes of electron within the signal region subtracting the weighted distribution of the sideband region	92
6.9	EM calorimeter shower shape distributions of the J/ψ signal, extracted using <i>sPlot</i> using pseudo-data	94
6.10	Fitted J/ψ mass distribution of the data	95
6.11	EM calorimeter shower shape distributions of the J/ψ signal, extracted using <i>sPlot</i> with data (1/2)	96
6.12	EM calorimeter shower shape distributions of the J/ψ signal, extracted using <i>sPlot</i> with data (2/2)	97
7.1	Timeline for LHC plan in preparation for the HL-LHC	100
7.2	Cross-sections of Standard Model processes at hadron colliders	101
7.3	Transverse impact resolution in Run-I vs Run-II	102
7.4	Total Integrated ATLAS Luminosity in 2015	103
7.5	Letter of Intent proposed layout for the ATLAS ITK tracker	105
7.6	n-type and p-type semiconductors with their corresponding band gaps	107
7.7	Reverse bias applied to a pn-junction	107
7.8	Structure of a n-in-p silicon particle detector device	108
7.9	Probability distribution for energy deposition for 500 MeV pions	110

7.10	Change of the effective doping concentration as a function of annealing time	113
7.11	Displacement damage in Silicon as a function of particle energy	114
7.12	Reverse current against bias voltage	115
7.13	Inverse capacitance squared against bias voltage	116
7.14	Charge collection measurements of an unirradiated sensor as a function of bias voltage	117
8.1	Metal dees at the Birmingham Cyclotron	121
8.2	Accelerated spiral path of ions within a cyclotron	122
8.3	Birmingham thermal chamber and scanning system	124
8.4	Scan path of six mini sensors traversing cyclotron beam	124
8.5	The lid and inside of the cold box	125
8.6	Gafchromic film used for alignment	126
8.7	Scan path of three mini sensors indicating beam in ‘Home’ position	128
8.8	Accuracy of achieved fluence compared to target	130
8.9	Gamma spectrum of a Nickel activation foil after irradiation	130
9.1	Charge collection measurements comparing sensors irradiated at different facilities	136
9.2	PCB materials irradiated at the Birmingham Irradiation Facility	137
9.3	I-V measurement of different fluence irradiations at the Birmingham Irradiation Facility	137
9.4	CCE measurements comparing sensors irradiated at the Birmingham Irradiation Facility with Los Alamos and KEK	138
9.5	Temperature measurements from room temperature with a 1 μ A simulated beam current using the miniheater	139
9.6	Prototype cold box with upgrades	140
9.7	Temperature measurements of LN2 evaporative cooling in the dummy cold box	141
9.8	Temperature measurements using different simulated beam currents with the LN2 cooling system	141
9.9	New carbon fibre frame for mounting samples	142
9.10	Silicon finger with PT1000s for in-beam temperature measurements	143
9.11	Temperature measurements of the silicon sensor using PT1000 sensors during an irradiation using different x-velocities	144
9.12	Temperature model predictions compared with data	145
9.13	Temperature model simulations of different beam currents at 4 mm s ⁻¹	146
9.14	Charge collection measurements of samples irradiated at the Birmingham Irradiation Facility with different beam currents	147
9.15	Charge collection measurements of a diode	147
9.16	Bragg peak of 27 MeV proton cyclotron beam	148
9.17	String mounting and charge collections showing absorption of low energy protons	149

9.18	Charge collection signal hitmaps of additional sensor close to beam and shielded sensor	149
9.19	Setup of Birmingham irradiations to test suitable mounting procedure	150
9.20	Charge collection measurements of sensors irradiated using different mounting configurations	151
9.21	Charge collection measurements of ATLAS12 sensors irradiated at different proton facilities	152

Author's Contribution

The content within this thesis builds upon the work performed by a large number of people within the ATLAS collaboration. The author's contributions during her degree is summarised in this section.

Upgrade Work

The author was part of the UK Irradiation Team and an expert operator of the robotic scanning system based at Birmingham, requiring weekly visits for approximately two years of her degree to run the system. Additionally, she was involved in commissioning the upgraded cooling system, performing temperature tests both at Sheffield and in Birmingham after installation.

Analysis

The author has contributed to several analyses; most notably in the HZZ working group working on the limit setting for the heavy Higgs search in the $H \rightarrow ZZ \rightarrow 4\ell$ channel. She produced a Public approved ATLAS plot of the first observation of the $\pi^0 \rightarrow \gamma\gamma$ peak with 13 TeV data in May 2015, and has also studied background subtraction techniques to compare the shower shapes of $J/\psi \rightarrow e^+e^-$ decays from data with Monte Carlo using 13 TeV data. This involved using the Tag And Probe technique.

Service Work

The author's service work task focused on studying a new electron reconstruction algorithm using topological clusters to form "superclusters". The aim of the new algorithm is to account for radiative losses to reduce the long low energy resolution tail. She has studied different clustering techniques, and later the calibration of the superclusters. This work has continued, after the service task was complete, and is currently being incorporated to the latest ATLAS software release.

Additional Contributions

The author has presented her work at a number of meetings at international conferences which include a poster presentation on the Birmingham Irradiation Facility at the STFC HEP Summer School, TIPP2014 conference poster presentation, and talks at the RESMDD14 and IOP HEPP 2015 conferences. She has also presented supercluster studies as a poster at ATLAS UK 2013, and talks at egamma workshops at Mainz 2013, and in Paris 2014, as well as many internal meetings. At ATLAS UK, Sussex 2015 the author presented a poster on the High Mass Higgs search in the Higgs to four-lepton channel.

The author has represented postgraduate students on the Sheffield Physics & Astronomy Department's Equality and Diversity committee for the Athena SWAN application, and the Department was awarded the Bronze Award in May 2014. She has also volunteered at a number of outreach events including; CERN Open Days, TEDxCERN event during her time on LTA at CERN and the Big Bang Exhibition at Birmingham NEC.

Chapter 1

Introduction

The primary goal of high energy particle physics is to further our understanding of the fundamental forces and particles in nature. The Large Hadron Collider (LHC) has been designed to fulfil a wide physics programme, including searches for the Higgs boson as well as for new physics. The scope of this thesis is based on the ATLAS experiment, with analysis of data collected, studies of the calorimeter performance and preparation for future upgrades to the ATLAS detector.

Chapter 2 gives an introduction to the Standard Model of particle physics and the four fundamental forces, providing a description of Electroweak Symmetry breaking and the limitations of the Standard Model which motivate searches for new physics at the LHC. Chapter 3 provides an overview of the LHC machine and a detailed description of the ATLAS detector.

Chapter 4 summarises the current ATLAS reconstruction algorithm for electron objects and introduces studies into a new algorithm. This new, novel superclustering algorithm aims to improve the energy response by accounting for radiative losses. Studies using this algorithm are presented as well as a calibration procedure and electron performance using superclusters. Electron identification within ATLAS is also discussed, introducing powerful discriminating variables used in analyses involving electrons.

Chapter 5 describes a search for an additional Heavy Higgs state in the $H \rightarrow ZZ^{(*)} \rightarrow 4\ell$ channel using 8 TeV data. An overview of the analysis procedure is given and in the absence of signal, 95% confidence level limits are presented for each of the main production mechanisms assuming the Narrow Width Approximation.

Chapter 6 presents the observation of the π^0 meson in the diphoton channel with first 13 TeV collisions and also discusses several background subtraction methods using $J/\psi \rightarrow e^+e^-$ events to determine the best technique to extract signal electrons to study.

Chapter 7 provides an introduction to the ATLAS Phase-II upgrades and an overview of the basic

principles of silicon particle detectors. The effect of radiation damage is also described along with characterisation techniques to assess device performance after exposure to high levels of radiation. The Birmingham Irradiation Facility is described in Chapter 8, giving details of the experimental setup and irradiation procedure, followed by a brief summary of other irradiation facilities. Chapter 9 reports the commissioning tests performed at the Birmingham Irradiation Facility, including device characterisation results and comparisons with other facilities.

Finally, Chapter 10 gives a brief summary and a few final concluding remarks about the research presented in this thesis.

Chapter 2

Theoretical Background

2.1 Introduction

This chapter introduces the Standard Model (SM) of particle physics which describes fundamental particles and their interactions. A brief qualitative introduction to the SM is given and then the gauge fields are mathematically constructed using the principle of local gauge invariance, starting with the Dirac Lagrangian. Spontaneous symmetry breaking of local gauge symmetry is described leading to the Higgs Mechanism. Finally, the limitations of the SM are discussed.

2.2 Overview of the Standard Model of Particle Physics

The Standard Model (SM) of particle physics is currently the best available model describing the fundamental particles and forces of nature. Whilst it is not a complete model, neglecting to incorporate fundamental concepts such as gravity, the SM successfully explains the properties of fundamental particles and forces, including the newly discovered Higgs boson [1, 2].

Fundamental particles can be classified using their internal angular momentum quantum number, spin. Fermions are particles with half-integer spin which includes leptons and quarks, and bosons have integer spin, mediating interactions.

Leptons and quarks consist of three generations of particles, where each generation has equivalent properties but different mass, as shown in Table 2.1. Fermions also have a corresponding anti-fermion counterpart of equal mass and opposite quantum numbers.

Each lepton generation includes an electrically charged lepton and a neutrino. Neutrinos are neutral particles and are treated as massless in the SM. In total, there are 6 leptons and 6 anti-leptons in the SM.

Generation	Leptons			Quarks		
	Particle	Mass (MeV)	Charge (e)	Particle	Mass (MeV)	Charge (e)
I	electron (e)	0.511	-1	up (u)	$2.3^{+0.7}_{-0.5}$	$+\frac{2}{3}$
	electron neutrino (ν_e)	$< 2 \times 10^{-6}$	0	down (d)	$4.8^{+0.7}_{-0.3}$	$-\frac{1}{3}$
II	muon (μ)	105.65	-1	charm (c)	1275 ± 25	$+\frac{2}{3}$
	muon neutrino (ν_μ)	$< 2 \times 10^{-6}$	0	strange (s)	95 ± 5	$-\frac{1}{3}$
III	tau (τ)	1776.82	-1	top (t)	173200 ± 800	$+\frac{2}{3}$
	tau neutrino (ν_τ)	$< 2 \times 10^{-6}$	0	bottom (b)	4650 ± 30	$-\frac{1}{3}$

Table 2.1: The properties of the three fermion generations within the Standard Model, with lepton and quark information from [3] (Units are used where $\hbar = c = 1$).

Force	Theory	Gauge boson	Mass (MeV)	Charge (e)	Coupling constant
Strong	Quantum Chromodynamics (QCD)	gluon (g)	0	0	$\alpha_s(m_Z) = 0.119$
Weak	Electroweak (EW)	W^\pm	80385 ± 15	± 1	$\alpha_w = 10^{-6}$
		Z	91188 ± 2	0	
Electromagnetic	Quantum Electrodynamics (QED)	photon (γ)	0	0	$\alpha = 1/137$

Table 2.2: The three forces described by the Standard Model with their corresponding theory and gauge bosons which mediate the force. The boson properties are from [3] (Units are used where $\hbar = c = 1$).

Similar to leptons, there are 6 flavours of quarks where each generation includes a quark with charge $+2/3$ and a quark with charge $-1/3$ [4]. Each quark carries an additional colour charge, with three types; red (r), green (g), blue (b). This generates 18 quarks and 18 anti-quarks in the SM.

The quark model and the concept of colour was motivated by the discovery of many different hadrons in the 1960s. Initially the Eightfold way was used [4], geometrically organising the many newly discovered, composite particles in patterns as a method of classification. The triangular patterns observed from these families of particles led to the quark model, predicting three flavours of quarks which are the elementary constituents forming these particles. On the discovery of Δ^{++} , made from three up-quarks, it was established that due to the Pauli exclusion principle, another quantum number must exist to allow three quarks of the same type. This quantum number was colour, introducing the three colour types. Following the quark model, many more composite particles were discovered, leading to the discovery of a fourth (c) and fifth (b) quark and finally a sixth quark (t) was predicted and later discovered in 1995.

No free quark states are observed in nature which is a phenomenon known as quark confinement. Only bound colourless states are observed, formed from two or three quarks to generate a composite particle with integer charge. These particles are known as hadrons. Two quark states are referred to as mesons and are formed from a quark and an anti-quark ($q\bar{q}$). Three quark states, such as protons and neutrons, are known as baryons and require each quark colour charge to be different.

Further to this, the observation of four and five quark states has recently been reported by the LHCb experiment [5, 6].

Bosons act as force carriers, mediating the strong, weak and electromagnetic (EM) forces, with the properties described in Table 2.2. The relative strength of each force is characterised by the coupling constants, which in the case of the strong force varies depending on distance between quarks and leads to the concept of asymptotic freedom [4]. At large (nuclear) distances, the relative strength is 1, however this decreases asymptotically at smaller distances, causing the quarks within a confined state to be free.

Massless photons are propagators of the electromagnetic force between electrically charged fermions, W and Z bosons mediate weak interactions between weakly charged fermions, and gluons are the quanta of the strong interaction field in quark interactions. Bosons are therefore the force fields and fermions are the matter fields. In terms of fermions, neutrinos interact only via the weak force, charged leptons interact with the EM and weak forces and quarks interact with all three forces.

The SM is a quantum field theory (QFT) which incorporates quantum mechanics and relativity to describe the dynamics of particles and their interactions. The particles, or quanta, associated with the interacting fields are gauge bosons and are treated as excitations of a field, carrying charge in fermion interactions. The SM can be formulated as a non-Abelian gauge theory whereby the Lagrangian is gauge invariant under local transformations.

In the 1940s and 1950s, the theory of the electromagnetic force, Quantum Electrodynamics (QED), was the first QFT developed to describe charged particles and their interactions [4]. Within the SM, the electromagnetic and weak forces are unified into a single theory, known as electroweak (EW) theory which is described by the $SU(2)_L \times U(1)_Y$ gauge group. The $U(1)_Q$ group describes the EM force, with one associated generator and $SU(2)_L$ describes the weak group with 3 associated generators, where L indicates coupling to left handed fermions only, as will later be discussed. If the EW group is invariant under local gauge transformations, the fields should be massless, as mass terms destroy the gauge symmetry. The physical fields arise from linear combinations of the gauge fields due to spontaneous symmetry breaking via the Higgs Mechanism.

The strong force is described by the theory of Quantum Chromodynamics (QCD) and is associated with the $SU(3)_C$ gauge group which is invariant under local gauge transformations, through 8 massless, self-interacting generators.

The SM is therefore represented by $SU(3)_C \times SU(2)_L \times U(1)_Y$ describing a total of 61 particles, including the Higgs boson, whose role will be explained in Section 2.7. Conservation laws arise

from the symmetries imposed by the local gauge invariance in accordance with Noether's Theorem, as presented in Table 2.3. As a result of the symmetry of the Lagrangian, current is conserved which is often referred to as charge. This will be shown mathematically in the following sections.

Symmetry	Conservation Law
Translation in Time	Energy
Translation in Space	Momentum
Rotation	Angular Momentum
Gauge Transformation	Charge

Table 2.3: Symmetries and their associated conservation laws corresponding to Noether's Theorem [4].

2.3 Quantum Electrodynamics (QED)

Quantum Electrodynamics (QED) describes electromagnetic interactions between electrically charged fermions and a massless gauge boson, the photon. QED is based on the $U(1)_Q$ Abelian gauge symmetry group, where Q is the electric charge, and the QED Lagrangian can be derived which describes all electrodynamics, free fermions and their corresponding interactions.

The Dirac Lagrangian can be used to describe spin- $\frac{1}{2}$ particles of mass m and charge q :

$$\mathcal{L}_{\text{Dirac}} = \bar{\psi} (i\gamma^\mu \partial_\mu - m) \psi. \quad (2.1)$$

The Dirac Lagrangian is invariant under global gauge transformations of the form:

$$\psi \rightarrow e^{i\theta} \psi, \quad \bar{\psi} \rightarrow e^{-i\theta} \bar{\psi}. \quad (2.2)$$

as each term is multiplied by $e^{i\theta} e^{-i\theta} \equiv 1$. However, if local gauge invariance is imposed:

$$\psi \rightarrow e^{i\theta(x)} \psi(x). \quad (2.3)$$

a dependence on position is introduced with the function $\theta(x)$, which results in an additional term in the Lagrangian due to the derivative. The Lagrangian is therefore no longer invariant under local

transformations, since,

$$\mathcal{L} \rightarrow \mathcal{L} - (\partial_\mu \theta \bar{\psi} \gamma^\mu \psi). \quad (2.4)$$

To restore gauge invariance under local transformations, an additional term is added by introducing a new vector gauge field, A_μ , representing an interaction field which couples to charged spin- $\frac{1}{2}$ particles. The Dirac Lagrangian becomes:

$$\mathcal{L} = \bar{\psi} (i\gamma^\mu \partial_\mu - m) \psi - q\bar{\psi} \gamma^\mu A_\mu \psi. \quad (2.5)$$

The gauge field must also be invariant under local gauge transformations, which results in the transformation:

$$A_\mu \rightarrow A_\mu + \partial_\mu \lambda. \quad (2.6)$$

The additional term contains a new function λ , which is defined as:

$$\lambda(x) = -\frac{1}{q}\theta(x). \quad (2.7)$$

When added to the transformation of the Lagrangian in Equation 2.4, the additional terms cancel and local phase invariance is restored. However, whilst this incorporates the interactions of the field with fermions, it does not describe the free field, A_μ . This requires a final ‘‘kinetic energy’’ term to describe a real, physical field:

$$F^{\mu\nu} = \partial^\mu A^\nu - \partial^\nu A^\mu. \quad (2.8)$$

which yields the following Lagrangian:

$$\mathcal{L}_{free} = -\frac{1}{4}F^{\mu\nu}F_{\mu\nu} + \frac{1}{2}m_A^2 A^\nu A_\nu. \quad (2.9)$$

In order to be invariant, m_A must equal 0, resulting in a massless gauge boson, the photon. The QED Lagrangian is derived by taking the Lagrangian from free Dirac fields and imposing a local gauge invariance, which leads to the Lagrangian:

$$\mathcal{L} = \bar{\psi} (i\gamma^\mu \partial_\mu - m) \psi - \frac{1}{4} F_{\mu\nu} F^{\mu\nu} - q\bar{\psi}\gamma^\mu A_\mu\psi. \quad (2.10)$$

The associated conservation from the symmetry of the QED Lagrangian according to Noether's theorem in Table 2.3 is electric charge, where the EM current density is:

$$J^\mu = q (\bar{\psi}\gamma^\mu\psi). \quad (2.11)$$

which agrees with the Maxwell equations of electrodynamics.

The covariant derivative can be introduced as a useful notation, which is defined in terms of the new field:

$$D_\mu \equiv \partial_\mu + iqA_\mu. \quad (2.12)$$

The covariant derivative can be used as a modified derivative in Equation 2.10 and whilst the derivative transforms as:

$$\partial_\mu\psi \rightarrow e^{-iq\lambda} [\partial_\mu - iq(\partial_\mu\lambda)]\psi. \quad (2.13)$$

as shown with the additional term in Equation 2.4, the covariant derivative transformation is equivalent to the transformation in ψ , in Equation 2.3. The covariant derivative transformation is given by:

$$D_\mu\psi \rightarrow e^{-iq\lambda} D_\mu\psi. \quad (2.14)$$

By introducing the covariant derivative to the Lagrangian, the local gauge invariance is restored.

This completes the conversion of a globally invariant Lagrangian into a locally invariant one, by introducing a new massless vector field and the final Lagrangian can be expressed as the Dirac Lagrangian, where ∂_μ has been modified to the D_μ , which transforms covariantly, and an additional “kinetic term”.

$$\mathcal{L}_{\text{QED}} = \bar{\psi} (i\gamma^\mu D_\mu - m) \psi - \frac{1}{4} F_{\mu\nu} F^{\mu\nu}. \quad (2.15)$$

Introducing the covariant derivative D_μ and gauge fields A_μ to the free Dirac Lagrangian produces a locally gauge invariant Lagrangian. This method can be generalised to non-Abelian Lie groups, $SU(N)$ to construct weak and QCD gauge theories.

2.4 Quantum Chromodynamics (QCD)

Quantum chromodynamics describes the interactions of quarks, mediated by gluons which carry colour charge [7]. QCD is based on the non-Abelian $SU(3)_C$ gauge group where invariance under local gauge transformations can be imposed, using a similar approach to QED, to derive the QCD Lagrangian. By definition, there are $N^2 - 1$ generators of an $SU(N)$ group, leading to one generator in QED under $U(1)$ symmetry, 3 generators for $SU(2)$ group, involving the three Pauli τ matrices and 8 generators in the $SU(3)$ QCD group which involve the eight Gell-Mann λ matrices.

Following the same procedure as Section 2.3, the Dirac Lagrangian in Equation 2.1 is used to describe spin- $\frac{1}{2}$ quarks. The field ψ is now a three component column vector, which describes the three equal mass Dirac fields corresponding to the three colours of a quark. ψ is defined as:

$$\psi \equiv \begin{pmatrix} \psi_r \\ \psi_g \\ \psi_b \end{pmatrix}, \quad \bar{\psi} \equiv (\bar{\psi}_r, \bar{\psi}_g, \bar{\psi}_b). \quad (2.16)$$

In QCD, the Dirac Lagrangian, Equation 2.1, is invariant under global transformations, as in QED, and local transformations of the $SU(3)_C$ gauge group take the form:

$$\psi \rightarrow e^{i\theta} e^{-ig\lambda\cdot\phi} \psi, \quad \bar{\psi} \rightarrow e^{-i\theta} e^{ig\lambda\cdot\phi} \bar{\psi}. \quad (2.17)$$

where in addition to the U(1) phase transformation, a transformation of the SU(3)_C group is introduced. λ represents the Gell-Mann matrices [4], and the vector $\boldsymbol{\phi} = -\mathbf{a}/g$, where \mathbf{a} is a vector of 8 real numbers and g is the strong coupling constant.

An additional vector field can be added which represents 8 massless gauge fields as the gluons, analogous to the photon field in QED. The derivative is replaced by the covariant derivative which is defined as:

$$D_\mu \equiv \partial_\mu + ig\boldsymbol{\lambda} \cdot \mathbf{A}_\mu. \quad (2.18)$$

It follows that the free term of the gauge field contains the Abelian (QED) result (Equation 2.8) plus an extra term:

$$\mathbf{G}^{\mu\nu} = \partial^\mu \mathbf{A}^\nu - \partial^\nu \mathbf{A}^\mu - 2g (\mathbf{A}^\mu \times \mathbf{A}^\nu). \quad (2.19)$$

The additional term is responsible for the gluon self-interaction as the gluons themselves carry colour charge, unlike the neutral charge mediator in QED. The cross-product of the free term can also be expressed as:

$$(\mathbf{B} \times \mathbf{C})_i = \sum_{j,k=1}^8 f_{ijk} B_j C_k. \quad (2.20)$$

where f_{ijk} are the real structure constants of the SU(3)_C group. The QCD Lagrangian can be written as:

$$\mathcal{L}_{\text{QCD}} = \bar{\psi} (i\gamma^\mu \partial_\mu - m) \psi - \frac{1}{4} \mathbf{G}_{\mu\nu} \mathbf{G}^{\mu\nu} - (g\bar{\psi}\gamma^\mu \boldsymbol{\lambda}\psi) \cdot \mathbf{A}_\mu. \quad (2.21)$$

which exhibits the same form as the QED Lagrangian and again, substituting the derivative with the covariant derivative leads to a simplified Lagrangian:

$$\mathcal{L}_{\text{QCD}} = \bar{\psi} (i\gamma^\mu D_\mu - m) \psi - \frac{1}{4} \mathbf{G}_{\mu\nu} \mathbf{G}^{\mu\nu}. \quad (2.22)$$

This has to be generated 6 times to account for all quark flavours, where m is the mass of each flavour. 8 colour currents arise, each associated with a field and are the source of QCD interactions in the same way that electric charge is the source of QED interactions. The colour current is defined as:

$$\mathbf{J}^\mu = g (\bar{\psi} \gamma^\mu \lambda \psi). \quad (2.23)$$

The free Dirac Lagrangian has been used to impose local gauge transformations within the QCD SU(3) group. Eight gauge fields, known as gluons, have been generated which propagate the colour charge.

2.5 Electroweak Unification

Electromagnetic and weak interactions are single manifestations of the electroweak force and on unification, four gauge fields arise; an isotriplet of vector bosons W and an isosinglet B , as described by Glashow-Weinberg-Salam [8, 9, 10]. The symmetry group which governs the electroweak force is a combination of $SU(2)_L \times U(1)_Y$, where $SU(2)_L$ refers to the weak isospin and involves left-handed fermions only, whilst $U(1)_Y$ refers to weak hypercharge and involves all fermion states. This means that the generator of the $U(1)_Y$ group commutes with the generators of the $SU(2)_L$ group. The weak isospin (I) of fermions can be related to the charge (Q) and the weak hypercharge (Y), where the third component of isospin (I_3) is defined as:

$$I_3 = Q - \frac{1}{2}Y. \quad (2.24)$$

The three generations of quarks and leptons have the property of chirality and are referred to as right-handed or left-handed. Left-handed fermions are described as weak isodoublets, whilst right-handed fermions form weak isosinglets. Due to the commuting generators, the left-handed fermions are grouped together and must carry the same hypercharge.

$$\psi_{\text{leptons}} = \begin{pmatrix} \nu_L^e \\ e_L \end{pmatrix}, e_R, \begin{pmatrix} \nu_L^\mu \\ \mu_L \end{pmatrix}, \mu_R, \begin{pmatrix} \nu_L^\tau \\ \tau_L \end{pmatrix}, \tau_R. \quad (2.25)$$

$$\psi_{\text{quarks}} = \begin{pmatrix} u_L \\ d_L \end{pmatrix}, u_R, d_R, \begin{pmatrix} c_L \\ s_L \end{pmatrix}, c_R, s_R, \begin{pmatrix} t_L \\ b_L \end{pmatrix}, t_R, b_R. \quad (2.26)$$

Using the same approach as QED and QCD, starting with the Dirac Lagrangian to describe the fermions, the EW Lagrangian can be derived, introducing four new gauge fields, $W_\mu^{1,2,3}$ and B_μ , corresponding to the $SU(2)_L$ and $U(1)_Y$ symmetry groups. The generators of the $U(1)_Y$ EW group mix the isosinglet (B_μ) and the third component of the isotriplet (W_μ^3). The covariant derivative is defined as:

$$D_\mu = \partial_\mu + ig_Y \frac{Y}{2} B_\mu + ig_W \frac{\boldsymbol{\tau}}{2} \cdot \mathbf{W}_\mu. \quad (2.27)$$

where g_Y and g_W are the coupling constants for each group and $\boldsymbol{\tau}$ represents the $SU(2)_L$ group Pauli matrices. There are then two charged vector bosons $W^{1,2}$ and two neutral ones, W^3 and B .

The invariant $SU(2)_L \times U(1)_Y$ Lagrangian is given by:

$$\mathcal{L}_{\text{EW}} = \bar{\psi} (i D_\mu - m) \psi - \frac{1}{4} \mathbf{W}^{\mu\nu} \cdot \mathbf{W}_{\mu\nu} - \frac{1}{4} B^{\mu\nu} B_{\mu\nu}. \quad (2.28)$$

Rewriting these terms as linear combinations of the weak and hypercharge vector fields, gives rise to the W^\pm , Z and A physical fields corresponding to the 3 weak gauge bosons and the photon, whereby the photon field is required to be the same electromagnetic field as in Section 2.3. The electroweak mediators are therefore defined as:

$$W_\mu^\pm = \frac{1}{\sqrt{2}} (W_\mu^1 \mp i W_\mu^2), \quad (2.29a)$$

$$Z_\mu = \cos \theta_W W_\mu^3 - \sin \theta_W B_\mu, \quad (2.29b)$$

$$A_\mu = \sin \theta_W W_\mu^3 + \cos \theta_W B_\mu. \quad (2.29c)$$

The angle θ_W is the weak mixing angle which yields the physical vector fields and also defines the relationship between the mass of the W and Z bosons, the next topic for discussion.

2.6 Spontaneous symmetry breaking (SSB)

In the electroweak Lagrangian, no mass terms are included. Simply adding mass terms would violate $SU(2)_L \times U(1)_Y$ symmetry and to incorporate the mass, electroweak symmetry must be broken via the Higgs mechanism [11, 12, 13, 14], introducing a new complex scalar doublet field. To construct a Lagrangian with mass terms, first, the simple case of a real scalar field is considered to introduce the concept of spontaneous symmetry breaking. Section 2.7 will extend this to the electroweak group.

Using the definition of the Lagrangian, $\mathcal{L} = \mathcal{T} - \mathcal{U}$, the potential involving a real scalar field, ϕ is:

$$\mathcal{U}(\phi) = -\frac{1}{2}\mu^2\phi^2 + \frac{1}{4}\lambda^2\phi^4. \quad (2.30)$$

This potential generates two minima at $\phi = \pm\mu/\lambda$, and the Lagrangian is,

$$\mathcal{L} = \frac{1}{2}(\partial_\mu\phi)(\partial^\mu\phi) + \frac{1}{2}\mu^2\phi^2 - \frac{1}{4}\lambda^2\phi^4. \quad (2.31)$$

In this case however, the mass term has the wrong sign, generating an imaginary and unphysical mass. To overcome this, the ground state is redefined by introducing a new field parameter η , where:

$$\eta \equiv \phi \pm \mu/\lambda. \quad (2.32)$$

The Lagrangian is now defined as:

$$\mathcal{L} = \frac{1}{2}(\partial_\mu\eta)(\partial^\mu\eta) - \mu^2\eta^2 \pm \mu\lambda\eta^3 - \frac{1}{4}\lambda^2\eta^4 + \text{const.} \quad (2.33)$$

In this Lagrangian, the mass term has the correct sign from the mass term with a mass of,

$$m_\eta = \sqrt{2}\mu. \quad (2.34)$$

The Lagrangian in Equation 2.33 contains higher order terms. This corresponds to triple and quartic scalar couplings.

The initial Lagrangian of a real scalar field in Equation 2.31 is of even symmetry, remaining invariant under the transformation $\phi \rightarrow -\phi$ and results in unphysical mass term, whilst in the Lagrangian in terms of η , the symmetry has been spontaneously broken by choosing an arbitrary ground state. The principle of spontaneous symmetry breaking can be extended, first to a complex field and then to a complex doublet of scalar fields, in the case of $SU(2)_L \times U(1)_Y$.

2.7 Electroweak symmetry breaking (EWSB) and the Higgs Mechanism

Applying the same spontaneous symmetry breaking principle to a single complex scalar field, in addition to requiring the Lagrangian to be invariant under local transformations, as in Section 2.5, gives rise to a mass term and a new field. In this case ϕ is defined as,

$$\phi = \phi_1 + i\phi_2. \quad (2.35)$$

and the most general potential of this field is given as:

$$\mathcal{U}(\phi) = -\frac{1}{2}\mu^2(\phi^*\phi) + \frac{1}{4}\lambda^2(\phi^*\phi)^2. \quad (2.36)$$

with a Lagrangian of,

$$\mathcal{L} = \frac{1}{2}(\partial_\mu\phi)^*(\partial^\mu\phi) + \frac{1}{2}\mu^2\phi^*\phi - \frac{1}{4}\lambda^2(\phi^*\phi)^2. \quad (2.37)$$

In the potential in Equation 2.36, only $\lambda > 0$ is considered to give a stable ground state with a circle of minima in the $\phi_1 - \phi_2$ plane at $\phi_1^2 + \phi_2^2 = \mu^2/\lambda^2$. This is shown as a ‘‘mexican hat potential’’ in Figure 2.1 which results in a non-zero minimum potential, where the blue ball at the top of the hat is at a potential of zero. For the circle of minima, the vacuum expectation value is therefore also non-zero.

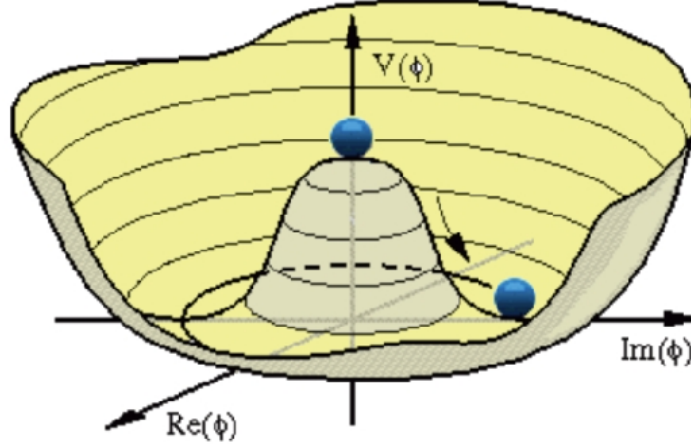


Figure 2.1: The potential of a complex scalar field often referred to as the mexican hat potential [15].

Using the same principle, imposing a local U(1) invariance under the transformation in Equation 2.3, a new field A_μ can be introduced. Using the definition of the covariant derivative from Equation 2.12 to replace the derivative, it follows that:

$$\mathcal{L} = \frac{1}{2} [(\partial_\mu - iqA_\mu)\phi^*][(\partial^\mu + iqA^\mu)\phi] + \frac{1}{2}\mu^2\phi^*\phi - \frac{1}{4}\lambda^2(\phi^*\phi)^2 - \frac{1}{4}F^{\mu\nu}F_{\mu\nu}. \quad (2.38)$$

By choosing an arbitrary vacuum state, two new fields arise:

$$\eta \equiv \phi_1 - \mu/\lambda, \quad \xi \equiv \phi_2. \quad (2.39)$$

This breaks the gauge invariance and yields a Lagrangian:

$$\mathcal{L} = \left[\frac{1}{2}(\partial_\mu\eta)(\partial^\mu\eta) - \mu^2\eta^2 \right] + \left[\frac{1}{2}(\partial_\mu\xi)(\partial^\mu\xi) \right] + \left[-\frac{1}{4}F^{\mu\nu}F_{\mu\nu} + \frac{1}{2}\left(\frac{q\mu}{\lambda}\right)^2 A_\mu A^\mu \right] + \dots \quad (2.40)$$

The first term is the same as in Equation 2.33 representing a scalar particle η of mass $\sqrt{2}\mu$, the second term represents a massless boson ξ and the third and fourth term describe the free gauge field A_μ , which has now acquired a mass of $q\mu/\lambda$. In addition to this, there are couplings of η , ξ , A_μ , and an interaction term which are not presented here.

The massless boson ξ is a consequence of Goldstone theory whereby spontaneous symmetry breaking of continuous global symmetries is always accompanied by one or more massless scalar particles which are referred to as Goldstone bosons [4]. This boson however introduces incorrect interactions into the Lagrangian and can be removed by choosing a specific gauge. For $\phi \rightarrow \phi'$, one can choose $\theta = -\tan^{-1}(\phi_2/\phi_1)$. ϕ' is therefore real resulting in $\phi'_2 = 0$ and removes the massless Goldstone boson.

By choosing a specific gauge, the Lagrangian for a complex scalar field contains a massive scalar η and a massive gauge field A_μ , where η can be interpreted as the Higgs boson, “giving mass” to a gauge boson.

This however is not the complete picture and the spontaneous symmetry breaking of the $SU(2)_L \times U(1)_Y$ requires an $SU(2)_L$ complex doublet of scalar fields, defined as:

$$\Phi = \frac{1}{\sqrt{2}} \begin{pmatrix} \phi_1 + i\phi_2 \\ \phi_3 + i\phi_4 \end{pmatrix}. \quad (2.41)$$

The covariant derivative is equivalent to Equation 2.27, incorporating the weak gauge fields, $W_\mu^{1,2,3}$ and B_μ and the consequent Lagrangian is defined as:

$$\mathcal{L} = (D_\mu \Phi)^\dagger (D^\mu \Phi) - \mu^2 (\Phi^\dagger \Phi) + \lambda (\Phi^\dagger \Phi)^2 \quad (2.42)$$

which is invariant under $SU(2)_L \times U(1)_Y$ gauge transformations. Again, a vacuum state must be chosen from the set of minima at $\Phi^\dagger \Phi = \mu^2/2\lambda$ to break the $SU(2)_L \times U(1)_Y$ symmetry. A non-zero vacuum expectation value is assigned to ϕ_3 and the fields are redefined as:

$$\phi_1 = \phi_2 = \phi_4 = 0, \quad \eta \equiv \phi_3 - v. \quad (2.43)$$

where $v = \sqrt{\mu^2/\lambda}$ and this choice of field variables removes the three Goldstone fields and their nuisance interaction terms. Imposing a local $SU(2)$ gauge invariance, as in the QED and QCD prescription in Sections 2.3 and 2.4, now yields four independent scalar fields. Similar to the case of the complex scalar field where one Goldstone boson is “gauged away”, the final Higgs Lagrangian produces mass terms for the three weak gauge bosons, a massless boson as well as field variables which predict a single massive scalar η . This is defined as the Higgs boson.

The mass term relations are defined as:

$$m_H = \sqrt{2}\mu, \quad (2.44a)$$

$$m_{W^\pm} = \frac{1}{2}vg_W, \quad (2.44b)$$

$$m_Z = \frac{1}{2}v\sqrt{g_W^2 + g_Y^2}, \quad (2.44c)$$

$$\cos\theta_W = \frac{m_W}{m_Z}. \quad (2.44d)$$

where $v = \sqrt{\mu^2/\lambda} = 246$ GeV, representing the vacuum expectation value of the Higgs field. The $SU(2)_L \times U(1)_Y$ symmetry has been spontaneously broken to $U(1)_Q$, consequently giving mass to the weak bosons via the Higgs mechanism.

Fermions also acquire mass through interactions with the Higgs field and an additional term arises in the EW Lagrangian, the Yukawa term for quarks and leptons.

The final SM Lagrangian therefore can be summarised by summing the W^\pm , Z and γ kinetic terms and self interactions, the lepton and quark kinetic terms and their interactions with W^\pm , Z and γ , the W^\pm , Z , γ and Higgs masses and couplings and finally the lepton and quark masses and coupling to Higgs - the Yukawa term. The full SM Lagrangian is:

$$\mathcal{L}_{SM} = -\frac{1}{4}\mathbf{W}^{\mu\nu} \cdot \mathbf{W}_{\mu\nu} - \frac{1}{4}B^{\mu\nu}B_{\mu\nu} \quad (2.45)$$

$$+ \bar{L}\gamma^\mu \left(i\partial_\mu - g_W \frac{\boldsymbol{\tau}}{2} \cdot \mathbf{W}_\mu - g_Y \frac{Y}{2} B_\mu \right) L + \bar{R}\gamma^\mu \left(i\partial_\mu - g_Y \frac{Y}{2} B_\mu \right) R \quad (2.46)$$

$$+ \left| \left(i\partial_\mu - g_W \frac{\boldsymbol{\tau}}{2} \cdot \mathbf{W}_\mu - g_Y \frac{Y}{2} B_\mu \right) \phi \right|^2 - V(\phi) \quad (2.47)$$

$$- (G_1 \bar{L}\Phi R + G_2 \bar{L}\Phi R + \text{hermitian conjugate}). \quad (2.48)$$

where L denotes left-handed fermions and R right-handed, and G_1, G_2 are the fermion Higgs couplings [16].

2.8 Limitations of the Standard Model

The discovery of the Higgs boson in 2012 [1, 2] provided evidence of the missing piece of the SM. Whilst the SM is a cornerstone of modern physics and describes particles and their interactions as one of the most successful theories, it has some major shortcomings. In summary, failing to incorporate gravity within QFT, Dark Matter is not explained, neutrinos are treated as massless and the matter-antimatter asymmetry of the universe is not accounted for. Also the SM has at least 19 parameters, which is often regarded as inelegant for a complete theory of nature.

To construct a complete theory, unification of all forces is essential. Theories beyond the SM have been postulated to incorporate some of the missing aspects whilst building on the successful features of the SM.

Beyond the SM theories (BSM) include extensions to the SM such as supersymmetry (SUSY) which introduces partners for all SM particles, assigning a bosonic partner to each fermion and vice versa. The Minimal Supersymmetric Standard Model (MSSM) introduces the minimum number of new particles (referred to as super-partners) and interactions, predicting new Higgs bosons, and potentially providing a dark matter candidate in the form of a weakly interacting massive particle (WIMP).

Several of the extensions to the SM theories predict heavy Higgs boson states in addition to the discovered Higgs boson at 125 GeV. Two commonly used benchmarks are the Electroweak Singlet Model (EWS) and the Two Higgs Doublet Model (2HDM) [17].

The simplest extension to the SM is the EWS model which has one new parameter compared to the SM and is compatible with current measurements of the light Higgs properties. The EWS model predicts two CP-even bosons where the couplings of the heavy Higgs boson are assumed to scale with respect to the SM and the light Higgs decays via the same modes with similar event kinematics to SM Higgs events. The heavy state includes additional decay modes and has a width which can be narrower or wider than the SM width, which can result in interference between the signal and non-resonant diboson backgrounds.

For the 2HDM to be compatible with current observations, five new parameters are required. The two Higgs doublets result in five Higgs bosons: two CP-even bosons (H and h), one CP-odd boson (A) and two charged scalars (H^\pm). The 2HDM models can be classified depending on which type of fermions couple to which doublet. Type-I and type-II 2HDM are relevant for bosonic decays of Higgs bosons and in these classifications the Higgs production modes are similar to SM production.

Chapter 3

The LHC and the ATLAS detector

3.1 Introduction

This chapter will describe the Large Hadron Collider (LHC) and the ATLAS detector [18, 19], including an overview of the CERN accelerator complex and a more detailed description of the individual subdetectors which contribute to the general purpose ATLAS detector. The work in this thesis is based on data collected by the ATLAS detector and mainly focuses on electrons and photons. Therefore, a greater focus is given to the subdetectors concerned with these particles. The LHC and ATLAS experiment are hosted by CERN, the European Organisation for Nuclear Research, in Geneva. As of 2015, there are 21 member states, facilitating international collaboration for research, technology and education [20].

3.2 The Large Hadron Collider

The LHC is currently the largest and most powerful particle accelerator in operation. At 26.7 km in circumference, approximately 100 m under the Swiss-French border, bunches of 1×10^{11} protons collide every 25 ns [21]. The high design luminosity enables the observation of rare processes at a reasonable rate.

The LHC is installed in the same tunnel constructed for the previous particle accelerator, the large electron-positron collider, LEP, which reached maximum centre of mass energy and ceased operation in 2000, in preparation for the LHC [3]. The LHC is designed to collide proton beams accelerating in opposite directions with a centre of mass energy of up to $\sqrt{s} = 14 \text{ TeV}$, with an energy of 7 TeV per proton beam. The LHC can also collide lead ions, however the scope of this work focuses on pp collisions and therefore collisions mentioned will refer only to protons.

To produce high energy proton beams, protons are gradually accelerated to the target energy at the CERN accelerator complex, shown in Figure 3.1. Before entering the accelerator complex, the first

stage is to extract the protons from hydrogen. Hydrogen atoms are stripped of their electrons using an electric field and are injected into a linear accelerator (LINAC2), followed by the BOOSTER, proton-synchrotron systems (PS) and SPS, where the protons are accelerated to 450 GeV and into the LHC [21]. The LHC is the final stage of the CERN accelerator complex. In the LHC, the protons are contained in two separate beam pipes and a system of superconducting dipole magnets steer the beams in opposite directions, whilst the quadrupole magnets focus the beam. Radio frequency cavities accelerate the beam energies to the required energy.

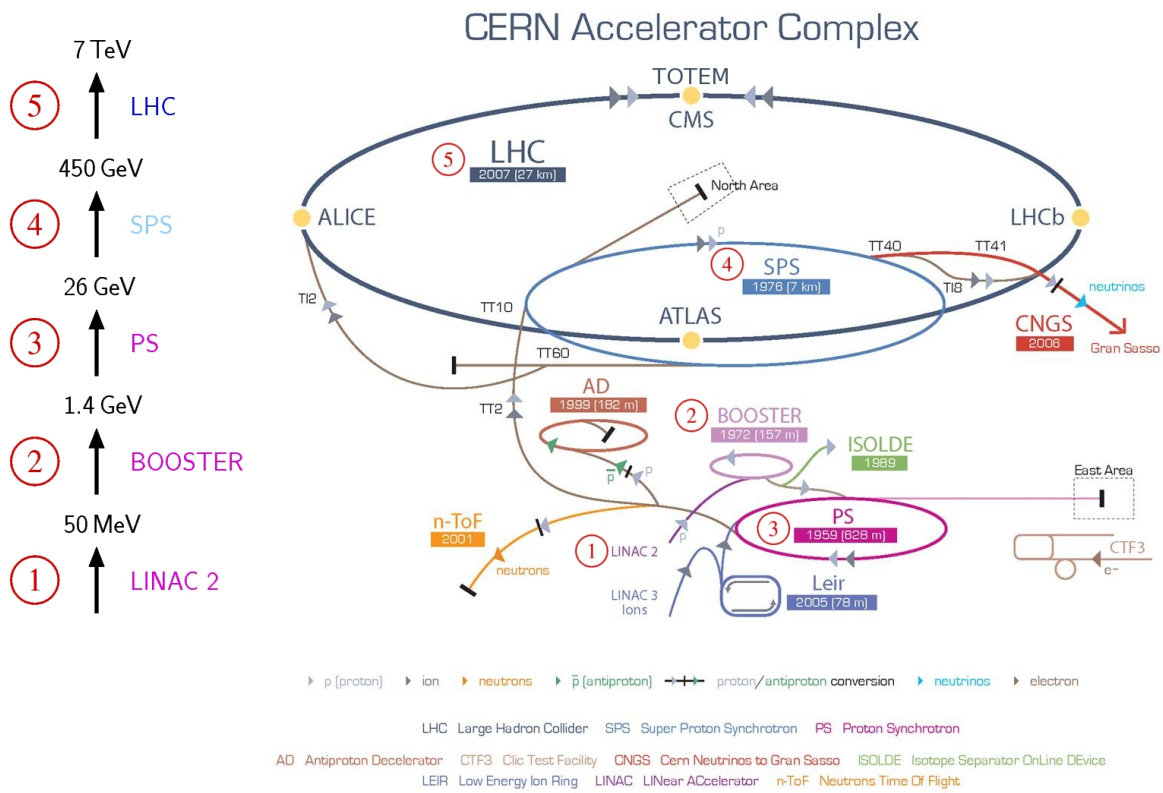


Figure 3.1: Schematic of the CERN accelerator complex showing the five stages of acceleration to an energy of 7 TeV through the LINAC2, BOOSTER, PS, SPS and into the LHC ring [22].

The proton beams are collided at four interaction points around the LHC ring, where four experiments are located to study collision events. A key property of a proton-proton collider is the luminosity, which depends on the beam parameters and the instantaneous luminosity which is defined as the rate of inelastic collisions per unit area. The LHC has a design luminosity of $1 \times 10^{34} \text{cm}^{-2} \text{s}^{-1}$ and achieved a peak luminosity of $8 \times 10^{33} \text{cm}^{-2} \text{s}^{-1}$ during Run-I, as shown in Figure 3.2.

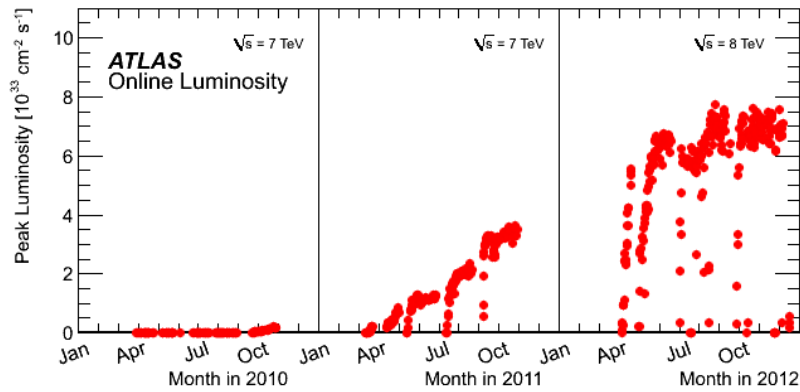


Figure 3.2: The peak luminosity delivered to ATLAS versus time during Run-I pp collisions in 2010, 2011 and 2012 [23].

3.3 The ATLAS Experiment

At 44 m in length, 25 m in height, and at 7000 tonnes, A Toroidal LHC ApparatuS (ATLAS) is the largest of the LHC experiments, and a schematic of the detector is shown in Figure 3.3 [18]. To fulfil a diverse physics programme, ATLAS is designed as a general purpose detector, capable of high precision measurements of Standard Model parameters, as well as the potential to search for new exotic particles beyond the Standard Model. In July 2012, alongside the Compact Muon Solenoid (CMS) experiment, the long anticipated discovery of the Higgs boson was announced [1, 2], a significant milestone for the LHC physics programme.

The following sections will outline the subdetectors of the ATLAS detector in the form of a tracker, calorimeter, muon detector, magnets and trigger system.

3.3.1 Overview of the ATLAS detector

The new physics processes and searches for a Standard Model Higgs boson set the requirements for the performance of the ATLAS detector system. To maximise the number of events from rare processes, high luminosity is essential. This however causes additional collisions within the same, or other bunch crossings as the event of interest, requiring excellent vertex measurement and particle identification capabilities close to the interaction point.

Figure 3.4 provides a schematic view of the particles traversing the ATLAS detector. The inner detector (ID) is designed to measure charged particle tracks and provide good pattern recognition. Three ID layers are provided for continuous tracking within a 2 T solenoidal magnetic field. These layers are the pixel detector, semiconductor tracker (SCT) and transition radiation tracker (TRT),

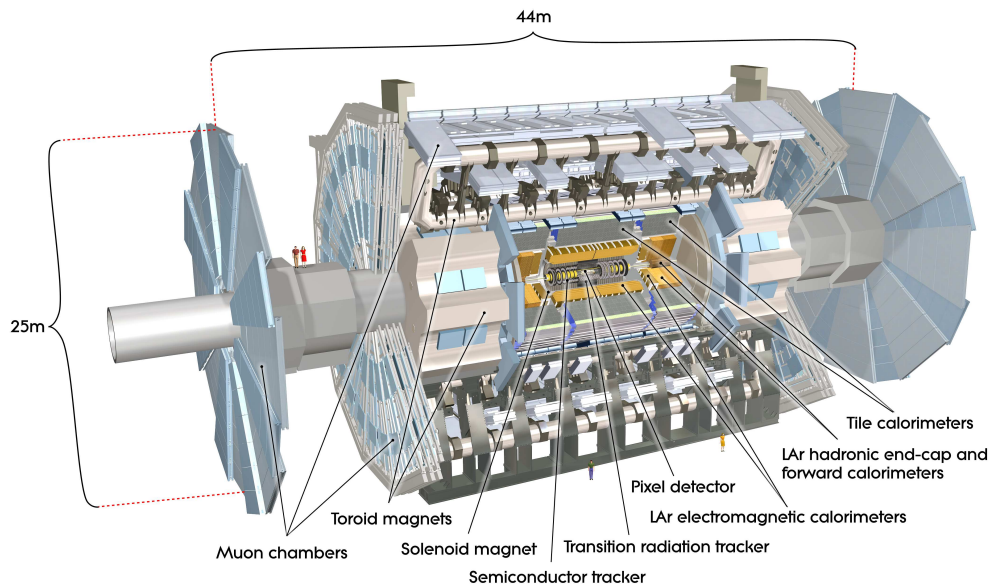


Figure 3.3: Cut-away view of the ATLAS detector showing the separate subdetector systems and four people to indicate the scale [18].

decreasing in granularity as radii from the interaction point increases. The electronics and detectors must also be able to cope with the high radiation environment and have a fast response time to reject background events. Within the inner detector, charged particles, such as electrons, muons and charged hadrons, leave tracks as they are bent by the magnetic field.

Outside the solenoid magnet is the calorimeter system. As particles interact with the absorbing and active material, they deposit energy and create particle showers, as in Figure 3.4. A liquid argon (LAr) electromagnetic calorimeter measures energy deposits and provides electron and photon identification, whilst the tile-scintillator hadronic calorimeter measures jets and missing transverse energy which accounts for particles which do not interact with the detector, such as neutrinos.

Finally, the muon spectrometer measures the momenta and charge of a wide range of p_T muons which are not stopped by previous sub-detectors. In combination with a large magnet system which dictates the layout of the ATLAS subdetectors, the general purpose detector is optimised for a wide physics program. The resolution requirements of the ATLAS detector for high precision measurements are presented in Table 3.1.

The ATLAS coordinate system uses a combination of cartesian and spherical coordinates. The interaction point acts as the origin and the positive x -axis points from the interaction point to the centre of the LHC ring, the positive y -axis points upwards and the z -axis follows the beam direction, where the positive z -direction is defined as “side-A” and negative “side-C”. The $x - y$ plane is transverse to the beam direction and is useful to define variables in this plane as there is negligible

Detector Component	Required Resolution	η coverage	
		Measurement	Trigger
Tracking	$\sigma_{p_T} / p_T = 0.05\% p_T \oplus 1\%$	± 2.5	
EM Calorimetry	$\sigma_E / E = 10\% / \sqrt{E} \oplus 0.7\%$	± 3.2	± 2.5
Hadronic calorimetry			
Barrel and endcap	$\sigma_E / \sqrt{E} = 50\% \oplus 3\%$	± 3.2	± 3.2
Forward	$\sigma_E / \sqrt{E} = 100\% \oplus 10\%$	$3.1 < \eta < 4.9$	$3.1 < \eta < 4.9$
Muon spectrometer	$\sigma_{p_T} / p_T = 10\%$ at $p_T = 1$ TeV	± 2.7	± 2.4

Table 3.1: Resolution requirements of the detector components of the ATLAS detector over the η coverage. The units for E and p_T are GeV [18].

net momentum and therefore conservation of momentum is applied. Transverse momentum (p_T), transverse energy (E_T) and missing transverse energy (E_T^{miss}) are defined in the $x - y$ plane.

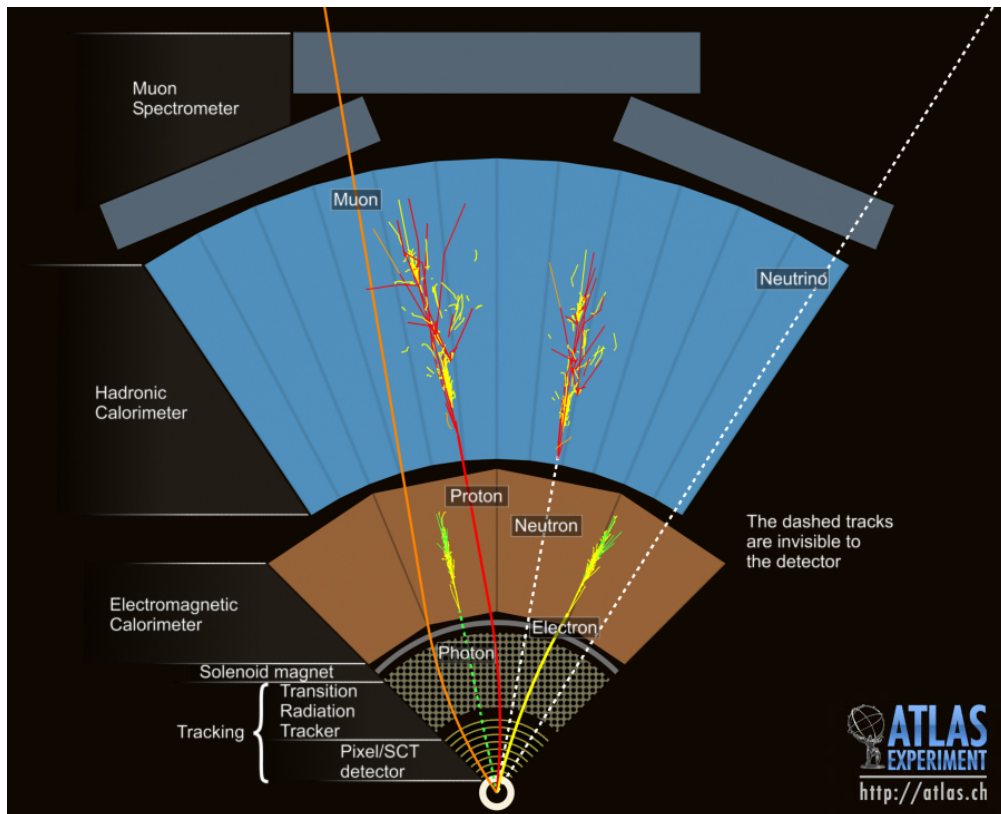


Figure 3.4: Schematic view of particles traversing through the ATLAS detector, demonstrating the curvature of particles through the tracker system, the energy deposition in the calorimeter systems and the muon spectrometer [20].

The ATLAS detector is forward-backward symmetric about the interaction point and provides full coverage in ϕ . Built in concentric cylindrical layers, spherical coordinates are also incorporated.

The azimuthal angle (ϕ) is measured around the z -axis and the polar angle (θ) is the angle from the z -axis. Quantities which are invariant under a Lorentz boost are preferred, since parton-parton collisions in the centre of mass frame are Lorentz boosted in the z -direction. A useful variable in high energy collisions is the rapidity, y , which can be paired with ϕ to give the positional coordinate. The angular separation between two objects, $(y_2 - y_1, \phi_2 - \phi_1)$ is Lorentz invariant, where rapidity is defined as:

$$y = -\frac{1}{2} \ln \left(\frac{E + p_z c}{E - p_z c} \right) \quad (3.1)$$

In the case of massless particles, the definition of rapidity is expanded and approximated to the pseudorapidity (η) [3]. η is used to describe particle coordinates in combination with ϕ , and is defined as:

$$\eta = -\ln \left[\tan \left(\frac{\theta}{2} \right) \right] \quad (3.2)$$

ΔR is defined as the distance in $\eta - \phi$ space between two objects, where:

$$\Delta R = \sqrt{(\Delta\phi)^2 + (\Delta\eta)^2} \quad (3.3)$$

These variables will be referred to extensively in the following chapters.

3.3.2 Inner Detector

The inner detector is comprised of three subdetectors which are designed to measure the momentum of charged particles. Two silicon systems cover the region up to $|\eta| < 2.5$ and are complemented by the transition radiation tracker (TRT); a series of straw tube detectors. The layout of these systems is illustrated in Figure 3.5.

Closest to the interaction point, at small radii, there is a large density of tracks. To distinguish the primary and secondary vertices with high precision, fine granularity is required. This is of particular importance for tagging of τ leptons or b -jets, which have displaced vertices. The granularity decreases at larger radii allowing continuous measurement of the trajectories of charged particles through the system.

The inner detector is encompassed by the central solenoid which generates a 2 T magnetic field. The strong bending power deflects charge particles and the hits in each detector layer are recorded and are used to reconstruct the charged particle trajectories. The trajectories are parameterised by: d_0 the transverse impact parameter, z_0 the longitudinal impact parameter, ϕ and θ determine the position and direction of the particle, and the ratio of q/p , the inverse momentum of the track multiplied by the charge of the particle [24]. In addition to this, it is essential that, being so close to the interaction point, the detectors are capable of withstanding high radiation levels whilst maintaining

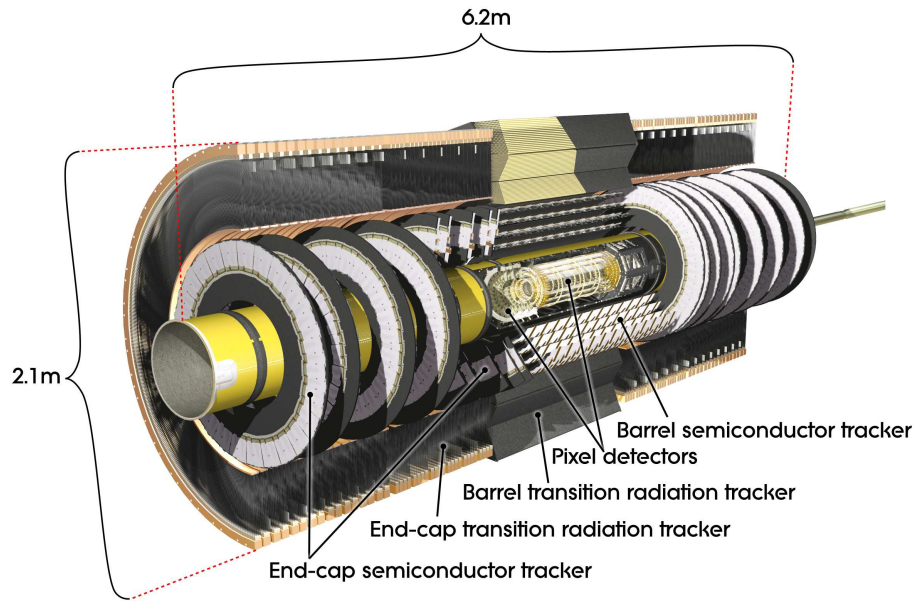


Figure 3.5: Layers of the ATLAS inner detector system in the barrel and endcap regions, with the pixel detectors, semiconductor tracker (SCT) and transition radiation tracker (TRT) layers [18].

performance, with a tracking resolution of $\sigma_{p_T}/p_T = 0.05\%$. Radiation damage and detector requirements will be discussed in Chapter 7.

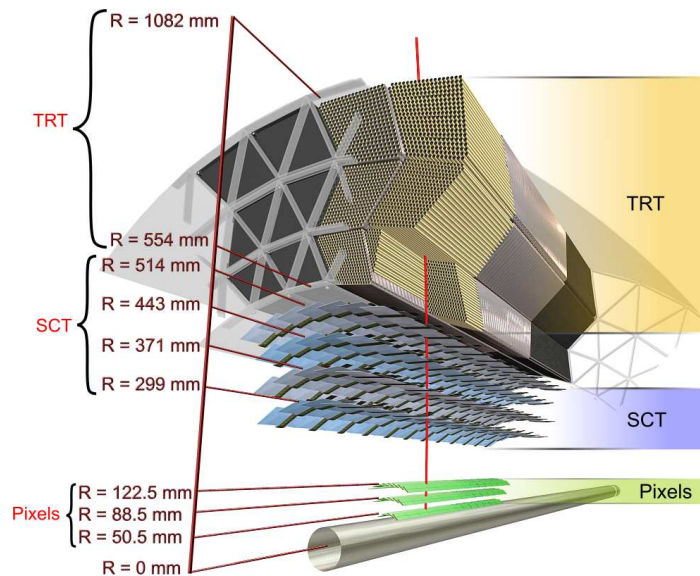


Figure 3.6: A particle traversing through the 3 subdetectors of the ATLAS inner detector system: the pixel detector, the semiconductor tracker (SCT), and the transition radiation tracker (TRT) [18].

Pixel detector

Closest to the interaction point, within $|\eta| < 2.5$, is the pixel detector with approximately 80 million readout channels distributed over 1744 pixel modules. Each module is constructed from $50 \times 400 \mu\text{m}^2$ detectors with 46 080 readout channels per module. This provides the highest inner detector resolution in $R - \phi$ [18]. With each particle track traversing three layers, tracks are reconstructed using pattern recognition algorithms. Figure 3.6 presents a diagram of a particle path through the inner detector system. The number of hits per particle track recorded in the innermost pixel layer provides discrimination of prompt electrons from photon conversions.

Semiconductor tracker

The semiconductor tracker system is situated outside the pixel layer. Similar to the pixel layer, the SCT also uses silicon detectors with the same modular design to provide high precision measurements of momenta, vertex position and the impact parameter. However, the SCT uses strip detectors in order to reduce the amount of material in front of the calorimeters and which are cheaper to fabricate than pixel detectors. The SCT has 6 million readout channels within 4088 modules and is constructed as four concentric layers in the barrel region and 9 disks for each endcap. The four layers are clearly presented in Figure 3.6, with the corresponding radius from the interaction point. The strips are offset by a stereo angle of 40 mrad, providing four double layers and consequently up to 8 hits per charged particle.

Transition radiation tracker

The TRT uses straw tube detectors, containing a gaseous mixture of xenon, carbon dioxide and oxygen. It is designed to measure the position and orientation of the charged particle track as the gas is ionised. Whilst this has a lower precision than silicon detectors, it enables continuous tracking due to the large number of hits, typically 36 per track [18]. Covering the region of $|\eta| < 2.0$, the TRT has 420 000 readout channels, from 320 000 polyamide straw drift tubes which are positioned axially in the barrel and radially in the endcaps, shown in Figure 3.6. As particles traverse between the straw tubes, transition radiation photons are emitted. The energy deposited by transition radiation in the TRT must pass an energy threshold and the ratio of high threshold hits is used to distinguish between electrons and hadrons, enhancing electron identification.

3.3.3 Calorimeter system

The calorimeters surround the inner detectors, outside of the solenoid, and are designed to measure the deposited energy as particles pass through the material, creating electromagnetic or hadronic showers. Covering the range $|\eta| < 4.9$, with a combination of liquid argon and plastic scintillator sampling calorimeters, the calorimeters cover many radiation lengths to contain the showers and prevent punch through to the muon spectrometer. The calorimeters require excellent energy and position resolution up to $|\eta| < 2.5$, coinciding with coverage from the inner detector, and full coverage up to $|\eta| < 4.9$ is essential to reconstruct jets and missing energy (E_T^{miss}) of all particles.

Liquid argon is the active medium used in the EM barrel (EMB), EM endcap (EMEC), hadronic endcap (HEC) and the forward calorimeters (FCal), whilst the central and extended barrel calorimeters use a plastic scintillator. The active material measures the energy deposited by particles and alternate with an absorber material which induces showering. The layout of the EM and hadronic calorimeters is shown in Figure 3.7 in the barrel and endcap regions. To account for upstream energy losses, a presampler layer is situated in front of the calorimeters in the region $|\eta| < 1.8$.

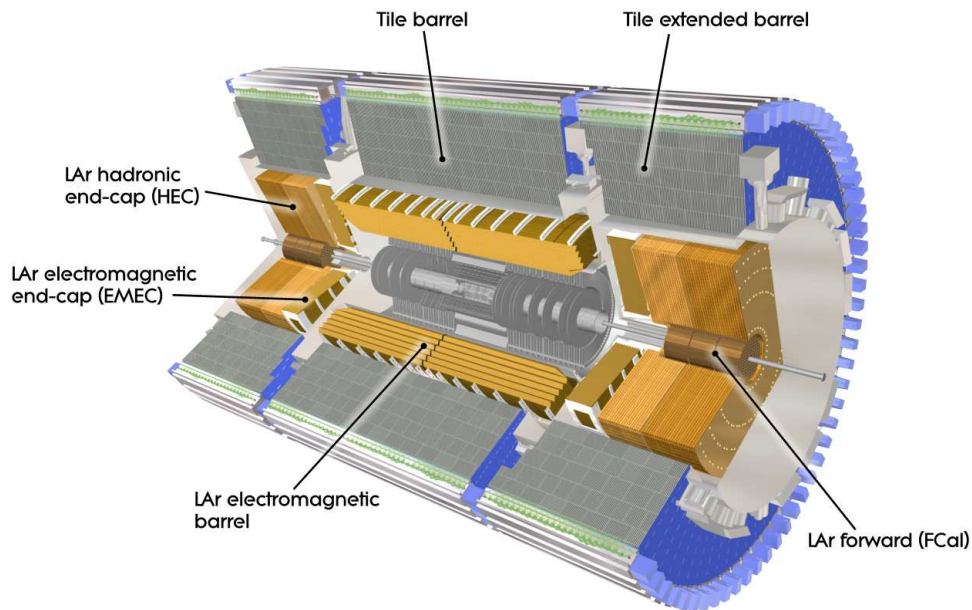


Figure 3.7: ATLAS EM and hadronic calorimeter systems in the barrel and endcap regions, demonstrating the use of tile scintillator and LAr in the different layers [18].

Electromagnetic calorimeter

To provide excellent energy and position resolution, the calorimeter has fine granularity in the region $|\eta| < 2.5$, crucial for precise measurements of electrons and photons which predominantly

undergo bremsstrahlung and pair production in the calorimeter above energies of ≈ 10 MeV. These interactions can be characterised by the radiation length (X_0) which is defined as the depth within matter where electrons lose all but $1/e$ of their energy by bremsstrahlung and is also used as $7/9$ of the mean free path for pair production by a high energy photon [3]. Each bremsstrahlung photon or electron-positron pair produced then undergoes further interactions, creating an EM shower within the calorimeter.

For accurate energy measurements within the EM calorimeter, as in Table 3.1, an energy resolution of $10\% / \sqrt{E(\text{GeV})}$ is required, to achieve the performance goals as constrained by Higgs and BSM signatures. This includes the $H \rightarrow \gamma\gamma$ channel where good mass resolution and hence good EM energy resolution is essential to identify a narrow resonance over the large $\gamma\gamma$ background.

The energy resolution improves with increasing energy and can be parameterised as:

$$\frac{\sigma}{E} = \frac{a}{\sqrt{E}} \oplus \frac{b}{E} \oplus c \quad (3.4)$$

where a , b and c are η dependent parameters, referred to as the sampling, noise and constant parameters, respectively. The energy resolution curve and its uncertainty as a function of E_T for electrons is presented in Figure 3.8 at $|\eta| = 0.2$ [25].

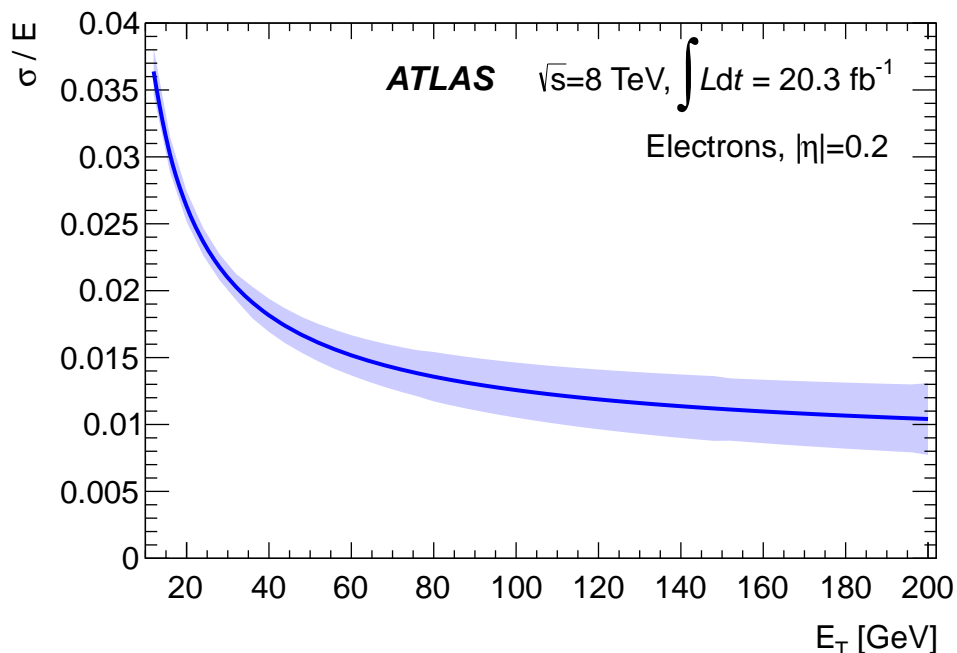


Figure 3.8: Energy resolution curve and its uncertainty as a function of E_T for electrons with $|\eta| = 0.2$ [25].

The EM calorimeter is also required to have high uniformity and the accordion geometry of the

LAr EM calorimeter provides complete symmetry in ϕ with alternating liquid argon-lead absorber plate layers to contain the EM shower. Segmented into three sampling layers, the calorimeter is subdivided into cells in η and ϕ , demonstrated in Figure 3.9. The first layer is finely segmented in η for precise measurements and to distinguish between prompt photons and photons from π^0 decays. The second sampling layer is many radiation lengths in depth to contain most of the EM shower and is divided into $\Delta\eta \times \Delta\phi = 0.0245 \times 0.025$ cells. In the third and outermost layer, only the tails of the EM shower are deposited and coarser granularity in η can be used ($\Delta\eta \times \Delta\phi = 0.0245 \times 0.05$). The lateral and longitudinal shower shapes exploit the segmentation of the EM calorimeter and these variables are used for further particle identification. Two endcap Lead-LAr calorimeters also provide coverage in the region $1.375 < |\eta| < 3.2$ in addition to the barrel region ($|\eta| < 1.475$). Within $|\eta| < 2.5$, the calorimeters overlap with the inner detector (pixel and SCT) and enable use of charged particle tracks matched to calorimeter objects to provide additional information.

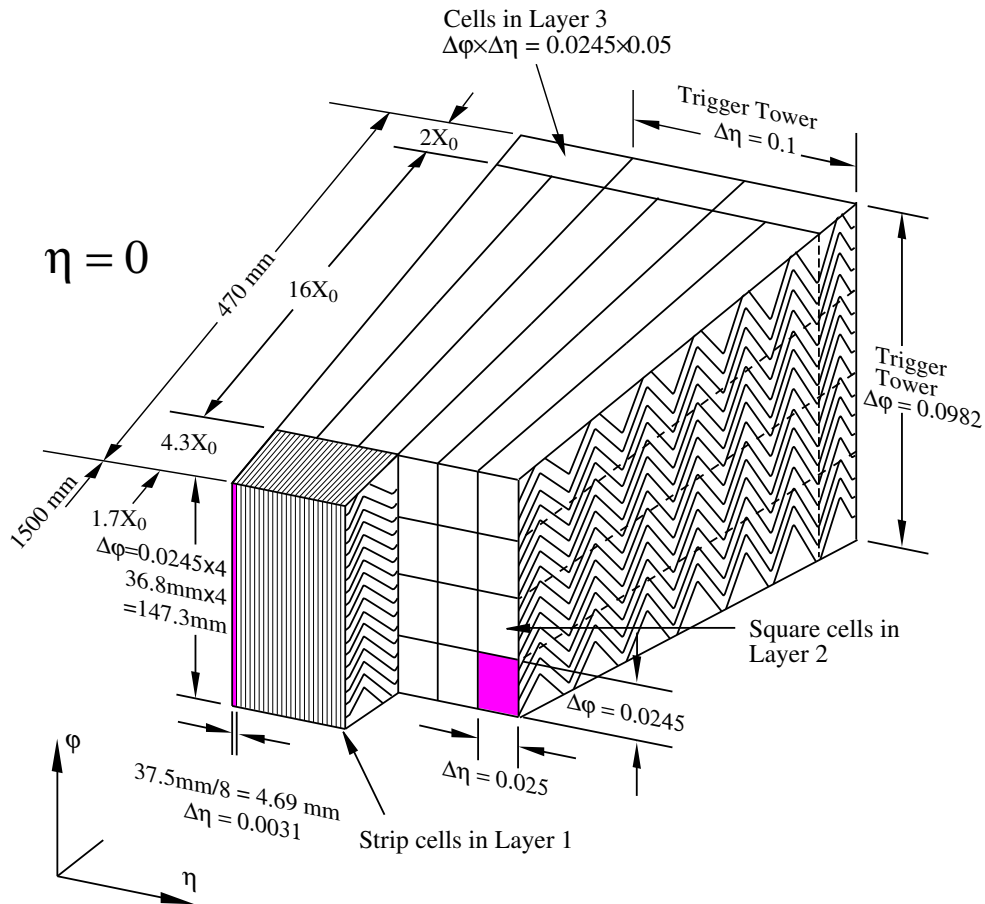


Figure 3.9: View of an electromagnetic calorimeter barrel module, illustrating the accordion layers over the three sampling layers and the granularities in η and ϕ [18].

Hadronic calorimeters

Several calorimeters are employed to measure jets and E_T^{miss} , two of which are LAr calorimeters. The LAr hadronic endcap (HEC) and forward calorimeters (FCal) share the cryostat with the LAr EM endcaps to optimise the uniformity of coverage in the calorimeters and to reduce the particle showers entering the muon spectrometer. The HEC provides coverage in $1.5 < |\eta| < 3.2$, overlapping with the tile and FCal and uses a copper absorbing material. The FCal comprises of three separate modules per endcap over the region of $3.1 < |\eta| < 4.9$, using a combination of copper and tungsten absorber plates. Arranged in a modular structure outside of the EM calorimeter are the hadronic tile calorimeters; central barrel ($|\eta| < 1.0$) and two extended barrel calorimeters ($0.8 < |\eta| < 1.7$). Both tile calorimeters use steel absorbers and scintillating tiles to contain the hadronic showers.

3.3.4 Magnet System

ATLAS has two large superconducting magnet systems which are illustrated in Figure 3.10, totalling 22 m in diameter and 26 m in length. The inner solenoid is aligned along the beam axis surrounding the inner detector system and provides a 2 T magnetic field to bend the charged particle tracks [18]. Its position is optimised to minimise the amount of material in front of the EM calorimeter, ensuring excellent performance and also causes the charged particles to create helical tracks through the ID, using the track curvature (q/p) to measure the momentum. The toroid system consists of three toroids, one barrel and two endcap, which are located outside of the calorimeter system and inside the muon spectrometer. The toroidal magnetic field is approximately 0.5 T, and 1 T for the muon spectrometer in the central endcap regions [18].

3.3.5 Muon spectrometer

The muon spectrometer measures charged particle trajectories to determine the momenta to high precision by using magnetic deflection. Charge identification through q/p measurements are performed based on the direction of curvature. The outermost detector of ATLAS contains three large superconducting air-core toroidal magnets, as described, and separate tracking and trigger chambers which cover the region $|\eta| < 2.7$ and 2.4 respectively [18]. To provide excellent resolution and fast trigger response, several types of gaseous detectors are used to form the Resistive Plate Chambers (RPC) and Thin Gap Chambers (TGC) providing the trigger in the barrel and endcap regions, and the Monitored Drift Tubes (MDT) and Cathode Strip Chambers (CSC) for high precision tracking in the barrel and forward regions. These chambers are arranged in three concentric cylindrical layers around the beam axis in the barrel, and three planar layers perpendicular to the beam in the endcap region. The muon system is shown pictorially in Figure 3.11.

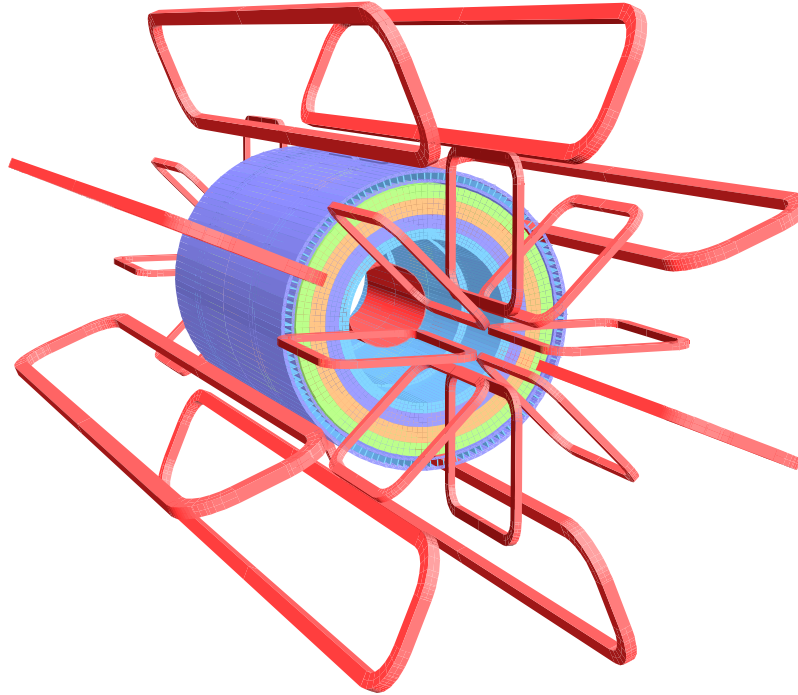


Figure 3.10: The spatial arrangement of the ATLAS magnet system (red) showing the 8 barrel toroid coils, the 8 endcap coils on each side of the calorimeter system and the solenoid, located within the calorimeter volume [18].

3.3.6 Trigger System

The ATLAS trigger system uses a multi-level trigger to reject background events with minimal dead time and provide high efficiency for physics processes of interest at a manageable rate. At Level 1 (LV1), limited detector information is used to select events, defining a region of interest (ROI) in η and ϕ which contains interesting features within $2.5 \mu\text{s}$. This reduces the event rate to 75 kHz. High level triggers (HLT), include the use of Level 2 (LV2) and Event Filter (EF) which have access to the full granularity from all detector systems to refine the LV1 decision. LV2 is seeded by the ROI and the decision is available within 40 ms, further reducing the rate to 3.5 kHz. The EF trigger is used with offline processing algorithms to reduce the rate to 200 Hz in the order of 4 s [18]. To select specific signatures, a list of selection criteria is used to form trigger menus, with LV1 and HLT menus. An event is selected if it passes the criteria which are specified based on distinguishing features in an analysis or process. Each event stored is approximately 1.3 MB, these events are used to perform analyses [18].

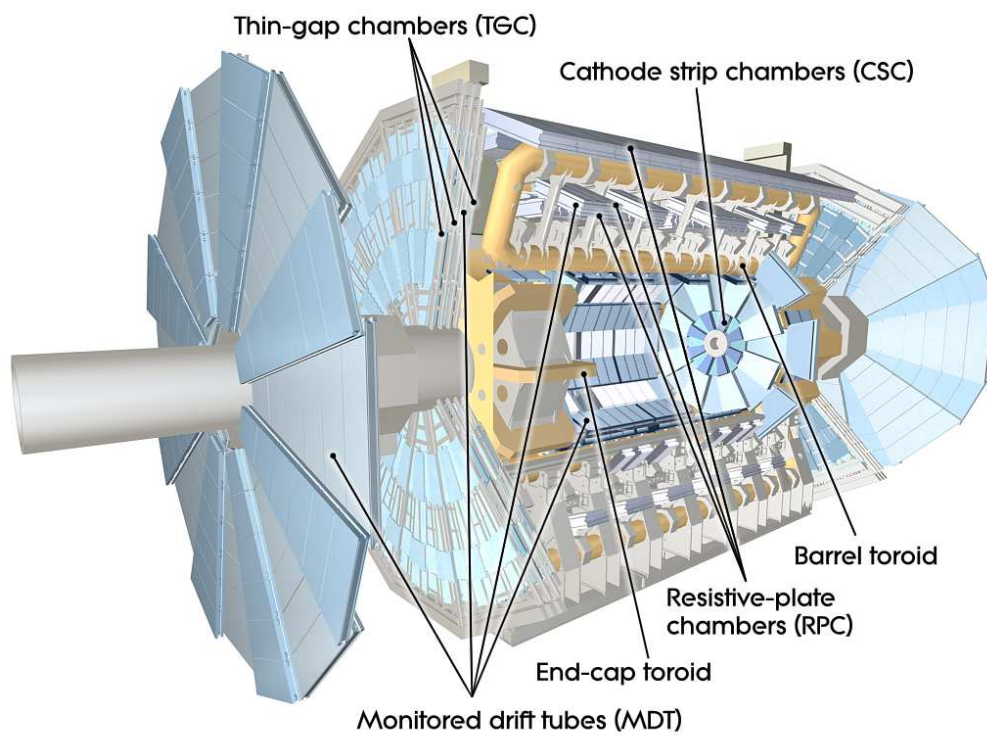


Figure 3.11: View of the ATLAS muon system showing the three superconducting air-core magnets, the trigger and tracking chambers [18].

Chapter 4

Electron Reconstruction

4.1 Introduction

The precise reconstruction and efficiency of electrons and photons at the LHC is essential to probe a wide range of SM and possible BSM processes. Events with electrons and photons in the final states are important signatures for many physics analyses, which in addition to SM processes also includes SUSY searches and searches for new physics. As described in Chapter 3, the ATLAS detector was designed to have excellent electron performance over the full p_T and η range and typically the decays of interest cover an energy range of a few GeV to several TeV. Many of these processes however have small cross-sections and large background contamination from SM events and jets, such as $H \rightarrow \tau\tau$ decays which can result in either two jet, one lepton and one jet, or two lepton final states, where the leptons include electrons or muons. Therefore high reconstruction and identification efficiency is required to overcome the low signal-to-background ratio.

An excellent electromagnetic energy resolution is also crucial to perform precise measurements. A significant challenge presented when reconstructing electrons is loss of energy due to bremsstrahlung. This is unavoidable due to interactions of particles with material upstream of the calorimeter and average corrections are applied to the calorimeter energy to account for these losses.

The reconstruction of electrons and photons in the region $|\eta| < 2.5$ starts from the energy deposition in the EM calorimeter layers and EM clusters are built using two different algorithms. Then using information from the inner detector, the clusters are matched to particle tracks which defines an electron object.

The author has been heavily involved in the development of a new reconstruction algorithm for electrons and has played a leading role in the calibration of these electrons. This chapter will give an introduction to the current ATLAS electron reconstruction algorithm, and a new novel algorithm, “superclusters” is also proposed. Performance studies and a comparison between the two algorithms

is performed using Monte Carlo (MC). The methods used for calibration are described and applied to both algorithms and finally, electron identification is discussed to provide an overview of the discriminating variables used in the selection menus applied in ATLAS analyses, such as those described in the subsequent chapters.

4.2 Electron Reconstruction

Electrons and photons, referred to as “egamma” objects, are reconstructed starting from the energy deposited within the electromagnetic calorimeter and electrons are defined as clusters which are matched to at least one inner detector track. Due to the granularity of the Lead-LAr sampling calorimeter, electromagnetic particles deposit energy in many cells when traversing the calorimeter, developing EM showers when interacting with the lead absorbers and ionising the LAr active area.

In order to form egamma objects, algorithms are used to group the EM cells into clusters and to sum the energy deposited by electrons and photons. Figure 4.1 shows the grouping of the cells into towers and clusters over the three calorimeter layers.

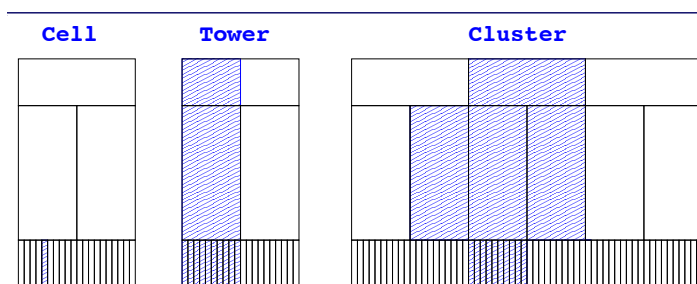


Figure 4.1: Description of reconstructed objects: cell, the smallest reconstructed object; a tower consists of a group of cells in a fixed $\Delta\eta \times \Delta\phi$ region; a cluster is a group of cells formed around a seed cell [26] using different reconstruction algorithms.

Following cluster formation, the inner detector information is used to match the cluster to a well-reconstructed track which forms an electron [25]. Clusters without an associated track are defined as unconverted photons, and inner detector information can also be used to reconstruct converted photons. Only electrons however will be discussed in this chapter.

As described in Chapter 3, the EM calorimeter shown in Figure 3.9, contains four active layers. The thin presampler (PS) layer is designed for energy loss correction upstream of the calorimeter, the first layer (S1) is segmented into high-granularity strips in η and can be used to discriminate single photons from overlapping showers from hadron decays, as will be described in Section 4.4. The middle layer (S2) contains the bulk of the energy deposition by photons and EM showers due to its large thickness, and finally the back layer (S3) contains high energy showers, correcting for leakage

beyond the EM calorimeter. Table 4.1 presents the η range of each sampling layer, as well as the granularity and thickness of each layer.

Calorimeter Layer		Presampler (PS)	Layer 1 (S1)	Layer 2 (S2)	Layer 3 (S3)
$ \eta $ region	Barrel	< 1.52	< 1.475	< 1.475	< 1.35
	End-cap	1.5 - 1.8	1.375 - 3.2	1.375 - 3.2	1.5 - 2.5
Granularity	$\Delta\eta$	0.025	0.0031	0.025	0.05
	$\Delta\phi$	0.1	0.0245 \times 4	0.0245	0.0245
Radiation Lengths		1.7 X_0	4.3 X_0	16 X_0	2 X_0

Table 4.1: Overview of the layers of the EM calorimeter $|\eta|$ regions, granularity and radiation lengths (X_0) [18].

The material before the calorimeter is shown in Figure 4.2. Material contributions from electronics, power distribution, cooling and mechanical support add significantly to the overall material budget and cause radiative losses to electrons. This can alter the curvature of the particle trajectory as it propagates through the magnetic field and can impact the electron track. Inner detector tracks are provided up to $|\eta| = 2.5$ using information from the pixel and SCT layers, and up to $|\eta| = 2.0$ using the TRT, and radiative losses are accounted for by considering material effects. The transition region between the barrel and endcap EM calorimeters, $1.37 < |\eta| < 1.52$, has a large amount of material in front of the first active calorimeter layer and the reconstruction efficiency decreases. This region is typically excluded from analyses involving electrons.

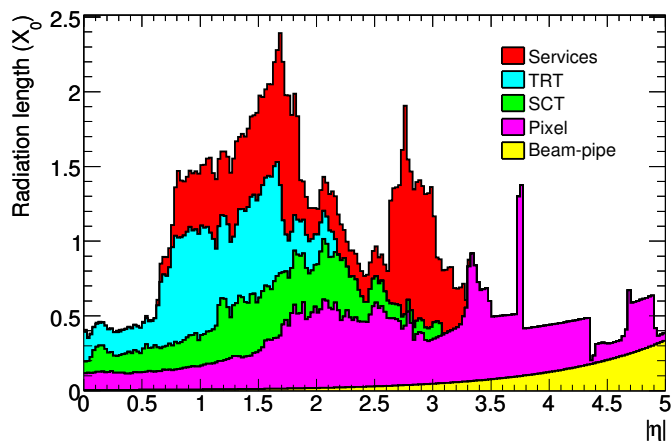


Figure 4.2: Material distribution at the exit of the inner detector as a function of $|\eta|$, averaging over ϕ . The breakdown indicates the contributions of external services and of individual sub-detectors, including services in their active volume [18].

Two types of clustering algorithms are used in ATLAS reconstruction: the “sliding-window” algorithm and topological clustering algorithm [26]. For egamma reconstruction, the sliding-window approach is the default algorithm and whilst this provides excellent reconstruction and track quality

efficiency of over 97% for electrons with $E_T > 15$ GeV, as shown in Figure 4.3, it is possible to improve this further. The sliding-window algorithm is seeded by towers with energy deposits $E_T > 2.5$ GeV and builds fixed-size rectangular clusters to reconstruct electrons, whilst a new algorithm has been developed using topological clusters which are dynamic as described in the Section 4.2.3.

The ability to reconstruct events correctly and identify an object which is electron depends on several factors. The total efficiency is therefore the product of the different efficiency terms:

$$\epsilon = \epsilon_{reco} \cdot \epsilon_{id} \cdot \epsilon_{isolation} \cdot \epsilon_{trigger} \quad (4.1)$$

where ϵ_{reco} is the reconstruction efficiency to find an EM cluster and match it to a reconstructed charged particle track, as presented in Figure 4.3 which compares ϵ_{reco} from 2011 (red) and the efficiency improvement in 2012 (blue) data. ϵ_{id} is the efficiency of the identification cuts relative to the reconstructed electron objects where the identification criteria will be discussed in Section 4.4. $\epsilon_{isolation}$ is the efficiency of any isolation requirement, if applied, limiting the presence of other particles close to the identified electron candidate and $\epsilon_{trigger}$ is the trigger efficiency with respect to all reconstructed and identified electron candidates [27].

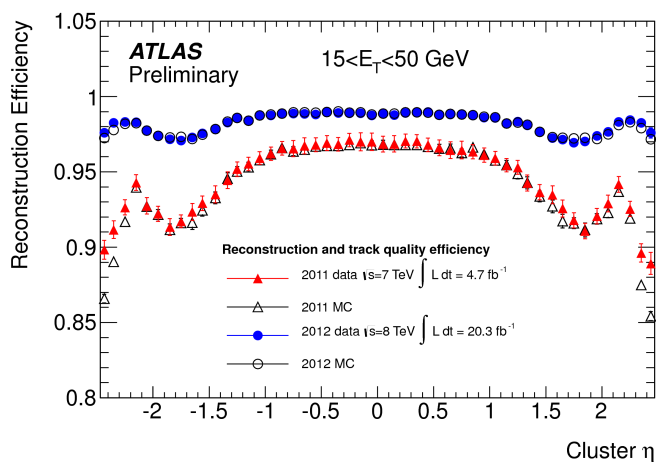


Figure 4.3: Reconstruction and track quality efficiency as a function of pseudorapidity η for electrons with transverse energy E_T between 15 and 50 GeV for data (filled markers) and MC (open markers) for 2011 (triangles) and 2012 (circles) data samples [28].

Electron efficiencies, as in Figure 4.3 are measured using the Tag and Probe (T+P) method which uses events containing well known resonance decays to electrons, namely $Z \rightarrow e^+e^-$ and $J/\psi \rightarrow e^+e^-$. Strict selection criteria are applied to one of the electron candidates (*tag*) and the other electron (*probe*) is studied. All valid combinations of electron T+P pairs are considered for instance an electron can be a *tag* in one pair and a *probe* in another. The *probes* are then used to measure the reconstruction, identification, isolation and trigger efficiencies after accounting for background contamination.

4.2.1 Cluster-track matching

After clusters are formed, track to cluster matching is applied which is an integral step in electron reconstruction. An electron is defined as one or more tracks which are matched to seed clusters in the central region $|\eta| < 2.5$, and therefore a cluster-track matching procedure must be performed. This ensures that the energy deposition in the EM calorimeter corresponds to a charged particle which has traversed the ATLAS detector, with associated tracks in the inner detector layers.

Track reconstruction is a two-step process of pattern recognition and track fitting. Standard track pattern reconstruction is used following the pion hypothesis and is complemented by a modified pattern reconstruction algorithm based on the Kalman Filter Formalism. The modified pattern recognition algorithm is used to estimate the energy loss at material surfaces and incorporates a maximum of 30% energy loss at each material surface due to bremsstrahlung [29, 30].

Initially tracks are extrapolated from their last measured point in the inner detector to the second calorimeter layer. The track momentum of the first inner detector measurement is rescaled and the η and ϕ coordinates of the cluster and track are compared. If at least one track has more than 4 silicon hits and is within close proximity in $\Delta\eta$ and $\Delta\phi$ to the seed cluster position, they are classified as matched and the tracks are refitted using the Gaussian Sum Filter (GSF) algorithm [31]. This estimates the process noise and energy loss by a sum of gaussians and provides a better estimation of the track parameters for electrons. This algorithm was introduced in 2012 and accounts for the improvement in efficiency in Figure 4.3 as tracks are better reconstructed. Following fitting, tighter $\Delta\eta$ and $\Delta\phi$ thresholds are imposed. If more than one track is matched to a seed cluster, a quality is assigned to the tracks. The tracks are ranked based on the ΔR between the extrapolated track and cluster and the number of inner detector hits is also considered. The ordered tracks are subsequently stored and the best-matched track is chosen as the primary track. The track matching uses a larger $\Delta\phi$ search window on the side where the extrapolated track bends as the electron transverses the magnetic field. This results in an asymmetric sign-dependent $\Delta\phi$ distribution [32].

4.2.2 Clustering Algorithms

The two types of clustering algorithms used in ATLAS reconstruction are:

- The sliding-window (SW) algorithm which has three steps: fixed-size tower building, see Figure 4.1, precluster (seed) finding and cluster filling. The SW algorithm moves a fixed-size window along the towers to find a local maximum in transverse energy (E_T). If this is above a threshold of 2.5 GeV, a precluster is formed. Smaller sized windows are then used to calculate the energy-weighted η and ϕ barycentres of all cells and to build a fixed-size cluster

around the seed, after track matching is performed using the seed cluster. The final cluster size depends on the particle type and the position within the EM calorimeter, see Table 4.2 for more details. Duplicate removal is then performed to remove overlapping clusters from nearby seed clusters [33].

- The topological clustering algorithm is based on signal over noise threshold which is defined as the ratio of the cell signal to the average (expected) noise (σ), and clusters are again built around seed cells over a σ value. There are two components to this algorithm: the cluster maker and the cluster splitter, these are described in more detail below. Topological clusters (topoclusters) have variable size based on the significance of each cell [34].

Electrons are currently built from sliding-window clusters by default in ATLAS egamma reconstruction. A new novel algorithm has been developed using topoclusters, these will therefore be discussed in more detail.

Step	$N_\eta \times N_\phi$	
1. Tower Building	200 × 256	
2. Seed Finding	3 × 5	
Position Calculation	3 × 3	
Overlap removal if within	2 × 2	
3. Cluster Filling	Barrel	Endcap
Electrons	3 × 7	5 × 5
Converted Photons	3 × 7	5 × 5
Unconverted Photons	3 × 5	5 × 5

Table 4.2: Size of clusters in the three steps of the window algorithm, Tower Building, Seed Finding and Cluster Filling. The window size grid $N_\eta \times N_\phi$ contains clusters of size $\Delta\eta \times \Delta\phi = 0.025 \times 0.025$ within $|\eta| < 2.5$ and $E_T > 2.5$ GeV taken from Ref. [26, 32]. After Seed Finding, the clusters are matched to ID tracks and the matched clusters are re-filled depending on their η and ϕ position within the calorimeter. Cluster filling starts from the middle layer using the precluster position, then builds the cluster in the strip layer based on the position in the middle layer, followed by the PS layer based on the strip position and finally the back layer is filled based on the middle position.

4.2.3 Topocluster formation

The two steps of topocluster formation are the cluster maker and the cluster splitter and build topological clusters based on the cell significance as described in this section. The cluster maker searches for the seeds and uses a topological based algorithm to add neighbouring and perimeter cells. The

cluster splitter follows the cluster maker and is used to find local maxima and separate clusters which may be too large due to multiple energy depositions in close proximity.

Cluster Maker

Initially the seeds are identified which have a signal to noise ratio (S/N) above the high seed threshold t_{seed} , see Table 4.3. These cells are then added to a seed list in descending S/N order and each seed forms a “proto-cluster”. The signal in the EM case is the cell energy and the total noise is the quadratic sum of the expected electronic and pile-up noise.

Parameter	Had 420	EMTopocluster430
Calorimeter	All	EM only
Seed signal definition	E	E
Cluster cut before splitting	$E_T > 0$ GeV	$E_T > 0.3$ GeV
t_{seed}	4	4
$t_{neighbour}$	2	3
t_{cell}	0	0

Table 4.3: Parameters used to build two types of EM topoclusters which are used in the supercluster algorithm [26], where 420 and 430 correspond to the S/N threshold of the seed, neighbour and cell.

For each seed cell, neighbouring cells, which are not seeds, with S/N above $t_{neighbour}$ are iteratively added to a neighbouring seed list and included in the adjacent proto-cluster. If a cell is neighbouring two proto-clusters, the proto-clusters are merged. Once the neighbouring cells are added to the proto-cluster, the perimeter cells are then added. For this step, the signal is always defined as the absolute value of energy. This is applied to each calorimeter layer, however if layers overlap in η and ϕ , then 3D neighbours are also included.

Finally, proto-clusters are sorted in descending E_T order and converted to clusters. An E_T cut is applied, removing clusters below the E_T threshold in Table 4.3. Both the “420” and “430” clusters, based on seed, neighbour and cell thresholds, are optimised to reconstruct low energy clusters without being overwhelmed by noise [34, 26]. The full list of parameters of topocluster construction are presented in Table 4.3.

Cluster Splitter

The cluster splitter is then used to separate overlapping signals. A local maximum is searched for in cells where $E_{seed} > 500$ MeV and reclustering is performed around the local maximum with the

same neighbour driven algorithm but no threshold or merging. Finally, cells which are at cluster borders are shared with energy and distance dependent weights [26]. These final clusters, topoclusters, are used in the following studies.

4.3 Superclusters

The new proposed algorithm for electron reconstruction uses “420” and “430” topoclusters to build “superclusters”. Superclusters are built from a seed cluster containing primary topoclusters, summed with nearby secondary satellite clusters which are added to account for radiative losses. On top of the asymmetric distribution of sliding-window electrons, low EM energy tails also arise and this is caused by bremsstrahlung and pair production, as demonstrated in Figure 4.4.

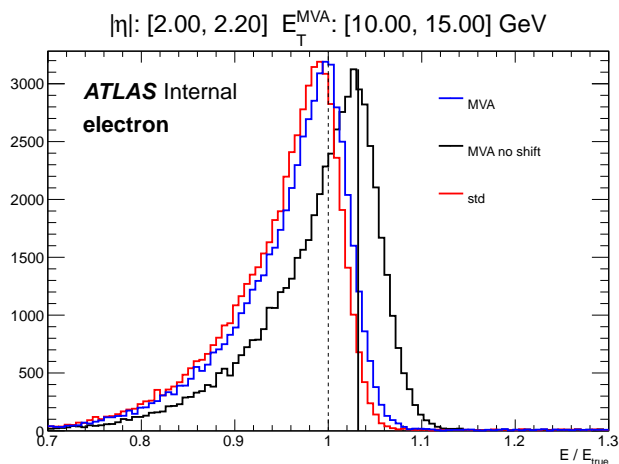


Figure 4.4: E/E_{true} distribution of calibrated single electrons reconstructed with the sliding-window clustering algorithm in the region $2.0 < |\eta| < 2.2$ with $10 < E_T^{MVA} < 15$ GeV. Standard calibration is the previous method using calibration hits, MVA no shift is the MVA calibration and MVA is the MVA calibration with further corrections to shift the peak value closer to 1. Note the asymmetric tails caused by bremsstrahlung [35].

Figure 4.4 presents the E/E_{true} distributions of single electron samples which have been reconstructed using the sliding-window clustering algorithm using Monte Carlo, where E is the calibrated energy and E_{true} is the true electron energy [35]. Figure 4.4 compares a standard calibration (red), and multivariate (MVA) calibration methods (blue, black), within $2.0 < |\eta| < 2.2$ and with MVA calibrated transverse energy of $10 < E_T^{MVA} < 15$ GeV. This demonstrates the asymmetric tails which are visible in all three calibrations in the egamma reconstruction currently used by ATLAS and provides motivation to improve the reconstruction algorithm. The aim of the superclusters, while making the E/E_{true} distribution more symmetric, is to reduce these tails by looking beyond a fixed-size window to include low E_T clusters to account for the energy loss due to bremsstrahlung.

The supercluster algorithm proceeds in two stages: first building a primary topocluster (Step 1-4 in Figure 4.5) by adding the cells of topoclusters with a barycentre within 3×5 cells of the seed topocluster, then searching for and adding secondary satellite clusters (Step 5) either by searching within a $\Delta\eta$ and $\Delta\phi$ window of the seed topocluster, or if this is unsuccessful, by looking for points of bremsstrahlung in the track, extrapolating to the calorimeter and comparing the satellite cluster position with the seed. If satellite clusters are found, they are added to the primary topocluster to build the supercluster object. Finally, the order of best tracks are re-ranked and the electron kinematics are recomputed (Step 6), such as the η and ϕ for the supercluster, which has accounted for energy losses due to bremsstrahlung, where energy depositions are not within the same cluster.

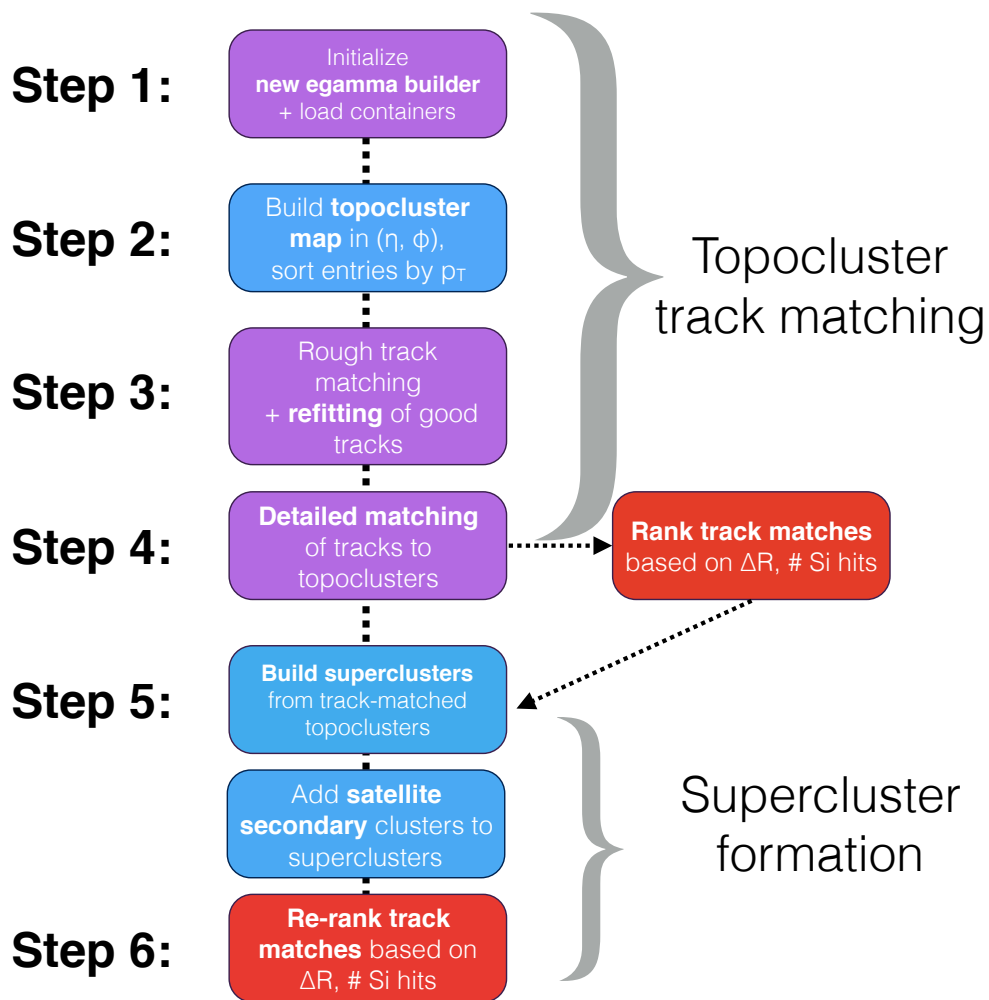


Figure 4.5: Code flow showing individual steps of the supercluster algorithm.

Following, in detail, the stages outlined in Figure 4.5, superclusters are built using the topocluster collection, Step 1. In Step 2 a map of the topocluster position in η and ϕ is built using the p_T -sorted topoclusters. This allows the highest p_T clusters to be identified as seed clusters and other nearby topoclusters are located. It is required that all topoclusters have $E_T > 400$ MeV and that the seed

cluster has $E_T > 1 \text{ GeV}$. Associated tracks are then loosely matched to the seed in Step 3, and good quality tracks undergo GSF refitting. More stringent matching thresholds are introduced to match the refitted tracks and clusters (Step 4), and these are ranked based on the ΔR between the seed and tracks and the number of silicon layer hits. It is also required that the best-matched track associated to a seed cluster has more than 4 silicon layer hits. In Step 5a, the primary electron is built by summing topoclusters with a lower E_T than the seed and within a 3×5 window around the seed cluster. The kinematics are recalculated after formation of the primary electron and a search for satellite topoclusters is performed in two ways in Step 5b. Firstly, satellite topoclusters can be added if they are matched to the same track as the seed clusters and are within $\Delta\eta < 0.075$ and $\Delta\phi < 0.15$ of the seed cluster. If no satellite is found, an algorithm is used on the track to determine if there is a point at which an electron undergoes bremsstrahlung by looking at significant “kinks” in the track when a photon is emitted and if so, extrapolating this point to match an EM calorimeter cluster. If the extrapolated bremsstrahlung point and EM cluster overlap within $\Delta\eta < 0.1$ and $\Delta\phi < 0.15$, the topocluster can be added as a satellite. The satellite topoclusters are added to the primary electron to form the supercluster and finally in Step 6, the track matches are re-ranked and the four-momentum is computed using a weighted average.

By adding the energy deposited in satellite clusters, superclusters aim to recover event-by-event radiative losses as opposed to applying average corrections. Also, starting with topological clusters to build the primary electron, only cells with significant S/N are included. When compared to the sliding-window clustering algorithm, the electron clusters include all cells within a 3×7 window, which may include noisy cells and neglects to include or search for significant energy deposits outside the window.

4.3.1 Calibration

The energy deposited within the three EM calorimeter layers is summed to generate the “raw cluster energy”, however this is not the true particle energy, due to energy losses, and corrections need to be derived to account for this.

The four main contributions to energy loss are [36]:

- Energy lost in front of the calorimeter,
- Energy deposited in the dead material of the calorimeter,
- Out of cluster energy,
- Leakage into the hadronic calorimeter.

Several steps are required to calibrate the energy response of electrons and photons, in accordance

with Figure 4.6. Multivariate techniques are used to derive calibration constants using simulated MC samples, the scales of the longitudinal layers are equalised in data with respect to MC and these corrections are then applied to data and MC samples. Further corrections are then applied and the final calibrated energy is validated using $J/\psi \rightarrow e^+e^-$ and $Z \rightarrow e^+e^-$ events.

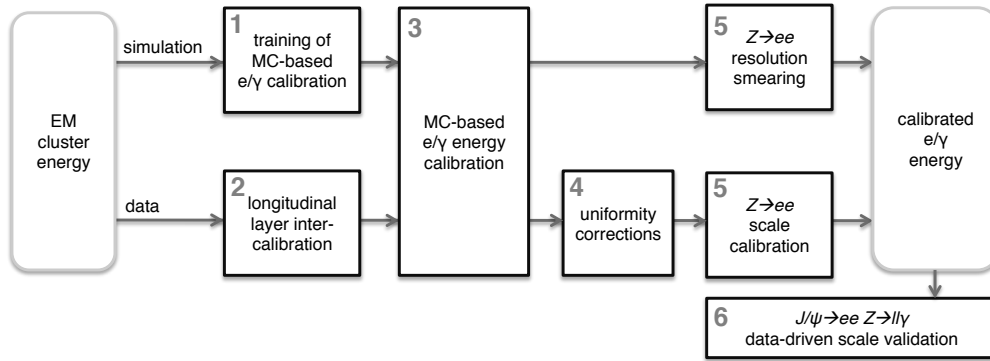


Figure 4.6: ATLAS calibration procedure for electron and photon energy response [25].

The training and testing of MC-based calibration (Steps 1 and 3) are the primary focus of this section. After building the energy clusters and reconstructing electrons, the raw cluster energy is determined, summing the energy in the three EM accordion calorimeter layers. A correction factor can then be determined by linear regression using multivariate algorithms, which are trained on large samples of fully simulated single electron events, and applied to further MC samples.

Multivariate analysis aims to minimise the root mean square (RMS) resolution by using boosted decision trees (BDT). Energy calibration is classified as a regression problem, whereby a model maps multiple input variables to a single target variable, typically with a value of one, such that the deviation of the output with respect to the target is minimised, illustrated in Figure 4.7. Using E/E_{true} as the target variable, an arbitrary number of input variables are used in order to remove any dependence of the energy response with quantities such as pseudorapidity η . Also, unlike previous calibration methods, MVA considers the correlation between the input variables.

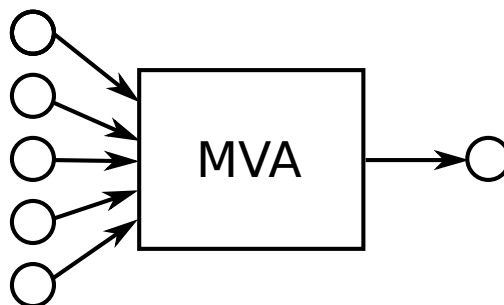


Figure 4.7: Sketch of an MVA algorithm with multiple input variables and one output variable [35].

The MVA is implemented using the Toolkit for MVA (TMVA) framework which provides a ROOT-

integrated environment designed for HEP applications [37]. A package, `egammaMVACalib` [38], has been developed to allow new calibration constants of `egamma` objects to be derived quickly and with the flexibility to incorporate new input variables. This package has been adapted to calibrate superclusters in addition to default `egamma` objects.

The MVA calibration is performed using two phases; training and application. The user defines the training sample, the input variables, the target quantity which is to be estimated and the MVA algorithm to be used. The fraction of events to be used for training is also defined by the user. Typically, 90% of events are used for training and 10% for testing however, this assumes significant statistics in the initial sample $O(10^6)$. Separating events into bins in η and E_T , the sample is independently trained in each bin to optimise the energy response in different regions of phase space. The output `TestTree` is used to study the performance of the calibration and the weights are stored in XML files which can be applied to further samples. Using Monte Carlo (MC) simulations of single electrons, the initial energy of the particles can be determined over the full range in η and p_T .

The output of the MVA leads to an optimisation in which the mean value of the output energy is close to E_{true} . However, due to the non-gaussian tails in the energy response, the most probable value and the mean do not coincide. Therefore, further shifts are required to adjust the peak position to the most probable value of 1 [35]. By default in this study, these shifts have not been applied to allow a simple comparison between the different reconstruction algorithms.

In this section, superclusters and sliding-window samples have been MVA trained using the same procedure and with equivalent statistics to allow a direct comparison of the performance [35]. A full technical description of the standard electron and photon MVA calibration procedure is presented in [35]. This section will outline the samples, variables, and the performance of calibrated electrons when reconstructed using the two different algorithms.

Samples

The samples used for the training contain 10^5 fully simulated single particles with E_{acc} distribution for electrons reconstructed using the sliding-window and supercluster algorithms presented in Figure 4.8, where E_{acc} is the accordion energy, which is the sum of energy deposited in the three calorimeter layers. There is good agreement between the algorithms. No pile-up effects are included in the sample used to train the MVA for calibration.

The energy response of the uncalibrated single electrons is presented in Figure 4.9. This compares the energy deposited in all layers of the EM calorimeter to the true energy for each algorithm. Ideally, the reconstructed energy should be as close to the true energy as possible, resulting in a narrow

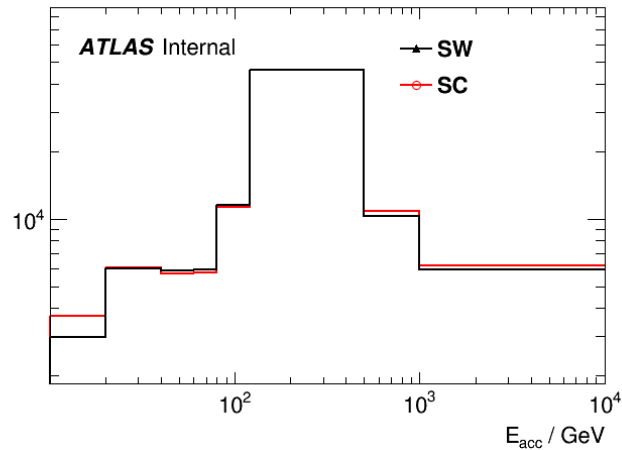


Figure 4.8: Full accordion energy distribution of supercluster and sliding-window particles in the single electron samples with no pile-up effects.

gaussian distribution with a peak at 1. However due to energy losses, an asymmetric distribution arises. Using the most probable value to define the peak, the peak position of the superclusters is closer to 1 than the sliding-window distribution and has a narrower gaussian core. The improvements can be observed for the supercluster as the peak position is 3.2% closer to 1 and 1.0% narrower gaussian core (width) when compared to sliding-window electrons, before calibration.

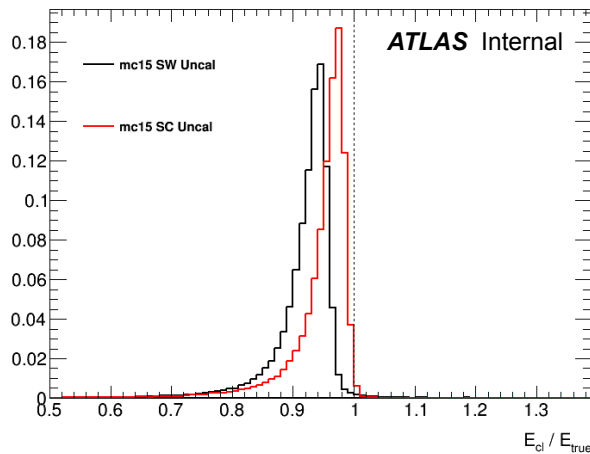


Figure 4.9: Uncalibrated energy response for superclusters (red) and sliding-window (black) single electrons.

To maximise the statistics of these samples, basic selection cuts are applied to both superclusters and sliding-window electrons:

- matching between the generated particle and reconstructed object (truth matching) is required,

- pseudorapidity of the cluster within $|\eta_{cl}| < 2.5$, excluding $1.37 < |\eta_{cl}| < 1.52$,
- require that the reconstructed object is identified as an electron.

Whilst further requirements of *loose* identification cuts and the difference between true and reconstructed energy with calibration hits method are specified during the default egamma procedure, these are not relevant for the superclusters and therefore the selection listed above is applied to both single electron samples which are generated using the sliding-window and supercluster algorithm.

Target variable, input variables and binning

In order to estimate the true energy of the electron from the quantities measured by the detector, the target variable is a correction factor to the energy measured in the accordion ($E_{\text{true}}/E_{\text{acc}}$). This correction should be close to 1.

The chosen input variables are the ones used as default for ATLAS egamma calibration and these quantities are listed and the corresponding distributions for superclusters and sliding-window single electron samples are presented in Figure 4.10:

- total energy in the accordion: E_{acc} , defined as the sum of the uncalibrated energies of the accordion layers (strips, middle and back),
- ratio of the energy in the presampler to the energy in the accordion: E_0/E_{acc} , used only for clusters within $|\eta| < 1.8$,
- cluster barycentre pseudorapidity in the ATLAS frame: η_{cl} , i.e. taking into account the misalignment of the detector, in order to correct for the variation of the material in front of the accordion, among other effects,
- cell index: an integer number between 0 and 99 defined as the integer part of the division $\eta_{calo}/\Delta\eta$ where η_{calo} is the pseudorapidity of the cluster in the calorimeter frame and $\Delta\eta = 0.025$ is the size of one cell in the middle layer,
- η with respect to the cell edge defined as the pseudorapidity (in the calorimeter frame) modulus the width of one cell of the middle layer ($\Delta\eta = 0.025$). This variable corrects for the variation of the lateral energy leakage due to the finite cluster size, which is larger for particles that hit the cell close to the edges. The uncorrected distribution, as for superclusters, forms a distribution with a peak at the centre η position of the cell and is corrected to be constant for sliding-window electrons.
- ϕ with respect to the lead absorbers corrects for the slight variations of sampling fraction seen by a particle. It is defined as ϕ (in the calorimeter frame) modulus $2\pi/1024$ in the barrel and $2\pi/768$ in the endcap, corresponding to the periodicity of lead sheets in each region,
- ratio of the energy in the strips to the energy in the middle layer of the calorimeter which

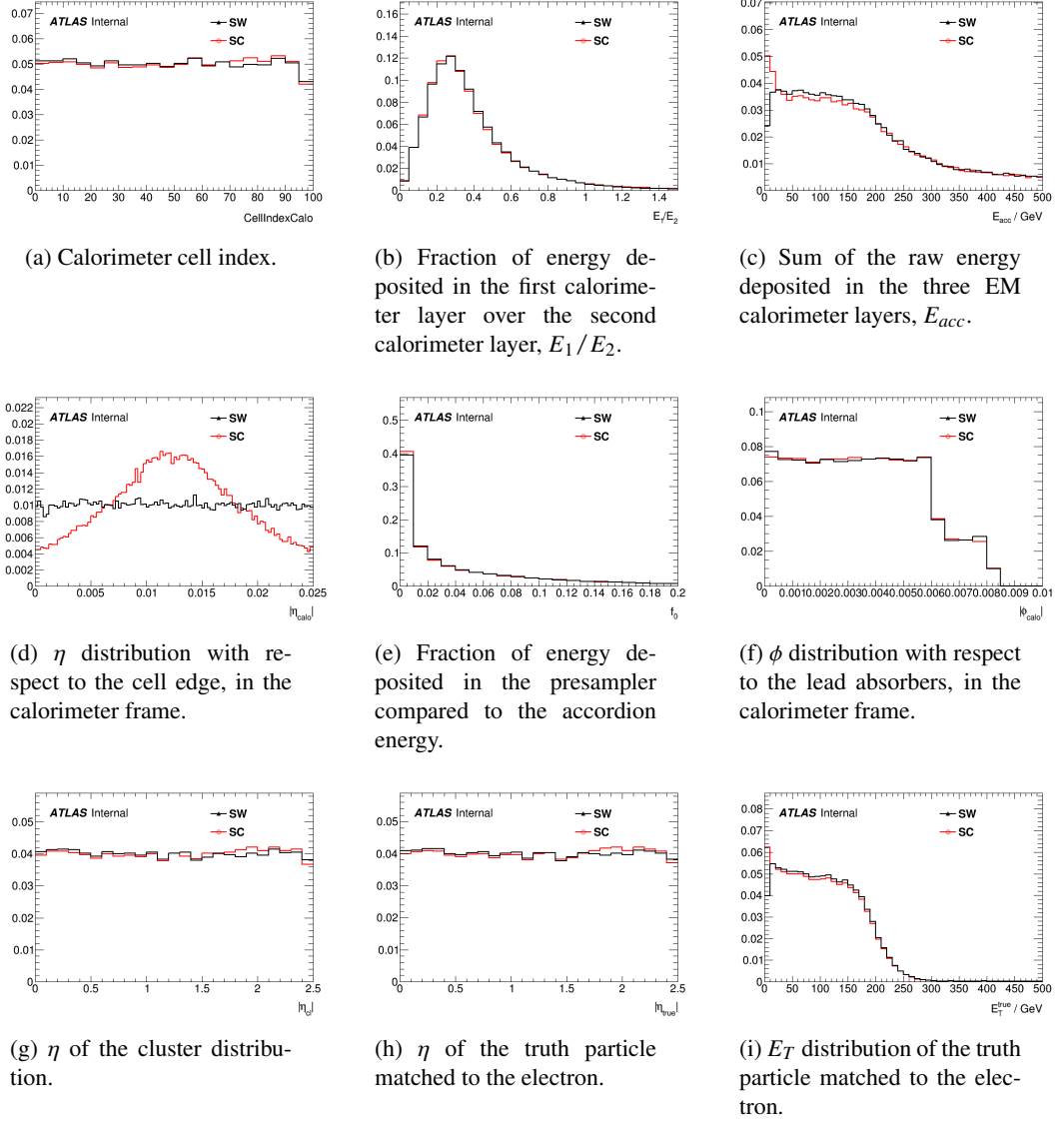


Figure 4.10: Distributions for superclusters and sliding-window single ϕ electrons of the input variables used for MVA Calibration.

determines the amount of material in front of the calorimeter and is sensitive to the radial distribution.

In order to help the MVA adjust the response as a function of the many input variables, which have different behaviours in different regions of the phase space, the sample is divided into bins in pseudorapidity ($|\eta_{cl}|$) and transverse energy in the accordion (E_T^{acc}). Particle type is also considered when electrons and photons are calibrated however, in this case only electrons are dealt with. A binning based on E_T allows the same bins to be used for all η regions, which would not be the case with an energy based binning [35]. The binning consists of 10×9 bins, with an additional 4×6

“special” bins for regions close to the edges of the two half-barrel modules. This totals 114 bins, with an MVA calibration also applied in the crack region.

- Bins in $|\eta_{cl}|$: 0,0.05,0.65,0.8,1.0,1.2,1.37,1.52,1.55,1.74,1.82,2.0,2.2,2.47,2.5 where 0 - 0.05, 1.37 - 1.52, 1.52 - 1.55, and 2.47 - 2.5 are special bins.
- Bins in E_T^{acc} : 0,10,20,40,60,80,120,500,1000 and 50 000 GeV.
- Bins in E_T^{acc} (special): 0,25,50,100,500,1000 and 50 000 GeV.

An independent optimisation is performed for each bin, producing a corresponding XML file containing the correction.

4.3.2 Performance

The performance is assessed by comparing the linearity, energy resolution and dependence of the response on several quantities. The `TestTree` events, which are not used in the training, are used to evaluate the performance to avoid any biases by using the same events to train and study the performance.

The estimators used to determine the linearity and resolution have been carefully selected due to the non-gaussian nature of the response. The mean and standard deviation cannot be used as estimators as they are unstable in the presence of outliers.

The linearity is therefore quantified by the peak position of E/E_{true} as a function of E_T^{true} , estimated by the most probable value of a gaussian function fitted to the core of the distribution in each range in E_T^{true} , $|\eta|$. The resolution is defined as the interquartile range of E/E_{true} : the distance between the first and last quarters of the data in each bin, divided by 1.349 in order to mimic the standard deviation in the case of a normal distribution.

	SC	SW
Peak	1.003	0.996
Width	0.019	0.021

Table 4.4: Peak and width values of the energy resolution, $E_{\text{acc}}/E_{\text{true}}$, peak and width values for MVA calibrated superclusters (SC, red) and sliding-window electrons (SW, black).

The inclusive energy response $E_{\text{acc}}/E_{\text{true}}$ of the single electrons, comparing the `TestTree` of superclusters and sliding-window electrons is presented in Figure 4.11. An improvement in the width and peak position of the superclusters with respect to sliding-window electrons is observed with

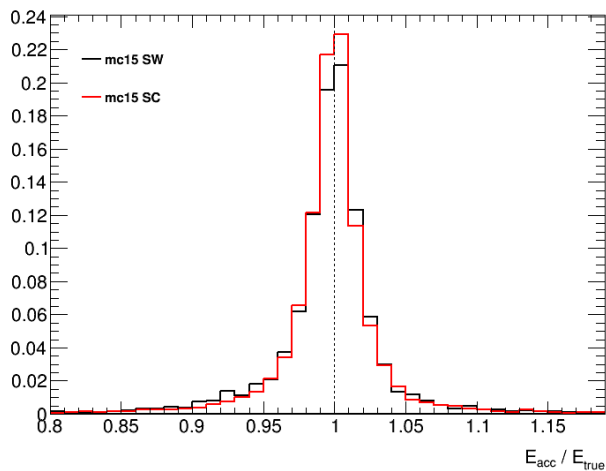


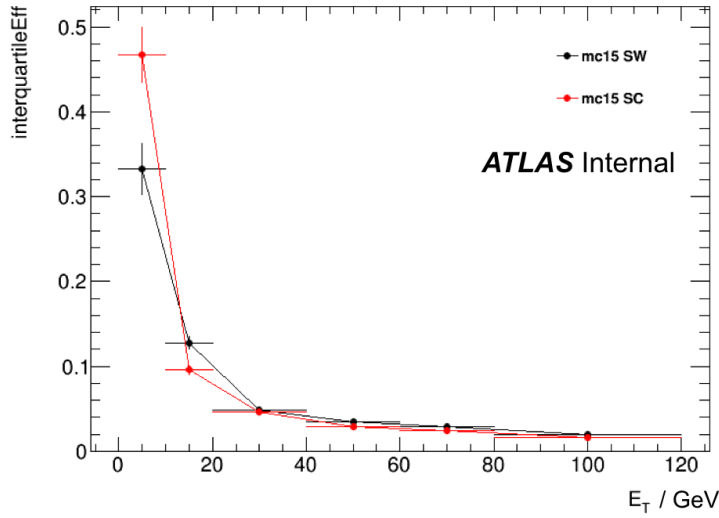
Figure 4.11: MVA calibrated energy response of the TestTree comparing superclusters (red) and sliding-window (black) single electrons

a 10.7% and 0.72% improvement. The peak and width values as a function of true E_T and η are presented in Figures 4.12 and 4.13.

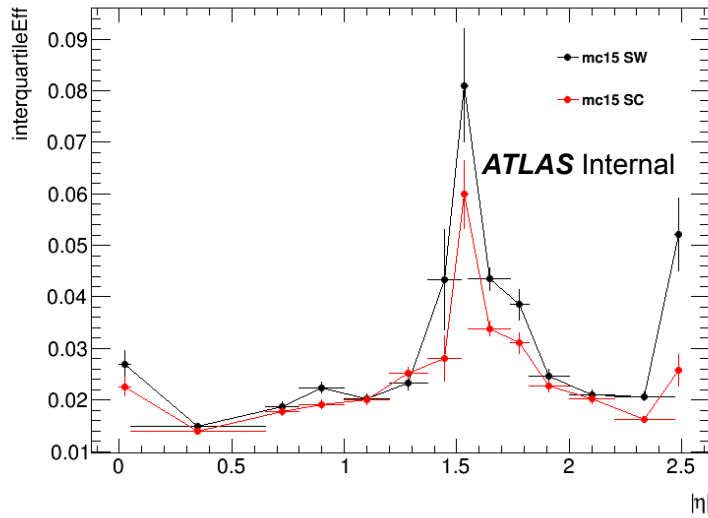
In all bins of true E_T in Figure 4.12a and η in Figure 4.12b, the width of the supercluster response is narrower than the sliding-window, except in the lowest true E_T bin. The energy response becomes narrower as true E_T increases, as expected from the detector resolution, and varies in true η which can be correlated with the material before the calorimeter, particularly with the large width in the region $1.37 < |\eta_{\text{true}}| < 1.52$. The overall improvement in the width of the superclusters compared to sliding-window electrons indicates that the core of the distribution contains more events, potentially reducing the low energy tails.

The linearity, the peak position as a function of E_T and η , fluctuates significantly, with discrepancies between the sliding-window and supercluster peak position in Figures 4.13a and 4.13b. As previously mentioned, a shift can be applied to the peak position which is particularly useful at low E_T however it has not been applied in this case. This should correct the peak positions to 1 by applying further MVA corrections calculated in smaller E_T bins.

Another limitation to the calibration study is the statistics of the samples which are trained. Whilst equivalent statistics of 10^5 single electron events have been used in both reconstruction algorithms, 20 million single electrons have been simulated for the egamma calibration currently applied in ATLAS egamma reconstruction. The large sample size enables excellent performance by having enough statistics in each bin to train the sample effectively. This means that an increase in sample size for the superclusters is particularly important and it may improve the calibration. Bins which have few events may lead to unstable calibration weights and when evaluating the performance, the



(a) Relative energy resolution as a function of true E_T .



(b) Relative energy response as a function of true η .

Figure 4.12: Uniformity as a function of true E_T and true η comparing supercluster (red) with sliding-window (black) response.

peak position can be miscalculated if the peak is not well-defined due to too few statistics.

This section has provided a preliminary assessment of the MVA calibration method when applied to superclusters, firstly demonstrating that the calibration is successful at improving the supercluster energy response when compared to the uncalibrated energy, correcting the cluster energies taking

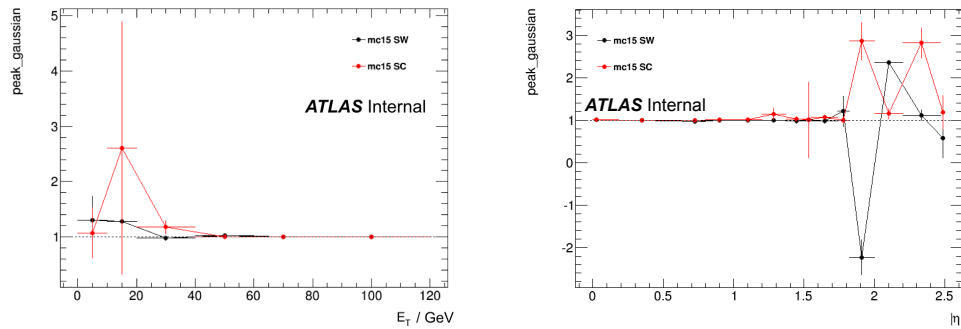
(a) Linearity as a function of true E_T .(b) Linearity as a function of true η .

Figure 4.13: Linearity as a function of true E_T and true η comparing supercluster (red) with sliding-window (black) response.

into consideration the material before the calorimeter and other shower shapes. Also when comparing superclusters and sliding-window electrons there is a potential improvement in energy resolution provided by superclustering, as demonstrated by the overall energy resolution in Figure 4.11 and an improvement in the width.

4.4 Electron Identification

As already discussed in the previous section, electrons are selected by matching ID tracks to EM calorimeter clusters. The segmentation of the calorimeter can be exploited to use the energy deposited in each layer to study the EM shower development. In addition to the clusters, the tracks are used to determine the charged particle trajectory and during track fitting the track parameters are estimated. This includes two impact parameters, d_0 and z_0 which describe the transverse and longitudinal positions and the direction of the charged particle, ϕ and θ . The information from both the calorimeter and inner detector track is used to generate a set of identification criteria for electron candidates and this section will describe the discriminating variables and identification criteria used in ATLAS analyses involving electrons. Many of the shower shape variables are also used to study the calorimeter performance and will be referred to in Chapter 6.

The reconstructed electron objects include signal electrons of interest, as well as contributions from background objects. The background must therefore be rejected whilst maintaining a high signal electron efficiency. To discriminate between isolated electrons and background which includes electrons from QCD jets, non-isolated electrons from b and c -quark decays, background electrons from meson decays or photon conversions, further rejection can be performed based on discriminating variables. The electron identification combines the variables to provide cut-based and likelihood selection menus with varying background rejection, where for the cut-based menu, selection criteria are applied sequentially on each variable, while the likelihood selection uses an MVA technique which simultaneously evaluates several properties of electron candidates when making a selection decision [27].

Clusters associated with egamma objects must satisfy a set of identification criteria based on the longitudinal and transverse shower shapes to ensure that they are consistent with expectations [25]. Variables which describe the properties of inner detector tracks and the matching between the tracks and clusters are also used to provide increasing discrimination between different sources of background electrons. These variables are presented in Table 4.5. The discriminating variables used in each of the three reference sets for the cut-based and likelihood (LH) based menus are presented in Table 4.6. In general for the cut-based identification, shower shape variables for the first and second calorimeter layers, the fraction of energy in the hadronic calorimeter and basic track quality and track-cluster matching requirements are used for the *loose* criteria. The *medium* criteria reduce the thresholds on these requirements in addition to d_0 , and fraction of TRT and innermost pixel layer (b-layer) hits. Finally, further increase in background rejection is achieved with the *tight* criteria, adding selection on the ratio of reconstructed energy to track momentum (E/p), tightens cuts on discriminating variables and a veto on reconstructed photon conversions is applied.

Table 4.5: Definition of electron discriminating variables taken from Ref. [30].

Type	Description	Name
Hadronic leakage	Ratio of E_T in the first layer of the hadronic calorimeter to E_T of the EM cluster (used over the range $ \eta < 0.8$ or $ \eta > 1.37$)	R_{Had1}
	Ratio of E_T in the hadronic calorimeter to E_T of the EM cluster (used over the range $0.8 < \eta < 1.37$)	R_{Had}
Back layer of EM calorimeter	Ratio of the energy in the back layer to the total energy in the EM accordion calorimeter	f_3
Middle layer of EM calorimeter	Lateral shower width, $\sqrt{(\sum E_i \eta_i^2) / (\sum E_i) - ((\sum E_i \eta_i) / (\sum E_i))^2}$, where E_i is the energy and η_i is the pseudorapidity of cell i and the sum is calculated within a window of 3×5 cells	$W_{\eta 2}$
	Ratio of the energy in 3×3 cells over the energy in 3×7 cells centered at the electron cluster position	R_ϕ
	Ratio of the energy in 3×7 cells over the energy in 7×7 cells centered at the electron cluster position	R_η
Strip layer of EM calorimeter	Shower width, $\sqrt{(\sum E_i (i - i_{\text{max}})^2) / (\sum E_i)}$, where i runs over all strips in a window of $\Delta\eta \times \Delta\phi \approx 0.0625 \times 0.2$, corresponding typically to 20 strips in η , and i_{max} is the index of the highest-energy strip	w_{tot}
	Ratio of the energy difference between the largest and second largest energy deposits in the cluster over the sum of these energies	E_{ratio}
	Ratio of the energy in the strip layer to the total energy in the EM accordion calorimeter	f_1
Track quality	Number of hits in the B-layer (discriminates against photon conversions)	n_{Blayer}
	Number of hits in the pixel detector	n_{Pixel}
	Number of total hits in the pixel and SCT detectors	n_{Si}
	Transverse impact parameter	d_0
	Significance of transverse impact parameter defined as the ratio of d_0 and its uncertainty	σ_{d_0}
	Momentum lost by the track between the perigee and the last measurement point divided by the original momentum	$\Delta p / p$
TRT	Total number of hits in the TRT	n_{TRT}
	Ratio of the number of high-threshold hits to the total number of hits in the TRT	F_{HT}
Track-cluster matching	$\Delta\eta$ between the cluster position in the strip layer and the extrapolated track	$\Delta\eta_1$
	$\Delta\phi$ between the cluster position in the middle layer and the extrapolated track	$\Delta\phi_2$
	Defined as $\Delta\phi_2$, but the track momentum is rescaled to the cluster energy before extrapolating the track to the middle layer of the calorimeter	$\Delta\phi_{\text{res}}$
	Ratio of the cluster energy to the track momentum	E / p
Conversions	Veto electron candidates matched to reconstructed photon conversions	isConv

Table 4.6: The variables used in the different selections of the electron identification menu taken from Ref. [30].

Name	Cut-based			Likelihood		
	<i>loose</i>	<i>medium</i>	<i>tight</i>	LOOSE	MEDIUM	VERY TIGHT
$R_{\text{Had}(1)}$	✓	✓	✓	✓	✓	✓
f_3		✓	✓	✓	✓	✓
$W_{\eta 2}$	✓	✓	✓	✓	✓	✓
R_{η}	✓	✓	✓	✓	✓	✓
R_{ϕ}				✓	✓	✓
w_{stot}	✓	✓	✓	✓	✓	✓
E_{ratio}	✓	✓	✓	✓	✓	✓
f_1				✓	✓	✓
n_{Blayer}		✓	✓	✓	✓	✓
n_{Pixel}	✓	✓	✓	✓	✓	✓
n_{Si}	✓	✓	✓	✓	✓	✓
d_0		✓	✓		✓	✓
σ_{d_0}					✓	✓
$\Delta p/p$				✓	✓	✓
n_{TRT}		✓	✓			
F_{HT}		✓	✓	✓	✓	✓
$\Delta\eta_1$	✓	✓	✓	✓	✓	✓
$\Delta\phi_2$			✓			
$\Delta\phi_{\text{res}}$				✓	✓	✓
E/p			✓			
isConv			✓			✓

The cut-based selections are optimised in 10 $|\eta|$ bins and 11 E_T bins, to account for the variations in the electron shower shapes. Cut-based electron identification was used from the beginning of data taking with improvements to the selection in 2011 and 2012 to improve background rejection, by introducing new variables and adjusting the cut thresholds.

The electron LH generates a discriminant combining the signal and background probability, using the probability distribution functions (PDFs) of the discriminating variables. A cut is applied to the discriminant which provides increasing background rejection with tighter LH [30].

Electron identification is achieved through the precise tracking and transition radiation detection in the ID and by using the fine segmentation of the EM calorimeter. The electrons can be classified as:

- Isolated electrons: true electrons,
- Non-isolated electrons: semi-leptonic heavy-flavour decays from a b or c-meson,
- Background electrons: including hadrons and photon conversions.

The isolated, non-isolated and background electron properties and the discriminating power of variables from Table 4.5 will be discussed in further details in the following section.

4.4.1 Calorimeter information

To efficiently identify electrons, the transverse and longitudinal segmentation of the EM calorimeter is exploited. The hadronic leakage variables can be used to discriminate between particles which deposit most of their energy in the EM calorimeter, which is typical of isolated electrons, requiring a small value of R_{Had} and R_{had1} . Large values of hadronic leakage indicate significant energy deposition in the hadronic calorimeter. Distributions of some calorimeter variables are presented in Figure 4.14.

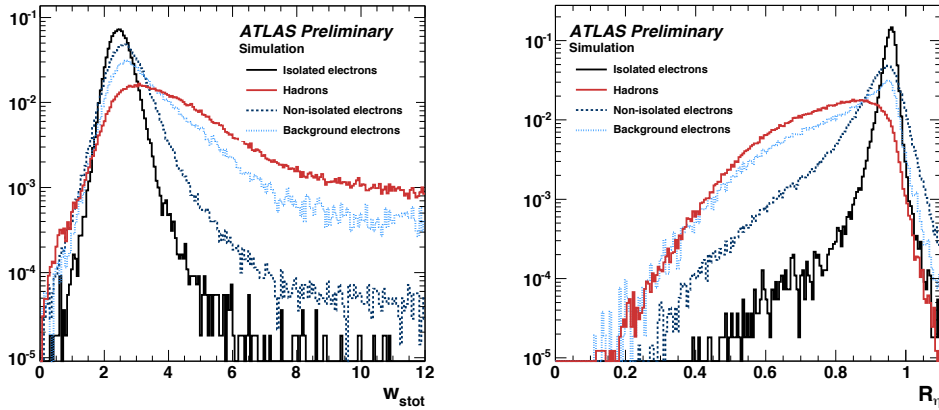
The shower width in the second sampling layer (S2) can be measured using $W_{\eta 2}$, or R_{η} . It is expected that in η , isolated (true) electron showers are narrower than those from jets and photon conversions and requiring narrower shower widths suppresses the background. The R_{η} distribution of isolated electrons and their main background is presented in Figure 4.14b with a narrow width, peaking at 1 for isolated electrons.

The fine granularity of the strips in the first sampling layer (S1) can be exploited to provide background separation using the shower width, w_{stot} , and also by using E_{ratio} . The shower width, similar to those in S2, is larger for background than for electrons, providing background separation, as in the w_{stot} distribution in Figure 4.14a. For E_{ratio} , isolated electrons do not have a significant second energy deposit, unlike jets which have multiple comparable maxima corresponding to multiple particles forming the electron. The isolated electrons form a significant E_{ratio} peak at 1, whilst lower values for the background, as demonstrated in Figure 4.14c.

Finally, the energy fraction in the third sampling layer (S3) f_3 , is used to separate isolated electrons, which deposit most of their energy in the second sampling layer, from high energy showers which reach the third layer, such as jets.

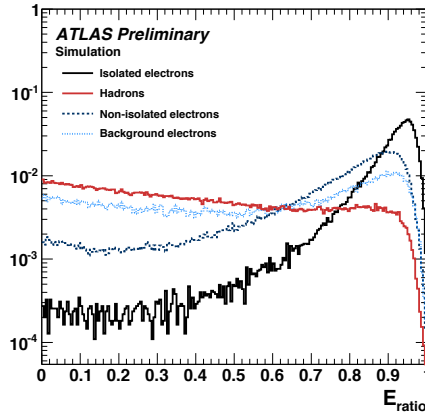
4.4.2 Track information

As described in Chapter 3, the inner detector system is formed of the pixel detector, the SCT and the TRT and the combined system provides precise reconstruction of tracks within $|\eta| < 2.5$. The three pixel layers allow 3 hits per track, four back-to-back single-sided silicon strip sensors account for up to 8 hits per track and the TRT typically contributes 35 hits per track within $|\eta| < 2.0$.



(a) Shower width in the first EM calorimeter layer.

(b) Ratio of energy in 3x7 over 7x7 cells in the second EM calorimeter layer.



(c) Ratio of the energy difference between the largest and second largest energy deposits in the cluster over the sum of these energies.

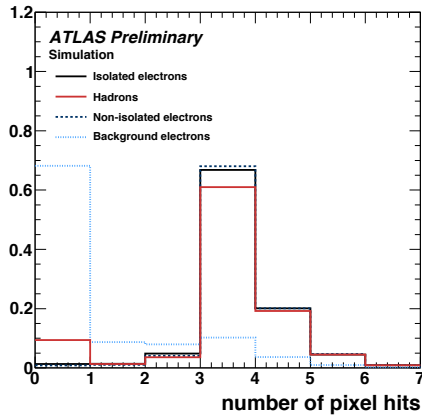
Figure 4.14: EM calorimeter discriminating variables w_{stot} , R_η and E_{ratio} used in electron identification menus to separate isolated electrons from the main backgrounds [32].

Electrons, as charged particles, leave tracks in the ID, unlike photons. This property can be exploited as there will be a smaller number of hits in the pixel and SCT detectors for photons compared to isolated electrons which will have hits in all traversed layers. Also, a hit in the innermost pixel layer can be used to discriminate between electrons and photon conversions which occur beyond this layer. Finally the transverse impact parameter, d_0 is used to discriminate background and non-isolated electrons, with tracks which are displaced from the interaction point from prompt, isolated electrons.

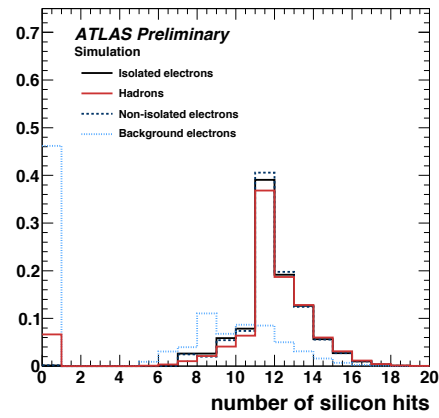
Figure 4.15 presents the number of hits in the ID for isolated electrons and the main backgrounds

and therefore the following track quality requirements are imposed to select isolated electrons:

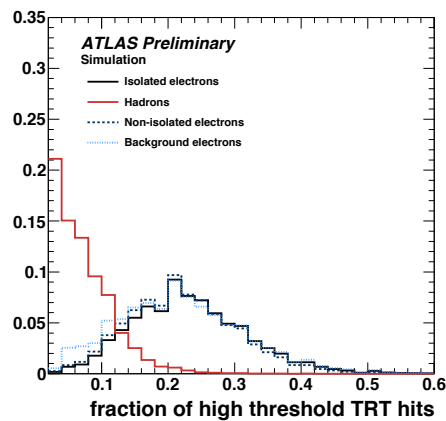
- Number of pixel hits ≥ 1 ,
- Number of silicon hits (pixel + SCT) ≥ 7 ,
- Number of innermost pixel layer hits ≥ 1 to reject photon conversions,
- $|d_0| < 5$ mm.



(a) Number of hits in the pixel detector.



(b) Number of hits in the pixel and SCT detectors.



(c) Ratio of the number of high-threshold hits to the total number of hits in the TRT.

Figure 4.15: Inner detector discriminating variables used in electron identification menus to separate isolated electrons from the main backgrounds [32].

TRT

Emission of transition radiation (TR) photons in the straw tube of the TRT is measured using the fraction of high threshold hits F_{HT} , where TR photons are present if there is a high F_{HT} . The probability of producing a TR photon is proportional to the inverse mass ($\gamma = E/m$) and is a threshold effect. The F_{HT} for conversions, non-isolated and isolated electrons is comparable. However, heavy pions and charged hadrons have a low probability of producing TR photons and therefore a low fraction of TRT hits. The F_{HT} therefore can be used to reject hadronic background, as shown in Figure 4.15c.

4.4.3 Combined track/calorimeter information

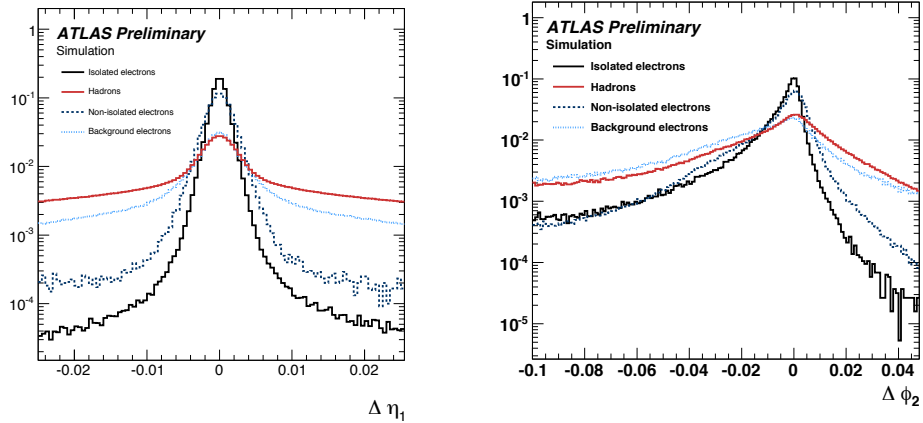
The cluster-track matching difference in η and ϕ between the track and cluster provides additional discriminating power. The difference for isolated electrons in η is small, with a narrow $\Delta\eta$ distribution as shown in Figure 4.16a. For $\Delta\phi_2$, the difference for electrons is small, and widens for jets and π^0 -mesons, demonstrated in Figure 4.16b. The charge dependency must therefore also be considered. Finally, the E/p can be used to identify isolated electrons, which have a peak at 1, with a long positive tail. Hadrons only deposit a fraction of their energy in the EM calorimeter, before traversing to the hadronic calorimeter and therefore will peak at a lower value, as in Figure 4.16c. Conversions have a larger E/p as the full energy will be deposited in the EM calorimeter, however these energy deposits correspond to several tracks.

The full list of discriminating variables is used in electron identification menus which are implemented in physics analyses to select isolated electrons and will be used in the subsequent chapters.

4.5 Summary

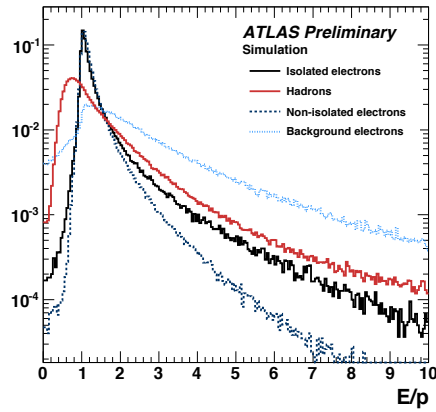
This chapter has discussed electron reconstruction and identification using the ATLAS detector. The current electron reconstruction algorithm can be improved by using topological clustering to build superclusters and account for energy loss due to bremsstrahlung.

The supercluster algorithm, including cluster formation and track-matching, has been described. MVA calibration methods are used to correct the energy in the accordion, estimating the initial electron energy and to account for any variations in the electron properties, removing dependency for example of the shower shapes on the amount of passive material before the EM calorimeter. The performance of the superclusters is compared to the sliding-window electrons and the impact of the



(a) $\Delta\eta$ between the cluster position in the strip layer and the extrapolated track.

(b) $\Delta\phi$ between the cluster position in the middle layer and the extrapolated track.



(c) Ratio of the cluster energy to the track momentum.

Figure 4.16: Combined track and calorimeter discriminating variables used in electron identification menus to separate isolated electrons from the main backgrounds [32].

different reconstruction algorithms when calibrated is studied with single electrons with a 10.7% improvement in the width of the calibrated electron response, and 0.72% in the peak position.

Finally, electron identification in ATLAS and selection menus are discussed, with emphasis on the discriminating power of variables in physics analyses which are useful for reference in subsequent chapters, including Chapter 5 and 6.

Chapter 5

Heavy Higgs search in the Higgs to four-lepton channel with 8 TeV data

5.1 Introduction

Dedicated experimental searches for the Higgs boson have been underway since the 1980s at LEP and TeVatron. From 1989-2000, LEP collided electrons and positrons at $\sqrt{s} = 91 - 209$ GeV within the tunnel which now houses the LHC, and set lower limits on the mass of the Higgs boson (m_h) of 114.4 GeV to 95% confidence level. Similarly, TeVatron, in operation from 1987-2011, excluded the region of $147 < m_h < 180$ GeV, colliding protons and anti-protons at energies up to $\sqrt{s} = 1.96$ TeV. Both machines operated up to the limit of their capabilities and the LHC rapidly achieved both higher energies and luminosities than its predecessors, with the potential to probe previously unexplored regions, initially confirming the limits set by the previous experiments. The lower limits set by LEP, TeVatron and the LHC up until 2012 are presented in Figure 5.1 with 10 fb^{-1} of TeVatron data.

Following the 2012 TeVatron limits, the LHC reported the discovery of a Higgs boson, h with a mass of approximately 125 GeV by the ATLAS and CMS experiments, with the local probability presented in Figure 5.2 [1, 2]. Further measurements of the Higgs bosons properties such as couplings, differential cross-sections, Higgs quantum numbers and a mass combination of ATLAS and CMS results have been performed, reporting a Higgs boson compatible with SM predictions [40, 41, 42, 43].

The proton-proton collisions at the LHC provides several mechanisms of production of a SM Higgs boson as shown in Figure 5.3 at 8 TeV. Higgs boson production is dominated by gluon-gluon fusion (ggF) whereby two gluons fuse via a quark loop (usually top) emitting a Higgs boson. Other production modes include vector boson fusion (VBF), associated production with a vector boson (VH) and associated production with a $t\bar{t}$ pair. The Feynman diagrams representing each of these

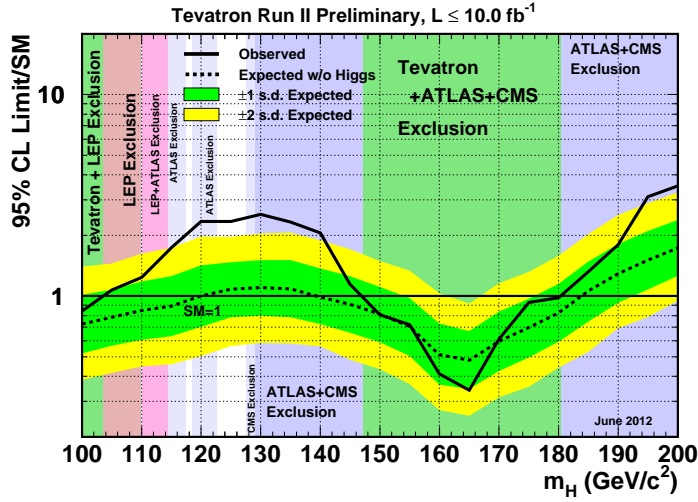


Figure 5.1: Observed and expected (median, for the background-only hypothesis) 95% CL upper limits on the ratios to the SM cross section, as functions of the Higgs boson mass. Results are presented for the combined CDF and D0 analyses and also including limits set by LEP and the LHC [39].

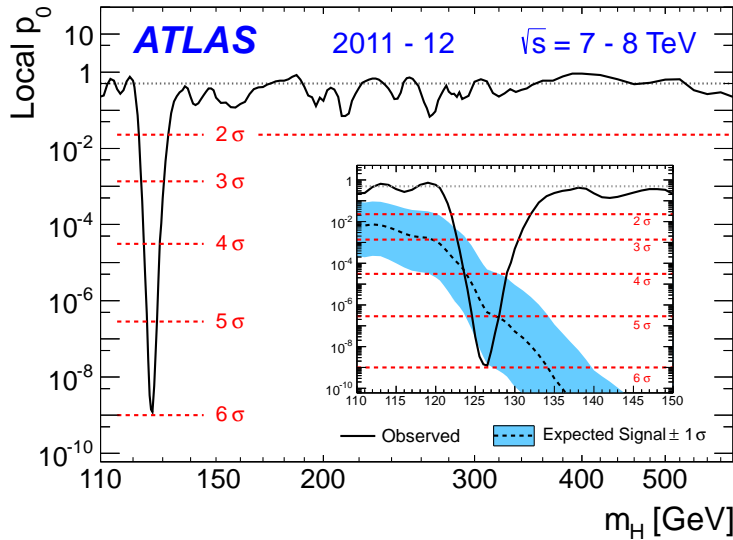


Figure 5.2: The local probability p_0 for a background-only experiment to be more signal-like than the observation, as a function of m_H . The dashed curve shows the median expected local p_0 under the hypothesis of a Standard Model Higgs boson production signal at that mass. The horizontal dashed lines indicate the p-values corresponding to significances of 1σ to 6σ [1].

mechanisms are shown in Figure 5.4. The Higgs boson can then decay via several different modes. The cross-section times branching ratio of each decay is presented in Figure 5.5 at 8 TeV.

A decay channel of particular interest and often referred to as “the golden channel” is $H \rightarrow ZZ^{(*)} \rightarrow 4\ell$.

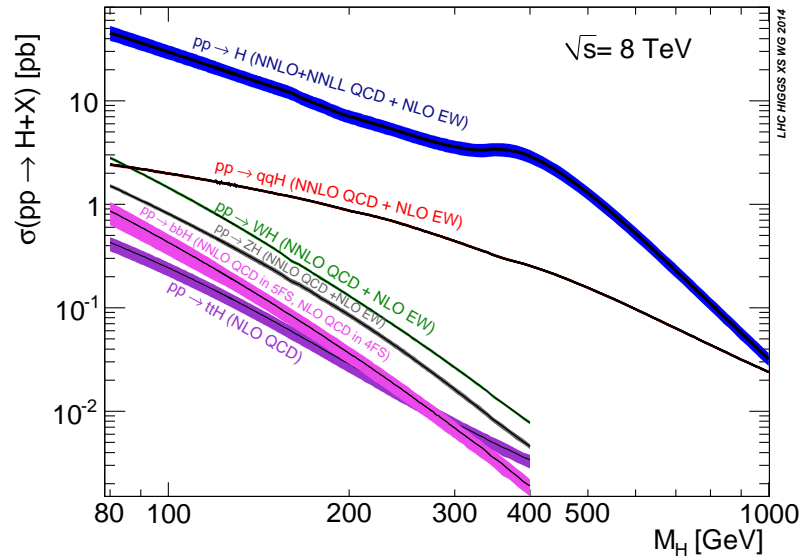


Figure 5.3: Cross-section for SM Higgs boson production at 8 TeV [44], including next-to-leading-order (NLO), next-to-next-to-leading-order (NNLO) and next-to-next-to-leading-logarithmic (NNLL) corrections.

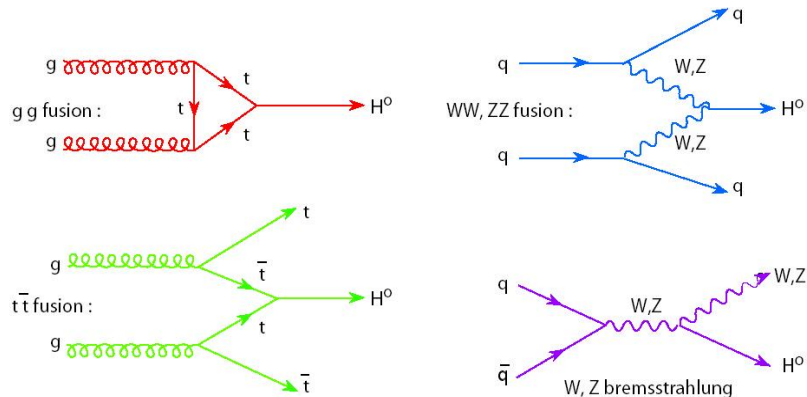


Figure 5.4: Feynman diagrams of the Higgs production mechanisms.

This channel is sensitive over a wide mass range and the Z bosons decay leptonically, providing a clean signal from four well-isolated leptons. This channel played a major role in the 2012 discovery of the Higgs boson at 125 GeV [1] and is also suitable for searches for additional Higgs bosons, which are postulated by extensions to the SM, also known as beyond the SM (BSM) theories as described in Section 2.8. The EWS and 2HDM models both predict additional Higgs bosons and results can be interpreted in the scenario of a new Higgs boson with a narrow width, as well as in Type-I and Type-II 2HDMs. In the $H \rightarrow ZZ \rightarrow 4\ell$ channel, the dominant background contribution arises from the SM ZZ continuum which is a well understood process and is estimated from theory. Further non-reducible backgrounds include Z +jets and $t\bar{t}$ which are estimated using data-driven techniques involving control regions.

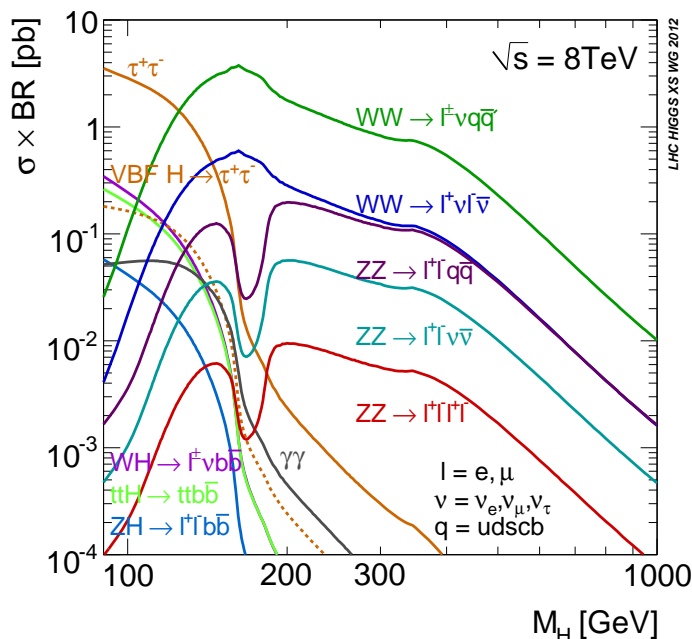


Figure 5.5: Cross-section times branching ratio for a SM Higgs boson at 8 TeV [44].

This chapter provides an overview of the heavy Higgs analysis in the $H \rightarrow ZZ^{(*)} \rightarrow 4\ell$ channel and presents cross-section times branching ratio limits [45] using 95% CL_s method [46]. The author's contribution to the search was the derivation of the statistical limits however, the analysis procedure will also be described in this Chapter for completeness.

5.2 Analysis Overview

The search for an additional Higgs boson in the $H \rightarrow ZZ^{(*)} \rightarrow 4\ell$ channel is motivated by extensions to the SM. This channel is particularly sensitive across a wide mass range with an excellent signal over background ratio and mass resolution. The $H \rightarrow ZZ^{(*)} \rightarrow 4\ell$ analysis is based on the $m_h = 125$ GeV (light Higgs) analysis and searches for narrow resonances are performed in the range $140 < m_H < 1000$ GeV using 20.3 fb^{-1} of 8 TeV data [1]. In this region there is no on-shell contamination from the light Higgs boson, however there is a small off-shell contribution, caused by the interference between ggF production of the light Higgs boson and the heavy Higgs ZZ background process. This contribution is treated as a background process and accounted for in the background samples, as will later be described. To ensure there is no overlap with light Higgs boson candidates, the four-lepton invariant mass ($m_{4\ell}$) is used as the discriminating variable and is limited to the range $135 < m_{4\ell} < 1200$ GeV.

The search for a heavy Higgs state in the four-lepton channel is performed using an unbinned fit

to the $m_{4\ell}$ mass distribution in the search ranges above [45]. An unbinned fit is particularly useful when there is a small amount of data expected in each bin and therefore each data point is plotted. The parameter of interest in the fit is the signal strength, μ which is the scale-factor on the number of expected signal events predicted by a reference cross-section and branching ratio [17]. The reference cross-section and branching ratio are chosen to be the SM values and the results are interpreted as model independent limits on an additional Higgs boson in the Narrow Width Approximation (NWA), assuming a narrow Higgs width where the effect of interference between signal and continuum background is negligible [17].

5.2.1 Event Selection

In the $H \rightarrow ZZ \rightarrow 4\ell$ channel, the Higgs boson decays to a pair of Z bosons, which decay to two pairs of highly energetic, oppositely charged leptons which provide a clean channel with a high signal-to-background ratio. There are four combinations of electron and muon pairs which lead to four final states: $4e$, 4μ , $2\mu 2e$, $2e 2\mu$, where the dilepton pairs are ordered by p_T , where the first pair has a dilepton invariant mass closest to the Z boson mass and are referred to as the leading leptons. The event selection is based on light $h \rightarrow ZZ^{(*)} \rightarrow \ell^+\ell^-\ell^+\ell^-$ analyses as described in detail in [47, 45], where dilepton pairs are built from leptons passing strict quality criteria. Dilepton mass cuts of $50 < m_{12} < 106$ GeV and $m_{threshold} < m_{34} < 115$ GeV are applied, where m_{12}, m_{34} correspond to the leading and sub-leading dilepton pair and $m_{threshold}$ varies as a function of $m_{4\ell}$. As mentioned, $m_{4\ell}$ is a powerful discriminating variable and is used as it has excellent resolution and is sensitive to m_H . Data quality cuts are also imposed to select events from stable beam periods which are recorded during nominal detector performance. The events must also pass a single-lepton or dilepton trigger to maximise acceptance. For this analysis, 20.3 fb^{-1} of 8 TeV data are used. The full event selection criteria are presented in Table 5.1, and a brief description of the object selection is presented in the following sections.

Electrons

Electrons are required to be well-reconstructed with GSF-refitted tracks which are associated with an EM cluster. The LOOSE likelihood offline electron identification criteria are specified, as described in Chapter 4.4, to discriminate between isolated electrons and jets. Further variables are used to discriminate against background sources as presented in Table 5.1. Electron energy calibration is applied to data and the MC signal and MC background, improving the energy resolution particularly in problematic regions of the EM calorimeter, such as the crack region $1.37 < |\eta| < 1.52$ [47].

Kinematically, electrons are required to be within $|\eta_{cl}| < 2.47$ with $E_T > 7$ GeV. For the MC,

Table 5.1: Summary of the event selection requirements of searches for a Higgs boson in the four-lepton channel, taken from Reference [45]. The two lepton pairs are denoted as m_{12} and m_{34} .

Event Pre-selection	
Electrons	
LOOSE LH quality electrons with $E_T > 7$ GeV and $ \eta < 2.47$	
Muons	
Combined or segment-tagged muons with $p_T > 6$ GeV and $ \eta < 2.7$	
Maximum one calo-tagged or standalone muon	
Calo-tagged muons with $p_T > 15$ GeV and $ \eta < 0.1$	
Standalone muons with $p_T > 6$ GeV, $2.5 < \eta < 2.7$ and $\Delta R > 0.2$ from closest segment-tagged	
Event Selection	
Kinematic Selection	<p>Require at least one quadruplet of leptons consisting of two pairs of same-flavour opposite-charge leptons fulfilling the following requirements:</p> <p>p_T thresholds for three leading leptons in the quadruplet 20, 15 and 10 GeV</p> <p>Select the best quadruplet from dilepton mass pairs where m_{12} is the leading lepton pair which is closest to the Z mass and m_{34} is the sub-leading lepton pair which is the next closest mass pair to the Z mass.</p> <p>Leading dilepton mass requirement $50 \text{ GeV} < m_{12} < 106 \text{ GeV}$</p> <p>Sub-leading dilepton mass requirement $m_{threshold} < m_{34} < 115 \text{ GeV}$</p> <p>where $m_{threshold} = 12 \text{ GeV}$ for $m_{4\ell} < 140 \text{ GeV}$,</p> <p>increasing linearly in the interval $m_{4\ell} \in [140 \text{ GeV}, 190 \text{ GeV}]$,</p> <p>where $m_{threshold} = 50 \text{ GeV}$ for $m_{4\ell} > 190 \text{ GeV}$</p> <p>Remove quadruplet if alternative same-flavour opposite-charge dilepton gives $m_{\ell\ell} < 5 \text{ GeV}$</p> <p>$\Delta R(\ell, \ell') > 0.10(0.20)$ for all same (different) flavour leptons in the quadruplet.</p>
Isolation	<p>Isolation cut applied on all leptons of the quadruplet</p> <p>Contribution from the other leptons of the quadruplet is subtracted</p> <p>Lepton track isolation ($\Delta R = 0.20$): $\Sigma p_T / p_T < 0.15$</p> <p>Electron calorimeter isolation ($\Delta R = 0.20$): $\Sigma E_T / E_T < 0.20$</p> <p>Muon calorimeter isolation ($\Delta R = 0.20$): $\Sigma E_T / E_T < 0.30$</p> <p>Stand-Alone muons calorimeter isolation ($\Delta R = 0.20$): $\Sigma E_T / E_T < 0.15$</p>
Impact Parameter Significance	<p>Apply impact parameter significance cut to all leptons of the quadruplet.</p> <p>For electrons : $d_0 / \sigma_{d_0} < 6.5$</p> <p>For muons : $d_0 / \sigma_{d_0} < 3.5$</p>

reconstruction and identification efficiency scale factors are applied to account for any discrepancies between data and MC.

Muons

After reconstruction, muons are split into categories depending on their tracks: combined muons have a full muon spectrometer track or track segment also with an inner detector track, segment-tagged muons only have muon track segments, calo-tagged have limited coverage within the muon spectrometer, with $|\eta| < 0.1$, and stand-alone muons which have $|\eta| > 2.5$ with a full muon spectrometer track but no inner detector track. A maximum limit of one stand-alone or calo-tagged muon per event is imposed.

The kinematic requirements vary depending on the category of the muon and the thresholds are presented in Table 5.1. As with electrons, the MC is reweighted using muon reconstruction efficiency scale factors and the p_T is corrected to improve the muon momentum scale.

Jets

Jets are used in the $H \rightarrow ZZ \rightarrow 4\ell$ analysis to categorise events according to the production mode, as described in Figure 5.6, where two high p_T jets are required, in addition to four-leptons, to be classified as VBF-enriched. Jets are reconstructed from topoclusters using the anti- k_T algorithm with a distance parameter of $R=0.4$ [48]. The topoclusters are corrected from EM scale to hadronic energy scale using p_T and η dependent jet energy scale determined from data. Jets from pile-up are removed using MC and also by requiring a jet vertex fraction (the fraction of tracks from the original primary vertex) to be greater than 50% for jets with $p_T < 50$ GeV and $|\eta| < 2.4$ at 8 TeV.

Overlapping objects

To ensure that no duplicate objects are reconstructed by different algorithms and that no clusters are overlapping, an overlap removal is performed by comparing the reconstructed objects. If two EM clusters share the same ID track, the lowest p_T track is removed. If an electron shares the same track as a segment-tagged or combined (calo-tagged) muon, the electron (muon) is removed. Also, if a jet overlaps with an electron which satisfies the selection criteria within $\Delta R < 0.2$, the jet is removed.

Quadruplet formation

Events which pass selection and contain four-leptons, two same flavour, opposite sign pairs are used to construct Higgs candidates. Additional cuts are imposed requiring the p_T of the three leading leptons to be greater than 20, 15, and 10 GeV and each event is required to have the triggering lepton(s) matched to one or two of the selected leptons. The leading dilepton (Z_1) is defined as the lepton pair with $m_{\ell\ell}$ closest to m_Z and to ensure that only one quadruplet is formed per event, if there is greater than four-leptons reconstructed, the sub-leading dilepton pair is chosen based on the next closest $m_{\ell\ell}$ to m_Z .

A summary of the full event selection is presented in Table 5.1. To ensure that the leptons are well-isolated, further reducing Z +jets and $t\bar{t}$ background, track and calorimeter isolation is required. The track isolation discriminant is defined as the sum of the p_T of the tracks inside a cone of size $\Delta R = 0.2$ around the lepton, excluding the lepton track, divided by the lepton p_T . The calorimeter isolation for electrons sums the cluster E_T in the EM and hadronic calorimeters with a barycentre inside a cone of size $\Delta R = 0.2$ around the electron cluster, excluding the cells corresponding to the core of the electron cluster, divided by the electron E_T . The calorimetric isolation discriminant for muons sums the calorimeter cell E_T inside a cone of $\Delta R = 0.2$ around the muon, subtracting the muon ionisation energy which is calculated as the sum of cells in a smaller cone, divided by the muon p_T [47]. The values of the lepton isolation requirements are in Table 5.1.

Impact parameter requirements are also imposed to exclude heavy quark decays whereby the vertices are displaced from the primary vertices, and to select the best quadruplets, cuts are applied to the leading and sub-leading lepton masses and quadruplets which pass the full selection are defined as $H \rightarrow ZZ^{(*)} \rightarrow 4\ell$ candidates.

In $H \rightarrow ZZ^{(*)} \rightarrow 4\ell$ events, low E_T photons may be emitted by Final State Radiation (FSR), resulting in less reconstructed energy than the true energy of the event, which can affect the $m_{4\ell}$ distribution. These events can be recovered by searching for photons in a ΔR cone around reconstructed leptons, which includes collinear photons emitted in $Z \rightarrow \mu^+\mu^-$ events, or non-collinear (far) photons in both $Z \rightarrow \mu^+\mu^-$ and $Z \rightarrow e^+e^-$ events. Also, to improve the dilepton mass resolution, the Z -lineshape and lepton momentum uncertainties can be exploited to recompute the four-momentum of the leading Z boson. This is performed using a constrained kinematic fit of m_Z . The fit uses a Breit-Wigner Z lineshape and a single gaussian to model the lepton momentum response function, where the width of the Gaussian σ is set to the expected resolution for each lepton. This is performed only for the leading dilepton pair which is predominantly produced in the decay of an on-shell Z boson [45, 47].

Event categorisation

Once the quadruplets are formed, each $H \rightarrow ZZ \rightarrow 4\ell$ candidate is assigned to one of four different categories based on the production mechanisms previously described in Section 5.1. The four categories are presented in Figure 5.6 and are VBF-enriched, VH-hadronic enriched, VH-leptonic enriched and ggF-enriched.

The production cross-sections for additional high mass Higgs bosons are not predicted by the SM and therefore the ratio of production modes is unknown when presenting results independent of a model. To avoid making assumptions about the ratios, the event categories are used [45]. Samples enriched in different production mechanisms are selected by means of an orthogonal categorisation, testing for each category following the procedure presented in Figure 5.6. An event is classified as VBF-like if, in addition to the four-leptons there are two high p_T jets with $p_T > 25$ GeV (30 GeV) for $|\eta| < 2.5$ ($2.5 < |\eta| < 4.5$) and the dijet mass $m_{jj} > 130$ GeV. If an event does not pass these criteria, it is considered for the VH-hadronic category, requiring the same jet selection however with a dijet mass of $40 < m_{jj} < 130$ GeV in addition to a multivariate discriminant which is based on a boosted decision tree (BDT) and is trained to discriminate VH-hadronic from ggF events. If the event then fails the VH-hadronic requirements, it is considered for the VH-leptonic category if there is an extra lepton in addition to the four-leptons which satisfies the same lepton requirements with $p_T > 8$ GeV. Finally, all remaining events which do not satisfy a previous category are classified as ggF-like.

In the $H \rightarrow ZZ \rightarrow 4\ell$ analysis, only a small number of events pass the VH criteria due to the decreasing VH production cross-section with m_H . VH-like events are therefore combined with VBF-like events to maximise statistics and will be referred to as VBF or VBF+VH events in the following sections.

5.2.2 Background Processes and Modelling

To estimate the background to the $H \rightarrow ZZ \rightarrow 4\ell$ search, the irreducible and reducible backgrounds are simulated. Irreducible backgrounds produce the same final states as the signal and reducible backgrounds contain final states which have been misidentified to be the same as the final state required.

The background processes in the $H \rightarrow ZZ \rightarrow 4\ell$ search include SM ZZ production, whereby the Z bosons are produced directly in pp -collisions and decay leptonically, resulting in a 4-lepton final state. The irreducible background, despite having the same final state as $H \rightarrow ZZ \rightarrow 4\ell$, is well-simulated and can therefore be modelled and estimated using MC. The ZZ background is modelled

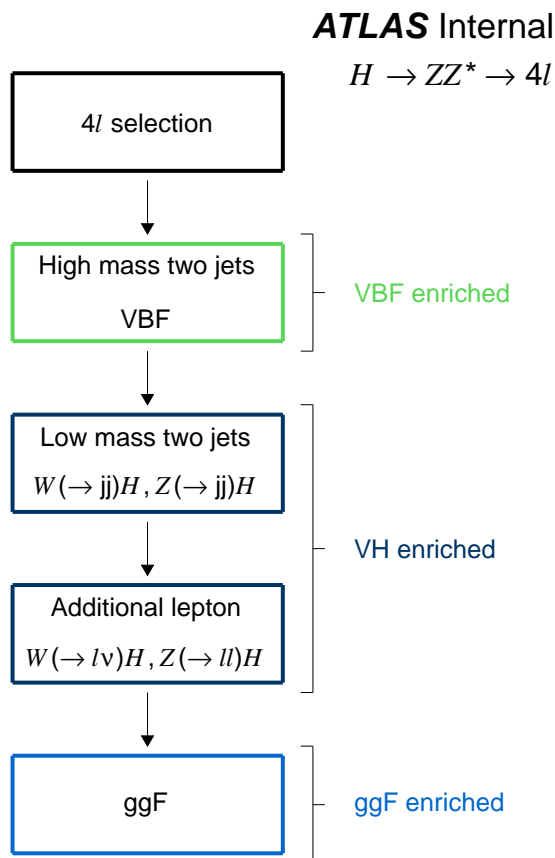


Figure 5.6: Schematic view of the event categorisation [49].

by separating the $gg \rightarrow ZZ^{(*)}$ and $q\bar{q} \rightarrow ZZ^{(*)}$ processes to allow the light Higgs contribution to the background to be incorporated in the $q\bar{q} \rightarrow ZZ^{(*)}$ process and to apply the correct scales and uncertainties to the MC. The generators used for the irreducible background are described in Table 5.2 and a full description can be found in Reference [49].

For the reducible background, data-driven methods are used to estimate the contribution. For the Z +jets background, a Z boson is produced in addition to light quark jets which are misidentified as leptons and for $Z+bb$, a Z boson is produced in association with a heavy (c or b) quark, which as they weakly decay produce non-prompt leptons in the final state. Leptonic $t\bar{t}$ decays occur via the weak force and eventually emit 4-leptons. Finally, events from WZ background also contribute, as the Z boson decays via $Z \rightarrow \ell^+ \ell^-$ and the W boson decays to $W \rightarrow \ell \nu$. If there is an additional lepton present or the jet is mis-identified as a lepton, then a second lepton pair may be included. In the reducible background, the signal is not identical to the $H \rightarrow ZZ \rightarrow 4l$ final state and may contain additional particles or particles which may be mis-identified as leptons. Therefore,

Physics process	$H \rightarrow ZZ$ final state	Generator	Cross-section normalization	PDF set	Tune
<i>W/Z boson + jets</i>					
$Z/\gamma^* \rightarrow \ell^+ \ell^- / \nu \bar{\nu}$	$\ell\ell\ell\ell$	ALPGEN 2.14	NNLO	CTEQ6L1	AUET2
<i>Top quark</i>					
$t\bar{t}$	$\ell\ell\ell\ell$	POWHEG-BOX r2129	NNLO+NNLL	NLO CT10	PERUGIA2011C
s -channel and Wt	$\ell\ell\ell\ell$	POWHEG-BOX r1556	NNLO+NNLL	NLO CT10	PERUGIA2011C
t -channel	$\ell\ell\ell\ell$	ACERMC 3.8	NNLO+NNLL	CTEQ6L1	AUET2
<i>Dibosons</i>					
$q\bar{q} \rightarrow ZZ(*)$	$\ell\ell\ell\ell$	POWHEG-BOX r1508	NNLO QCD NLO EW	NLO CT10	AUET2
EW $q\bar{q} (\rightarrow h) \rightarrow ZZ(*) + 2j$	$\ell\ell\ell\ell$	MADGRAPH 5 1.3.28		CTEQ6L1	AUET2
$gg (\rightarrow h^*) \rightarrow ZZ$	$\ell\ell\ell\ell$	MCFM 6.1	NNLO	NLO CT10	AU2
$q\bar{q} \rightarrow WZ$	$\ell\ell\ell\ell$	SHERPA 1.4.1			SHERPA default
$q\bar{q} \rightarrow WW$	$\ell\ell\ell\ell$	POWHEG-BOX r1508	NLO	NLO CT10	AUET2
<i>Signal</i>					
$gg \rightarrow H \rightarrow ZZ(*)$	$\ell\ell\ell\ell$	POWHEG-BOX r1508	—	NLO CT10	AU2
$q\bar{q} \rightarrow H + 2j$; $H \rightarrow ZZ(*)$	$\ell\ell\ell\ell$	POWHEG-BOX r1508	—	NLO CT10	AU2
$q\bar{q} \rightarrow (W/Z)H$; $H \rightarrow ZZ(*)$	$\ell\ell\ell\ell$	PYTHIA 8.163	—	CTEQ6L1	AU2

Table 5.2: Details of the generation of simulated signal and background event samples. For each physics process, the table gives details of the $H \rightarrow ZZ \rightarrow 4\ell$ analysis, the generator, the PDF set, and the underlying-event tune. For the background samples, the order in α_S used to normalize the event yield is also given; for the signal, the normalization is the parameter of interest in the fit. The SM $h \rightarrow ZZ$ boson contribution, along with its interference with the continuum ZZ background, is included in the diboson samples [45].

analysis cuts are optimised to reduce these backgrounds.

Several data-driven methods can be applied to extrapolate the background yield by using orthogonal signal and control regions. These methods are described in detail in [49] and will not be described here. The reducible backgrounds are treated separately depending on the flavour of the sub-leading pair ($Z+\mu\mu$ or $Z+ee$) due to the different contributions to each process from background sources. The fraction of reducible background in each event category (VBF, VH, ggF) is evaluated using simulation, and the systematic uncertainty in the event categorisations includes the differences between the fraction from simulation and from the reducible background control region.

5.2.3 Signal Modelling

For each production mode, corresponding signal samples are simulated. The generators used to simulate the signal are presented in Table 5.2. However, to generate signal samples for the full m_H range, due to limited samples at specified m_H , an interpolation is used to obtain signal shapes and normalisations between the samples. The SM cross-section is used for normalising samples, this however does not impact the final results, which are presented as model independent cross-section times branching ratio limits, cancelling out the contribution from SM cross-section. For $m_H > 300$ GeV there are two sets of signal samples which apply different treatments for the Higgs lineshape. In this analysis, only the Narrow Width Approximation (NWA) is used which models the Higgs boson using a Breit-Wigner lineshape with a fixed width of 4.07 MeV. The full list of signal samples used for each m_H region are listed in Appendix A.1.

Due to the interpolation of the samples, statistical fluctuations arise in the $m_{4\ell}$ distributions from the MC. In order to remove these fluctuations and smooth the sample, a kernel estimating your shape (KEYS) PDF is used. The same procedure is used for the background shapes, estimating the shape of the distribution using a sum of gaussians centred at each data point. The smoothed PDF describes the MC well [49].

The number of expected events to be used in the fit is calculated by using the acceptances multiplied by the SM Higgs cross-section multiplied by the branching ratio.

5.2.4 Uncertainties

For each source of uncertainties, a nuisance parameter is assigned and the uncertainties can be categorised as experimental (related to the detector or reconstruction algorithms), theoretical or from the reducible background. Experimental uncertainties arise from uncertainties within the detector

system, the dominant sources being from the luminosity, electron and muon efficiency uncertainties and the jet energy scale. The reducible background uncertainty arises from the difference between the different data-driven methods used, uncertainties in the factors used to extrapolate the signal yields from the control region to the signal region and from limited statistics in the control region. The theoretical uncertainties arise from the categorisation and acceptance for the signal and from the PDF and QCD scale uncertainties for the reducible ZZ background.

5.3 Statistical Interpretation

When searching for new processes in particle physics, the compatibility of data with theory must be assessed. This involves statistical analysis using frequentist methods to characterise the exclusion of a signal or an observation of excesses. A very brief overview of the statistical procedure will be given in this section.

Probability can be defined using either Frequentist or Bayesian methods. The frequentist interpretation is defined as the limit of long term frequency and the bayesian approach defines probability as the degree of belief, assuming a prior theory and updating the probability as more information is acquired. Both frequentist and bayesian methods allow the compatibility of observed events to be quantified with respect to a given hypothesis H . The level of incompatibility is used by convention, “excluding” a signal to a degree of confidence level (CL), such as 95% CL.

When searching for new phenomena, hypothesis tests are constructed based on null and alternative hypotheses. The background-only hypothesis can be referred to as the null hypothesis, defined as H_0 , and describes known processes. This is then tested against an alternative hypothesis, H_1 . In the case of limit setting, H_0 is used for the signal plus background model and is tested against the background-only hypothesis, H_1 [50].

In order to discriminate signal-like from background-like events, a test statistic q_μ can be constructed. Using a frequentist approach, the log-likelihood ratio, $-2\ln Q$, can be used as a test statistic (q_μ) which is a powerful discriminant of two hypotheses. In Higgs searches, limits are typically set on the signal strength μ , a scale-factor on the number of expected signal events predicted by a reference cross-section and branching ratio, which can be defined as the parameter of interest. A set of parameter values, known as “nuisance parameters”, θ , for both the background and signal models are also included in the test statistic, and are fitted from the dataset.

To prevent excluding insensitive signals, a conservative approach is taken by introducing a modified frequentist approach using the CL_s method [46]. This method is used to calculate the 95% confidence level for exclusion of signal, deriving the upper limits on the model parameters using the

ratio of CL_{s+b} to CL_b which are calculated from the p -values associated with the observation for the hypothesis H_0 and H_1 . Figure 5.7 demonstrates the PDFs of the test statistic assuming the two hypotheses and the corresponding CL_{s+b} and CL_b values.

In the case of an excess of events, the background-only hypothesis is used to construct a test statistic q_0 , whereby rejecting the $\mu = 0$ hypothesis leads to a discovery. The level of incompatibility is quantified using the p -value, which can be converted to a significance.

Determining the significance and the expected significance for a dataset involves either Monte Carlo calculations, or the use of approximate methods by replacing the ensemble of simulated datasets by a single representative one. This is referred to as the Asimov dataset. In addition to the significance, the sampling distribution is required for the test statistic to calculate the p -value and PDFs of the corresponding test statistic are required for the hypothesis being tested. At the LHC, a profile likelihood test statistic is preferred, where the nuisance parameters are “profiled” meaning that they are fit to the data. The profile likelihood ratio ($-2\ln Q(\mu)$) can be approximated using asymptotic formulae as the distribution follows a non-central χ^2 distribution and the Asimov dataset is used to estimate the standard deviation of μ , required for the asymptotic formulae. The Asimov dataset is defined such as to make estimators for all parameters equal to their true values [50]. Using these approximations therefore removes the need for computationally expensive Monte Carlo calculations.

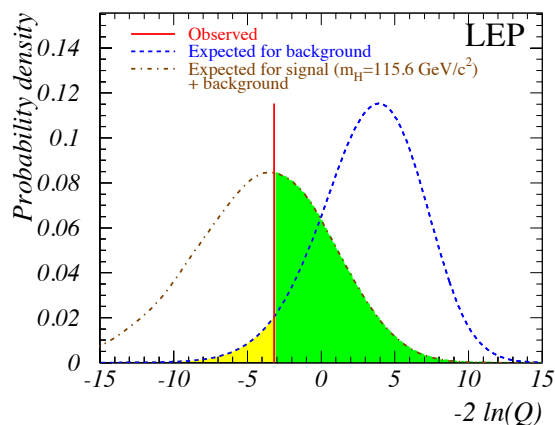


Figure 5.7: Combined LEP Higgs search for the background and signal plus background hypothesis for $m_H = 115.6$ GeV. The observed value is indicated by the vertical red line and the shaded region to the left of the line indicates $1 - CL_b$ and the shaded region to the right is CL_{s+b} [46].

When no excesses are observed, the limit setting procedure is performed and can be summarised as follows [51]:

- (1) Construct the likelihood function $\mathcal{L}(\text{data} | \mu, \theta)$, for observed data, see Section 5.3.1.
- (2) Compare the compatibility of data with the H_1 and H_0 using a suitable test statistic, see

Section 5.3.2.

- (3) Find the value of the test statistic for the observed data.
- (4) Find the values of the nuisance parameters best describing the observed data for H_0 and H_1 .
- (5) Generate toy Monte Carlo pseudo-data to construct PDFs assuming a signal strength μ in the signal plus background hypothesis, and $\mu = 0$ for background-only, constraining the nuisance parameter values from data. Using a profile-likelihood test statistic allows the use of asymptotic formulae and PDFs can be approximated using a representative Asimov dataset.
- (6) Define p -values associated with observed data for H_0 and H_1 , where:

$$p_\mu = P(\tilde{q}_\mu \geq \tilde{q}_\mu^{obs} \mid \text{signal} + \text{background}), \quad 1 - p_b = P(\tilde{q}_\mu \geq \tilde{q}_\mu^{obs} \mid \text{background-only}). \quad (5.1)$$

- (7) Calculate CL_s ratio:

$$CL_s(\mu) = \frac{p_\mu}{1 - p_b}. \quad (5.2)$$

- (8) To derive 95% CL_s upper limits, μ is adjusted until $CL_s = 0.05$.

This procedure calculates the observed limit, using the likelihood of the H_0 and H_1 hypotheses with respect to the observed data. The expected limit is generated using the background-only hypothesis, using pseudo-data and repeating the procedure several times to generate the $\pm 1, 2\sigma$ expected limits.

In this analysis, the profile-likelihood is used as a test statistic due to its asymptotic properties, approaching a χ^2 distribution. The CL_s method is used to calculate the observed limits and asymptotic formulae are used to derive the expected limits, using a representative Asimov dataset, instead of toy Monte Carlo [50]. The model independent cross-section \times branching ratio 95% CL limits are calculated for the ggF and VBF+VH production modes.

5.3.1 Likelihood Fits

To derive 95% CL_s upper limits for the cross-section of an additional Higgs boson, an unbinned profile likelihood fit is performed. This is approximately a frequentist method.

The likelihood function is a product of a Poisson term representing the probability for observing n events and a weighted sum of signal and background probability density functions (PDFs) evaluated at all observed events.

$$\mathcal{L}(x_1 \dots x_n \mid \mu) = \text{Pois}(n \mid \mu S + B) \left[\prod_{e=1}^n \frac{\mu S f_S(x_e) + B f_B(x_e)}{\mu S + B} \right]. \quad (5.3)$$

where the signal-strength μ , the ratio of the number of signal events to the SM expectation, is the parameter of interest in the fit, defined as:

$$\mu = \frac{\sigma \times BR}{\sigma_{SM} \times BR_{SM}}. \quad (5.4)$$

S and B are the expected SM signal and background yields. The terms f_S and f_B are the PDFs in $m_{4\ell}$ for the signal and background. The PDF for the signal depends on m_H . The expected number of signal and background events and the shape of the PDFs depends on the systematic uncertainties which are described by a set of nuisance parameters (θ_i). Gaussian constraints are used to ensure the values of the nuisance parameters fit to nominal values within the expected uncertainties. This therefore means that the likelihood is a function of the signal strength (μ), m_H and θ_i .

5.3.2 Test Statistic

To measure the compatibility of data with the chosen hypotheses, a test statistic is constructed. The profile-likelihood (\tilde{q}_μ) test statistic is defined as:

$$\tilde{q}_\mu = -2 \ln \frac{\mathcal{L}(\mu, \hat{\theta}_\mu)}{\mathcal{L}(\hat{\mu}, \hat{\theta})}, \quad \hat{\mu} \leq \mu. \quad (5.5)$$

In the denominator, $\hat{\mu}$ and $\hat{\theta}$ values maximise the likelihood, while in the numerator $\hat{\theta}_\mu$ are the values of the nuisance parameters which maximise the likelihood at a given μ .

This test statistic is used with the CL_s [46] modified frequentist method to calculate exclusion limits. When generating the null-hypothesis Asimov dataset for the expected limits, the parameters of interest are set to zero and the nuisance parameters are conditioned to the data. For the null-hypothesis, Asimov data is used to compute the observed limits, then when setting limits on one production mode, the other is conditioned to data with the other NPs [49].

5.3.3 Fit Model

The signal shapes, expected yield and the background shapes are used to create final signal and background models. The events are categorised according to the production modes (VBF, VH, $ggF \rightarrow 4\mu$, $ggF \rightarrow 4e$, $ggF \rightarrow 2\mu 2e$, $ggF \rightarrow 2e 2\mu$) and for each category the background and signal

model are separated and the six categories are fit simultaneously. As the ratio of ggF to VBF is unknown, model independent limits are set separately on μ for ggF and VBF+VH. When setting limits on μ_{ggF} , μ_{VBF+VH} is allowed to float freely and vice-versa.

5.4 Results

Figure 5.8 shows the $m_{4\ell}$ distribution of the $H \rightarrow ZZ \rightarrow 4\ell$ candidates in the ggF and VBF categories compared to the background expectation for $m_H = 400$ GeV. To obtain limits on the $\sigma \times BR$ in the NWA as a function of m_H , the CL_s procedure in the asymptotic limit is applied [46] [50] using the test statistic already defined.

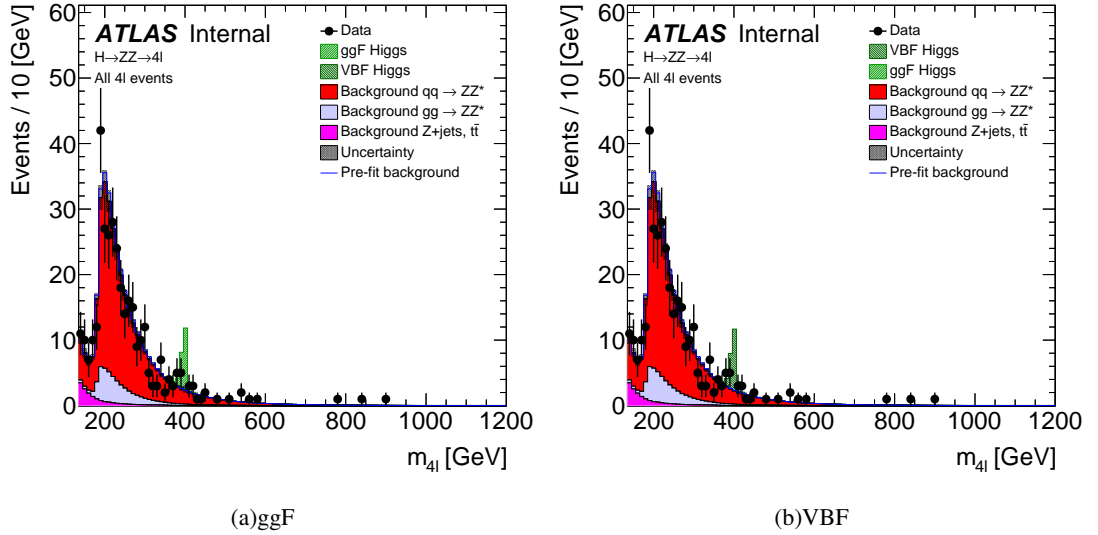


Figure 5.8: $m_{4\ell}$ distribution for $m_H = 400$ GeV for ggF and VBF categories. The ggF signal is normalised to a cross-section corresponding to five times the observed limit while the VBF signal is normalised to the best-fit value from a fit where the VBF signal floats freely and the ggF signal is set to zero and vice-versa.

Figure 5.9 presents the 95% CL upper limits of $\sigma \times BR(H \rightarrow ZZ)$ for the ggF and VBF+VH production modes. The corresponding numerical limits are presented in Appendix A.2 in Tables A.1 to A.3.

No significant excesses are observed in the search for a heavy Higgs state in the $H \rightarrow ZZ \rightarrow 4\ell$ channel and 95% upper limits are derived over the mass range $140 < m_H < 1000$ GeV for the VBF and ggF production modes. This corresponds to a $\sigma_{ggF} \times BR(H \rightarrow ZZ)$ upper limit of 109 fb at $m_H = 400$ GeV compared to an expected value of 125 fb. For the $\sigma_{VBF+VH} \times BR(H \rightarrow ZZ)$, an upper limit of 88 fb has been set at $m_H = 400$ GeV compared to an expected value of 95 fb.

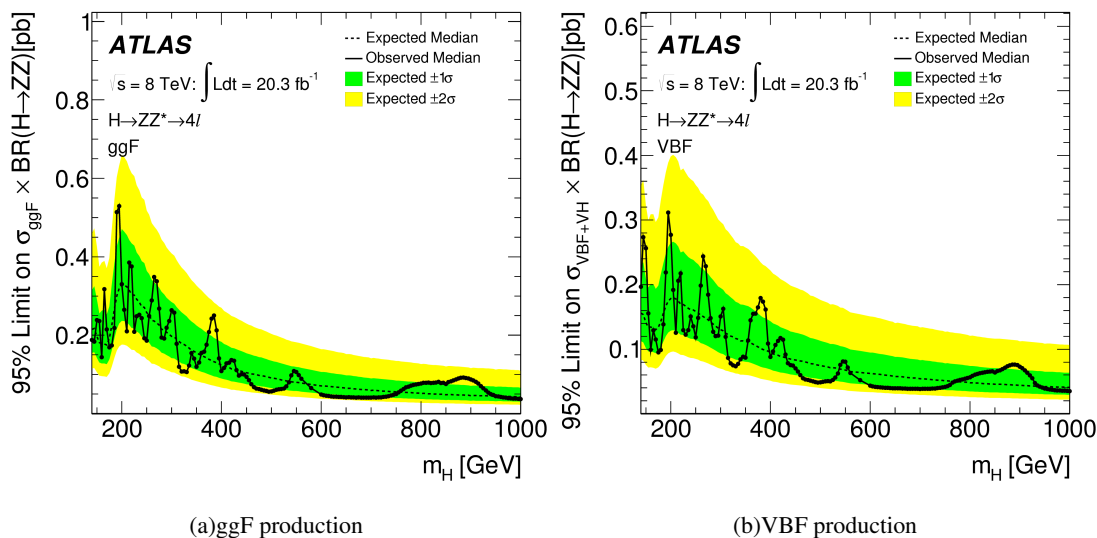


Figure 5.9: 95% CL upper limits for $\sigma \times BR(H \rightarrow ZZ)$ in the NWA for (a) ggF production and (b) VBF production.

5.5 Summary

A search for an additional Higgs boson has been performed in the $H \rightarrow ZZ^{(*)} \rightarrow 4\ell$ channel in the range $140 < m_H < 1000$ GeV using 20.3 fb^{-1} of $\sqrt{s} = 8$ TeV data. The events are separated into categories based on production modes: ggF, VBF and VH-like events. The observed event rates are compatible with MC predictions for SM $ZZ^{(*)}$ production and data-driven estimated for Z+jets and $t\bar{t}$ production. With no excess observed, 95% CL ggF and VBF+VH $\sigma \times BR(H \rightarrow ZZ)$ limits have been set assuming a SM-like heavy Higgs boson in the Narrow Width Approximation (NWA). A $\sigma_{ggF} \times BR(H \rightarrow ZZ)$ limit of 330 fb (38 fb) has been set at $m_H=200$ GeV (1000 GeV) compared to an expected value of 329 fb (43 fb). For the $\sigma_{VBF+VH} \times BR(H \rightarrow ZZ)$, a limit of 277 fb (35 fb) has been set at $m_H=200$ GeV (1000 GeV) compared to an expected value of 179 fb (41 fb).

Chapter 6

Calorimeter studies at 13 TeV using $\pi^0 \rightarrow \gamma\gamma$ and $J/\psi \rightarrow e^+e^-$ events

6.1 Introduction

At the end of May 2015, the LHC delivered the first 13 TeV collisions during the Run-II beam commissioning period. ATLAS recorded 21.3 M minimum bias events and the first $\pi^0 \rightarrow \gamma\gamma$ signals at 13 TeV were observed. “Stable beam” status was achieved in early June, with dedicated 50 ns collisions followed by 25 ns collisions in late August. ATLAS recorded 3.9 fb^{-1} total integrated luminosity during stable beam periods for pp -collisions at 13 TeV in 2015. These events have been used to study $J/\psi \rightarrow e^+e^-$ events and the performance of the EM calorimeter.

This chapter presents analyses of 2015 13 TeV data including the observation of the π^0 mass peak in the $\pi^0 \rightarrow \gamma\gamma$ channel, using low energy clusters to reconstruct the diphoton mass spectrum. A fit of the combinatorial background and π^0 signal has been performed and compared with Monte Carlo simulation. Different background subtraction methods have also been studied in the $J/\psi \rightarrow e^+e^-$ channel, to determine the best technique to extract the EM calorimeter variables which are described in Table 4.5. The variables which describe the EM shower for the signal electrons are compared with Monte Carlo simulation.

6.2 Observation of the $\pi^0 \rightarrow \gamma\gamma$ peak

With pp collisions, a significant number of low p_T electrons and photons are reconstructed and the majority of photons are from π^0 decays. At higher transverse energies, neutral hadron decays are the main source of background photons, with $\pi^0 \rightarrow \gamma\gamma$ decays occurring at a significant rate. These photons are therefore interesting to study, to determine the calorimeter performance during early collisions.

6.2.1 Data samples

The $\pi^0 \rightarrow \gamma\gamma$ combinatorial signals were collected during the beam commissioning period at the end of May 2015, at the start of Run-II. The LHC was operating at a pp centre of mass energy of $\sqrt{s} = 13$ TeV and the data was triggered using the Minimum Bias Trigger Scintillators (MBTS). The trigger selects inelastic events using loose selection criteria, with as little bias as possible [52], these events are typically non-diffractive interactions which produce low- p_T particles in the central region. The corresponding luminosity for the three runs is 0.3-0.4 nb^{-1} and contains 21.3 M events, with 4.1 M diphoton candidates.

The Monte Carlo sample used to compare with early Run-II data contains 19.6 M non-diffractive minimum bias events at $\sqrt{s} = 13$ TeV, generated with PYTHIA8 [53].

6.2.2 Photon pair selection

As described in Chapter 4, egamma objects with a transverse energy greater than 2.5 GeV are reconstructed using the sliding window algorithm. For lower energy photons however, topological clusters are used as a seed to identify the cell with the largest energy deposit, and a fixed sized window of 3×5 cells in the middle layer is built around the seed. These photons are referred to as topo-seeded photons and use a calibration derived with the longitudinal weights (LW) method. The LW method calculates the reconstructed energy (E_{rec}) by using a linearly weighted sum of the layer responses: $E_{rec} = s(b + W_0E_0 + E_1 + E_2 + W_3E_3)$ where $E_{i=0,1,2,3}$ are the cluster energies in the presampler and three calorimeter layers. The coefficients s, b, W_0 and W_3 are the longitudinal weights which depend only on the cluster position in η . The weights are derived by a χ^2 minimisation of $\frac{(E_{true} - E_{rec})^2}{\sigma_E^2}$ using Monte Carlo, where σ_E is the expected energy resolution and E_{true} is the true particle energy in the MC.

The LW calibration applied to the topo-seeded photons is based on data collected in 2009 [54]. In addition to the calibration, an overlap removal is applied during reconstruction to prevent double counting clusters which would result in a miscalculation of energy. Only the cluster with highest E_T is accepted if there are multiple clusters overlapping within $\Delta\eta < 0.05$ and $\Delta\phi < 0.1$. Using topo-seeded clusters, photons with $E_T > 1.5$ GeV are reconstructed.

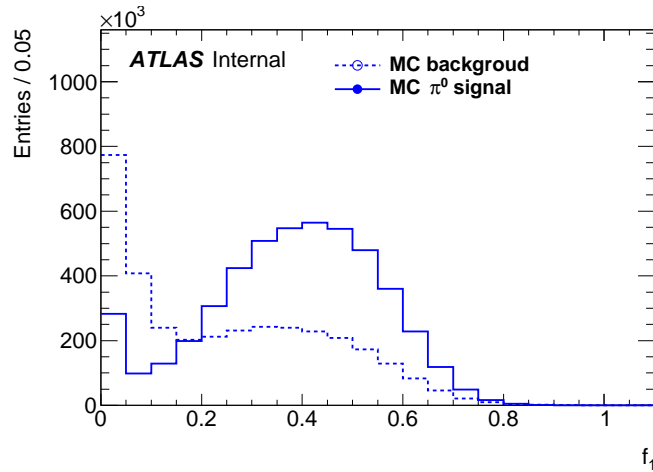


Figure 6.1: f_1 distribution, the fraction of energy in the first calorimeter layer $E_1/(E_1 + E_2 + E_3)$, for signal photon candidates from π^0 decays (solid blue line) and background photons (dashed blue line) using non-diffractive minimum bias Monte Carlo.

To extract the π^0 signal from the combinatorial background, the following criteria are applied:

- Reconstructed clusters are required to be within $|\eta| < 2.47$ and must not be reconstructed within the transition region between the barrel and the end cap, between $1.37 < |\eta| < 1.52$, where $|\eta|$ is the cluster- η in the second EM calorimeter sampling layer.
- The fraction of energy in the strips, the first EM calorimeter layer, f_1 which is defined as $E_1/(E_1 + E_2 + E_3)$, is required to be greater than 0.1 in order to remove background photon candidates. The f_1 distribution from simulation is shown in Figure 6.1, where the background distribution is dominated by charged hadrons which deposit a significant amount of energy in the hadronic calorimeter, beyond the EM calorimeter, and therefore do not deposit a lot of energy in the first calorimeter layer, unlike photons.

The distribution of the main kinematic variables of the photon candidates after selection are shown in Figure 6.2 comparing data with Monte Carlo. The simulation agrees well with the distributions in the data and therefore, the photons are used to search for π^0 -mesons.

Generating all possible combinations of photon pairs which pass the selection criteria, 4.1 M photon pairs are selected in data and 4.7 M in Monte Carlo simulation. These combinatorial pairs are used to reconstruct the diphoton invariant mass distribution.

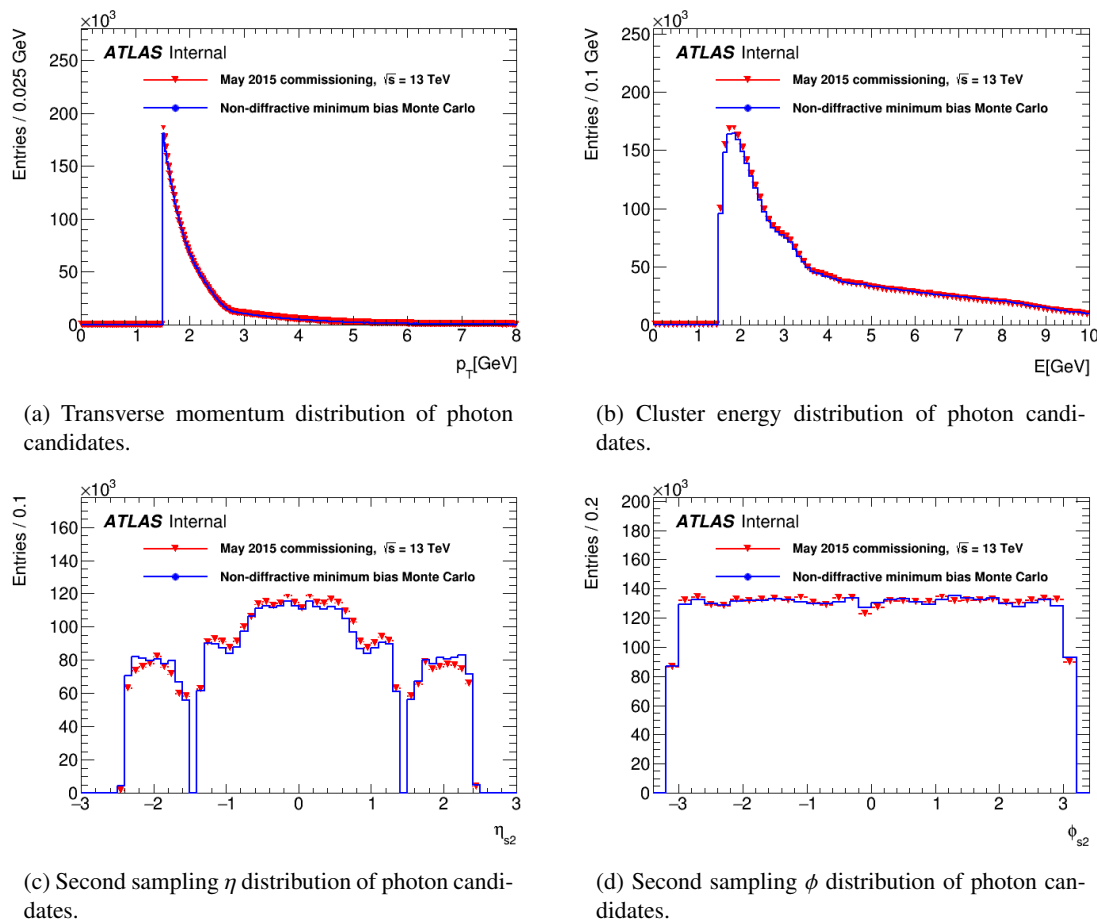


Figure 6.2: Kinematic distributions of photon candidates after selection criteria are applied comparing data (red triangles) to non-diffractive minimum bias Monte Carlo (blue line). The Monte Carlo is normalised to the same number of entries as data.

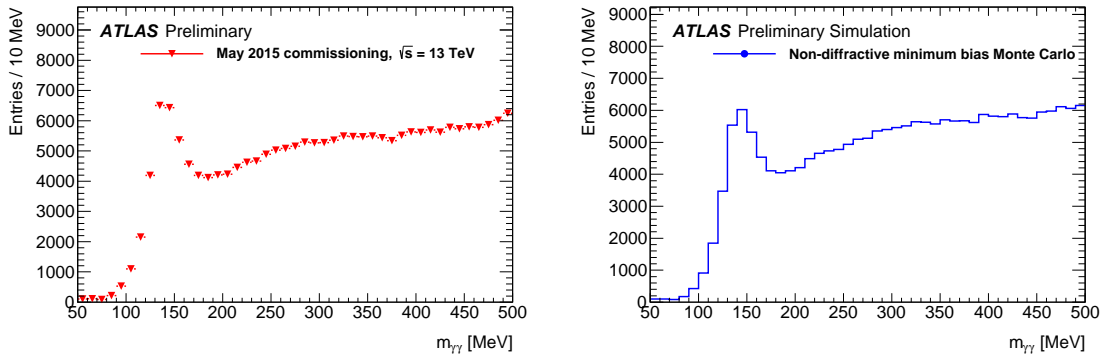
6.2.3 π^0 mass fit

The invariant mass distribution of photon pairs is shown in Figure 6.3. A clear excess of events is observed near the π^0 mass at 135 MeV in both the data and Monte Carlo, compared to the π^0 PDG mass which is 134.9766 ± 0.0006 MeV [55].

The diphoton mass is then fit to the background and signal components, which are compared with Monte Carlo in Figure 6.4. The signal is described by the sum of a Gaussian and a Crystal-Ball function of the form, $f_{CB}(x; \alpha, n, \bar{x}, \sigma)$, featuring a gaussian-core with a long tail [56]¹. The combinato-

¹The Crystal-Ball function is defined as: $f(x; \alpha, n, \bar{x}, \sigma) = N \cdot \begin{cases} \exp\left(-\frac{(x-\bar{x})^2}{2\sigma^2}\right) & \text{if } \frac{x-\bar{x}}{\sigma} > -\alpha, \\ A \cdot \left(B - \frac{x-\bar{x}}{\sigma}\right)^{-n} & \text{if } \frac{x-\bar{x}}{\sigma} < -\alpha. \end{cases}$

Where $A = \left(\frac{n}{|\alpha|}\right)^n \cdot \exp\left(-\frac{|\alpha|^2}{2}\right)$ and $B = \frac{n}{|\alpha|} - |\alpha|$. N is a normalisation factor, \bar{x}, σ are the mean and standard deviation, n is the power law parameter and α is the tail parameter which can be fit to data.



(a) Diphoton mass distribution for 13 TeV collision data recorded in May 2015

(b) Diphoton mass distribution for 13 TeV Monte Carlo, normalised to the same number of entries as data

Figure 6.3: The photon candidates are required to fulfil $E_T > 1.5$ GeV, $|\eta| < 2.47$ excluding $1.37 < |\eta| < 1.52$ and to deposit more than 10% of their energy in the first layer of the electromagnetic calorimeter. No data-driven energy scale corrections are applied.

rial background is described with a 4th order Chebyshev polynomial of the first kind, characterised by a smooth increasing background.

The parameters of the signal and background normalisation are free parameters for the fit applied to the data, while the parameters of the Chebyshev polynomial, the Gaussian and the Crystal-Ball tail parameters have been extracted and constrained from the fit to simulation. The measured π^0 mass is 140.0 ± 0.3 MeV for the data and 142.6 ± 0.3 MeV for the simulation. The number of π^0 candidates extracted from the fit is $3.31 \pm 0.23 \times 10^4$ in data and $5.61 \pm 0.23 \times 10^4$ in Monte Carlo. The large deviation of the π^0 mass in data and MC from the PDG mass value can be attributed to the low energy photon calibration applied. These corrections were determined using 900 GeV data, at the beginning of Run-I and therefore need to be recalculated for Run-II performance.

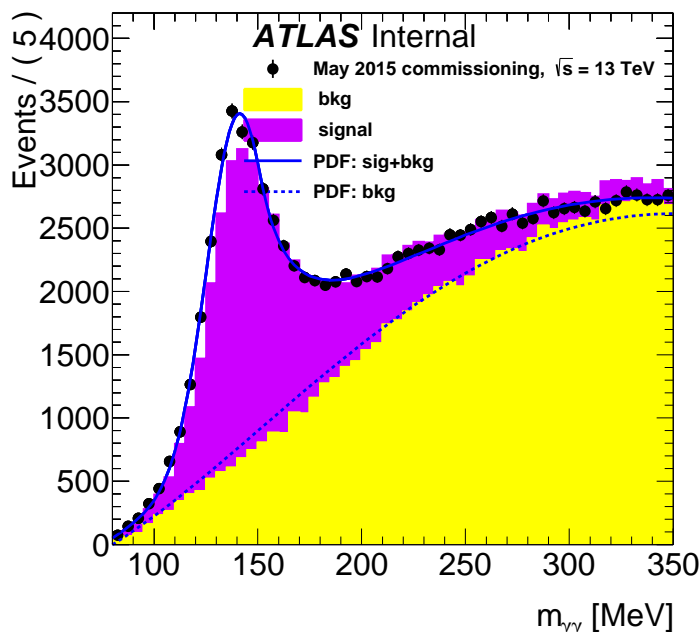


Figure 6.4: The photon candidates are required to fulfil $E_T > 1.5$ GeV, $|\eta| < 2.47$ excluding $1.37 < |\eta| < 1.52$ and to deposit more than 10% of their energy in the first layer of the electromagnetic calorimeter. No data-driven energy scale corrections are applied. The background is described by a 4th order Chebyshev of the first kind and the signal is the sum of a Gaussian and a Crystal Ball function. The data is represented by black points, the MC fit by the shaded areas and the fit to data by the blue lines.

6.3 Background subtraction methods in the $J/\psi \rightarrow e^+e^-$ channel

J/ψ and Z bosons are used for electron performance and efficiency studies, providing a source of electrons which are well isolated from hadronic activity, making them prime candidates to study.

At the LHC, J/ψ mesons are produced both in prompt pp collisions and in b -hadron decays where the J/ψ then decays to a pair of oppositely charged electrons. $J/\psi \rightarrow e^+e^-$ decays have been observed with the ATLAS detector with the full 2015 dataset using 3.2 fb^{-1} of data at 13 TeV. This channel provides a sample of prompt isolated electrons which are similar to events of interest in other physics analyses, and the $J/\psi \rightarrow e^+e^-$ analysis is performed using the Tag and Probe (T&P) method [30, 56]. This method is used to select an unbiased sample of electrons (*probes*), selecting events based on the electron-positron invariant mass and applying strict selection criteria to the second electron (*tag*). The T&P method is used to extract efficiencies by applying a requirement to the *probe* sample after accounting for background contamination, and this method is also used with W and Z -boson decays.

In this analysis, $J/\psi \rightarrow e^+e^-$ decays are studied, selecting events around the J/ψ mass peak to study several alternative background subtraction techniques and extract the isolated electron EM calorimeter variables from the data, to be compared with Monte Carlo simulation.

The calorimeter variables in Table 4.5 describe the EM showers of electrons in the calorimeter and are useful to study the performance of the calorimeter. These variables are often referred to as shower shape variables or electron shower shapes and depend on both the energy of the electrons and the amount of material traversed by the electrons before reaching the calorimeter. The shower shape distributions estimated by Monte Carlo must be in good agreement with data by using an appropriate background subtraction technique in the T&P method to extract only electrons from prompt $J/\psi \rightarrow e^+e^-$ decays to be studied. The dominant systematic uncertainty in efficiency calculations is caused by the background subtraction and therefore it is crucial to use a stable technique [56].

6.3.1 $J/\psi \rightarrow e^+e^-$ selection

$J/\psi \rightarrow e^+e^-$ events are used to study electrons with low- E_T , however at such low energies, the *probe* sample suffers from a significant background fraction due to non-prompt $J/\psi \rightarrow e^+e^-$ decays and also studying all combinations of electron-positron pairs leads to a combinatorial background. The invariant mass distribution of the *tag* and *probe* pairs is used to estimate the background and further selections are applied to separate the prompt isolated electrons from the non-prompt, which arise due to J/ψ production from b -hadron decays. For prompt J/ψ events, the decay occurs close to the primary event vertex, whilst the b -hadrons have a relatively long lifetime and are displaced from the primary vertex when the decay occurs. This means that the displacement of the J/ψ vertex with respect to the primary vertex in the transverse plane (L_{xy}) will be significant for the non-prompt background and pseudo-proper time can be used as a discriminating variable [30]. Pseudo-proper time (τ) is defined as:

$$\tau = \frac{L_{xy} \cdot m_{PDG}^{J/\psi}}{p_T^{J/\psi}}. \quad (6.1)$$

where $m_{PDG}^{J/\psi}$ is the PDG-mass [3] and $p_T^{J/\psi}$ is the transverse momentum of the reconstructed J/ψ -meson. To select events dominated by prompt J/ψ production, with well-isolated electrons, the pseudo-proper time is restricted to short times of $-1 \text{ ps} < \tau < 0.2 \text{ ps}$.

To reconstruct prompt J/ψ decays, events are required to be recorded with nominal detector operation, during stable beam periods, and are selected by five dedicated $J/\psi \rightarrow e^+e^-$ triggers. The triggers require tight identification and an electron E_T above a threshold for one of the two trigger objects, while only requiring an electromagnetic cluster above a certain E_T threshold for the other.

At least one primary vertex is required with at least three tracks associated with the event and events must have at least two electron candidates with a transverse momentum $p_T > 5$ GeV, within the pseudorapidity range $|\eta| < 2.47$. The full list of selection criteria are summarised in Table 6.1.

Table 6.1: Summary of the event selection requirements applied to $J/\psi \rightarrow e^+e^-$ events using the Tag and Probe Method.

Requirements on all electrons	
	All objects must fulfil basic object and track quality including at least one primary vertex with at least 3 tracks.
Kinematic	Require at least two electrons which fulfil the following requirements:
Selection	$p_T > 5$ GeV and $ \eta < 2.47$
	Separation between the <i>tag</i> and <i>probe</i> must be $\Delta R > 0.1$ with an invariant mass between $1.0 < m_{ee} < 6.0$ GeV.
tag requirements	
Kinematic	The tag must satisfy the π_{HLT} identification selection
Selection	and tags in the crack region $1.37 < \eta < 1.52$ are excluded.
	Must match a trigger object with $\Delta R < 0.005$.
probe requirements	
	Probe must satisfy track quality criteria of greater than 6 hits in the Inner Detector pixel layer, and at least 7 hits in the SCT and pixel layers.
	Must match a trigger object with $\Delta R < 0.005$ with E_T at least 1 GeV higher than the corresponding trigger threshold.

The *tag* electron candidate must be matched to a tight trigger electron object within $\Delta R < 0.005$ and satisfy the cut-based *tight* identification selection. The other electron, the *probe*, needs to pass the track quality criteria with at least one hit in the pixel detector and at least seven hits in the pixel and SCT detectors. The *probe* is also required to match an electromagnetic trigger object of the $J/\psi \rightarrow e^+e^-$ triggers within $\Delta R < 0.005$ with transverse energy that is at least 1 GeV higher than the corresponding trigger threshold. It is further required that the *tag* and the *probe* candidates are separated by $\Delta R_{\text{tag-probe}} > 0.1$ to prevent one object from affecting the identification of the other. Finally, the invariant mass distribution of the *tag* and *probe* pair must be in the mass region $1.0 < m_{ee} < 6.0$ GeV.

6.3.2 Background subtraction techniques

Several different background techniques can be used to separate the signal and background components in data. In the $J/\psi \rightarrow e^+e^-$ analysis, the invariant mass of the electron-positron pair is used as the discriminating variable to extract the distributions of several control variables. The sum of the contributions from the J/ψ signal, $\psi(2S)$ resonance and background electrons is used to fit the invariant mass. The signal is described by a Crystal Ball (CB) function and a small contribution from $\psi(2S)$ resonance is also described by the same shape, with independent CB parameters except for the mean, where an offset is applied to account for the mass difference between the J/ψ meson and $\psi(2S)$ resonance. The background is modelled by a Chebyshev polynomial of the first kind and a fit of the background and signal models to the data is performed.

Study of alternative background subtraction techniques

In order to study several different techniques and determine the most effective method to use in data, pseudo-data is generated and compared with Monte Carlo. The aim is to extract calorimeter shower shape distributions for signal electrons in data and compare to signal Monte Carlo. The signal electron shower shapes are extracted using a suitable background subtraction technique, where only signal electrons are remaining. As a closure test, to assess the validity of each technique, the Monte Carlo sample is compared to pseudo-data after background subtraction.

The pseudo-data is generated in two steps. Firstly, the invariant mass distribution of the pseudo-data is generated by summing the invariant mass distribution of the signal MC sample and the background invariant mass which is taken from a fit to 13 TeV data (see Figure 6.10). Then, the pseudo-data shower shape variables are formed using the signal MC distributions summed with a random gaussian distribution centred at zero to describe the background shower shapes.

The pseudo-data therefore represents the J/ψ signal (from MC) plus background distributions and can be used to study various background subtraction techniques. The invariant mass of the pseudo-data compared to the MC signal sample is presented in Figure 6.5.

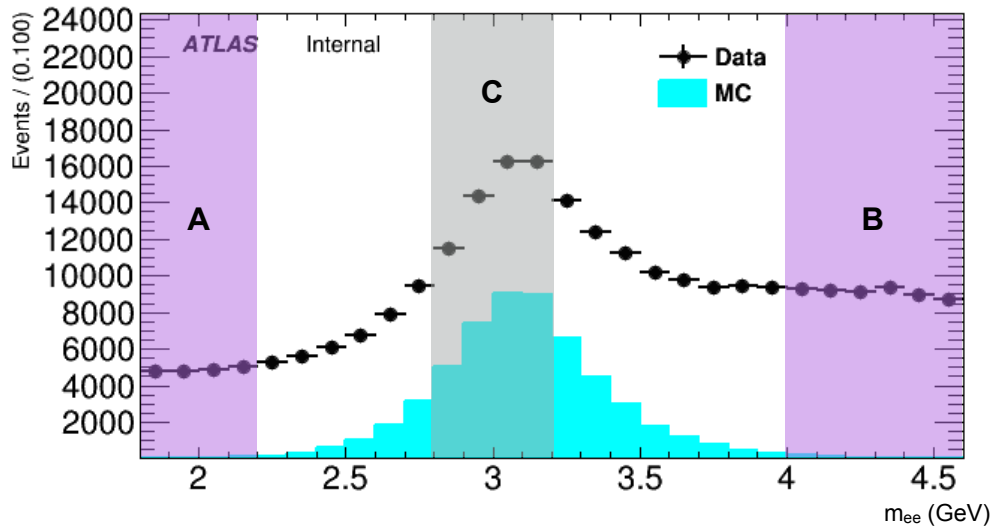


Figure 6.5: Invariant mass distribution of the electron-positron pair decaying from J/ψ events, comparing the MC (blue) to the pseudo-data (black points) indicating the signal region, C, containing signal and background events between $2.8 < m_{ee} < 3.2$ GeV, and the two sideband regions, dominated by background, A $1.8 < m_{ee} < 2.2$ GeV and B $4.0 < m_{ee} < 4.5$ GeV.

Method 1: Study electrons around the J/ψ mass peak

A simple approach to suppress background is to study electron pairs with mass, m_{ee} , close to the J/ψ mass at 3.1 GeV, where the J/ψ PDG mass is 3.097 GeV [55], requiring m_{ee} to be within a mass window of 2.8 to 3.2 GeV, defined as region C as in Figure 6.5. The invariant mass for the pseudo-data and prompt Monte Carlo over the range 1.8 to 4.6 GeV is presented in Figure 6.5, clearly showing the contamination from background in the region C.

The shower shape variables of *probes* in the signal region C, in the mass window $2.8 < m_{ee} < 3.2$ GeV are shown in Figure 6.6, where the MC is normalised to the number of pseudo-data entries, and there is a large discrepancy between the MC and pseudo-data arising from the large background contributions in pseudo-data in the signal region C.

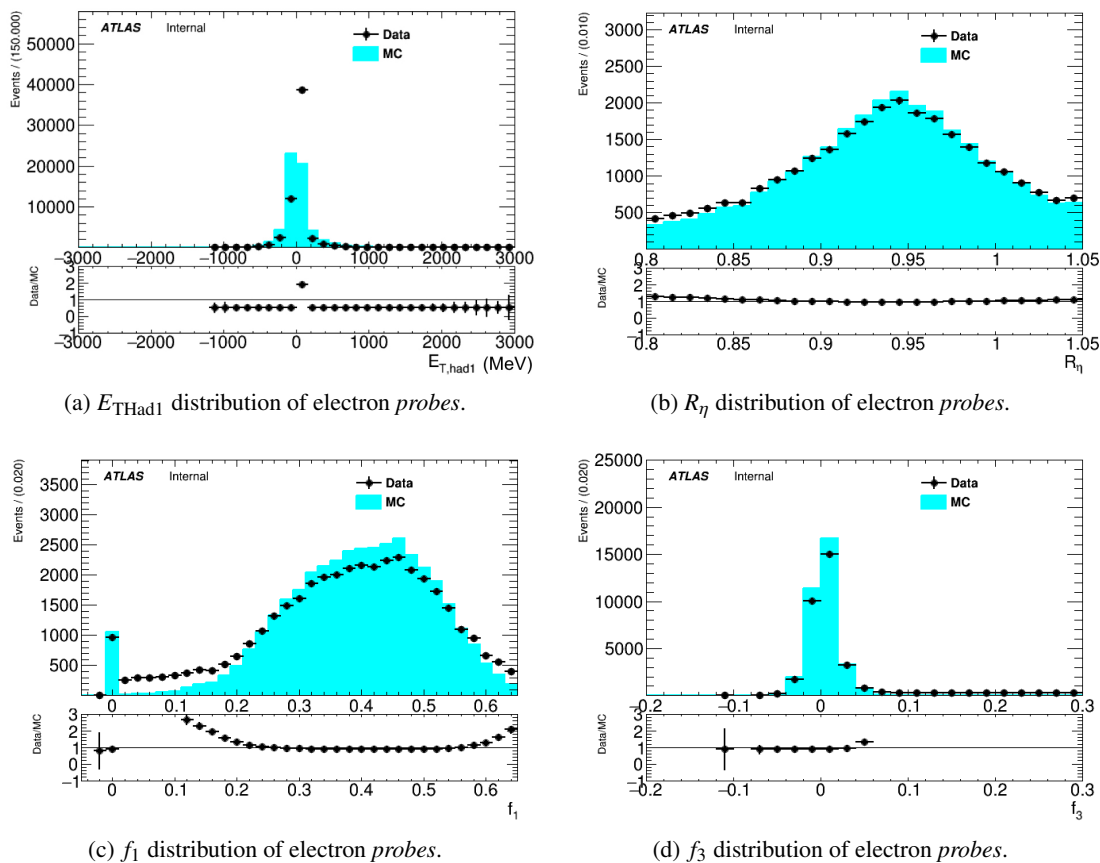


Figure 6.6: Shower shape distributions of electron *probes* within the $2.8 < m_{ee} < 3.2$ GeV range, comparing MC (blue) with pseudo-data (black points). The MC is normalised to the number of pseudo-data entries.

Due to the nature of the shower shapes of the background contribution in the pseudo-data, which are generated using a random gaussian centred at 0, shower shapes with values of 0 are particularly

sensitive to the background, with large deviations in pseudo-data compared to MC. This is demonstrated in the E_{THad1} (Figure 6.6a) distribution, which is the energy deposited in the first layer of the hadronic calorimeter. Shower shapes with distributions further from 0, for example close to 1, do not suffer from contamination and exhibit excellent agreement between pseudo-data and MC, as in the R_η (Figure 6.6b) distribution. Method 1 is not sufficient as it does not remove the background therefore, to extract the required signal shower shapes the background must be subtracted.

Method 2: Sideband subtraction

To remove the background contribution in region C, described in Method 1, the weighted shower shape distribution of the sideband regions, which are dominated by background events, can be subtracted. Two sideband regions are constructed, sideband A has $1.8 < m_{ee} < 2.2$ GeV, and sideband B with $4.0 < m_{ee} < 4.5$ GeV. The weighted shower shapes from the sideband regions (A, B) are subtracted from the shower shapes in the signal region (C). These regions are demonstrated in Figure 6.5.

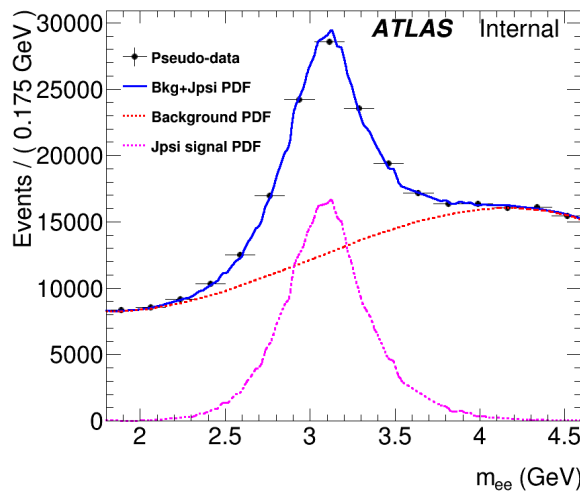


Figure 6.7: Pseudo-data invariant mass distribution of the electron-positron pair decaying from J/ψ events. The signal is modelled by a Crystal Ball function (pink), the background is by a Chebyshev polynomial of the first kind (red) and the sum of these, the full model (blue) is fit to the pseudo-data (black points).

The weighted sideband shower shapes are subtracted from the signal region shower shapes, where the weight is calculated as the ratio of the integral of signal region (C), to the integrals of the sideband regions (A, B). This is then multiplied by the yield, the fraction of background events in the signal region, which is estimated by a fit to pseudo-data, as shown in Figure 6.7, with a fraction

of 0.45. The subtraction formula is:

$$\mathcal{S}_{\text{signal}} = \mathcal{S}_C - \frac{f_{\text{bkg}} \cdot n_C}{(n_A + n_B)} \mathcal{S}_{A,B} \quad (6.2)$$

where \mathcal{S} is the shower shape distribution, f_{bkg} is the fraction of background events and n_A, n_B, n_C are the integrals of the shower shape distribution in each mass region.

Subtracting the sideband distribution shows good agreement between the pseudo-data and MC shower shapes, as shown in Figure 6.8, whilst in the R_η distribution in Figure 6.8b too much background has been subtracted, as this was mostly dominated by signal initially.

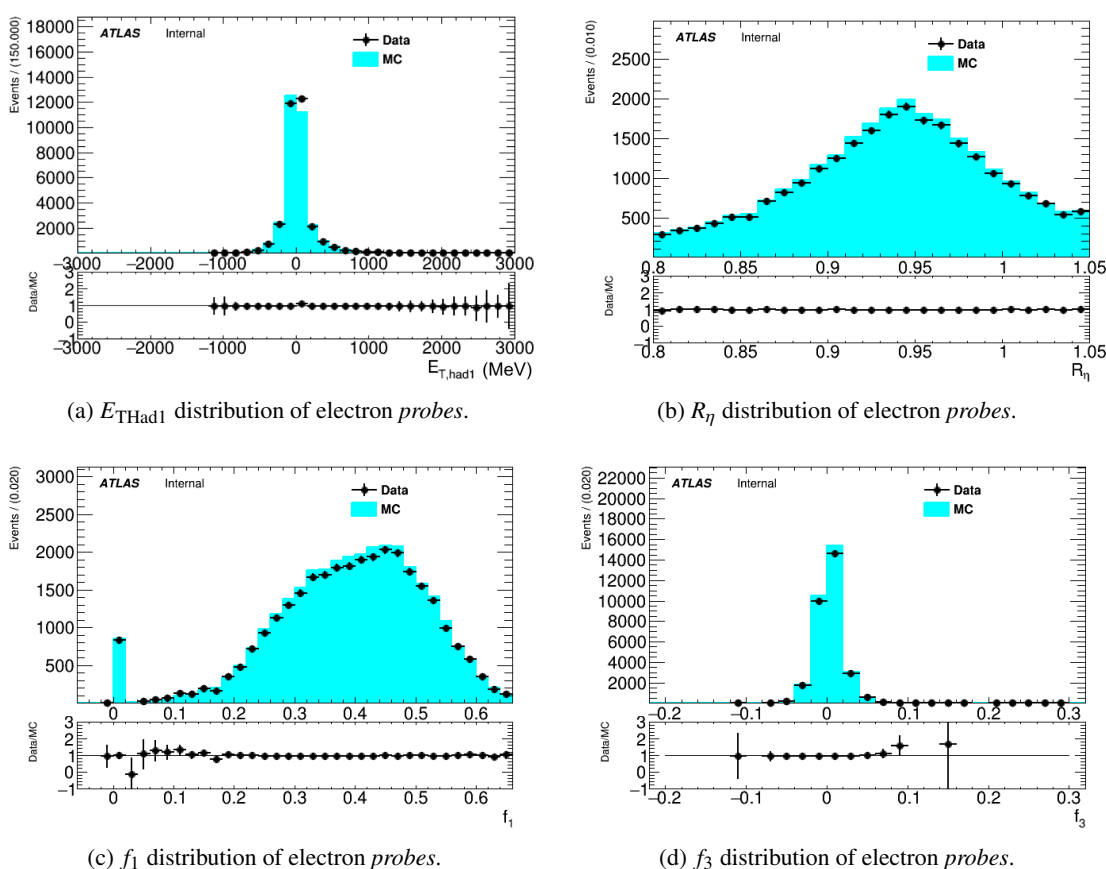


Figure 6.8: Shower shape distributions of electron probes within the $2.8 < m_{ee} < 3.2$ GeV range subtracting the weighted distribution of the sideband regions $1.8 < m_{ee} < 2.2$ GeV and $4.0 < m_{ee} < 4.5$ GeV, comparing MC (blue) with pseudo-data (black points). The MC is normalised to the number of pseudo-data entries.

Method 3: $sPlot$ Technique

The background subtraction method using the sideband regions allows the signal shower shapes to be extracted effectively however a more sophisticated approach for background subtraction also based on applying weights to the shower shapes is the $sPlot$ technique.

$sPlot$ is a statistical technique and tool which unfolds the contributions of any observable coming from different populations in the sample [57, 58] allowing the background to be removed using per event weights. This is achieved by dividing the variables into two categories: discriminating variables for which the distribution of the signal populations are known, and control variables for which one wishes to extract the unknown distribution. The invariant mass of the electrons is used as the discriminating variable and the shower shapes are the control variables for which the signal distributions are required, the same choice as the sideband method. Each candidate enters the control variable distribution with a weight, similar to the sideband method, however in this case, the weight is calculated from a likelihood fit to the discriminating variables. The discriminating variables must therefore be uncorrelated with the control variables in order to extract information in an unbiased manner, which has been previously checked to be fulfilled for the variables studied here [56].

After the likelihood fit is performed where weights are extracted, $sPlot$ builds histograms of the control variable, keeping all signal events and removing all background events [58].

The signal and background contributions are fit to pseudo-data using the signal and background models previously described and the electron invariant mass distribution is presented in Figure 6.7, as used to extract the fraction of background events in the signal region for the sideband method. In the fit, the MC (blue) with background (red) and signal (pink) contributions are in agreement with the pseudo-data (black points). The shower shapes, extracted using $sPlot$ are presented in Figure 6.9, which show excellent agreement between the MC and pseudo-data. Using this technique also allows an extended invariant mass range to be studied as the weights are generated for the fit range $1.8 < m_{ee} < 4.6$ GeV and therefore the shower shapes can be extracted over this m_{ee} range instead of just around the peak.

Background subtraction technique comparison

Using pseudo-data, several techniques for studying signal events have been considered. In Method 1, the shower shapes in the signal region are presented in Figure 6.6, however as the signal region suffers from background contamination, it is not a useful technique to study only the signal events of interest. Method 2 removes some contributions from background by subtracting the weighted sideband shower shapes from the signal region shower shapes. Whilst the shapes in Figure 6.8

show good agreement with the MC, the fraction of the background in the signal region (f_{bkg}) is not a constant value and $sPlot$ method accounts for this by providing a per-event weight which accounts for this.

The $sPlot$ technique is shown to efficiently remove the background contribution with good agreement in R_η between pseudo-data and MC in Figure 6.9b which was problematic for the sideband method. The $sPlot$ method will be used for background subtraction for data in the following section to extract shower shapes in data.

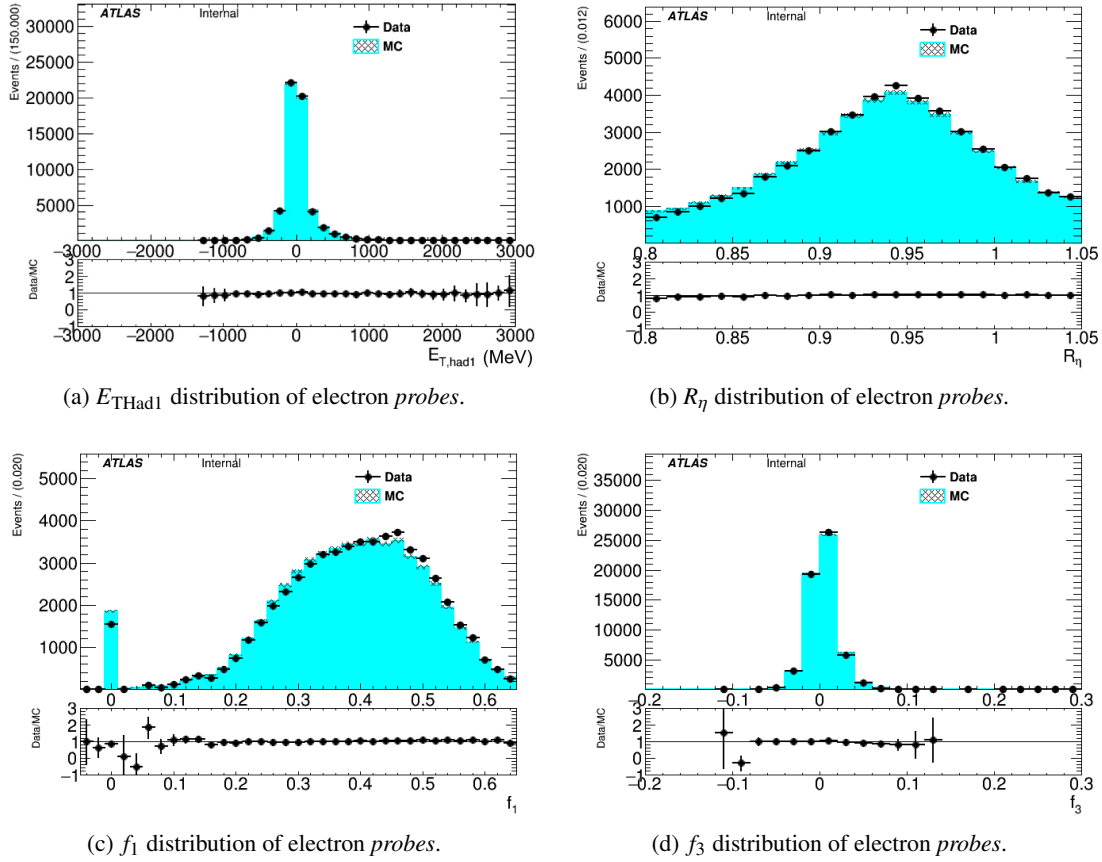


Figure 6.9: Shower shape distributions of electron probes within the $1.8 < m_{ee} < 4.6$ GeV range subtracting the background contribution using the $sPlot$ technique comparing MC (blue) with pseudo-data (black). The MC is normalised to the number of entries in data.

6.3.3 J/ψ Shower Shapes in data

The invariant mass distributions, described by the signal, background and $\psi(2S)$ models are fit to the data for the full η and E_T range, in the mass region $1.8 < m_{ee} < 4.6$ GeV. The fit is presented in Figure 6.10 which is used with $sPlot$ to remove the background as described in the previous section. The mean value of the J/ψ peak, determined by the crystal ball fit for the signal component, is $3.09073 \pm (1.0 \times 10^{-4})$ GeV which is in excellent agreement with the PDG mass.

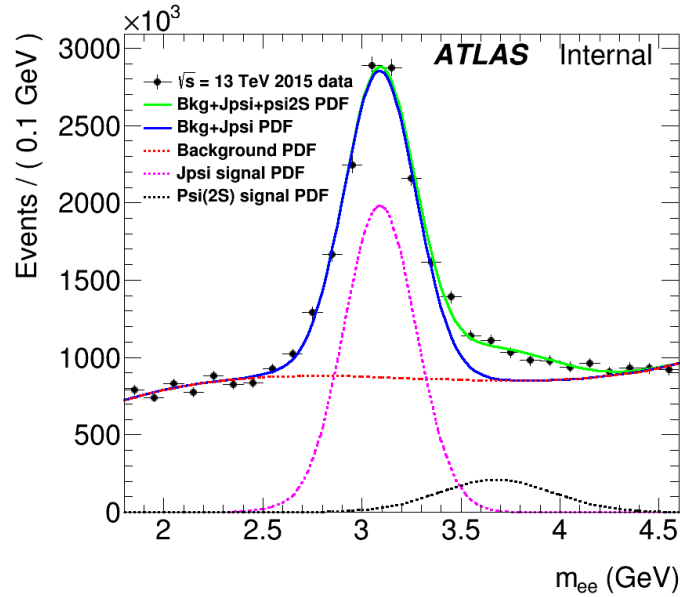


Figure 6.10: Data invariant mass distribution of the electron-positron pair decaying from J/ψ events. The signal is modelled by a Crystal Ball function (pink), the background by a Chebyshev polynomial of the first kind (red) and the sum of these, the full model is fit to the data (black points). The MC is normalised to the number of data entries.

Using the $sPlot$ technique, the signal shower shapes are extracted and presented in Figures 6.11 and 6.12 for the full η and E_T range, where $E_{T\text{Had}}$ is the energy deposited in the hadronic calorimeter. The calorimeter shower shapes show good agreement between the data and Monte Carlo. There are some slight shifts in the MC with respect to data, which are expected, but the overall shape of each extracted shower shape variable is described well.

6.4 Summary

The first π^0 signals have been observed at 13 TeV and compared to minimum bias Monte Carlo. The diphoton invariant mass distribution is fit to a Chebyshev polynomial to describe the background contribution and the sum of a Gaussian and a Crystal Ball function to describe the π^0 peak. The

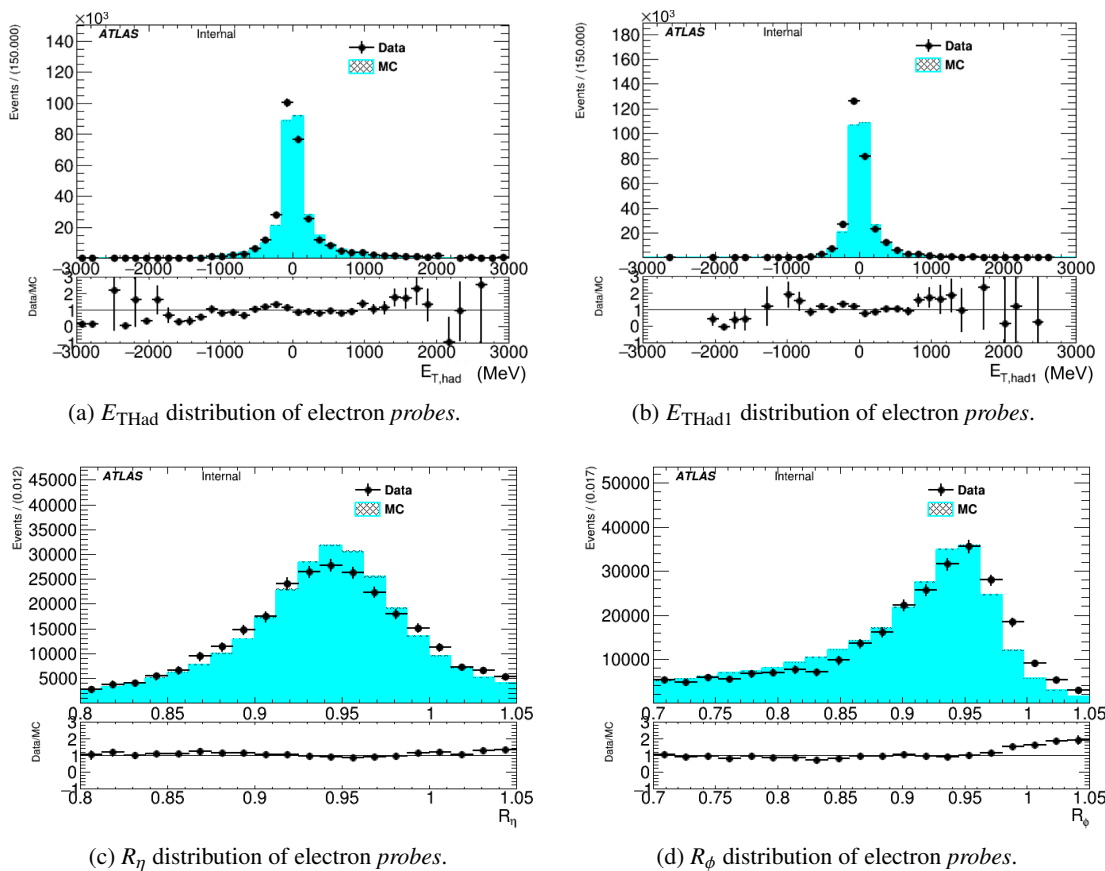


Figure 6.11: Shower shape distributions of electron probes within the $1.8 < m_{ee} < 4.6$ GeV range subtracting the background contribution using the $sPlot$ technique comparing MC (blue) with 13 TeV data (black) (1/2).

measured π^0 mass is 140.0 ± 0.3 MeV for the data and 142.6 ± 0.3 MeV for the MC, and the discrepancy between these values and from the PDG mass can be attributed to the calibration applied to the low-energy photons which was derived in 2009.

The Tag and Probe Method has been used to search for isolated electrons from $J/\psi \rightarrow e^+e^-$ decays using the full 2015 13 TeV dataset, and several background subtraction techniques have been studied to evaluate the most reliable technique to extract the calorimeter shower shapes of the isolated electrons from prompt J/ψ decays. It has been observed that the $sPlot$ technique provides better agreement in all shower shapes and kinematic variables when a closure test using MC and pseudo-data has been performed and therefore, the $sPlot$ technique has been used in data. Using $sPlot$ the background contribution in data has been subtracted and the signal calorimeter shower shapes are extracted to compare with Monte Carlo. Overall, there is very good agreement in the shower shapes of Run-II data with MC, with some shifts which are expected.

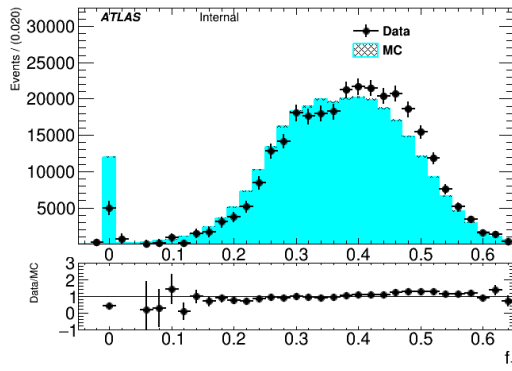
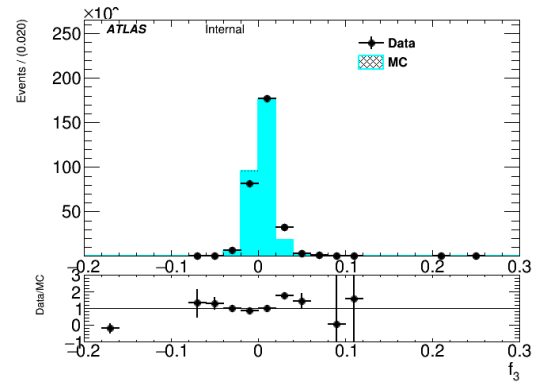
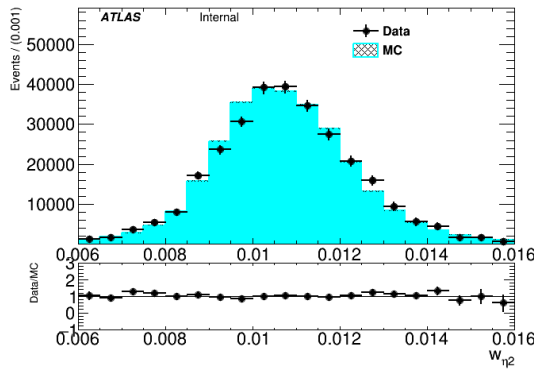
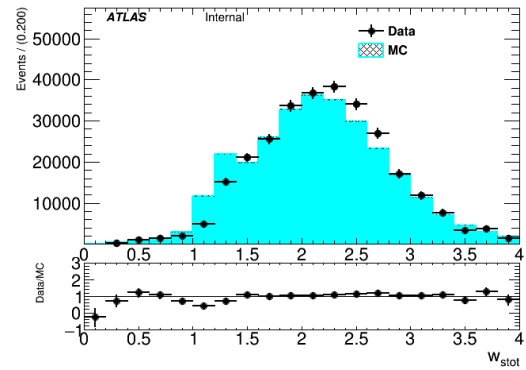
(a) f_1 distribution of electron probes.(b) f_3 distribution of electron probes.(c) W_{p2} distribution of electron probes.(d) w_{stot} distribution of electron probes.

Figure 6.12: Shower shape distributions of electron probes within the $1.8 < m_{ee} < 4.6$ GeV range subtracting the background contribution using the $sPlot$ technique comparing MC (blue) with 13 TeV data (black) (2/2).

Chapter 7

Phase-II ATLAS Upgrades

7.1 Introduction

A significant amount of the work in this thesis was motivated by the ATLAS Phase-II Upgrade which is currently planned to start in 2024 [59]. This chapter will outline the proposed upgrades and provide an overview of the basic principles of silicon particle detectors.

An introduction to the LHC Upgrades is given in Section 7.2, with particular focus on Phase-II and the new components which are proposed for the upgraded ATLAS tracker system. The use of semiconductor devices as high energy physics detectors will be briefly discussed in Section 7.3, introducing basic semiconductor theory and the operation principles of silicon detectors. Section 7.4 describes radiation damage mechanisms in silicon detectors, followed by a description of the characterisation methods which are used by ATLAS to determine the projected performance during the 10 years of the High Luminosity LHC (HL-LHC). Finally, Section 7.7 will provide a summary of the upgrades.

7.2 LHC Phase-II Upgrade

In 2026, the first collisions of the HL-LHC are scheduled to begin [60]. The HL-LHC aims to provide an additional integrated luminosity of 2500 fb^{-1} over ten years, contributing to an expected total integrated luminosity of 3000 fb^{-1} . This corresponds to a received fluence, the number of particles passing through the detector, of $1.4 \times 10^{16} \text{ cm}^{-2} \text{ s}^{-1}$ at the innermost layer of the upgraded ATLAS tracker, at a radius of 40 mm which is dominated by charged hadrons, and $1.7 \times 10^{15} \text{ cm}^{-2} \text{ s}^{-1}$ at a radius of 250 mm [60], beyond which radiation damage is expected mainly due to neutrons [61, 62]. In order to maintain the current detection capabilities of the ATLAS detector during HL-LHC operation, upgrades to the system are planned in accordance with the timeline in Figure 7.1. By 2024, some detector components will have been in operation for between 10 and 15 years and will require replacing; other upgrades are also necessary to cope with the harsh radiation environment.

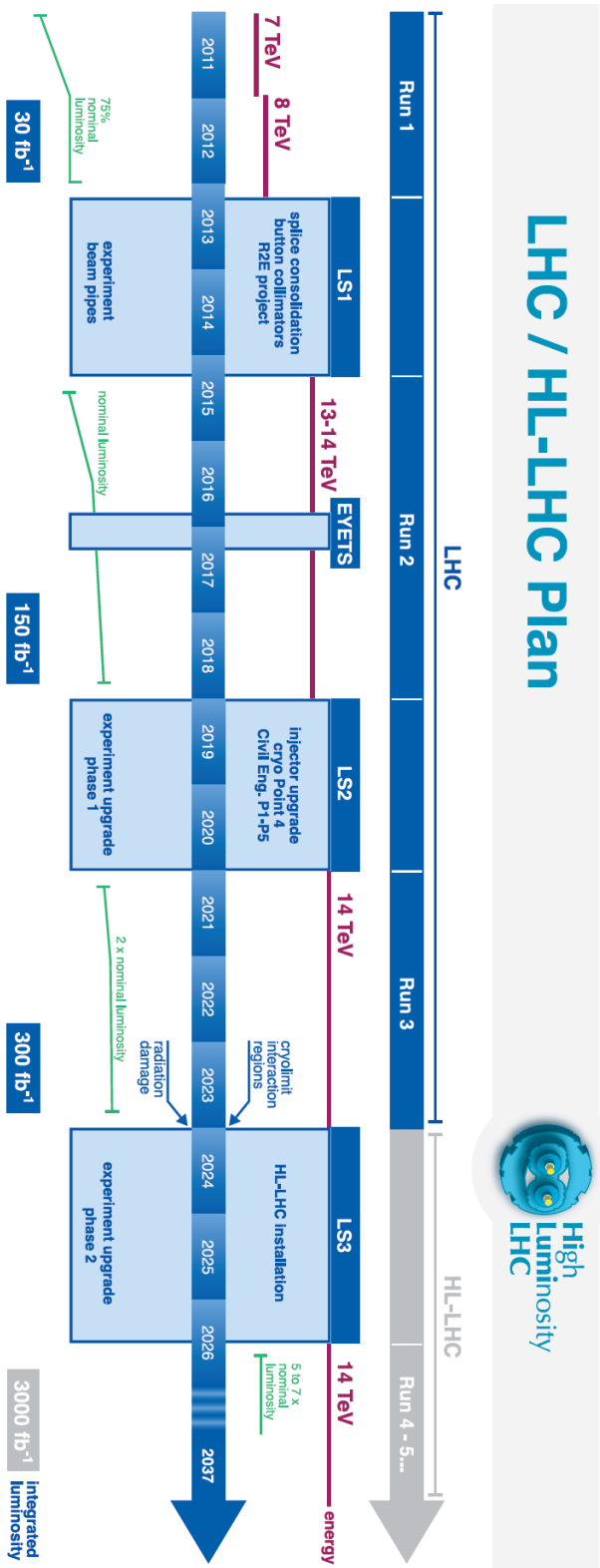


Figure 7.1: High Luminosity LHC plan beyond 2015, updated according to the CERN Medium Term Plan (MTP) for 2016-2020 [60].

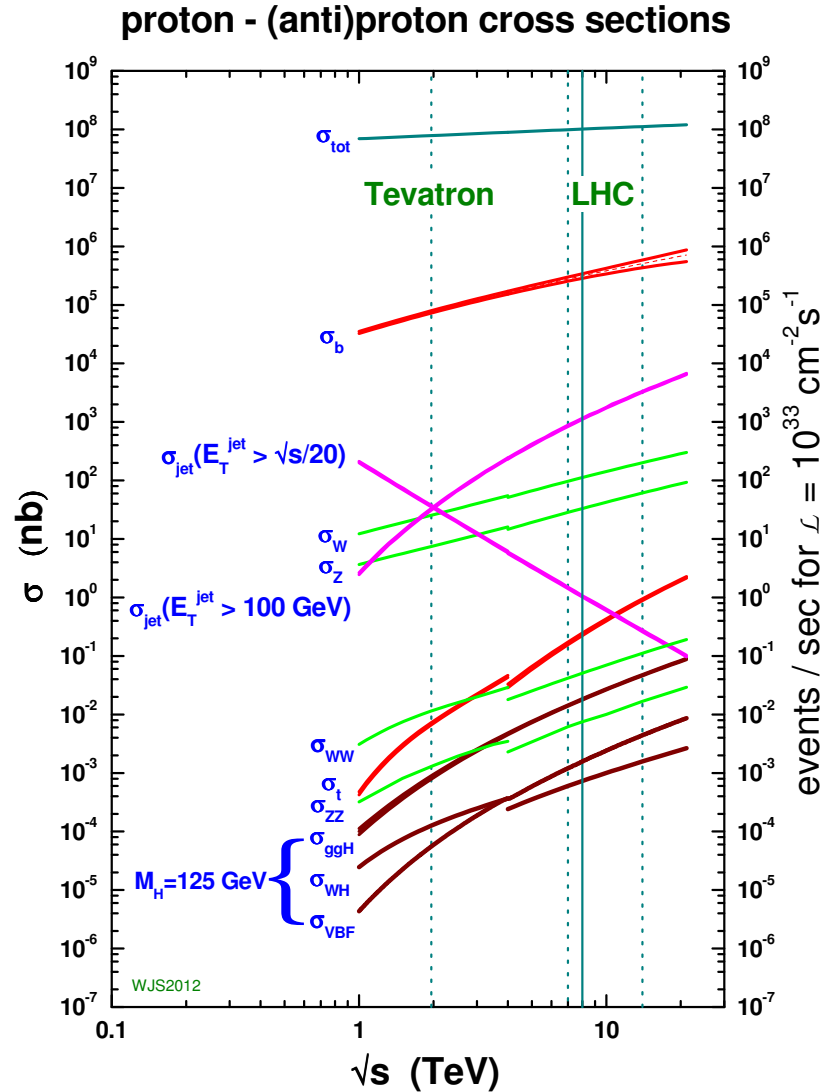


Figure 7.2: Standard Model process cross-sections at hadron colliders as a function of centre-of-mass energy [63]. Generated using NLO Martin-Stirling-Thorne-Watt (MSTW2008) parton distribution functions with a 125 GeV Higgs boson [64].

With an increase in the proton-proton centre of mass energy to $\sqrt{s} = 13 \text{ TeV}$ during Run-II in 2015, the production cross-sections for many SM processes are almost double those of Run-I at 7-8 TeV but are still of the order of nb , as shown in Figure 7.2. Due to this small production rate, an increase in luminosity is essential to maximise the number of events. The unprecedented luminosity at the HL-LHC also presents an opportunity to probe the multi-TeV region in searches for new physics and to perform precision measurements of the properties of the Higgs boson. However the high luminosity poses significant challenges to the ATLAS detector and trigger systems. A series of

upgrades are planned in three phases to prepare for high luminosity and the consequent increase in radiation levels. The scheduled run programme and the corresponding upgrade design parameters are presented in Table 7.1.

Period	Year	Luminosity [$10^{34}\text{cm}^{-2}\text{s}^{-1}$]	Integrated luminosity [fb^{-1}]	Pile-up [events/BX]
Run-I	2009-2013	0.75	7 TeV 5.1	9.1
			8 TeV 21.3	20.7
Run-II	2015-2018	1	50-100	23
Run-III	2020-2023	2.2	300-400	55
HL-LHC	2026-2035	5-7.5	3000	140-200

Table 7.1: Summary of the three phase LHC Upgrade programme and corresponding parameters [59, 60, 23].

During the first upgrade period, Long Shutdown 1 (LS1), between Run-I and Run-II operation, an additional pixel layer has been inserted into the current inner detector system. Situated at a radius of 3.3 cm from the beam pipe, the new layer, known as the Insertable B-Layer (IBL) [65], is complementary to the ID system described in Section 3.3.2 and has been installed prior to Run-II operation in preparation for higher luminosities. The IBL is a new subdetector in the ID system which provides an additional space point layer close to the IP using silicon sensors. Increasing the number of hits in the inner detector at a closer proximity to the IP maintains the efficiency of vertexing and identification of b -jets with an improved impact parameter resolution, as demonstrated in Figure 7.3, comparing Run-I and Run-II d_0 resolution [66]. Also, the low occupancy of the IBL preserves tracking performance with the increased pile-up effects at high luminosity.

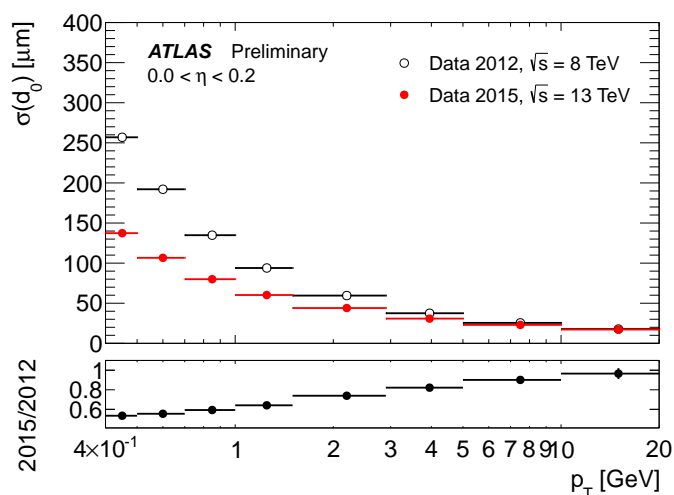


Figure 7.3: Transverse impact parameter resolution (d_0) measured from data in 2015 at 13 TeV with the Inner Detector including the IBL as a function of p_T for values of $0.0 < \eta < 0.2$ compared to data measured in 2012 at 8 TeV [66].

The LHC machine is currently operating in the Run-II period, from 2015-2018, where between

50 - 100 fb⁻¹ will be delivered with a peak luminosity of $1 \times 10^{34} \text{cm}^{-2} \text{s}^{-1}$. In 2015, ATLAS recorded 3.9 fb⁻¹ of data at centre of mass energy of 13 TeV, with the delivered and recorded luminosity presented in Figure 7.4.

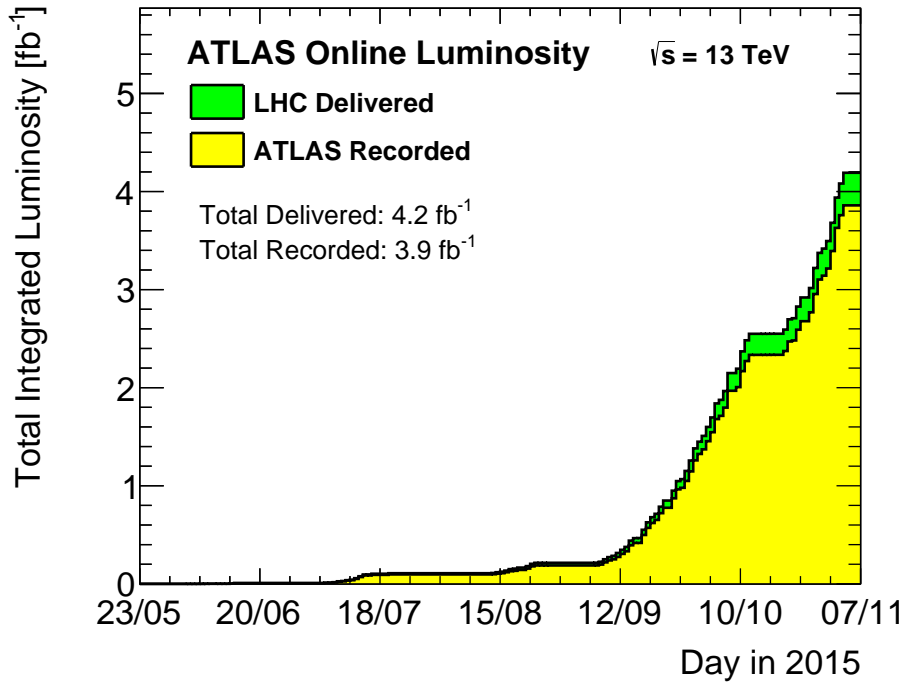


Figure 7.4: Cumulative luminosity versus time delivered to (green) and recorded by ATLAS (yellow) during stable beams for pp -collisions at 13 TeV centre-of-mass energy in 2015. These plots show the estimated integrated luminosity with the preliminary 13 TeV luminosity calibration (December 2015) [67].

During a second shutdown (LS2), currently scheduled for 24 months in 2019-2020, upgrades and maintenance work to the accelerator and to ATLAS will be performed in preparation for Phase-I. LHC operation will resume in 2020 and the peak instantaneous luminosity will increase to $2.2 \times 10^{34} \text{cm}^{-2} \text{s}^{-1}$, delivering an integrated luminosity of 300-400 fb⁻¹ by 2023. This requires upgrades to the trigger system to cope with the increase in event rate and to prevent the need to increase threshold cuts which would reduce signal efficiency [68]. At Level 1 (LV1), the trigger thresholds for low- p_T isolated leptons must be maintained. This is crucial for Higgs precision measurements as well as supersymmetry (SUSY) searches and searches for new physics. The High Level Trigger (HLT) is also to be upgraded to achieve accurate tagging and efficient isolation of τ leptons and b -jets at the increased luminosity [68]. Both the LV1 and HLT systems require information from the IBL and therefore, this must be operational and performance must be optimised during Run-II.

In 2024-2026, a third shutdown (LS3) is planned, where significant upgrades to the ATLAS detector will be required to preserve or improve the detector capabilities with a further increase in

luminosity of the LHC to the HL-LHC [59]. During Phase-II, the HL-LHC will operate at approximately five times the nominal LHC luminosity, with a peak instantaneous luminosity of $(5 - 7.5) \times 10^{34} \text{cm}^{-2}\text{s}^{-1}$. The increase in instantaneous luminosity results in an increase in the number of mean interactions per bunch crossing to approximately 140-200 [69]. This means that the detector occupancy, data rates and total radiation exposure will increase and the ATLAS detector must be able to cope with these challenging conditions.

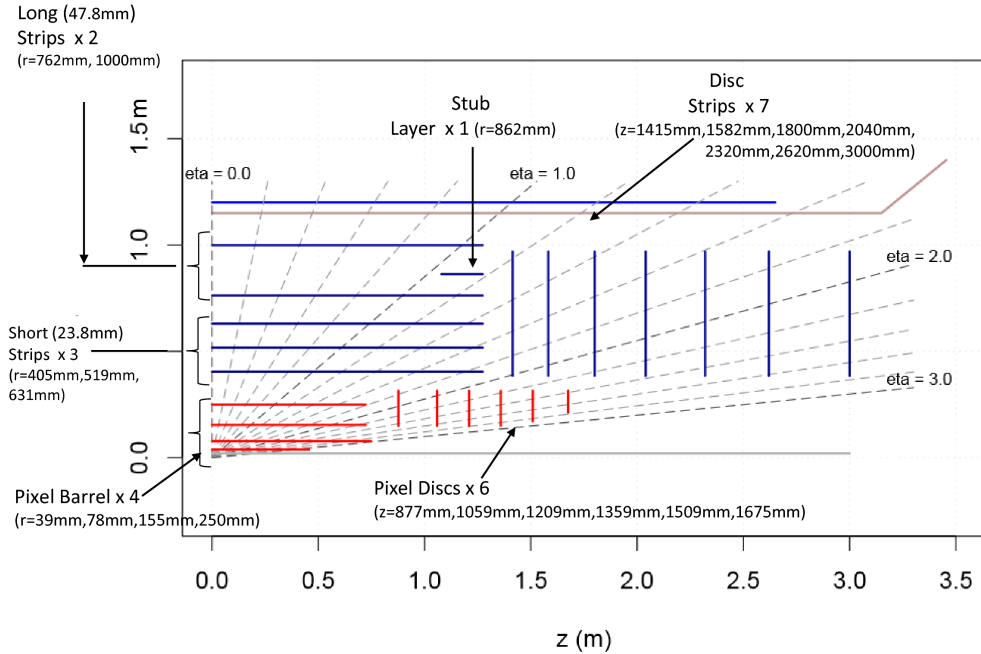
For ATLAS to operate optimally, the Inner Detector (ID) system, described in Chapter 3.3.2, will be replaced by an all-silicon inner tracker system (ITK) to maintain tracking performance within the high occupancy environment. Experience of the current tracker system and the radiation tolerance of silicon during Run-I has led to designs which combine a number of pixel layers, close to the interaction point, surrounded by a system of strip detectors [59]. Many different layouts have been proposed and in order to assess the performance of the new detectors, the prototype sensors are irradiated to HL-LHC fluences. One of the ITK design layouts is shown in Figure 7.5a and the corresponding projected fluences, simulated in FLUKA [70], are presented in Figure 7.5b.

The layout must be optimised to minimise the material and improve tracking performance. New, light weight carbon fibre reinforced plastic (CF) support structures have been introduced and these, as well as other materials for the upgraded ATLAS detector, are required to be irradiated to HL-LHC fluences to determine their durability and performance [71, 72]. To complement the silicon sensors, the corresponding readout chips and electronic components must be upgraded to provide an increased bandwidth and also accommodate the new trigger architecture. The calorimeter and muon readout electronics must also be replaced to provide full calorimeter granularity and improve the muon p_T resolution [59].

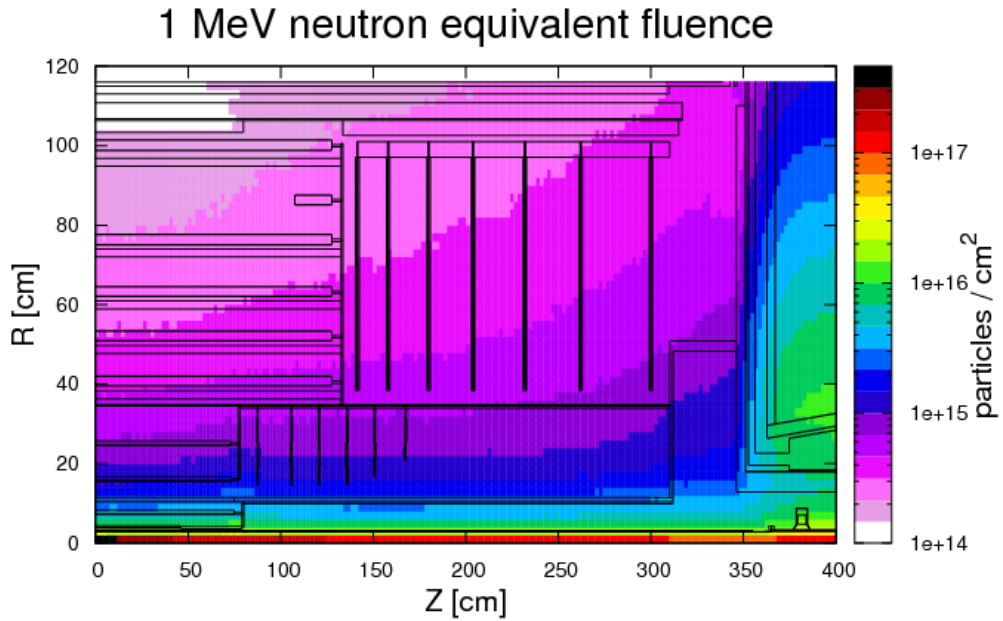
Overall, a large effort is essential to perform the necessary upgrades to ensure that ATLAS will be able to “fully exploit the physics potential of the HL-LHC” [59], and crucial to this is ensuring that the materials are robust and performance is not compromised with high accumulation of radiation fluence and at higher occupancies. This is key motivation for the work presented in the following Chapters, as irradiations to a fluence equivalent to 10 years at the HL-LHC are performed at the Birmingham Irradiation Facility and the materials can be characterised to determine their suitability for the use in the upgraded ATLAS detector. Irradiation work and sensor characterisation results performed by the author and the UK Irradiation Team are presented in Chapter 9.

7.3 Silicon Particle Detectors

Silicon detectors are currently used in the Inner Detector as discussed in Section 7.2. Their main purpose is to provide accurate tracking and pattern recognition. This is accomplished by using high



(a) ITK tracker cross-section with LoI design plans.



(b) R-z map of the fluence in the ITK region.

Figure 7.5: (a) A cross-section of an ATLAS ITK tracker design presented in the LoI showing the coverage of the pixel detector in red and strip detector in blue. The rapidity coverage extends up to $|\eta| = 2.7$ and is matched to the coverage of the muon system. The blue line outside the ITK volume represents the coil of the solenoid magnet [60]. (b) RZ-map of the 1 MeV neutron equivalent fluence in the Inner Tracker region, normalised to 3000 fb^{-1} of 14 TeV minimum bias events generated using PYTHIA8 [53, 59].

precision position measurements to reconstruct and identify vertices using many silicon layers. For the HL-LHC, the detector performance at different fluences and bias voltages must be considered to determine the optimum operating conditions, including power, cooling and detector configuration to be used.

Within ATLAS, a large active area of detectors is required to measure particles with high precision and a fine granularity is essential to cope with the high occupancy [73]. Silicon is advantageous over many other materials as large, pure wafers of single silicon crystals can be produced at a low cost. A variety of growth techniques can be used, which determines the properties of the sensor. Two common high purity crystal growth techniques are the Czochralski (Cz) and Float zone (FZ) methods. The Cz method uses a seed crystal which is dipped in molten doped silicon. The seed is slowly pulled against gravity and rotated, forming a single silicon rod [74, 75]. The FZ method uses the principle of vertical zone melting, starting with a seed crystal and polycrystalline rod which are positioned face-to-face and are rotated. The molten zone is moved along the polycrystalline rod, touching the seed onto the melt which solidifies and produces a single crystal. This technique is performed in an inert environment, where an inert gas is used to add dopants to the crystal [75]. The FZ technique has been used to manufacture silicon p-type wafers for ATLAS12 devices [61]. Sensors are fabricated on these thin wafers and silicon semiconductor devices are then processed using the principle of pn-junctions in order to create a large depletion region [74] which enables the device to act as a solid state ionisation chamber, detecting traversing particles.

7.3.1 Semiconductor devices

In accordance with Band Gap Theory, semiconductors consist of a filled valence band (E_V), a band gap (E_G) and a conduction band (E_C) [76], this is shown in Figure 7.6.

Silicon is a group IV semiconductor with a band gap energy of 1.1 eV at 302 K [77]. The electrical and optical properties, determined by the band gap, can be adjusted by adding small quantities of group III or V elements to generate either p or n-type materials. The majority carriers in n-type materials are electrons whereby donors atoms contribute an additional electron to the conduction band of the silicon. This causes the Fermi energy (E_F) to shift closer to the conduction band as in Figure 7.6. Conversely, p-type materials require one less electron where the impurity atoms act as acceptors, accepting electrons from the valence band of silicon and shifting the Fermi level toward the valence band.

By joining n-type and p-type materials, a pn-junction may be formed. Due to the concentration gradient, the charge carriers close to the junction diffuse, electrons to the p-side and holes to the n-side, where they recombine with majority charge carriers. This diffusion leaves a fixed positive

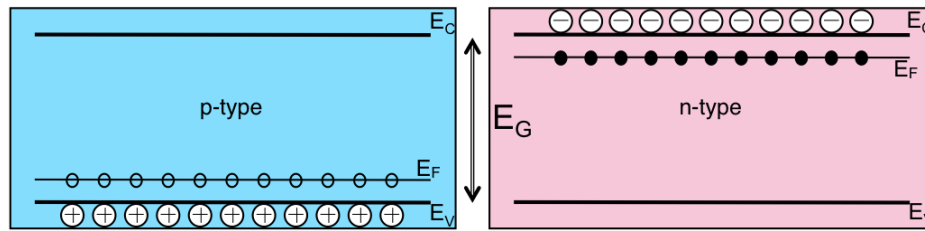


Figure 7.6: n-type and p-type semiconductors, with the valence band, E_V , conduction band, E_C , separated by a band gap E_G .

charge at the n-side and negative charge on the p-side. Consequently, a region where no fixed charge remains builds up. This is known as the depletion region.

An electric field arises in the depletion region due to Coulombic force, and forms a built-in potential (V_{bi}) across the junction. When the junction is reversed-biased with voltage V , the depletion region widens and in the case of a n-in-p silicon sensors, widens into the p-type bulk whereby electrons are collected at the n-type electrodes. The reverse bias pn-junction is demonstrated in Figure 7.7.

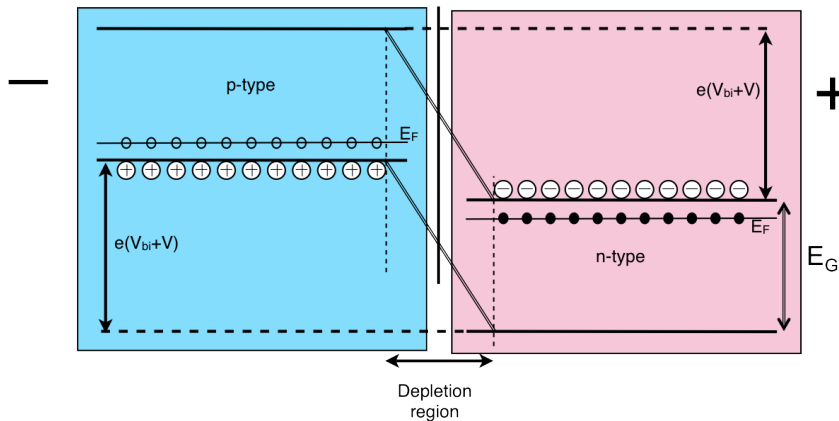


Figure 7.7: Band structure of a pn-junction with an applied reverse bias.

In particle physics, heavily doped junctions are often preferred, using higher concentrations in the front and back planes. This allows the depletion region to form asymmetrically into the less doped region which is beneficial as the electrodes can be attached to the thin front or back layers of the device. To maximise the depletion volume, increasing the probability of detecting particles, a layer is sandwiched between these thin layers. This layer, often referred to as the bulk, is a thicker layer

and can be fully depleted due to the concentration gradient between the front layer and the bulk [74], as shown in Figure 7.8.

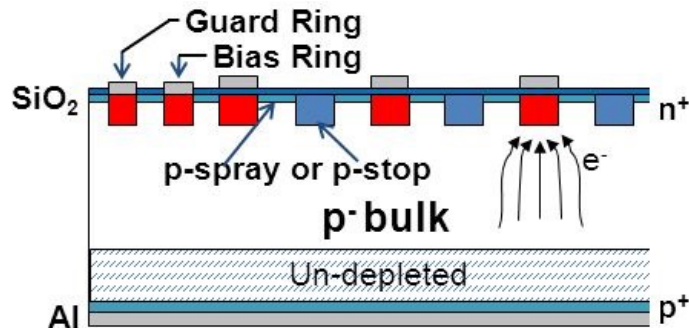


Figure 7.8: Structure of an n-in-p silicon sensor with the n⁺ front plane containing the electrode contacts, the p-type bulk acting as the depletion region and the p⁺ implant on the back plane, with electrons being collected at the n⁺ strips [78].

7.3.2 Particle detector operation

Using the semiconductor device as a particle detector requires reverse bias, as mentioned. This means that when an ionising particle passes through the silicon detector, electron-hole pairs are generated inside the detector bulk due to energy deposition by the ionising particle. The electrons and holes are separated by the electric field and drift to the electrodes, where they are collected. For all charged particles there is a common minimum in the energy deposition as the particle traverses a material. Particles with this energy loss are defined as minimum ionising particles (MIPs) with an energy loss of approximately 3.7 MeV cm^{-1} in silicon [79, 80].

The readout of the sensors uses amplifying electronics and is segmented to provide the required spatial hit resolution when a signal is formed. In an n-in-p device, the bulk is p-type with n-type electrodes collecting electrons, as in Figure 7.8. The implants on the front-side of the device are n⁺ and these are segmented to form either strip or pixel detectors. The back plane consists of one large p⁺ implant and therefore the device only requires single side processing during manufacturing, making it suitable for a large active area due to the reduced cost.

Strip and pixel detectors

The readout electrodes of silicon detectors are segmented into long rectangular shaped strips, or into smaller grids of variable size and shape. These are defined as either strip or pixel detectors. Typically, the dimensions are 16-22 μm wide strips with a pitch of 74.5-100 μm [61], and can be

of variable lengths. This forms a one-dimensional array to detect the particle position and for high precision measurements several layers, positioned at different orientations, are required to provide full coverage. Two prototype sensors (ATLAS07 and ATLAS12) have been fabricated by Hamamatsu Photonics to test their radiation tolerance [81, 61].

Pixel detectors form a two-dimensional (2D) array readout, providing 2D spatial information for each device. This provides excellent accuracy, separating high multiplicity events close to the interaction point, however the readout is significantly more complicated than strip detectors and generates a high electrode density [82].

Furthermore, each electrode must be connected to its respective readout channel and this can be connected at either, or at both ends of a strip device, whilst each electrode in the pixel 2D array must be connected to the corresponding readout chip [82]. Further to this, the readout chips must be radiation hard and require a very high channel density and large bandwidth, particularly to process information at HL-LHC rates. This reinforces the necessity for smaller transistor technology which increases the cost, and requires bump bonding of the sensor to the readout chip, which is very difficult and is the most expensive step in the fabrication process.

In preparation for Phase-II upgrades of the ATLAS inner detector system, different ITK designs have been studied. An alternative to the LoI design proposes 5 pixel and 4 strip layers. Whilst the additional pixel layers may be expensive, they contribute to a large increase in the pixel volume and provide better track rejection which is essential with the increase in pile-up. The overall layout has been developed to be cost neutral when compared with a 4 pixel and 5 strip layer design, by positioning the layers to optimise performance, for example with one extra high resolution pixel hit to compensate the loss of two strip hits [59].

7.3.3 Signal collected

Particles interact with the silicon crystal lattice via a range of mechanisms to generate a signal. On average, one electron-hole pair is generated per 3.6 eV of energy loss [79]. This means that thermal excitations as well as ionisation from particles traversing through the detector generates a signal. The number of collisions and energy lost per particle however is not constant; they are subject to statistical fluctuations which results in an energy spectrum and an asymmetric distribution of signal with long energy tails from single particle collisions [75], described by the shape of a Landau distribution. For thin absorbers such as silicon devices, the Landau distribution fails to describe energy loss due to a lower peak position caused by δ -rays which do not deposit all their energy within the thin device. The energy loss in different widths of silicon is presented in Figure 7.9 [3].

For a 300 μm silicon sensor, on average a MIP deposits approximately 111 keV which corresponds to 30 800 electron-hole pairs [80]. However, due to the asymmetric distribution, the mean value cannot be extracted accurately and the peak value, referred to as the most probable value (MPV) is preferred. The MPV is approximately 70% of the mean and therefore for a 300 μm unirradiated silicon device, 21 500 electron-hole pairs are generated when the device is fully depleted. To reduce signals from thermal excitations, detectors are cooled whilst in operation. This is also important to prevent thermal instability when the detectors incur radiation damage, as will be discussed in Section 7.4.

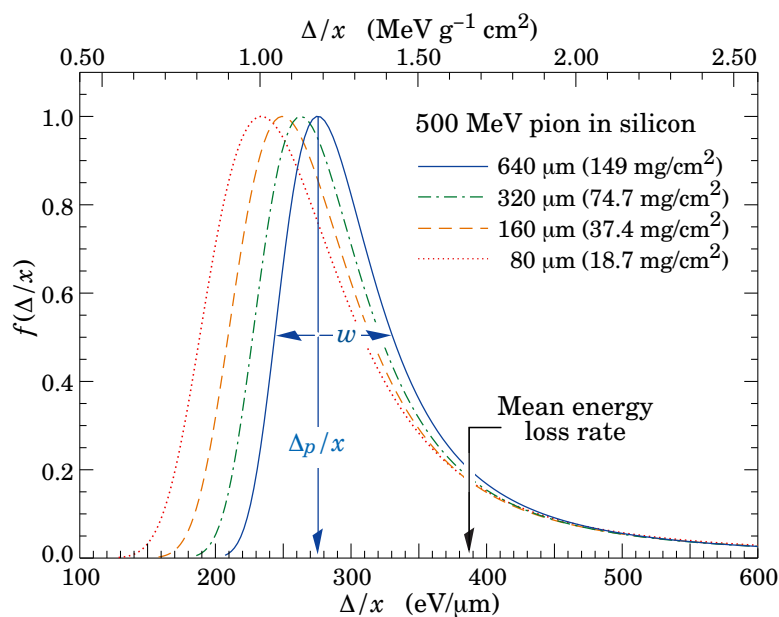


Figure 7.9: Probability distribution for energy deposition (Δ/x) for 500 MeV pions in different thickness of materials normalised to unity at the most probable value (Δ_p/x), and where w is the full width at half maximum [3].

7.4 Radiation Damage

The basic principles of detector operation have been briefly discussed in Section 7.3. For LHC experiments, silicon detectors must fulfil certain criteria, allowing operation at high voltages and generating a signal well separated from noise. Detectors aim to cope with fluences above $1 \times 10^{15} \text{ 1 MeV n}_{eq} \text{ cm}^{-2}$ and must be robust against both charged and neutral particles [61]. Silicon detectors must also have high resistivity ($> 1 \text{ k}\Omega \text{ cm}$), to ensure that the bulk is depleted, where the resistivity depends on the growth technique used [74]. The number of particles impinging on a strip must be small to allow track separation and the detectors must also have a high minority carrier lifetime in order to reduce the noise caused by leakage current [61].

Radiation damage can be classified as either macroscopic damage, caused by electrically active microscopic defects [74] and also known as bulk damage, or microscopic damage which is due to ionising energy loss or surface effects, often referred to as surface damage. Within the bulk of the detector, with increasing radiation, the properties of the detector can deteriorate causing increases in sensor leakage current, depletion voltage and a reduction in signal strength [83]. With good process technologies and design, radiation hard material for the bulk is manufactured to allow operation after irradiation and at high voltages. An advantage of using n-in-p detectors is that no radiation induced type inversions occur, unlike p-in-n detectors which read out holes. The n-type bulk carrier concentration decreases with irradiation, effectively becoming p-type, experiencing type inversion and the sensors undergo rapid deterioration [73, 84].

7.4.1 Bulk damage

When a particle passes through the detector, it may have sufficient energy to remove a silicon atom from its lattice site. The minimum displacement energy is 15 eV, and when the atom is displaced, a primary knock-on atom (PKA) may be generated. With enough energy, PKAs can displace other silicon atoms, causing defects within the crystal lattice.

These radiation induced defects are responsible for several electronic effects, changing the characteristics of the device. These include:

- **Increase in the leakage current** proportional to the fluence causes the noise and temperature to increase. The rise in temperature will increase the leakage current further, producing thermal runaway [85].
- **Reduction of signal strength** due to additional energy levels in the band gap reducing the signal and the charge collected [84].
- **Changes to the effective doping concentration** which impacts the depletion voltage and can cause n-type bulk to become p-type under type inversion [82]. Increases in the depletion voltage results in underdepletion of the sensor, when operated at the same voltage, reducing the efficiency of the device.

7.4.2 Surface damage

Microscopic damage occurs when there is a build up of trapped charge within the oxide layer due to electron-hole recombination or, when bulk crystal damage results in clusters of defects introducing

new energy levels in the band gap at the Si-SiO₂ interface, resulting in a build up of surface charge. The trapped charge attracts negative charge carriers and the consequent conductive accumulation layer of electrons impacts inter-electrode isolation which becomes insufficient at high fluences [82].

7.4.3 Annealing

The mobility of defects within an atom is heavily dependent on temperature as they are loosely bound to lattice positions. When temperature is increased, defects can migrate to form new complex defects, disappear into a sink or they may return to their original lattice position, recovering the damage [74]. These temperature induced defect mechanisms are referred to as annealing and depending on the mechanism two forms of annealing occur: beneficial annealing which causes an increase in carrier concentration, or reverse annealing where carrier concentration decreases. Several models have been developed to describe the behaviour of a sensor, the depletion voltage and charge collection, as a function of annealing time. The depletion voltage of a sensor is determined by:

$$V_{dep} = \frac{ed^2|N_{eff}|}{2\epsilon} \quad (7.1)$$

where e is the electric charge, d is the depletion depth in the silicon and ϵ is the permittivity in silicon. The effective doping concentration, N_{eff} is a function of fluence ϕ , temperature T and time t and the change in N_{eff} with respect to the value before irradiation is described by Equation 7.2.

$$\Delta N_{eff}(\phi, T, t) = \Delta N_c(\phi) + \Delta N_\alpha(\phi, T, t) + \Delta N_y(\phi, T, t) \quad (7.2)$$

where N_c is the stable damage which depends only on the fluence received, N_α is the beneficial annealing term which reduces the doping concentration at short time scales, and N_y is the reverse annealing term which increases the doping concentration at larger time scales. Figure 7.10 presents the three contributions as a function of annealing time. The Hamburg model parameterises the reverse annealing term as a modified first order process which reduces to first order parameterisation for short annealing times [85]. To reduce the radiation damage effects after irradiation, annealing is performed for approximately 80 min at 60 °C. Within this region, beneficial annealing is dominant [61].

7.5 Test Beam Environment

To assess the radiation damage and how the detectors will perform during the 10 year programme of HL-LHC operation, irradiation facilities are used to irradiate sensors to HL-LHC fluences and the detectors are characterised before and after irradiation, and post-annealing.

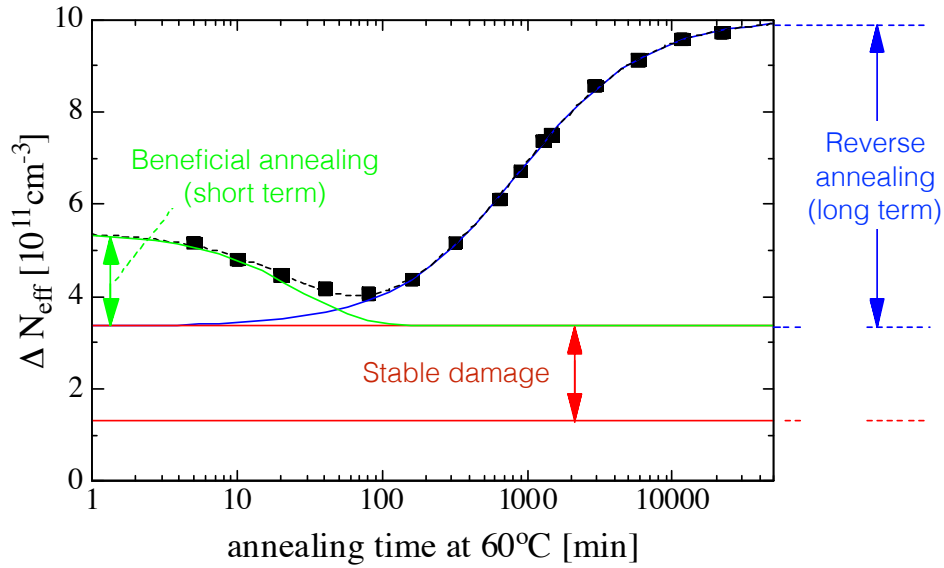


Figure 7.10: Change of the effective doping concentration as a function of annealing time at a temperature of 60 °C showing contributions from beneficial annealing, stable annealing and reverse annealing, adapted from [86].

Many different facilities are used, which can use different particles, energies and techniques to perform the irradiations. The focus of Chapters 8 and 9 is the Birmingham Irradiation Facility, with a brief overview of other facilities for comparison.

Radiation damage in silicon detectors is caused by particle interactions with electrons via ionisation, and by non-ionising energy loss (NIEL) with particles interacting with the crystal lattice. NIEL is responsible for the bulk damage caused by displacements in the silicon lattice.

To enable evaluation of the radiation damage of detectors, irrespective of the facility, the NIEL scaling hypothesis is used. The hypothesis states that displacement damage scales linearly with energy and models the damage from radiation. The damage as a function of energy for several particles is presented in Figure 7.11. To directly compare results, damage is normalised with respect to 1 MeV neutrons and fluence is quoted in terms of 1 MeV neutron equivalents (n_{eq}) by using a hardness factor κ as defined by:

$$\kappa = \frac{\int D(E)\phi(E)dE}{D(E_n = 1\text{MeV}) \cdot \int \Phi(E)dE} = \frac{F_{n_{eq}}^{1\text{MeV}}}{F}, \quad (7.3)$$

where the $D(E)$ is displacement damage cross-section which is assumed to be equivalent to the NIEL and for 1 MeV neutrons is $D(E_n = 1 \text{ MeV}) = 95 \text{ MeV mb}$. $F = \int \phi(E)dE$ is the irradiation fluence and $F_{neq}^{1\text{MeV}}$ is the equivalent fluence needed for 1 MeV neutrons to cause the same damage as the irradiation particles. The NIEL scaling hypothesis is assumed in the facilities described in Chapter 8, however it is not valid to used for silicon devices fabricated using developed radiation hardening by Oxygenation (DOFZ), where less damage has been observed than expected assuming the NIEL hypothesis.

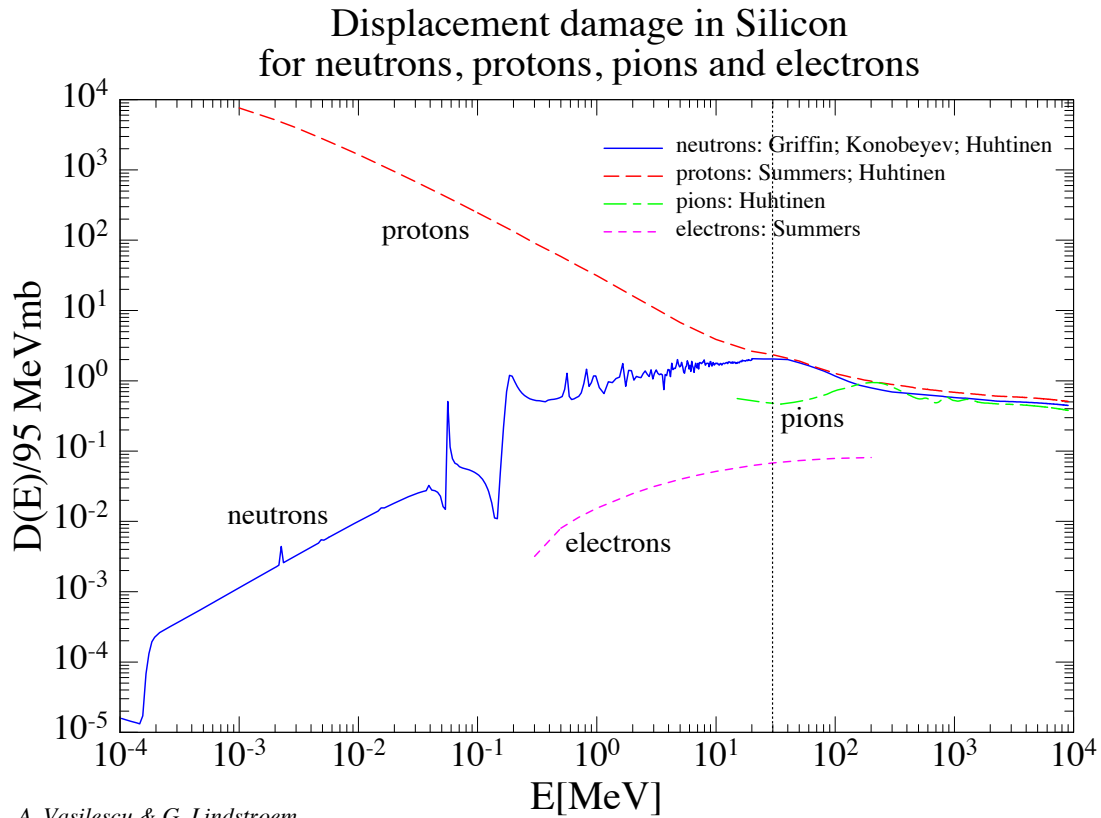


Figure 7.11: Displacement damage in Silicon as a function of particle energy [87].

7.6 Detector Characterisation

Several characterisation measurements can be performed to determine the effect of radiation on detector performance. These techniques will be referred to in Chapter 9 and therefore will be briefly explained in this section.

I-V measurements

The reverse current, often referred to as leakage current, is largely dependent on temperature and radiation damage. Different types of defects contribute to the leakage current, and can cause significant increases, proportional to the fluence received. The leakage current is also proportional to the depletion depth, saturating at voltages above the depletion voltage and current-voltage (I-V) measurements can be made to determine the amount of damage incurred and performance at high voltages. The current is expected to increase with voltage, as in Figure 7.12, until fully depleted and these measurements are performed at sub-zero temperatures to minimise the temperature effect. The measurements are normalised to a reference temperature, typically 20 °C and allow comparison between different irradiations [82].

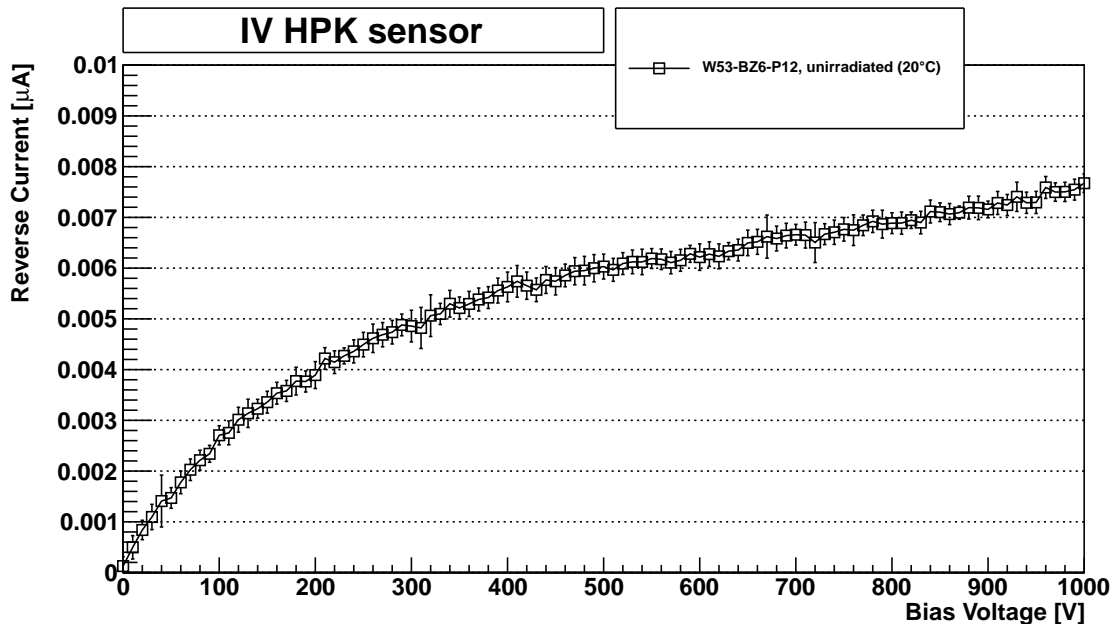


Figure 7.12: Reverse current measured as a function of bias voltage for an unirradiated detector [88].

C-V measurements

Capacitance voltage (C-V) characteristics are measured at $-25\text{ }^{\circ}\text{C}$ to reduce annealing effects after irradiation and the bulk capacitance is measured using a LCR meter. An AC signal is applied with an amplitude and frequency of 1 V and 1 kHz, applying reverse bias voltage from -10 to -1000 V [85]. To determine the depletion voltage, the relationship between capacitance and voltage is used, depletion depth, $d \sim \sqrt{V}$ and capacitance $C \sim 1/d$, therefore the voltage $V \sim 1/C^2$, where $1/C^2$ increases linearly with voltage until saturation, as shown in Figure 7.13. Two straight lines are fitted, before and after saturation and the intercept is determined to be the depletion voltage.

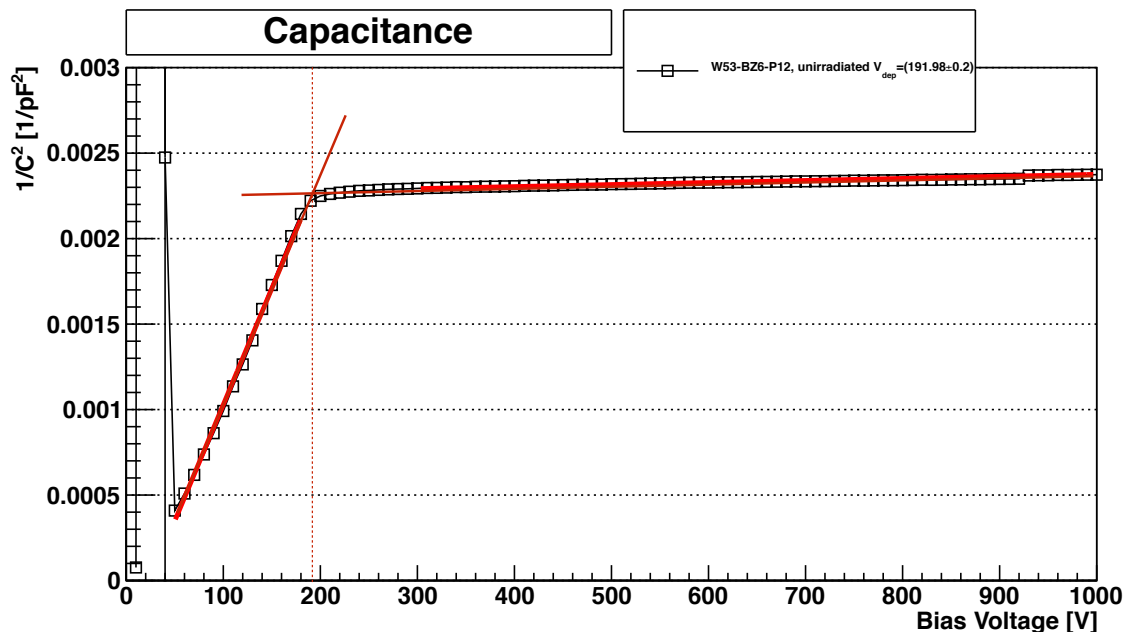


Figure 7.13: Ideal inverse capacitance squared against bias voltage for an unirradiated detector. The red lines clearly demonstrate the linearly increasing and saturated regions which can be fitted, extracting the depletion voltage from the point of intercept [88].

Charge collection efficiency

To determine the charge collected by the sensor as a function of bias voltage, charge collection measurements (CCE) are made using an ALiBaVa readout system. The sensor is bonded to a daughter board in the system which contains two readout chips used to acquire the detector signals. A mother board is used to process the analogue data and communicate with the software on a PC via USB. A radioactive source setup is used with a ^{90}Sr β source [89, 90]. ^{90}Sr undergoes β^- decay with an energy of 0.55 MeV to ^{90}Y , which in turn β^- decays with an energy of 2.2 MeV. The electrons emitted have two distinct sets of energies, one from 0-0.55 MeV and the other from 0-2.2 MeV.

To determine the charge collection, the ALiBaVa system must trigger only on electrons with energies greater than approximately 1 MeV. To do this, a dual coincidence is used, with two scintillators placed underneath the daughter board, to ensure that the electron has traversed the sensor and both scintillators. In order to pass through both scintillators, the electron must have high enough energy to make it minimum ionising.

The number of electron-hole pairs collected by a device depends on the thickness of the device and the source deposits the energy of a minimum ionising particle. A signal is generated and calibration data is used to convert this into collected charge (number of electrons). A Landau distribution is

generated from a time cut on the signal pulse shape and the most probable value is extracted at each bias voltage, as discussed in Section 7.3.3. Charge collection measurements of an unirradiated 300 μm thick sensor [85] are presented in Figure 7.14, with a plateau at approximately 22k electrons, as expected, when the sensor is fully depleted.

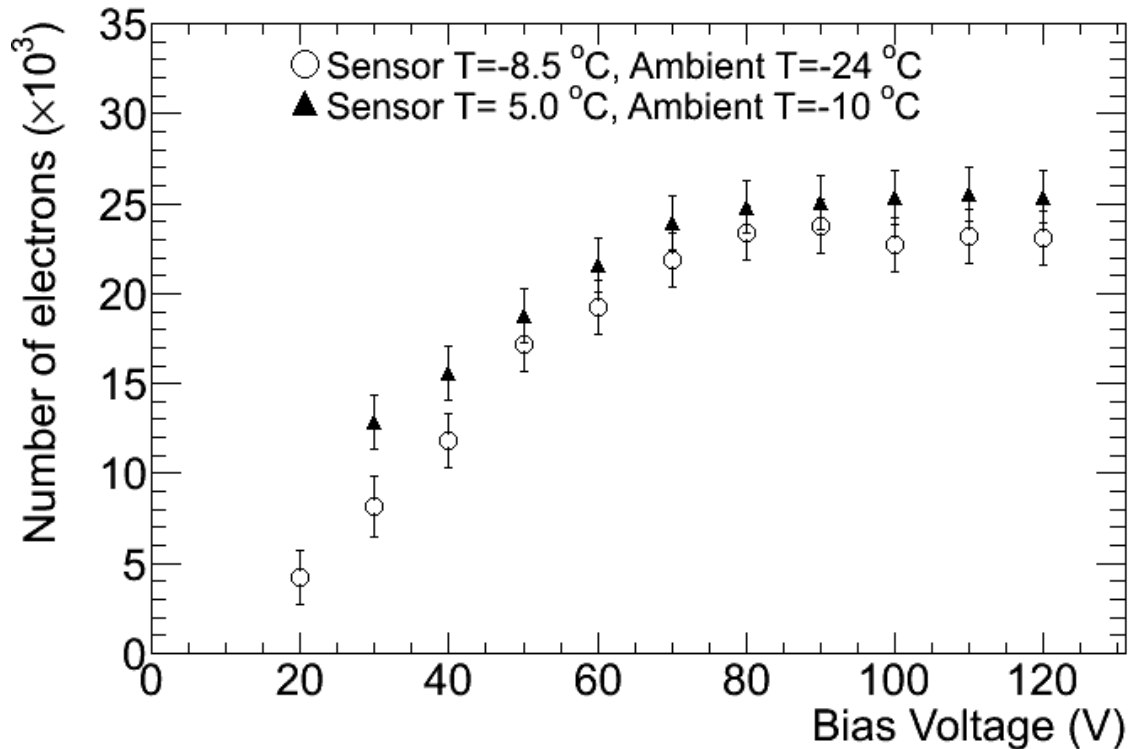


Figure 7.14: Unirradiated charge collection measurements of a strip detector as a functions of bias voltage reaching a plateau of approximately 22.5k electrons.

When irradiated, the charge collection will deteriorate as a consequence of radiation damage, as discussed in Section 7.4. Bulk damage can cause additional energy levels within the band gap, trapping charge carriers within the readout time of the electronics and reducing the signal which is read out. Changes to the effective doping concentration can also reduce the signal collected as the depletion voltage is increased. If operated at the same bias voltage as when unirradiated, the device will not be fully depleted and signal read out will be reduced.

Reduced signal collection limits the use of silicon devices, particularly after exposure to high fluences. This means that within ATLAS, track reconstruction and vertex identification may be difficult if detectors close to the IP fail to read out signal.

To recover some of the damage to the devices, controlled annealing is performed, heating the device to 60 °C for 80 min within the beneficial annealing region. Charge collection measurements are made pre and post-annealing [91].

Cluster size measurements

As particles traverse the sensor, a signal will be created at a number of channels and often in their adjacent channels. The cluster size is defined as the number of strips in one cluster. Cluster measurements can be performed to determine the number of strips read out in charge collection measurements.

Typically the MIP interacts with one or two strips which corresponds to one or two hits however, if the sensor has been damaged more clusters may be produced. The charge is then spread across multiple strips, generating less charge per strip and resulting in a decrease in charge collection.

7.7 Summary

This chapter has given a brief overview of the Phase-II upgrades, in order to provide the relevant background information to the work presented in Chapter 9.

In Section 7.2, the proposed Phase II upgrade of the ATLAS experiment has been described. Section 7.3 has introduced basic concepts of semiconductor devices which are fundamental to understanding ATLAS silicon sensors. Finally, Section 7.4 describes the basic radiation damage mechanisms and the consequences for performance and functionality.

Chapter 8

Irradiation Facilities

8.1 Introduction

As mentioned in Chapter 7, the performance of materials to be used in the upgraded ATLAS detector need to be assessed after exposure to a high radiation environment, equivalent to 10 years of operation at the HL-LHC. An irradiation facility has been installed at the University of Birmingham, using the MC40 cyclotron [92] as a source of protons. Materials to be used in the upgraded ATLAS detector are distributed to irradiation sites globally to undergo irradiation and to then evaluate their performance.

According to the Phase-II Letter of Intent [59], the expected fluences received by the innermost pixel layer after 10 years of operation is $1.4 \times 10^{16} \text{ 1 MeVn}_{eq}\text{cm}^{-2}$, incorporating a safety factor of up to 2 to account for uncertainties in the simulated predictions [68]. Materials require a homogeneous irradiation and sensors must be cooled to sub-zero temperatures during irradiations at proton facilities.

The author has been involved in the commissioning and development of the Birmingham Irradiation Facility. This includes preparing and monitoring irradiation runs, contributions to upgrades of the cooling system, analysis of temperature data and sensor testing. This chapter gives an overview of the setup of the Birmingham Irradiation Facility and a brief introduction to other Irradiation facilities. Chapter 9 will then detail the performance of the Birmingham Irradiation Facility, with reference to the setup described in this chapter and compare results to irradiations performed at other facilities.

8.2 The Birmingham Irradiation Facility

The Birmingham Irradiation Facility has been in operation in the high intensity beam area since early 2013 using the MC40 Medical Physics cyclotron at the University of Birmingham. The cy-

clotron provides a beam of protons which are collimated to 1 cm^2 to irradiate existing detector technologies as well as new components and materials to be used for the upgraded ATLAS detector. A range of proton energies between 11 and 37 MeV can be achieved using the cyclotron [92]. An energy of 27 MeV has been chosen as HL-LHC fluences can be achieved on a significantly shorter time scale than the CERN-PS facility at this energy, and is comparable to the facility at KIT, as described in Section 8.6. During the shut down of the PS between 2012-2015, the Birmingham Irradiation Facility provided beam time and allowed the ATLAS irradiation programme to continue.

The facility uses the high intensity beam area within the Birmingham cyclotron, with a separate beam line installed for the purpose of high beam current irradiations. The initial development of this area required additional shielding in the form of high density cement blocks to be installed between the irradiation area and the control room. Adding an extra 400 mm of shielding blocks stopped neutrons and allowed beam currents of up to $2\text{ }\mu\text{A}$ to be safely achieved. A 1 m thick wall was also installed to separate the high and low intensity areas in the beam room. The samples to be irradiated are contained within a thermal chamber on a scanning table. An XY-axis cartesian robot system (referred to as the scanning system), moves the thermal chamber in a pre-configured path through the fixed beam position to allow uniform irradiations and remove any beam inhomogeneities. Until September 2015, over 200 samples have been irradiated since commissioning in early 2013 however, due to the high intensity of the beam, some issues from high temperatures and annealing of sensors were encountered. These problems required extensive tests to be performed using variable beam currents, an alternative setup and upgrades to the cooling system. These studies will be discussed in more detail in Chapter 9.

The thermal chamber temperature was initially set to $-15\text{ }^\circ\text{C}$ to control annealing effects and prevent irreversible damage to the sensors which can result in thermal runaway and increase leakage currents when operated. After upgrades to the cooling system, the thermal chamber was cooled to $-50\text{ }^\circ\text{C}$, to maintain sub-zero temperatures on the sensors whilst irradiated. Sensors are not typically biased during an irradiation run, which is consistent with other facilities. Other samples may have specific requirements during irradiation and therefore the setup must be flexible enough to include irradiations of a variety of samples to a range of fluences. After irradiation, samples are stored in a freezer in a radiation controlled laboratory. They are then dispatched to different test sites, or are tested at the University of Birmingham.

The majority of irradiations performed at the Birmingham Irradiation Facility are sensors, which require careful handling and cooling. On testing these samples, post-irradiation measurements are made, and after a controlled annealing for 80 minutes at $60\text{ }^\circ\text{C}$, which is optimal for restoring damage within the sensors, the tests are repeated. During controlled annealing, beneficial annealing dominates and drives the full depletion voltage to a minimum which results in more stable measurements allowing direct comparisons between sensors irradiated at different facilities [85].

8.2.1 The University of Birmingham MC40 Cyclotron

The MC40 Medical Physics cyclotron has been operational since 2004 and is housed in the basement of the University of Birmingham Medical Physics Department. The cyclotron is primarily used to produce medical isotopes for distribution to hospitals and is also used as a proton source for the Birmingham Irradiation Facility.

To produce the cyclotron beam, an ion source is accelerated by large D-shaped metal blocks, referred to as ‘dees’. One of the dees is held at ground whilst an alternating voltage is applied to the second dee, between which there is narrow gap. Conventionally, cyclotrons are constructed from two dees, but the acceleration at the Birmingham is provided by two 90° dees, whilst another two dees alternate and are held at ground, as in Figure 8.1.



Figure 8.1: Four hollow metal dees at the MC40 Birmingham Cyclotron with two grounded and two which apply radio frequency (RF) voltage. The dees alternate between grounded and RF [93].

A uniform magnetic field, B , is applied to the dees, causing charged ions to move in a circular orbit from the ion source located at the centre between the dees, and accelerate when crossing the dees. Due to the alternating voltage across the dees, the radius of the orbit increases, resulting in a spiral path, see Figure 8.2.

The velocity, v of the particle of mass m and charge q in a uniform magnetic field B , is related to the radius r via:

$$\frac{mv^2}{r} = qvB. \quad (8.1)$$

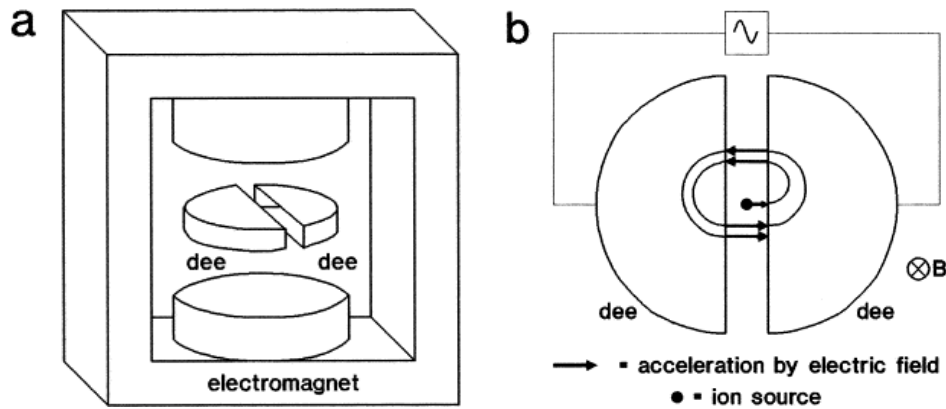


Figure 8.2: Illustrated 3D and 2D view of a cyclotron, demonstrating the spiral path of the ions as they are accelerated by the electric field [94].

At radius R , after approximately 500 orbits [93], the beam reaches the outside of the cyclotron, and the magnetic field on the magnets is adjusted to the required final energy, where the kinetic energy is:

$$E = \frac{1}{2}mv_R^2 = \frac{1}{2}m\left(\frac{qB}{m}\right)^2 R^2 = \frac{R^2}{2} \frac{q^2}{m} B^2. \quad (8.2)$$

This means that with a radius of 53 cm and 1.8 T magnetic field, the maximum energies of ions used at the cyclotron can be calculated. These energies are presented in Table 8.1.

Particle type	Energy [MeV]
Protons	40
Deuterons	20
Alphas	40
${}^3\text{He}^{2+}$	53

Table 8.1: Maximum beam energies for the MC40 cyclotron at Birmingham at $R = 53$ cm, $B_{max} = 1.8$ T [93].

The different ions are used for medical isotope production, medical physics research and nuclear research at the University of Birmingham [93]. A separate beam line has been added for high current irradiations which are necessary to study radiation damage in HL-LHC environments using protons.

8.2.2 The scanning system and initial thermal chamber

To irradiate samples uniformly, a scanning system was developed by the University of Sheffield. The silicon sensors must be irradiated in a cold environment to prevent annealing and thermal runaway. Based on the CERN PS recirculating glycol system, using indirect air circulation to remove heat on the sensors, a thermal chamber was developed. This sits on the scanning system and moves samples, mounted within the thermal chamber, typically referred to as the cold box, through the 1 cm^2 beam. Figure 8.3 shows the cold box and scanning system set up within the high intensity beam area. The scanning system is controlled using a NI CompactRIO Real-Time programmable controller [95, 96], with a relay control for the x-motion, moving with velocities as low as 1 mm s^{-1} and up to 8 mm s^{-1} during an irradiation run. The movement in the y-axis is driven by a third party servo drive and moves at 25 mm s^{-1} . The scanning system and cold box communicate with an NI LabVIEW GUI [95, 97] which has a pre-configured scan path and requires input parameters from the user to calculate the path and number of runs. The program is designed to perform an irradiation to achieve a fluence of $1 \times 10^{15} \text{ 1 MeVn}_{eq}\text{cm}^{-2}$ uniformly over the entire scan area. The fluence is calculated using the beam current, the area to irradiate and the x-axis velocity, as in Section 8.2.4.

In order to remove any beam inhomogeneities, the step size is set to 0.5 cm (half of the beam size) to scan each area twice per run. This is another parameter which can be changed by the user, however 0.5 cm is used by default.

Due to the fast y-axis velocity, it is crucial to ensure that the beam is not incident on the samples whilst it traverses in this axis; this prevents over irradiating the edges of the samples where the correct scan is demonstrated in the y-movement at the maximum x-axis position in Figure 8.4. The y-movement at $x = 0$ in Figure 8.4 demonstrates overscanning and should be avoided. For the x-axis, there is a 0.5 cm overlap when traversing the top and bottom of the irradiation area. Figure 8.4 shows an example scan path for six $1 \times 1 \text{ cm}^2$ mini sensors.

The LabVIEW program also communicates with sensors within the thermal chamber to set the required temperature of the glycol system and operate the fans which are located at the base of the box. The humidity and temperature within the cold box are also monitored, using 1000Ω platinum resistors, PT1000 [99, 100] sensors, to measure temperatures during an irradiation run. The box is also purged with dry nitrogen before and after an irradiation run to flush out the air and prevent condensation forming within the box.

Figure 8.5 shows the cold box and the lid, where a mounting bracket is attached. Custom-made carbon fibre reinforced plastic (CF) frames have been used after irradiation of a CF sandwich for ATLAS Upgrade Stave structures. Post-irradiation mechanical tests were performed [71, 72] and the CF maintained its rigidity and did not degrade from the high intensity beam. The results indicated

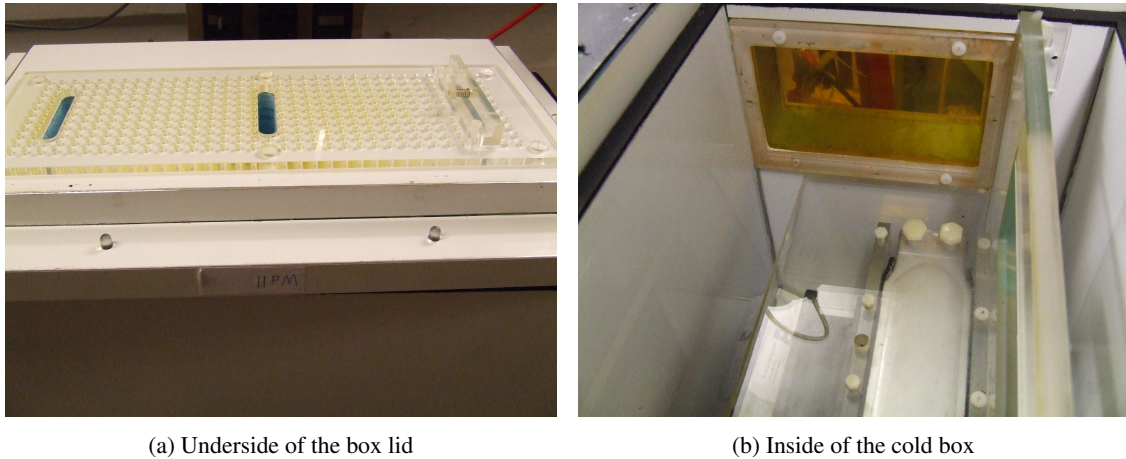


Figure 8.5: The inside and lid of the cold box with the matrix of holes and spring mount to position and attach frames containing samples to be irradiated.

that the strength and shape maintained after irradiation made carbon fibre a suitable material to be used as a frame for sensors and 400 μm -thick CF sheets were used to design two types of frame. Mini frames hold nine mini sensors, with three rows of three $11 \times 11 \text{ mm}^2$ holes cut out. Pixel frames are designed to hold two double pixel sensors and a single pixel sensor of dimensions $4.2 \times 1.9 \text{ cm}^2$ and $2.2 \times 1.9 \text{ cm}^2$. These CF-based frames have been used since early in the project.

The top of the frames contain three holes, the one in the centre fits into a spring-loaded release mount on the top of the box lid, and two outer holes match the positioning screws, as can be seen in Figure 8.6. This attaches the frame holding the sensors to the cold box lid and the position of the frame within the irradiation area is known to $\pm 1 \text{ mm}$. Kapton tape is used to secure the sensors in position within the frame, however, as will later be discussed, recent improvements have been made to reduce the amount of tape required.

8.2.3 Irradiation Run Procedure

An irradiation run at the Birmingham Irradiation Facility can be broken down into several stages starting with pre-irradiation run preparation. The user, who provides the samples, must specify the target fluence and details for the sample so that the scan path can be calculated using the required fluence, area of the scan and the beam current, as discussed in Section 8.2.2. For silicon sensors, the samples can be mounted with the carbon fibre frames and kapton tape, however for other materials and irregular shaped samples, these require more preparation. Nickel activation foils, cut to the size of each sample, are added either in another CF frame, or taped to the samples, to be used for offline dosimetry, as described in Section 8.2.5

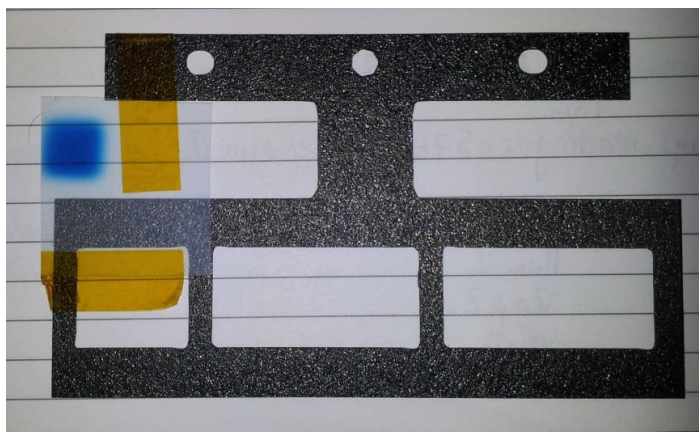


Figure 8.6: Carbon fibre pixel frame used to mount samples and attach to the lid of the cold box. Three holes at the top of the frame are used for alignment; outer holes are for positioning, middle is used to attach to the spring mount. Gafchromic film after exposure to the proton beam is shown which is used to measure the offset of the beam from the position of the samples and for alignment.

Secondly, the beam position and profile is measured. This is done by mounting the sample in the thermal chamber, whilst warm, and attaching a sheet of gafchromic film to the frame [101]. The box is moved to ‘Home’ position where the beam is incident on the gafchromic film. The beam is turned on, at a low beam current, $O(nA)$ for a few seconds. During this short exposure to the beam, the film develops showing a $1 \times 1 \text{ cm}^2$ blue profile of the beam, as shown in Figure 8.6. Any adjustments to the beam are made at this stage to ensure that the beam profile is uniform during the irradiation run. The sample position within the frame is measured with respect to the ‘Home’ position which is used as reference point by the scanning program. ‘Home’ position is controlled by limit switches and therefore has a known x and y position, whereby the box starts and ends each scan. By measuring the sample area with respect to ‘Home’, the location of the area to be irradiated can be determined to within $\pm 1 \text{ mm}$.

Next, the samples are mounted for the run. The glycol cooling system and fans are turned on, and the box is purged with dry nitrogen once the lid is closed to prevent any condensation within the cold box. The cool down time is approximately 2 hours to achieve -15°C with the glycol chiller system. During this time, the cold box can be moved out of the beam line, in to ‘Park’ position so that the cyclotron team can set up the beam at the required current in preparation for the irradiation run. In ‘Park’ position, the beam does not interact with any material from the cold box and is aligned with a Faraday cup, which is used to measure the current to determine the number of charged particles incident on the block of carbon. The block of carbon absorbs and stops the protons and measures the charge using a sensitive electrometer located in the control room. The carbon block is located within an aluminium cylinder and is insulated from the cylinder, giving an independent measurement of the number of protons in the beam. During a run, when the sample and cold box obstruct the beam path, less current is measured as some of the beam is stopped prior to reaching the Faraday cup,

therefore the current on the collimators is used to monitor and adjust the beam during the run.

Once the cold box reaches $-15\text{ }^{\circ}\text{C}$, the next stage can begin; the irradiation run. Parameters are inserted into the NI LabVIEW GUI to calculate the scan path, and the run is started. A 27 MeV proton beam can achieve a fluence of $1 \times 10^{15} \text{ 1 MeVn}_{eq}\text{cm}^{-2}$ in 80 s using a $1\text{ }\mu\text{A}$ beam current. However, to ensure a uniform dose, the scanning system moves the samples at 1 mm s^{-1} through the fixed beam position and returns to ‘Home’ position after each scan to calibrate and reset the alignment of the robotic scanning system. To irradiate three mini sensors to a fluence of $1 \times 10^{15} \text{ 1 MeVn}_{eq}\text{cm}^{-2}$ using a $1\text{ }\mu\text{A}$ beam current and a total scan area of $53 \times 15\text{ mm}$ requires 4 scans, with run time of 20 min.

The sensors are positioned in the top three positions in the mini sensor frame in Figure 8.7. To irradiate these three sensors, a scan area of $53 \times 15\text{ mm}$ is used. In the x-direction there are three 11 mm sensors, two 5 mm spacings and a 5 mm overlap at each end, ensuring the beam is not incident on the sensor edges during vertical movement, totalling 53 mm. In the y-direction, a multiple of 5 mm is used, which is the y increment: as the sensor is 11 mm, a height of 15 mm is used. This means that during Pass 1, the beam will be incident on 5 mm of the sensor, whilst during Pass 4, 1 mm is irradiated. The x and y-offset from the bottom left of ‘Home’ position to the bottom left of the sensor in position 1 in Figure 8.7 are measured. To these offset values 5 mm is subtracted in y and 10 mm is subtracted in x to ensure that only the top 5 mm is irradiated in Pass 1 and also to prevent overscanning the sensor during y-movement as previously discussed.

During the run, the Faraday cup measures the charge collected and the total number of protons can be determined. Nickel activation foils are also used for dosimetry and can be used to cross-check the incident dose.

After the irradiation run is complete, the samples are left to cool. Once the activity within the irradiation area is at a safe level of approximately $100\text{ }\mu\text{Sv h}^{-1}$, the samples are moved from the cold box to a freezer within a radiation controlled laboratory. The samples are maintained at low temperatures until the radiation level is negligible and the samples are safe to be tested at Birmingham, or transported to other test locations. For the dosimetry, the gamma spectrum of the Nickel activation foils is measured as discussed in Section 8.2.5.

8.2.4 Fluence calculation

The fluence delivered during a uniform irradiation of area A , over a time t , with proton current I , can be calculated by:

$$F = \frac{I \cdot t}{q_{el} \cdot A}. \quad (8.3)$$

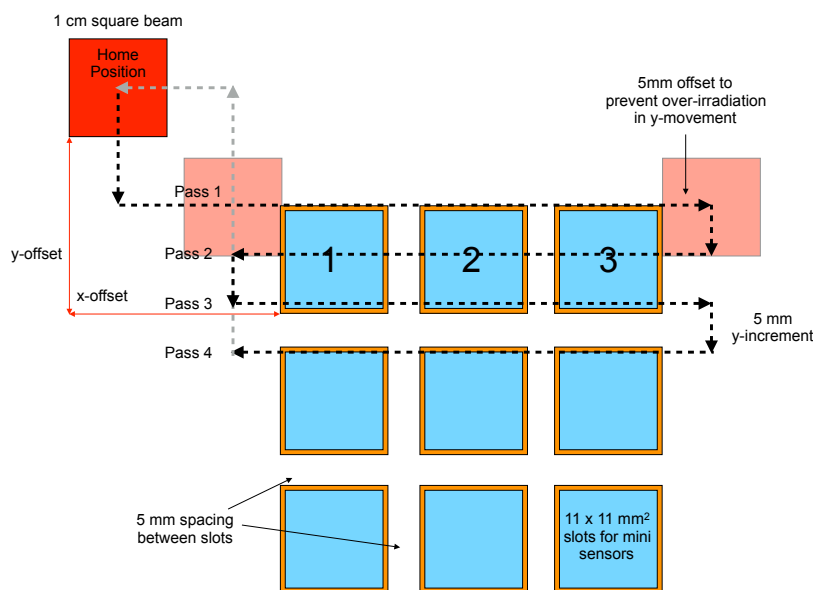


Figure 8.7: Diagram demonstrating the scan path of sensors in the mini frame, with the ‘Home’ position indicated and the x-offset and y-offset with respect to this position. The spacing of the mini frame and sensor position is indicated, as well as the overscan in the x-direction to avoid over-irradiating when traversing in y.

The step size in the y axis is 5 mm, in order to scan the sample area twice per run and remove any beam inhomogeneities. Also the area is only irradiated when traversing in the x-direction, to avoid overscanning. The default speed used is 1 mm s^{-1} and the beam current can be adjusted and input into the programme to calculate the number of scans required to achieve $1 \times 10^{15} \text{ 1 MeVn}_{eq}\text{cm}^{-2}$. As the programme indicates the irradiation time to achieve a preset fluence of $1 \times 10^{15} \text{ 1 MeVn}_{eq}\text{cm}^{-2}$, the beam current or number of scans may be tuned to achieve an alternative fluence. For example, to achieve a target fluence of $5 \times 10^{14} \text{ 1 MeVn}_{eq}\text{cm}^{-2}$, either the current or the number of scans can be halved from the value calculated in the programme.

Within the LabVIEW GUI, the preset target fluence is $1 \times 10^{15} \text{ 1 MeVn}_{eq}\text{cm}^{-2}$. A damage factor (κ) of 2.0 has been used for 27 MeV protons, based on similarities with the proton cyclotron beam at Karlsruhe, see Section 8.6. $1 \times 10^{15} \text{ 1 MeVn}_{eq}\text{cm}^{-2}$ has an equivalent proton fluence of $5 \times 10^{14}\text{cm}^{-2}$, using NIEL scaling hypothesis:

$$F_{n_{eq}}^{1\text{MeV}} = \kappa F. \quad (8.4)$$

For reference, to irradiate an area of 1 cm to 1×10^{15} $1 \text{ MeVn}_{eq}\text{cm}^{-2}$ at a proton beam current of $1 \mu\text{A}$, the irradiation time is ~ 80 s. This means that using the default speed, to achieve the target fluence, 4 runs at 1 mm s^{-1} are required. The damage factor when interpolated from Huhinen and Summers data [87], see Figure 7.11, gives an alternative damage factor value of approximately 2.2 for 27 MeV protons. Due to the discrepancy between these values, experimental measurement of the damage factor at Birmingham is required and is planned for the future.

Using the pre-configured scan path which returns to ‘Home’ position after scanning over the sample area, during irradiations with a large number of runs, a significant fraction of the overall run time is spent traversing to and from the ‘Home’ position. This occurs either during high fluence irradiations, fast scan speed runs or when using a low beam current. To avoid the additional irradiation time, an alternative irradiation procedure has been introduced. For samples approximately the same size as the beam spot, such as mini strip sensors, a point-to-point irradiation is performed whereby the position of the sample is determined and moved into the beam path, and the beam is incident on the area for a manually measured amount of time, depending on the target fluence.

8.2.5 Dosimetry

Nickel activation foils are used for offline dosimetry and are measured using a germanium spectrometer. During an irradiation, the $25 \mu\text{m}$ foils are mounted in front of the samples to be irradiated, where the proton beam is first incident on the foils. When protons interact with the foils, ^{57}Ni is produced, which decays to ^{57}Co with a half life of 35.7 h and the number of incident protons can be calculated by measuring the gamma spectra of the foils. A distinct peak is produced at 1377 keV which corresponds to ^{57}Co . When a spectrum is taken immediately after the irradiation, there are a range of short-lived isotope peaks and over time only distinct peaks remain which includes the ^{57}Co peak and an annihilation peak due to electron-positron collisions at 511 keV. The gamma spectrum of Nickel foil from a sensor irradiation is presented in Figure 8.9 and the number of protons is calculated using the intensity of the peak, and the ^{57}Co production cross-section. Using the proton fluence, the n_{eq} fluence is calculated and irradiations at Birmingham achieve the required target fluence with an accuracy of 10%, see Figure 8.8.

During the irradiation run, a Faraday cup is used to measure the current and determine the number of charged particles. The faraday cup is aligned with the beam, and is placed downstream of the cold box. When the faraday cup is in the direct path of the beam, the exact number of charged particles may be recorded and can be cross-checked with the foils. However, during the irradiation run, the faraday cup is obstructed by the box and some particles may be stopped or scattered out of the beam. This means that the faraday cup reading is expected to be less than the fluence measured by the foils.

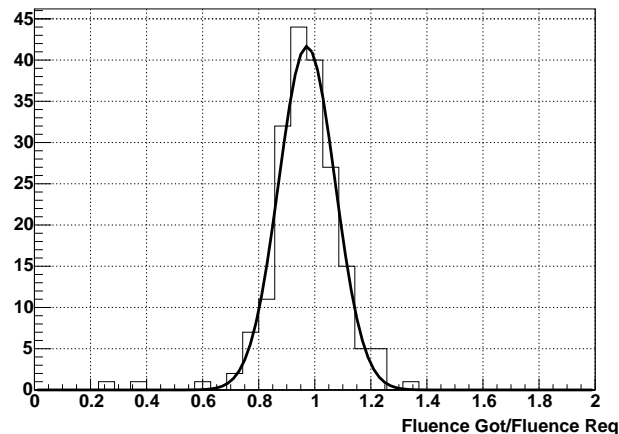


Figure 8.8: The accuracy of the irradiation fluence achieved compared to the required fluence is 10%, as measured by the Nickel activation foils which are in agreement with the Faraday cup over 194 irradiations.

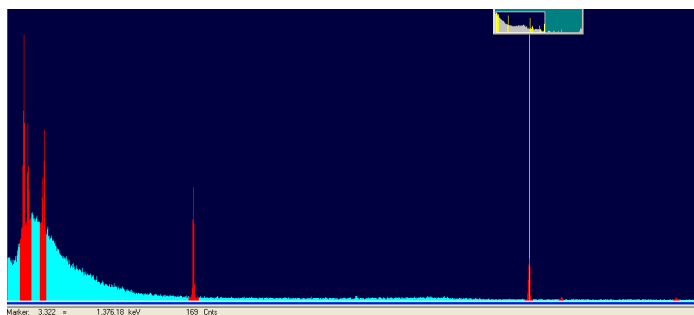


Figure 8.9: Gamma spectrum of a Nickel activation foil after irradiation, screenshot of Maestro. The peak highlighted corresponds to the ^{57}Co peak, used to calculate the incident number of protons.

8.3 Birmingham Irradiation Facility Summary

The Birmingham MC40 cyclotron can provide various particle beams with energies up to 40 MeV. For the purpose of irradiations to HL-LHC fluences, 27 MeV protons are used which have a damage factor of 2.0/2.2, to perform irradiations on a short time-scale. A robotic scanning system moves a thermal chamber through the fixed beam to ensure homogeneous irradiations of a range of samples of up to 15×15 cm. The beam is collimated to an area of 1 cm^2 and the uniformity and beam profile is measured using gafchromic film. Beam currents of up to $2 \mu\text{A}$ can be achieved and are chosen to adjust the target fluences or irradiation times. Typically an irradiation of sensors to a fluence of $1 \times 10^{15} \text{ 1 MeVn}_{eq}\text{cm}^{-2}$ to $1 \times 10^{16} \text{ 1 MeVn}_{eq}\text{cm}^{-2}$ can be achieved during one session. Active dosimetry is performed using a Faraday cup which measures the charge of beam incident on the samples during the run, and Nickel activation foils are used as an offline measurement, where a $\pm 10\%$ dosimetry error has been observed.

8.4 TRIGA Mark III research reactor, Ljubljana

The Triga Mark III research reactor is located at the centre of Jozef Stefan Institute (JSI) in Ljubljana. Irradiations are performed with reactor neutrons which have a continuous energy spectrum with energies between 100 keV - 15 MeV available, with a measured damage factor of 0.9. The power of the reactor is adjustable, with a maximum power of 250 kW. The flux scales with reactor power and can achieve a flux of $1-4 \times 10^{12} \text{cm}^{-2}\text{s}^{-1}$ depending on the size of the samples. Samples with a diameter of up to 4 cm can be irradiated, with uninterrupted irradiation times of up to 16 h available. The fluence is measured indirectly with 10% accuracy, using the flux of reactor which is calibrated by measuring leakage current of silicon diodes used for reference [102, 103, 104, 82].

8.5 IRRAD, CERN PS

The IRRAD facility uses the CERN PS system to irradiate samples. The 24 GeV pulsed proton beam is delivered in spills of approximately 5×10^{11} protons, with typically 6 spills, each approximately 2 s long, per minute. This allows irradiations with the standard beam diameter of $12 \times 12 \text{cm}^2$ which can achieve fluences of $1 \times 10^{16} \text{1 MeVn}_{eq}\text{cm}^{-2}$ in 5 days. The beam size is variable and using a smaller beam, smaller samples can be irradiated to higher fluences in a similar time frame, or a scanning table can be used to irradiate larger samples. A flux of up to $2 \times 10^{11} \text{pcm}^{-2}\text{s}^{-1}$ can be achieved, and a damage factor of 0.62 is measured. If required, a cryogenic system is available which cools to -20°C . Aluminium activation foils are used for dosimetry with an accuracy of 10%, and the activation is measured with a sodium-iodide or germanium spectrometer [105, 102, 82].

8.6 Karlsruhe (KIT)

Zyklotron AG cyclotron at the Karlsruhe Institut für Technology (KIT) is used to perform proton irradiations. The 23 MeV beam, which has an energy of 25 MeV on extraction from the cyclotron, has a measured damage factor of 2.0. The proton beam has an adjustable beam current of up to $2 \mu\text{A}$ to produce a flux of $2 \times 10^{13} \text{pcm}^{-2}\text{s}^{-1}$. The cyclotron generates a 7 mm diameter beam spot, and a scanning table is used to move the beam and irradiate larger samples. Samples can be cooled to -30°C during irradiations and depending on the size and cooling requirements, fluences of $1 \times 10^{15} \text{1 MeVn}_{eq}\text{cm}^{-2}$ to $1 \times 10^{16} \text{1 MeVn}_{eq}\text{cm}^{-2}$ can be achieved per session. Nickel activation foils are used for dosimetry, with an error of approximately 14%, and the gamma spectrum is measured using a germanium spectrometer [79, 102, 106].

8.7 Los Alamos

At Los Alamos National Laboratory (LANL), US, irradiations are performed using a 800 MeV LINAC proton beam with variable beam size of 2 - 5 cm. A flux of $5 \times 10^{11} \text{ p cm}^{-2} \text{ s}^{-1}$ can be achieved with damage factor of ~ 0.71 [107, 102].

8.8 CYRIC

Located at the AVF cyclotron in Tokyo, Japan, the Cyclotron and Radioisotope Center (CYRIC) uses a 70 MeV proton beam to irradiate samples within a scanning box. The maximum size of the sample is $11 \times 11 \text{ cm}^2$ and there are 15 sample slots available, with the option to cool to sub-zero temperatures in a dry nitrogen environment. The proton beam uses currents up to $1 \mu\text{A}$ and irradiation times vary between a few minutes to 6 h. Aluminium foils are used for dosimetry, measuring the activation to determine the fluence [108, 104, 102].

8.9 Summary

This chapter has introduced the Birmingham Irradiation Facility and provided detail about the running of the facility and the irradiation procedure. A brief summary of the CERN, KIT, JSI and CYRIC facilities is given in Table 8.2 which presents an overview of the different irradiation facilities. Due to the high number of sensors and components required to be irradiated and tested for upgrades to the LHC experiments, many irradiation facilities are essential. Further to this, the damage caused by different particles at different energies can be studied and compared, enhancing our understanding of materials in high radiation environments.

Institution	Facility	Source	Particle	Energy (MeV)	Damage factor	Maximum flux ($\text{cm}^{-2}\text{s}^{-1}$)
Birmingham	Birmingham Irrad. Fac.	MC40 Cyclotron	protons	27	2.0/2.2	1.5×10^{13}
JSI	Triga Mark-III	Reactor	neutrons	<15	0.9	4×10^{12}
CERN	IRRAD	CERN PS	protons	24000	0.62	2×10^{11}
KIT	Karlsruhe	Compact Cyclotron	protons	23	2.0	2×10^{13}
Los Alamos	LANL	LINAC	protons	800	0.71	5×10^{11}
CYRIC	CYRIC	Cyclotron	protons	70	1.5	7×10^{12}

Table 8.2: Overview of the different irradiation facilities with corresponding beam parameters [102].

Chapter 9

Results of irradiations and tests performed at the Birmingham Irradiation Facility

9.1 Introduction

The following chapter will discuss the initial commissioning of the Birmingham Irradiation Facility, analysis of temperature data, developments to the facility and the final results to determine a stable irradiation procedure to produce irradiated results which are comparable to other facilities.

9.2 Initial Results

Prior to commissioning the facility and installing the scanning system and cold box, the beam was compared to other facilities. An ATLAS07 sensor was irradiated to $5 \times 10^{15} \text{ 1 MeVn}_{eq}\text{cm}^{-2}$ at the Birmingham Irradiation Facility, and the charge collection was measured and compared to a proton irradiation at Karlsruhe and a neutron irradiation at Ljubljana [95]. Karlsruhe uses a cyclotron setup with 25 MeV protons on extraction and Ljubljana uses reactor neutrons, as described in Chapter 8. While the other facilities can also irradiate to high fluences, the Birmingham facility is able to attain a target fluence in a short time due to the high current, continuous beam with comparable irradiation times to Karlsruhe [102]. The damage factors used at both Karlsruhe and Ljubljana are determined experimentally and the damage factor used at Birmingham was initially implemented based on similarities of the proton beam between Karlsruhe, where the beam energy on extraction from the cyclotron is 25 MeV [106] and 27 MeV at Birmingham. The Karlsruhe experimental value of 2.0 is used in the scanning program, however a value 2.2 can be extracted from Figure 7.11 and is used for manually timed irradiations, incorporating an error of 10%.

The Birmingham irradiation was performed at $1 \mu\text{A}$ and the results are presented in Figure 9.1. The comparable results between the facilities motivated the Birmingham Irradiation Facility programme,

as the 27 MeV proton beam was shown to generate equivalent damage to other facilities when scaled to 1 MeV neutron fluence, which is consistent with the NIEL hypothesis described in Chapter 7.

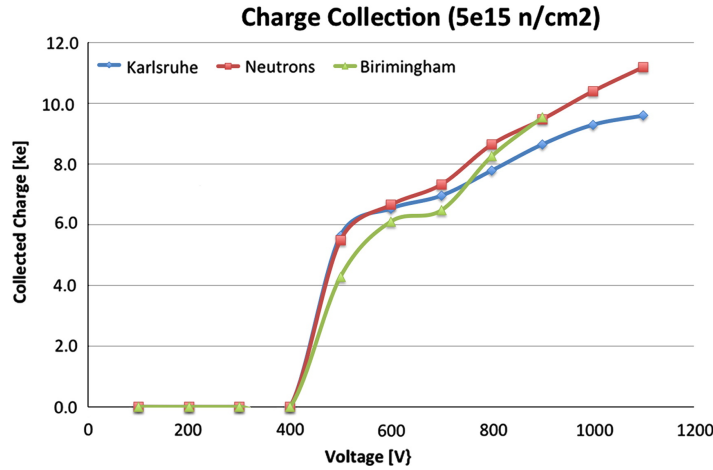


Figure 9.1: Charge collection measurements comparing sensors irradiated at different facilities to a fluence of $5 \times 10^{15} \text{ 1 MeVn}_{eq}\text{cm}^{-2}$ irradiated at Birmingham, Karlsruhe and Ljubljana. The results at the different facilities are in good agreement [95].

The first irradiations performed with the scanning system and cold box were based on the experience of the CERN PS facility [109]. The cooling system was built assuming that the cooling capacity was equivalent to that at the CERN PS facility, and the mounting technique was also mimicked. Frames were initially constructed using cardboard and kapton tape to mount the sensors and attach to the cold box lid. However, 27 MeV protons deposit 1.1 MeV in 300 μm of silicon, with 1.1 W generated by a 1 μA beam. This energy deposition caused singeing of the cardboard and therefore a new frame material was required. The initial programme involved irradiations of a variety of sensors, to determine the best layout and type of sensors to be used for the ATLAS Phase-II pixel and strip upgrade. In addition to sensors, irradiations of carbon fibre sandwiches for staves were performed to test their mechanical strength [71, 72], as well as irradiations of JFETs and PCB material. It was clear after the material irradiations that despite scanning over the samples at an x-velocity of 1 mm s^{-1} , the beam deposits significant energy within the samples, which causes large temperature increases. This can be seen from the blackening of PCB material in Figure 9.2. Fortunately the heating effects observed at the Birmingham Irradiation facility will not be significant at the HL-LHC, where the fluence will be accumulated over years, as opposed to hours at Birmingham.

Initially, beam currents of up to 2 μA were used in order to achieve HL-LHC fluences of up to $1 \times 10^{16} \text{ 1 MeVn}_{eq}\text{cm}^{-2}$ within the allocated beam time for irradiation work, of the order of hours [110]. Typically, the irradiation team book the facility for approximately 5 hours on a weekly basis, with longer irradiations possible when scheduled well in advance. The beam time is arranged around medical isotope production, which is the main use of the cyclotron, therefore minimising irradiation time by increasing the beam current allows more irradiations to be performed.

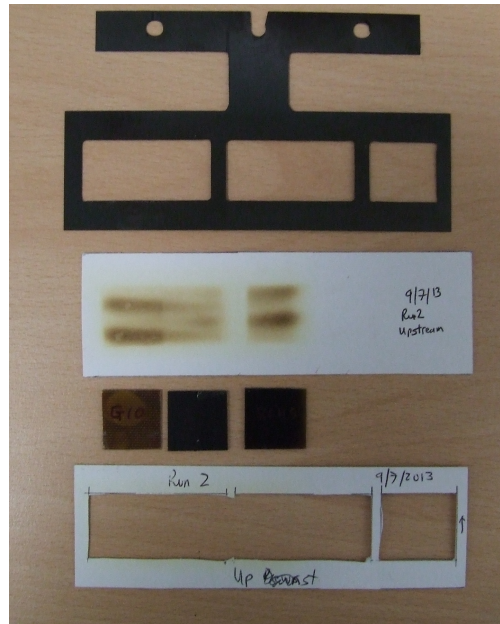


Figure 9.2: Three different types of PCB material after irradiation, showing various degrees of blackening due to the high intensity proton beam.

After moving to carbon fibre frames, as discussed in Section 8.2.2, with kapton tape for securing the sensors in place, no direct evidence of over-heating was observed. However, I-V measurements of a set of pixel sensors, irradiated at different currents to achieve a range of fluences showed some unusual results in Figure 9.3. The highest fluence of 5×10^{15} $1 \text{ MeVn}_{eq}\text{cm}^{-2}$ (blue) was irradiated using a beam current of $2 \mu\text{A}$ and shows evidence of annealing with a decrease in the measured current compared to the 1×10^{15} $1 \text{ MeVn}_{eq}\text{cm}^{-2}$ (purple) sensor, irradiated at $1 \mu\text{A}$. The results suggest that over-heating of the sensors caused annealing at $2 \mu\text{A}$ and therefore the beam current was too high.

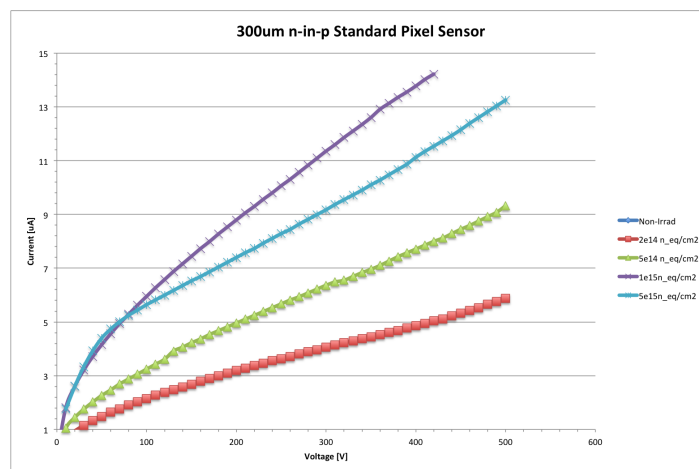
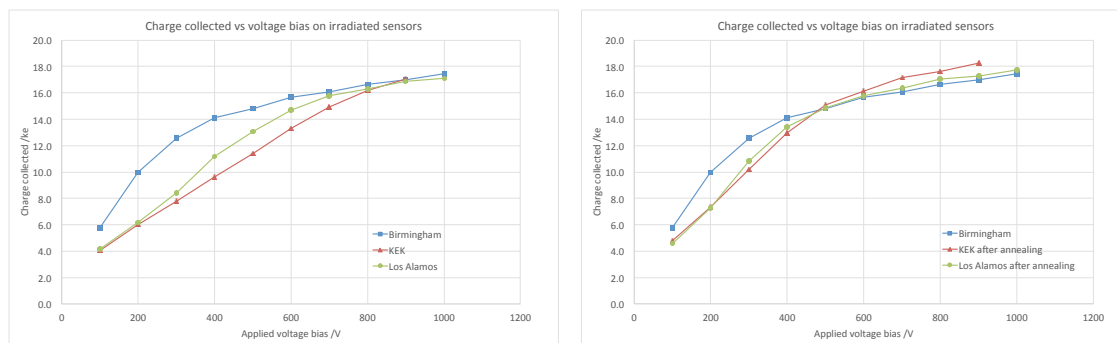


Figure 9.3: I-V measurements of sensors irradiated to different fluences, with different beam currents at the Birmingham Irradiation Facility [110].

To study this effect further, charge collection measurements of a sensor irradiated to a fluence of $1 \times 10^{15} \text{ 1 MeVn}_{eq}\text{cm}^{-2}$ at Birmingham are compared to other facilities. Charge collection measurements of the sensors are presented in Figure 9.4, which shows the sensors after irradiation, where Los Alamos and KEK measure a similar charge collection, whilst Birmingham collects more charge, indicating that the sensor received less radiation damage. To investigate further, the Los Alamos and KEK sensors were annealed for 80 min at 60°C and compared with the unannealed Birmingham sensor. The charge collection of the annealed sensors compare well with the Birmingham sensor, suggesting that this sensor has also been annealed which is likely to be caused by over-heating during irradiation.



(a) Charge collection measurements before annealing.

(b) Charge collection measurements after annealing.

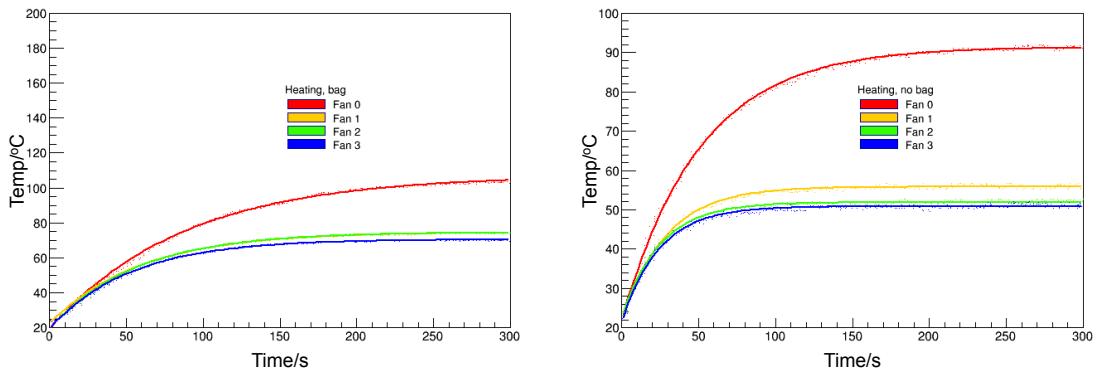
Figure 9.4: Charge collection measurements comparing sensors irradiated to $1 \times 10^{15} \text{ 1 MeVn}_{eq}\text{cm}^{-2}$ irradiated at Birmingham, Los Alamos and KEK. The sensors irradiated at other facilities are comparable to the Birmingham sensors when annealed, suggesting that Birmingham facility anneals sensors during the irradiation run [98].

To prevent over-heating, further irradiations were performed with a beam current limit of $0.5 \mu\text{A}$, whilst a dummy cold box was designed to simulate the heat dissipated by the beam. Using a standalone set up of a dummy cold box at room temperature with a fan directing air onto the sample, PT1000 sensors were used to measure the temperature increase on the sensor when a mini heater deposits 1.1 W of heat, the equivalent of a $1 \mu\text{A}$ beam current of 27 MeV protons incident on a $300 \mu\text{m}$ silicon sensor. The PT1000 is glued directly to one face of the sensor, whilst a series of mini heaters are applied to the opposite face, simulating the beam current.

Temperature measurements using a simulated $1 \mu\text{A}$ beam, within the dummy box are presented in Figure 9.5, where two configurations are tested, with and without an insulating bag. Sensors are usually enclosed in kapton tape to hold the samples in position during an irradiation run, this reduces the air flow over the samples and as the mini heater is attached to the sensor, the bag is used to study the maximum temperature with different fan settings. A maximum temperature increase of 77°C is observed with minimal air flow or, 46°C with maximal insulation but using the highest fan setting. In the best case scenario, when the sensor has full exposure to air with no insulating bag, and using

the highest fan speed setting, a temperature increase of 25 °C is measured. Therefore, to reduce the temperature increase during irradiation, the highest fan speed must be used to ensure good air flow, and the amount of kapton tape used to mount the sample must be reduced.

The in-beam temperature of sensors during an irradiation is very difficult to measure as when PT1000 sensors are placed in the beam and irradiated by protons, they heat up due to the energy deposited by the traversing beam. This results in larger temperature readings than experienced by the sensor alone. Whilst the maximum temperature on the sensor is unknown, it is clear that the cooling capacity of the glycol system is not ideal for a cyclotron beam. To reduce the temperature within the box and therefore on the samples, the system is required to remove more heat, or the baseline temperature within the box must be reduced by 25-50 °C, depending on how insulated the samples are, to maintain sub-zero temperatures.



(a) Temperature measurements with a bag covering the samples.

(b) Temperature measurements with full exposure.

Figure 9.5: Temperature tests with different running configurations with a 1 μA simulated beam currents using the miniheater, starting at room temperature in a dummy cold box. Fan 0 corresponds to no fan, and fan 1, 2, 3 correspond to slow, medium and high fan speeds.

9.3 Development of an improved cooling system

In order to develop a new cooling system and upgrade the thermal chamber, a prototype system was designed using an evaporative cooling technique with liquid nitrogen. A schematic of the prototype cooling system is shown in Figure 9.6 and was first tested independently of the scanning system in the dummy box, constructed using Dow Styrofoam, the same material as the initial cold box [96]. Whilst the material from the glycol cold box was coated in 0.8 mm thick aluminium and 0.2 mm thick formica, for the dummy box, the styrofoam remained exposed to observe any structural damage that may be caused by the liquid nitrogen (LN2). A Norhof liquid nitrogen dispensing system [111] was used along with the mini heater described in Section 9.2 to simulate

the beam current. Temperature tests were again performed to determine whether the fan speed or use of insulating kapton tape had an effect on the heat dissipation or air flow over the samples and therefore the maximum temperature on the sensors. The requirement of the improved system is to maintain sub-zero temperatures on the sensor during an irradiation without reducing the beam current, which would result in significant increases to the irradiation time.

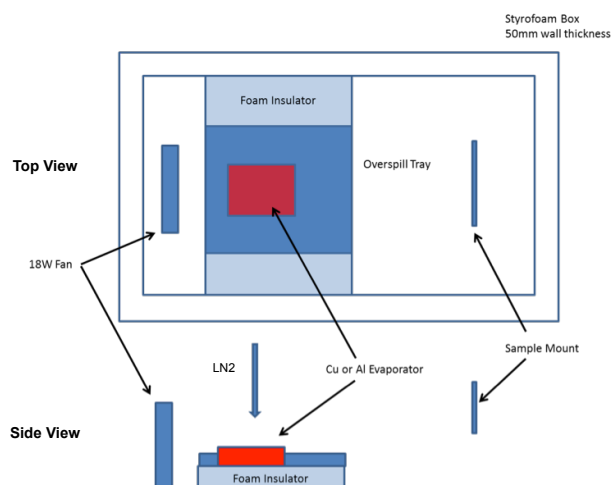


Figure 9.6: Prototype for the upgrades to the cold box implemented in the dummy cold box, using evaporative LN2 cooling to maintain sub-zero temperatures.

Initial tests of the capabilities of the LN2 showed that a stable temperature of $-48\text{ }^{\circ}\text{C}$ could be achieved within the cold box in 7 minutes, see Figure 9.7, and after repeatedly immersing the dummy cold box in LN2 to test the integrity of the materials, other than some cracking of the uncoated foam which recovered extremely quickly, no damage was observed.

The LN2 cooling system is designed to use evaporative cooling by dripping LN2 on to a metal heat sink within the box. The heat sink is placed in an overspill tray and is thermally isolated from the bottom of the box to avoid damage from direct contact with the LN2. A fan is again used to circulate the cold gas. Temperature tests were performed with the new setup using the prototype cold box and results are presented in Figure 9.8. Different simulated currents are applied using a series of mini heaters attached directly to a sensor with a PT1000 glued to the back and temperature measurements were performed when the LN2 system was in operation. The temperature increases with current and whilst a large temperature increase is measured when a simulated beam current of $2\text{ }\mu\text{A}$ is applied, the baseline temperature has been reduced by $40\text{ }^{\circ}\text{C}$ compared to the glycol system, and therefore, limiting the beam current to $1\text{ }\mu\text{A}$, the sensor maintains sub-zero temperatures during irradiations.

Several improvements were made to the thermal chamber and the mounting procedure to maximise air flow and minimise the temperature on the sensor based on the temperature studies out of the

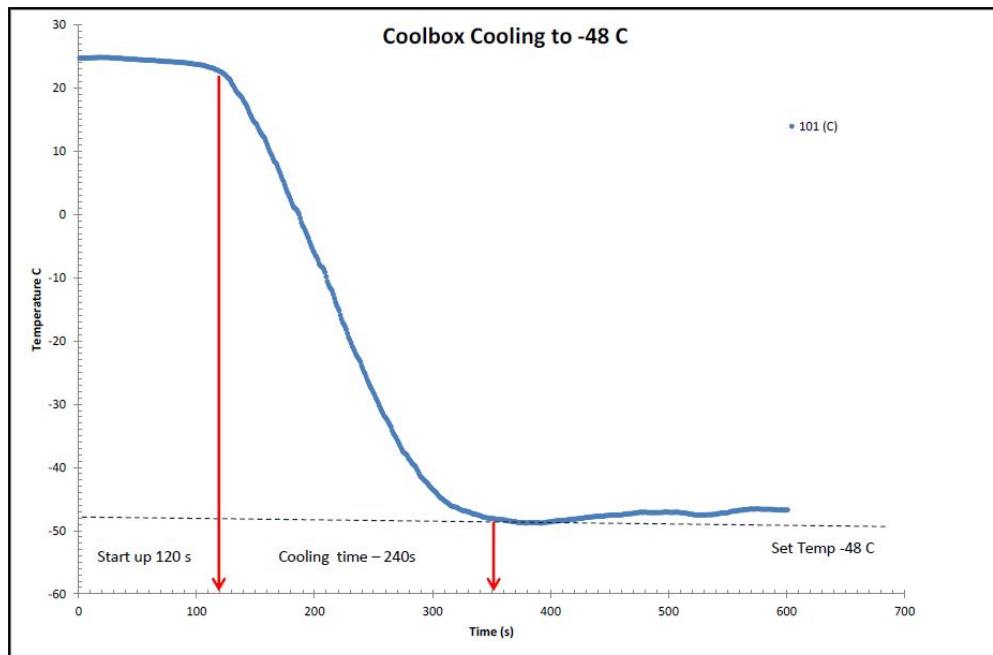


Figure 9.7: The LN2 system cool down to -48°C as a function of time from. The LN2 system was started at 120 s at room temperature and measurements were taken until a stable temperature was achieved.

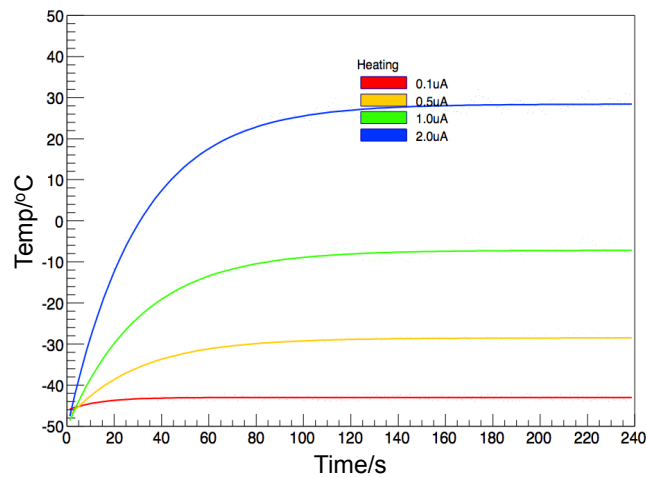


Figure 9.8: Temperature measurements, simulating different beam currents using a mini heating and the LN2 cooling system within the prototype cold box.

beam. A ramp was installed at the bottom of the cold box, beneath the sample mount, to allow LN2 to be directed on to the samples to maintain good air flow, quickly removing heat from the samples. In addition to this, square recesses, in to which 1 cm^2 mini sensors can fit, have been added to the CF mini frames to reduce the amount of kapton tape needed to secure the samples, shown in Figure 9.9. This allows more exposure to the cold nitrogen gas in order to maintain sub-zero temperatures on

the sensors. The cold box has been made with a larger volume and window size, to allow irradiations of larger samples, and a more powerful fan, which operates at temperatures as low as -50°C , has been installed.

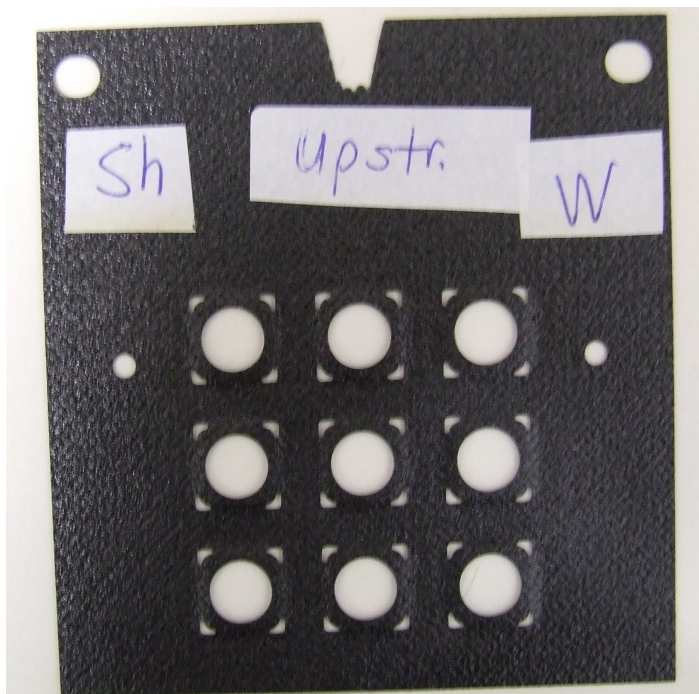


Figure 9.9: New carbon fibre mini sensor frame with square recesses to allow more airflow and less kapton tape to secure the sensors in the frame.

9.4 Commissioning of the LN2 system

The run procedure has been adjusted to account for the upgrades to the cooling system and cold box. With a shorter cool-down time, preparation time is reduced which allows longer irradiations to be performed, enabling higher fluence irradiations or a lower beam current to be used. With the LN2 system, the box must also be purged with dry nitrogen before, as well as after a run, to prevent any condensation from the exposure to warm air which could damage the sensors if moisture builds up on the surface. This increases the wait time prior to a run, as approximately ten volume changes of the cold box are required to ensure the system is fully flushed. Adjustments to the mounting procedure have also been implemented to allow the samples maximum exposure to cool air. Less kapton tape has been used, and as a replacement, string has been introduced to hold sensors in position.

Several studies have been performed to determine the optimal running procedure to ensure sensors are not damaged during irradiation. These are discussed in the following subsections.

9.4.1 Scan speed

Initially, changes to the scan speed have been studied. Using the glycol system, an x-velocity of 1 mm s^{-1} was used as default to irradiate samples. At this velocity, the beam will be incident on a $1 \text{ by } 1 \text{ cm}^2$ sensor for 20 s, depositing 1.1 W with a $1 \mu\text{A}$ beam current. This results in an increase in temperature, and to determine a suitable scan speed where the maximum temperature on the sensor is below the annealing threshold, temperature measurements have been performed.

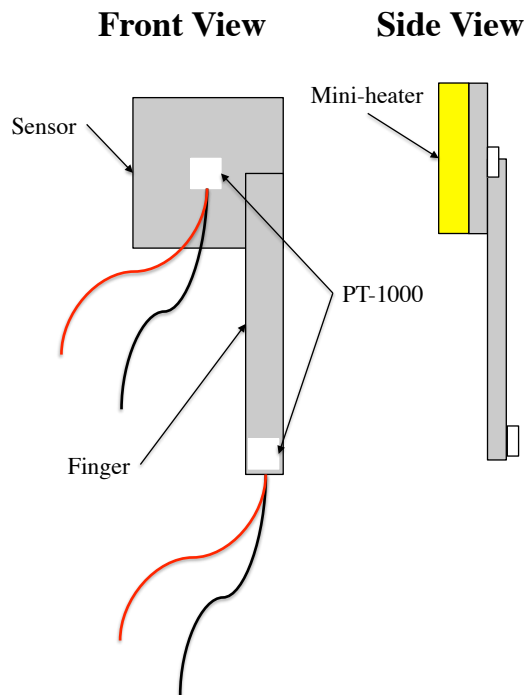


Figure 9.10: Silicon finger glued to sensor with PT1000s attached in the centre of the sensor and the end of the finger, to perform in-beam temperature measurements. Left: Front view with finger overlapping by 0.5 cm on $1 \times 1 \text{ cm}^2$ sensor. Right: Side view with mini-heater.

As already discussed, the in-beam temperature measurements of the sensor using a PT1000 are very difficult, therefore an alternative temperature measurement method has been developed using a thin finger of silicon, which is identical to the sensor. The finger is glued to the sensor with an overlap of 0.5 cm , as illustrated in Figure 9.10, and PT1000 sensors are glued to both the centre of the sensor and the end of the finger, placing the sensor in the top right position of the mini frame. Several scanning speeds were tested; 1 mm s^{-1} , 2 mm s^{-1} , 4 mm s^{-1} , 8 mm s^{-1} , and scanned over three times. This corresponds to three well separated temperature peaks at low speeds, where the increase in temperature of the sensor corresponds to the beam traversing the sensor for three scans. The time the beam is incident on the sensor is 20 s for a speed of 1 mm s^{-1} . At this speed, the sensor is able to cool down when the beam is traversing the rest of the frame and before the next scan of the beam across the sensor. At higher speeds, such as 4 mm s^{-1} , the temperature peaks become broader

and less resolved for each scan. This is demonstrated in Figure 9.11, and the short time between scans does not allow the sensor to cool, and results in the peaks overlapping, where the first scan is a shoulder.

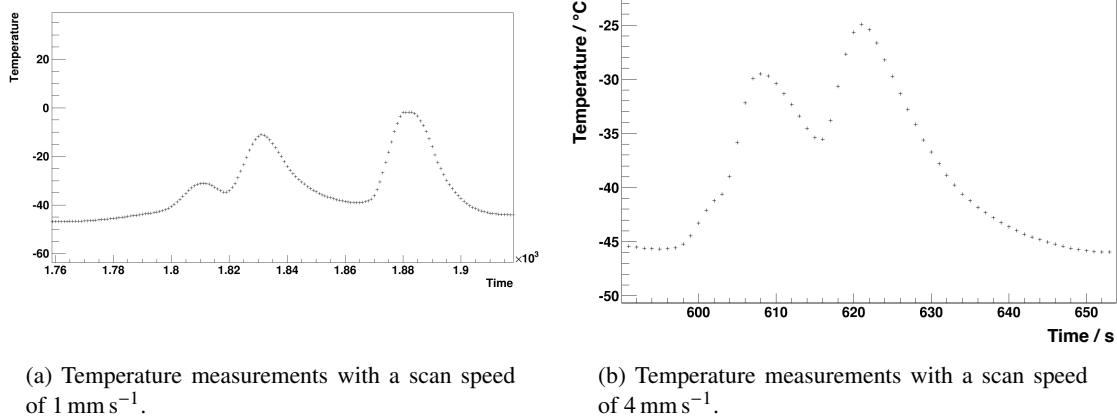


Figure 9.11: Temperature measurements of the silicon sensor using PT1000 on the finger during an irradiation using different x-velocities [98].

Overall, the temperatures measured at higher speeds are lower than those measured at the default x-velocity, however at higher speeds, the sensors are exposed to the beam for more runs to achieve the same target fluence. To minimise the temperature increase, a scan speed of 4 mm s^{-1} has been used, whereby a measured increase of approximately 20°C is measured in Figure 9.11b.

9.4.2 Temperature Model

The temperatures presented in Figure 9.11 are the temperatures measured on the PT1000 positioned on the finger during the irradiation. However, to determine the exact temperature on the sensor, thermodynamic modelling has been used to calculate the temperature difference between the PT1000 on the sensor and the PT1000 on the finger. The model has been used to simulate the temperatures during an irradiation and can be compared with experimental results. The model suggests that the maximum temperature at an x-velocity of 4 mm s^{-1} is -12°C with a beam current of $1 \mu\text{A}$, which is a temperature increase of 36°C . The simulated temperature curves of the finger and the sensor as predicted by the model are presented in Figure 9.12 and compared to temperature measurements of the finger during an irradiation.

Temperature measurements of the finger, set up as in Figure 9.10 have been used to develop a thermodynamic model based on heat transfer from the beam to the attached mini sensor. The model has allowed simulations of an irradiation, predicting the temperature experienced by a solitary finger and by a sensor. Figure 9.12 presents in red the temperatures of a simulated irradiation experienced

by a sensor which is positioned in the top left hand corner of a mini frame, as in Figure 8.7. On pass 1 of the beam, it experiences a temperature peak, then pass 2 and 3 are consecutive resulting in two overlapping peaks. The solo finger model in blue is the predicted temperature experienced by a finger, where the finger is placed in the top right position of the mini frame. The first pass of the beam is followed by the second, with two overlapping peaks in temperature. The third pass then corresponds to a final single peak. The finger model is compared to temperature measurements collected during an irradiation of a finger and the agreement between them allows the model to be used to predict the temperature experienced by sensors in different irradiations.

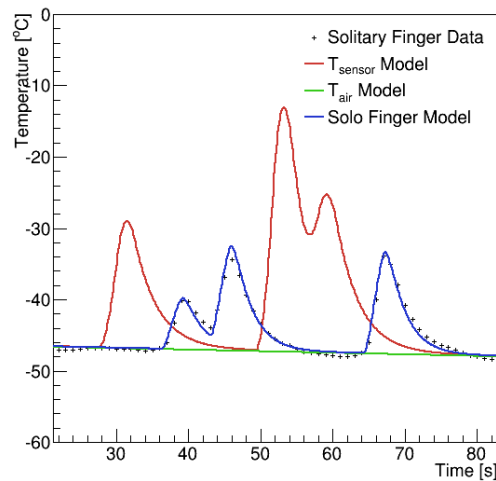


Figure 9.12: Temperature measured using the PT1000 on the finger, compared with simulated temperatures of the finger and the sensor using thermodynamic modelling. The finger predicted and measured temperatures are in excellent agreement [112].

Using the model, the temperature on the sensor can be estimated at different x -velocities and beam currents. Figure 9.13 presents the temperature measurements at 4 mm s^{-1} using different beam currents when the temperature within the cold box is -30°C . A maximum temperature of 6°C is observed using a beam current of $1 \mu\text{A}$, with a temperature increase of 36°C in agreement with Figure 9.13, and the temperature difference increases with beam current, as expected.

In summary, the model suggests that a maximum temperature of -12°C is experienced by the sensor when irradiated at 4 mm s^{-1} with a beam current of $1 \mu\text{A}$, or 6°C if the cold box temperature is increased from -50°C to -30°C . These temperatures experienced by the sensors should not cause annealing effects, and therefore other damage mechanisms should be considered.

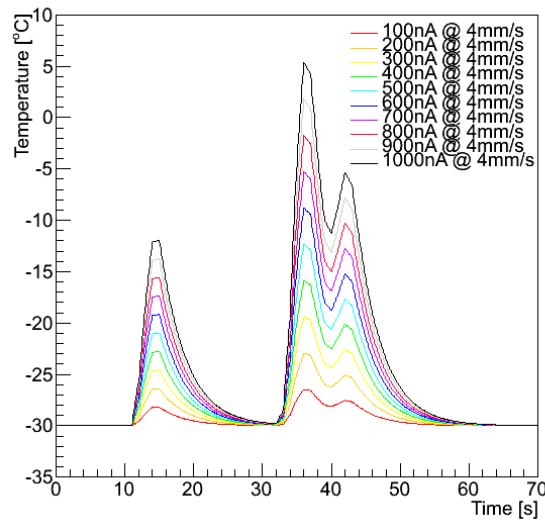


Figure 9.13: Estimated temperature of the sensor using the thermodynamic model, simulating an x-velocity of 4 mm s^{-1} with different beam currents [112].

9.4.3 Beam current studies

Using a scan speed of 4 mm s^{-1} , irradiations of ATLAS12 sensors were performed using different beam currents, irradiated to a fluence of $5 \times 10^{14} \text{ 1 MeVn}_{eq} \text{ cm}^{-2}$. Studies of ATLAS12 sensors have observed that most irradiated sensors experience no breakdown up to bias voltages of 1000 V [61]. Charge collection measurements were made of each sensor and compared in Figure 9.14. The shape of the signal is as expected and pre-annealing the charge collection of irradiations at all three beam currents are very similar. Post-annealing however, the charge collection drops when it should increase after some of the damage is recovered.

The charge collected is shown to be independent of the beam current with these results, which provides further evidence that the damage is not caused by a heating effect. Cluster size measurements performed during charge collections indicate that the decrease in signal post-annealing correlates with increased broadness of clusters. This means that an increased number of strips are required to collect the signal, suggesting that the effect may be due to surface damage, accumulating charge on the surface and degrading the signal.

9.4.4 Diode studies

To determine whether the damage to the sensors is the result of surface damage, a diode, a simple p-n junction with no oxide layer, was irradiated. The charge collection measurements are presented

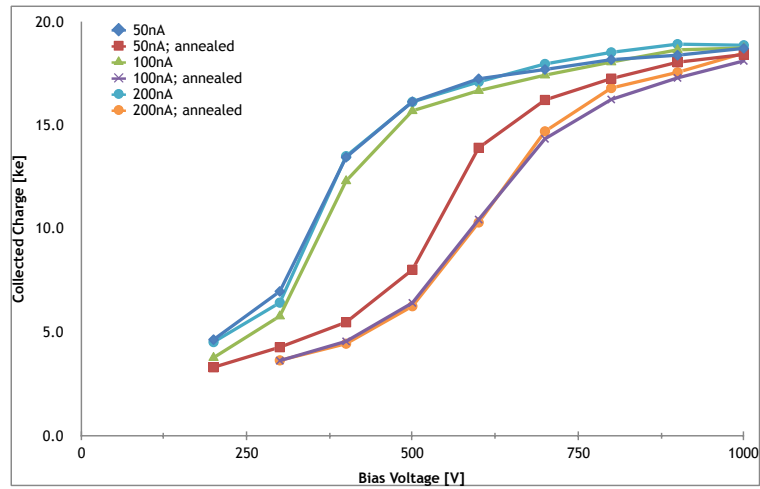


Figure 9.14: Charge collection measurements of sensors irradiated to $5 \times 10^{14} \text{ 1 MeVn}_{eq}\text{cm}^{-2}$ with an x-velocity of 4 mm s^{-1} and different beam currents [113, 88].

in Figure 9.15 and using a beam current of 200 nA, the charge collection is the expected shape with an increase in signal post-annealing. The 500 nA charge collection pre-annealing is similar to the annealed 200 nA results, suggesting that this sensor was annealed during irradiation. However, the signal distributions of both sensors are more consistent with the expected shape than the irradiated strip sensors.

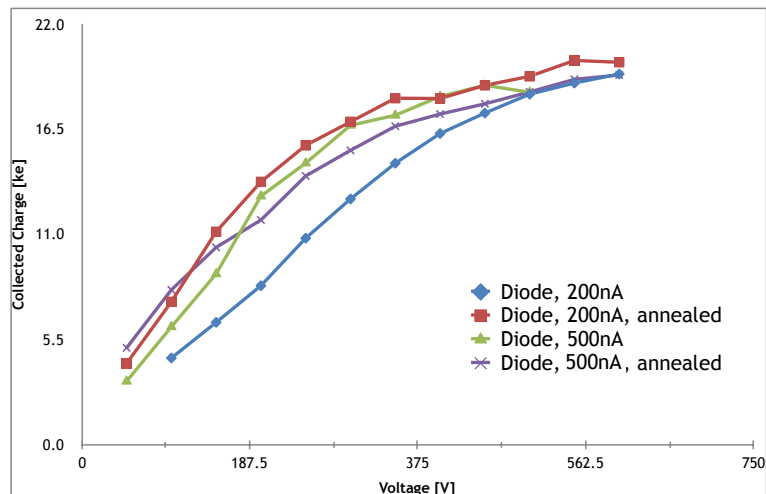


Figure 9.15: Charge collection measurements of a diode irradiated to $5 \times 10^{14} \text{ 1 MeVn}_{eq}\text{cm}^{-2}$ using two different beam currents of 200 and 500 nA both before and after annealing [113, 88].

9.4.5 Energy of cyclotron proton beam

To establish the cause of the damage, the energy of the proton beam has been measured 1 m downstream of the beam pipe, applying corrections for the energy loss in the beampipe window and the intervening 1 m of air. As shown in Figure 9.16, the energy peaks at 26.85 MeV with a spread of 0.15 MeV. This is in agreement with the expected energy of 27 MeV, for which the NIEL factor has been applied to calculate the fluence received. However, due to the large separation between the beam pipe and the apparatus, it is possible that low energy protons have been absorbed by air and therefore are not observed in Figure 9.16 yet are incident upon sensors during irradiations.

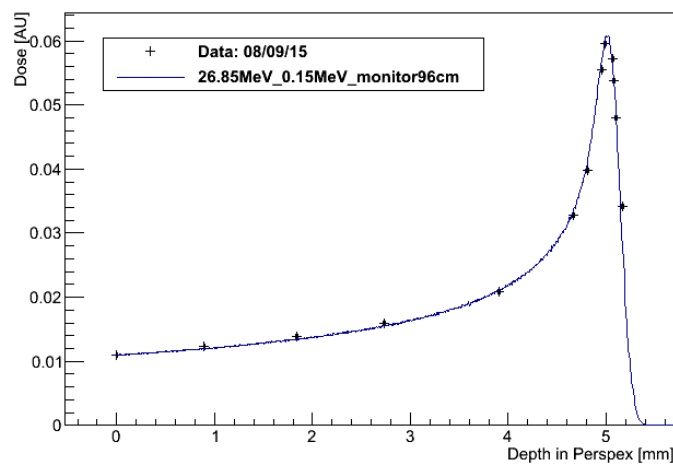
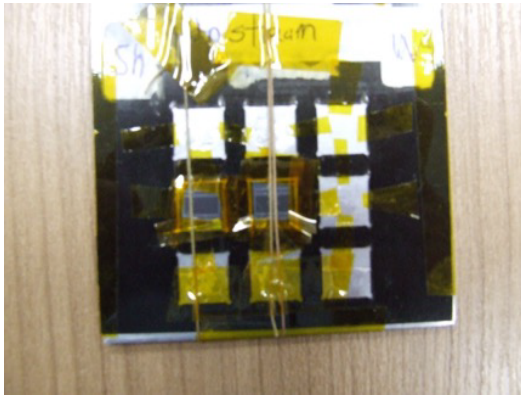


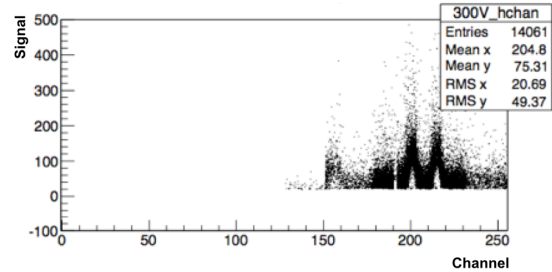
Figure 9.16: Bragg peak of cyclotron 27 MeV proton beam [114].

As described previously, to improve the air circulation on the sensors, the amount of kapton tape used to mount the samples was reduced. The frames were designed with square recesses and the corners of the sensors were secured in place with kapton, whilst one face of the sensor was fully exposed. To ensure that the sensors did not move during the irradiation scan 270 μm diameter string was incorporated, as shown in Figure 9.18a, and during charge collection measurements, the channels which correspond to the position of the string show an increase in signal, shown in Figure 9.18b. The increase in signal is more consistent with expected results and suggests that low energy particles for these channels are stopped by the string. This effect however was not observed using Nickel activation foils in front of the sensors during irradiations as the 25 μm Nickel activation foils only stop protons of energy less than 0.05 MeV.

In order to test this theory, an additional sensor was mounted upstream of the sensor to be irradiated. The two sensors are identical, 300 μm ATLAS12 sensors, and the string has been removed, using kapton tape to fully secure the sensors. The “camel” effect is no longer observed and the signal collected on the additional sensor, closest to the beam, is lower than the shielded sensor. This is again



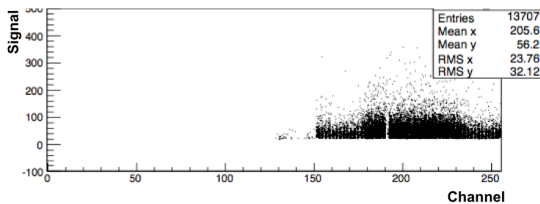
(a) Mounted sensors using minimal kapton tape and 270 μm string.



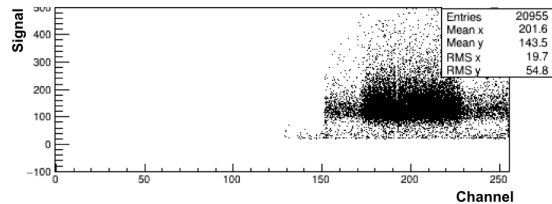
(b) Signal collected corresponding to the irradiated sensor in the middle position.

Figure 9.17: Mounting the sensors using 270 μm string results in a “camel” effect with a double hump, where low energy particles have been absorbed, collecting more signal during charge collection measurements [114].

a strong indication that the low energy protons are stopped by the first sensor, which cause lower collected signal, and the signal collected by the second sensor, which is irradiated with 27 MeV protons with no low energy contamination, is more consistent with expectation.



(a) Additional sensor mounted in position closest to the beam, usually the foil position, directly in front of sensor to be irradiated.



(b) Sensor mounted in default position, shielded by an additional sensor.

Figure 9.18: Signal hitmaps for charge collection measurements of a sensor positioned in the foil mounting position, close to the beam and directly in front of a sensor to be irradiated which is consequently shielded [114]. The shielded sensor collects a higher charge than the additional sensor, which absorbs low energy particles.

To derive a suitable mounting procedure which provides an irradiation result consistent with other facilities, several possible configurations have been tested, irradiating under the same conditions. A 300 μm aluminium foil is used in place of the additional sensor, to absorb low energy particles and the four configurations are described in Table 9.1, corresponding to the setup in Figure 9.19 and all sensors are irradiated to a fluence of 5×10^{14} $1 \text{ MeVn}_{eq}\text{cm}^{-2}$.

The charge collection measurements before and after annealing are presented in Figure 9.20 and irradiations performed with the aluminium foil show an increase in collected charge with respect to

	Sensor 1	Sensor 2	Sensor 3	Sensor 4
Enclosed with kapton	✓	✓	X	X
Nickel foils	✓	X	X	✓
300 μm aluminium absorber	✓	X	✓	X

Table 9.1: Different configurations of test irradiations to determine the optimal layout [114]. Corresponding to the setup in Figure 9.19.

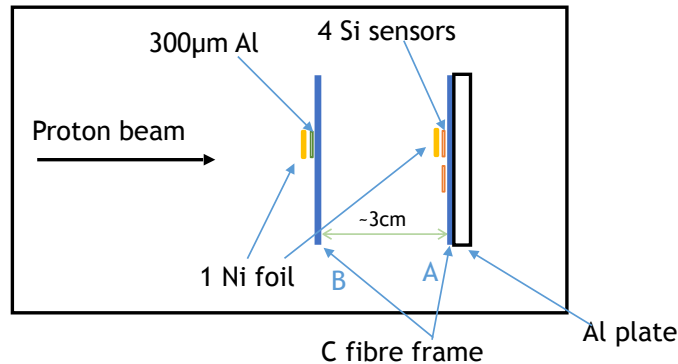


Figure 9.19: Setup of mounting for Birmingham irradiations to be used with different configurations to determine the optimal layout [114].

the sensors without the aluminium and also the charge collected increases further after annealing at 60 °C for 80 min, as expected.

A summary of charge collection measurements from irradiations at different facilities and measurements at different sites is presented in Figure 9.21. There is good agreement of the charge collection measurements of Sensors 1 and 3 (with the aluminium absorber) in Figure 9.20 to irradiations of $5 \times 10^{14} \text{ 1 MeV}_{n_{eq}}\text{cm}^{-2}$ performed at other irradiation facilities in Figure 9.21.

9.5 Summary

An irradiation facility has been commissioned using the MC40 Birmingham cyclotron based on the CERN PS system, to perform proton irradiations of materials to HL-LHC fluences. Early irradiations of pixel sensors indicated that annealing occurred during irradiation and that the cooling capacity of a glycol chiller system was not sufficient to maintain sub-zero temperatures on sensors during irradiations with a cyclotron beam.

Developments to the cooling system, in favour of a LN2 system using evaporative cooling were studied. Out of beam temperature tests using a prototype system achieved $-48 \text{ }^\circ\text{C}$ within the cool

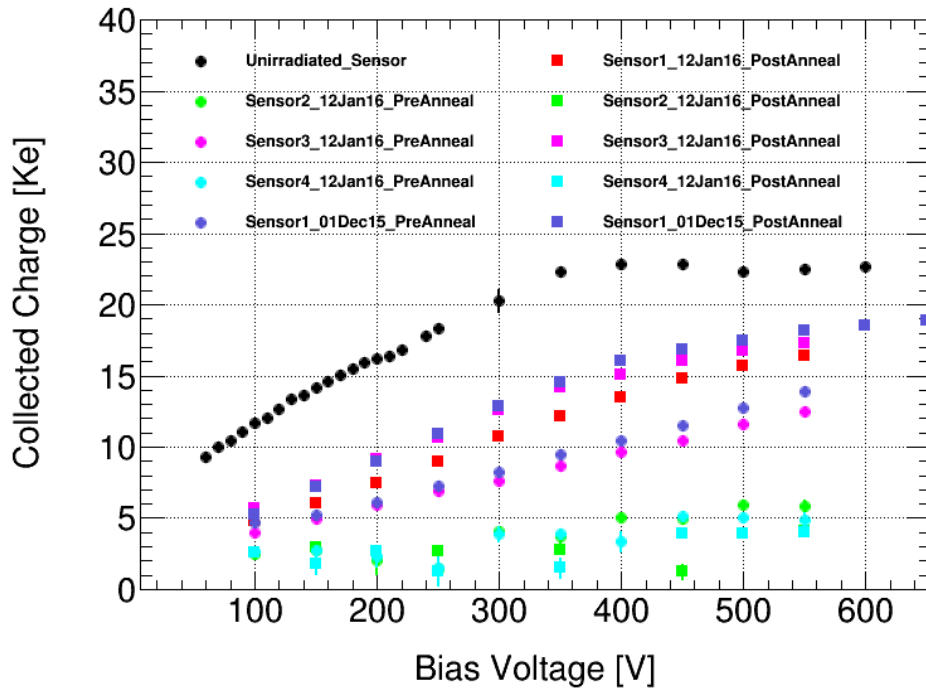


Figure 9.20: Charge collection measurements comparing sensors irradiated using different mounting configurations. Sensor1_01Dec15 (purple) corresponds to the shielded sensor and Sensor1 to 4 correspond to the configurations in Table 9.1 [114].

box and simulations of a beam current using a mini-heater indicated that this was capable of maintaining sub-zero temperatures during irradiations.

After installation of the upgraded cooling system, initial irradiations were performed to determine the optimal run conditions to prevent annealing due to over-heating. A thermodynamic model was developed, simulating the temperature on the sensor during irradiations and comparing to in-beam temperature measurements. Results indicated that the maximum temperature on the sensors during irradiations is -12°C at a beam current of $1\ \mu\text{A}$ with an x -velocity of $4\ \text{mm s}^{-1}$, eliminating temperature induced annealing effects.

Irradiations of ATLAS12 mini sensors at different beam currents showed agreement in charge collection before annealing and the discrepancy in the annealing results has been attributed to the broadening of clusters. This suggests that the damage is caused by surface effects and irradiations of diodes show improved charge collection results compared to the ATLAS12 strip sensors.

Finally, after unusual charge collection measurements were observed, where signal distribution varied over the sensor due to shielding from $270\ \mu\text{m}$ string, used to mount the sensors, it was suggested that the proton beam incident on the sensors, was contaminated by low energy particles. This con-

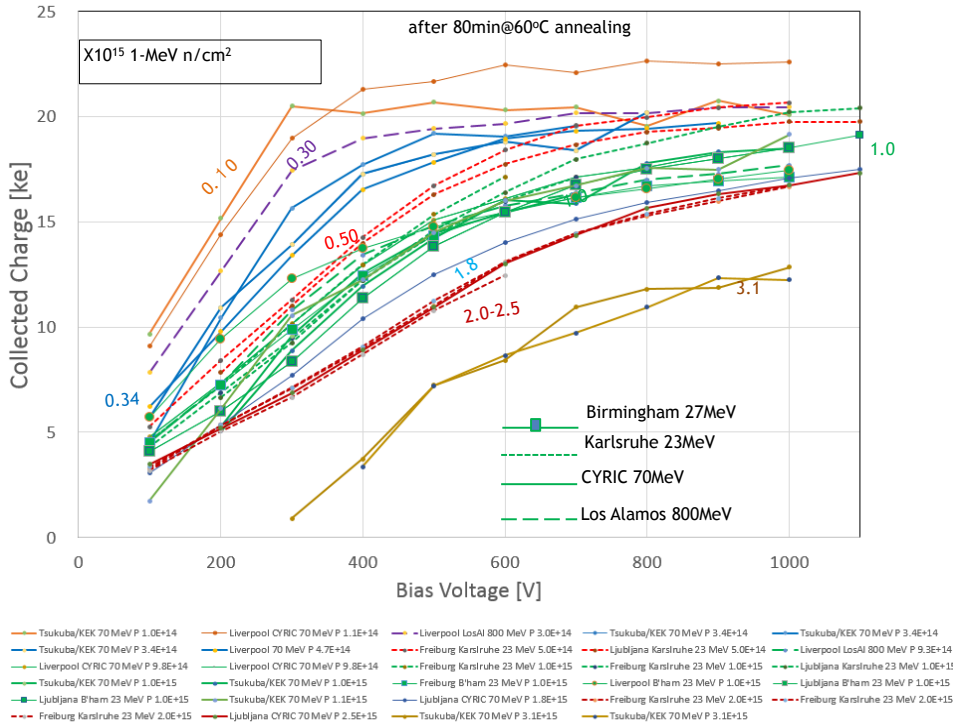


Figure 9.21: Charge collection measurements of ATLAS12 sensors irradiated at different proton facilities [104].

tamination was observed to be responsible for the charge collection results and introducing a 300 μm absorber material in front of the sensors to be irradiated, produces sensors with behaviour consistent with expectation, and in agreement with other facilities.

Further studies to fully qualify the facility are immediate. However, the procedure and different techniques have been explored and a configuration has been determined to perform stable irradiations, which are in agreement with irradiations performed at other facilities.

Chapter 10

Summary

This thesis consists of a number of studies using electrons and photons with the ATLAS detector. A new, novel reconstruction algorithm for electrons is described in Chapter 4, providing potential improvements to the energy resolution in the calorimeter by using a topological-based clustering algorithm to build superclusters. With an increase in pile-up events, excellent reconstruction efficiency and understanding of the EM calorimeter is essential and using a dynamic, as opposed to a fixed-size window, should enhance the pile-up robustness of electron reconstruction for future increases in luminosity. Chapter 6 studies the calorimeter shower profiles of electrons with 13 TeV data and the observation of $\pi^0 \rightarrow \gamma\gamma$ decays with the first 13 TeV data. The calorimeter shower shapes in data are compared with Monte Carlo distributions and a good agreement is observed.

A search for an additional heavy Higgs state in the decay via dibosons to four-leptons is described in Chapter 5. This search has used 20.3 fb^{-1} of 8 TeV data and no significant excesses were observed. The 95% CL_s upper limits for the cross-section of heavy Higgs production in the ggF and VBF channel have been derived, independent of a model in the Narrow Width Approximation.

A significant amount of work in this thesis is focused on the Birmingham Irradiation Facility. In preparation for the HL-LHC, materials are irradiated to high fluences in order to determine their performance and durability in this environment. The facility has been developed to use a cyclotron to irradiate to HL-LHC fluences within a short time-scale using a robotic scanning system to move samples within a thermal chamber, through the fixed beam spot. Chapter 7 describes the planned upgrades to the LHC and detector characterisation techniques, Chapter 8 outlines the Birmingham Irradiation Facility, irradiation procedure and a brief overview of other facilities and Chapter 9 presents results from irradiations, upgrades to the system and tests performed to understand the proton beam. Final qualification of the facility is underway, aiming to finalise the run procedure with expert understanding of the facility and its performance.

It is an exciting time for physics, with the LHC in Run-II operation. Protons are collided at a centre of mass energy of 13 TeV which enhances the cross-section of many SM and BSM processes, allowing further precision measurements and probing unexplored regions of parameter space. Preparation for LHC upgrades are also underway, with the layout and materials to be used for the ATLAS de-

tector during Phase-II operation being finalised. The full potential of the LHC has not yet been met, and as more data is collected, probing new frontiers, a more complete model of the fundamental forces and particles of nature can be achieved.

Appendix A

Heavy Higgs search in the Higgs to four-lepton channel Additional Material

A.1 Signal Samples for the Heavy Higgs search in the $H \rightarrow ZZ \rightarrow 4\ell$ channel

The signal samples used in this analysis are as follows (all using NWA unless specified) [49]:

Gluon-Gluon Fusion (ggF) Samples:

- $140 < m_H \leq 200$ GeV in steps of 10 GeV
- $200 < m_H \leq 300$ GeV in steps of 20 GeV
- $300 < m_H \leq 600$ GeV in steps of 20 GeV
- $600 < m_H \leq 1000$ GeV in steps of 50 GeV

Vector Boson Fusion (VBF) Samples:

- $140 < m_H \leq 200$ GeV in steps of 10 GeV
- $200 < m_H \leq 300$ GeV in steps of 20 GeV
- $300 < m_H \leq 1000$ GeV in steps of 25 GeV
- $600 < m_H \leq 1000$ GeV in steps of 50 GeV

Associated Production (ZH & WH) Samples: NB - the WH and VH samples use the SM width.

- $140 < m_H \leq 200$ GeV in steps of 5 GeV, with SM width.

- $200 < m_H \leq 400$ GeV in steps of 20 GeV, with SM width. NB, for WH there is a problem with the 400 GeV sample and it cannot be used.
- Contribution for $m_H > 400$ GeV is negligible.

A.2 NWA Limits for the Heavy Higgs search in the $H \rightarrow ZZ \rightarrow 4\ell$ channel

m_H [GeV]	Limit on ggF $\sigma \times BR (H \rightarrow ZZ)$ [fb]						m_H [GeV]	Limit on ggF $\sigma \times BR (H \rightarrow ZZ)$ [fb]					
	Obs.	-2σ	-1σ	Exp.	$+1\sigma$	$+2\sigma$		Obs.	-2σ	-1σ	Exp.	$+1\sigma$	$+2\sigma$
140	188	459	315	215	155	115	360	155	314	216	148	107	79
145	184	472	325	217	157	117	365	158	307	211	145	105	78
150	239	425	291	197	142	106	375	208	295	202	139	100	75
155	236	374	255	181	131	97	380	242	290	198	135	98	73
160	144	385	262	178	128	96	385	250	283	193	133	96	71
165	317	389	265	178	128	95	390	212	278	190	130	94	70
170	215	370	253	175	126	94	395	141	273	186	127	92	68
175	169	397	273	192	138	103	400	109	270	183	125	90	67
180	174	469	328	225	162	121	405	117	262	178	122	88	66
185	219	545	384	267	192	143	410	128	258	175	120	87	65
190	514	603	427	300	216	161	415	130	254	172	118	85	63
195	529	633	448	319	230	171	420	137	249	168	114	82	61
200	330	660	470	329	237	176	425	135	247	166	113	82	61
205	265	654	464	328	236	176	430	111	244	164	112	80	60
210	210	643	455	323	233	174	435	97	240	162	110	79	59
215	385	626	442	314	227	169	440	101	237	160	108	78	58
220	375	613	434	304	219	163	445	100	233	157	107	77	57
225	209	606	429	302	218	162	450	94	229	154	105	75	56
230	248	582	411	292	210	156	455	86	226	152	103	74	55
235	252	569	402	285	205	153	460	75	224	150	102	73	55
240	244	551	389	273	197	146	465	68	221	148	101	72	54
245	192	545	384	271	195	145	470	64	219	146	99	72	53
250	186	518	364	258	186	138	475	63	216	144	98	71	53
255	249	507	356	251	181	135	480	61	215	143	97	70	52
260	289	486	341	238	171	128	485	60	212	141	96	69	51
265	349	477	334	236	170	127	490	58	209	139	94	68	51
270	338	469	328	231	167	124	495	56	206	137	93	67	50
275	268	458	321	226	163	121	500	57	203	135	91	65	49
280	194	444	310	216	155	116	505	59	201	133	90	65	48
285	192	435	304	213	153	114	510	61	199	132	89	64	48
290	219	424	295	207	149	111	515	62	197	130	88	63	47
295	236	415	289	202	146	109	520	63	194	128	86	62	46
300	264	409	285	197	142	106	525	64	192	126	85	61	46
305	257	403	280	196	141	105	530	70	189	125	84	60	45
310	178	391	272	190	137	102	535	80	187	123	83	60	44
315	119	381	265	185	133	99	540	98	184	121	81	58	44
320	108	373	259	178	128	96	545	109	183	120	81	58	43
325	108	366	253	176	127	95	550	106	182	119	80	58	43
330	106	358	248	172	124	92	555	98	181	118	80	57	43
335	123	349	241	167	121	90	560	89	179	117	78	56	42
340	154	340	235	162	117	87							
345	140	334	230	159	114	85							
350	120	326	225	155	112	83							
355	131	320	220	152	109	81							

Table A.1: Expected and observed ggF limits on $\sigma \times BR (H \rightarrow ZZ)$ in fb (1/2)

m_H [GeV]	Limit on ggF $\sigma \times BR (H \rightarrow ZZ)$ [fb]						m_H [GeV]	Limit on ggF $\sigma \times BR (H \rightarrow ZZ)$ [fb]					
	Obs.	-2σ	-1σ	Exp.	$+1\sigma$	$+2\sigma$		Obs.	-2σ	-1σ	Exp.	$+1\sigma$	$+2\sigma$
							790	74	129	81	53	38	28
							795	76	128	80	52	38	28
580	66	172	112	75	54	40	800	77	126	79	51	37	28
600	49	164	107	71	51	38	805	79	127	79	52	37	28
605	47	164	106	71	51	38	810	79	126	78	51	37	28
610	46	163	105	70	51	38	815	79	125	78	51	37	27
615	45	162	105	70	50	37	820	78	125	77	51	36	27
620	44	160	103	69	50	37	825	79	124	77	50	36	27
625	44	159	103	68	49	37	830	79	124	77	50	36	27
630	43	158	102	68	49	36	835	81	123	76	50	36	27
635	43	156	101	67	48	36	840	78	123	76	49	36	27
640	43	155	100	66	48	36	845	79	122	76	49	35	26
645	42	154	99	66	47	35	850	76	121	74	49	35	26
650	42	152	98	65	47	35	855	81	122	75	49	35	26
655	42	152	97	65	47	35	860	82	122	75	49	35	26
660	41	151	97	64	46	35	865	85	121	74	48	35	26
665	42	150	96	64	46	34	870	87	121	74	48	35	26
670	41	149	95	63	46	34	875	90	120	74	48	35	26
675	41	147	94	63	45	34	880	91	120	73	48	34	26
680	41	146	93	62	45	33	885	92	119	73	47	34	25
685	41	145	92	61	44	33	890	91	119	73	47	34	25
690	41	144	92	61	44	33	895	90	118	72	47	34	25
695	41	143	91	61	44	33	900	87	116	71	46	33	25
700	41	141	90	59	43	32	905	85	117	72	46	33	25
705	41	142	90	60	43	32	910	81	117	71	46	33	25
710	41	141	90	59	43	32	915	77	116	71	46	33	25
715	41	140	89	59	42	32	920	70	116	71	46	33	25
720	42	139	88	58	42	31	925	65	116	71	46	33	25
725	43	139	88	58	42	31	930	59	116	70	46	33	25
730	43	138	87	57	41	31	935	54	115	70	46	33	24
735	45	137	87	57	41	31	940	50	115	70	45	33	24
740	46	136	86	56	41	30	945	48	114	70	45	32	24
745	48	136	86	56	40	30	950	44	112	68	44	32	24
750	50	134	84	55	40	30	955	44	114	69	45	32	24
755	55	134	84	55	40	30	960	43	114	69	45	32	24
760	58	133	84	55	40	30	965	42	113	69	44	32	24
765	63	132	83	55	39	29	970	41	113	68	44	32	24
770	67	132	83	54	39	29	975	40	112	68	44	32	24
775	69	131	82	54	39	29	980	39	112	68	44	32	23
780	71	130	82	54	39	29	985	39	112	68	44	31	23
785	73	130	81	53	38	29	990	39	111	67	43	31	23
							995	38	111	67	43	31	23
							1000	38	109	66	43	31	23

Table A.2: Expected and observed ggF limits on $\sigma \times BR (H \rightarrow ZZ)$ in fb (2/2)

m_H [GeV]	Limit on VBF $\sigma \times BR (H \rightarrow ZZ)$ [fb]						m_H [GeV]	Limit on VBF $\sigma \times BR (H \rightarrow ZZ)$ [fb]					
	Obs.	-2σ	-1σ	Exp.	$+1\sigma$	$+2\sigma$		Obs.	-2σ	-1σ	Exp.	$+1\sigma$	$+2\sigma$
140	196	353	230	156	112	84	360	145	252	164	110	79	59
145	273	362	234	154	111	82	365	155	248	161	108	78	58
150	256	321	209	141	102	76	370	155	244	159	106	76	57
155	155	299	195	134	96	72	375	165	240	156	104	75	56
160	99	309	201	134	97	72	380	179	234	152	101	73	54
165	129	309	201	133	96	71	385	174	231	149	99	72	53
170	115	297	193	130	94	70	390	162	228	148	98	71	53
175	95	304	199	134	97	72	395	109	225	146	97	70	52
180	99	330	215	143	103	77	400	88	222	143	95	69	51
185	138	354	233	156	112	84	405	97	217	140	93	67	50
190	219	373	247	167	120	89	410	106	215	138	92	66	49
195	311	389	258	174	126	94	415	113	212	136	90	65	49
200	277	399	265	179	129	96	420	117	208	134	89	64	48
205	192	401	266	180	130	96	425	115	206	133	88	63	47
210	125	397	264	178	128	95	430	92	204	131	87	63	47
215	206	391	259	174	126	94	435	78	202	129	86	62	46
220	217	377	250	170	122	91	440	75	198	127	84	61	45
225	130	380	251	169	122	91	445	74	197	126	84	61	45
230	122	373	247	167	120	89	450	70	195	125	83	60	45
235	130	367	242	163	118	88	455	65	194	125	83	60	44
240	151	363	240	161	116	86	460	60	192	123	82	59	44
245	136	360	238	161	116	86	465	55	191	123	81	58	44
250	118	354	234	158	114	85	470	53	189	121	80	58	43
255	148	350	231	156	113	84	475	52	186	119	79	57	42
260	198	342	226	152	110	82	480	51	183	117	78	56	42
265	243	339	224	151	109	81	485	50	182	117	77	56	41
270	228	333	220	148	106	79	490	49	180	115	76	55	41
275	185	329	217	145	105	78	495	48	179	114	75	54	41
280	148	322	212	142	102	76	500	49	176	113	74	54	40
285	127	315	207	139	100	75	505	49	175	112	74	53	40
290	120	308	202	136	98	73	510	50	173	111	73	53	39
295	121	301	197	132	95	71	515	51	172	110	72	52	39
300	151	297	195	130	94	70	520	50	169	108	71	51	38
305	162	293	192	128	92	69	525	52	169	108	71	51	38
310	119	286	186	125	90	67	530	56	168	107	71	51	38
315	87	282	184	123	89	66	535	62	167	106	70	51	38
320	78	277	180	120	87	65	540	76	165	105	69	50	37
325	75	272	177	119	86	64	545	81	164	104	69	49	37
330	73	266	173	116	84	63	550	81	162	103	68	49	36
335	77	264	172	115	83	62	555	72	160	101	67	48	36
340	84	260	169	113	81	61	560	63	157	99	66	47	35
345	88	259	169	113	81	60							
350	87	257	168	112	81	60							
355	114	255	166	111	80	60							

Table A.3: Expected and observed VBF limits on $\sigma \times BR (H \rightarrow ZZ)$ in fb (1/2)

m_H [GeV]	Limit on VBF $\sigma \times BR (H \rightarrow ZZ)$ [fb]						m_H [GeV]	Limit on VBF [fb]					
	Obs.	-2σ	-1σ	Exp.	$+1\sigma$	$+2\sigma$		Obs.	-2σ	-1σ	Exp.	$+1\sigma$	$+2\sigma$
790							54	123	75	49	35	26	
795							55	122	75	49	35	26	
580	52	154	97	64	46	34	800	57	121	74	48	35	26
600	43	150	95	62	45	33	805	59	121	74	48	35	26
605	42	150	95	62	45	33	810	61	120	73	48	34	26
610	42	149	94	62	44	33	815	62	120	73	47	34	25
615	41	149	93	61	44	33	820	63	119	73	47	34	25
620	41	148	93	61	44	33	825	63	118	72	47	34	25
625	40	147	92	60	43	32	830	64	118	72	47	34	25
630	40	145	91	60	43	32	835	65	117	71	46	33	25
635	40	144	90	59	43	32	840	65	117	71	46	33	25
640	40	143	90	59	42	32	845	66	117	71	46	33	25
645	40	142	89	58	42	31	850	64	116	70	46	33	25
650	39	140	88	58	42	31	855	66	116	70	46	33	25
655	39	141	88	58	42	31	860	67	116	70	46	33	24
660	39	140	88	57	41	31	865	69	116	70	45	33	24
665	39	140	87	57	41	31	870	71	116	70	45	33	24
670	39	139	86	57	41	30	875	74	115	70	45	32	24
675	39	138	86	56	40	30	880	75	115	69	45	32	24
680	39	137	85	56	40	30	885	76	114	69	45	32	24
685	39	136	85	55	40	30	890	76	114	69	44	32	24
690	39	136	84	55	40	30	895	75	113	68	44	32	24
695	39	135	84	55	40	29	900	73	112	68	44	32	24
700	38	134	83	54	39	29	905	70	113	68	44	32	24
705	39	134	83	54	39	29	910	67	112	68	44	31	23
710	39	133	83	54	39	29	915	64	112	67	43	31	23
715	39	133	82	54	39	29	920	60	111	67	43	31	23
720	39	132	82	53	38	29	925	55	111	67	43	31	23
725	39	131	81	53	38	28	930	48	111	67	43	31	23
730	39	130	80	52	38	28	935	44	110	66	43	31	23
735	40	130	80	52	38	28	940	42	110	66	43	31	23
740	40	129	79	52	37	28	945	41	109	66	42	30	23
745	41	128	79	51	37	28	950	39	109	65	42	30	23
750	42	127	78	51	37	27	955	38	109	65	42	30	23
755	43	127	78	51	37	27	960	38	109	65	42	30	22
760	44	126	78	51	36	27	965	37	108	65	42	30	22
765	48	126	77	50	36	27	970	37	108	65	42	30	22
770	50	125	77	50	36	27	975	36	108	64	41	30	22
775	51	125	76	50	36	27	980	36	107	64	41	30	22
780	52	124	76	50	36	27	985	36	107	64	41	30	22
785	53	123	76	49	35	26	990	36	107	64	41	30	22
							995	35	107	64	41	30	22
							1000	35	107	63	41	29	22

Table A.4: Expected and observed VBF limits on $\sigma \times BR (H \rightarrow ZZ)$ in fb (2/2)

Bibliography

- [1] ATLAS Collaboration, *Observation of a new particle in the search for the Standard Model Higgs boson with the ATLAS detector at the LHC*, *Phys. Lett. B* **716** (2012) , [arXiv:1207.7214 \[hep-ex\]](https://arxiv.org/abs/1207.7214). <http://arxiv.org/abs/1207.7214>.
- [2] CMS Collaboration, *Observation of a new boson at a mass of 125 GeV with the CMS experiment at the LHC*, *Phys. Lett. B* **716** (2012) , [arXiv:1207.7235 \[hep-ex\]](https://arxiv.org/abs/1207.7235). <http://arxiv.org/abs/1207.7235>.
- [3] J. Beringer et al., *The Review of Particle Physics*, *Phys. Rev. D* **86** (2012) . <http://link.aps.org/doi/10.1103/PhysRevD.86.010001>.
- [4] D. Griffiths, *Introduction to Elementary Particles, 2nd, Revised Edition*. John Wiley & Sons, New York, USA, 1987.
- [5] LHCb Collaboration, R. Aaij et al., *Observation of the resonant character of the $Z(4430)^-$ state*, *Phys. Rev. Lett.* **112** (2014) no. 22, 222002, [arXiv:1404.1903 \[hep-ex\]](https://arxiv.org/abs/1404.1903).
- [6] LHCb Collaboration, R. Aaij et al., *Observation of J/ψ Resonances Consistent with Pentaquark States in $\Lambda_b^0 \rightarrow J/\psi K^- p$ Decays*, *Phys. Rev. Lett.* **115** (2015) 072001, [arXiv:1507.03414 \[hep-ex\]](https://arxiv.org/abs/1507.03414).
- [7] W. N. Cottingham and D. A. Greenwood, *An Introduction To The Standard Model of Particle Physics*. Cambridge University Press, 2007.
- [8] S. L. Glashow, *Partial-symmetries of weak interactions*, *Nuclear Physics* **22** (1961) no. 4, 579 – 588. <http://www.sciencedirect.com/science/article/pii/0029558261904692>.
- [9] S. Weinberg, *A Model of Leptons*, *Phys. Rev. Lett.* **19** (1967) 1264–1266. <http://link.aps.org/doi/10.1103/PhysRevLett.19.1264>.
- [10] A. Salam, *Weak and Electromagnetic Interactions*, *Conf. Proc.* **C680519** (1968) 367–377.
- [11] P. W. Higgs, *Broken symmetries, massless particles and gauge fields*, *Phys. Lett.* **12** (1964) 132–133.

- [12] P. W. Higgs, *Broken Symmetries and the Masses of Gauge Bosons*, *Phys. Rev. Lett.* **13** (1964) 508–509. <http://link.aps.org/doi/10.1103/PhysRevLett.13.508>.
- [13] F. Englert and R. Brout, *Broken Symmetry and the Mass of Gauge Vector Mesons*, *Phys. Rev. Lett.* **13** (1964) 321–323. <http://link.aps.org/doi/10.1103/PhysRevLett.13.321>.
- [14] G. S. Guralnik, C. R. Hagen, and T. W. B. Kibble, *Global Conservation Laws and Massless Particles*, *Phys. Rev. Lett.* **13** (1964) 585–587. <http://link.aps.org/doi/10.1103/PhysRevLett.13.585>.
- [15] J. Ellis, M. K. Gaillard, and D. V. Nanopoulos, *A Historical Profile of the Higgs Boson*, [arXiv:1201.6045](https://arxiv.org/abs/1201.6045) [hep-ph].
- [16] F. Halzen and A. D. Martin, *Quarks & Leptons: An Introductory course in Modern Particle Physics*. John Wiley & Sons, 1984.
- [17] G. Carrillo-Montoya, D. Charfeddine, S. Diglio, C. Gwilliam, S. Rompotis, R. Tanaka, T. Vickey, and W. Wagner, *Benchmarks for Heavy Higgs boson searches in the electroweak bosons decay channels in the ATLAS detector*, Tech. Rep. ATL-COM-PHYS-2014-258, CERN, Geneva, Mar, 2014. <https://cds.cern.ch/record/1692903>. ATLAS Internal Access Only.
- [18] ATLAS Collaboration, G. Aad et al., *The ATLAS Experiment at the CERN Large Hadron Collider*, *JINST* **3** (2008) S08003.
- [19] ATLAS Collaboration, A. Airapetian et al., *ATLAS detector and physics performance: Technical Design Report, 1*. Technical Design Report ATLAS. CERN, Geneva, 1999. <http://cds.cern.ch/record/391176>.
- [20] CERN, *CERN Accelerating Science*, <http://cern.ch>.
- [21] L. Evans and P. Bryant, *LHC Machine*, 2008. *JINST* **3** (2008) S08001.
- [22] F. Fayette, *Strategies for precision measurements of the charge asymmetry of the W boson mass at the LHC within the ATLAS experiment*. PhD thesis, Paris U., VI-VII, 2009. [arXiv:0906.4260](https://arxiv.org/abs/0906.4260) [hep-ex]. <http://inspirehep.net/record/823897/files/arXiv:0906.4260.pdf>.
- [23] ATLAS Collaboration, *Luminosity Public Results*, <https://twiki.cern.ch/twiki/bin/view/AtlasPublic/LuminosityPublicResults>. Accessed: 2016-03-02.

- [24] ATLAS Collaboration, *Alignment of the ATLAS Inner Detector and its Performance in 2012*, Tech. Rep. ATLAS-CONF-2014-047, CERN, Geneva, Jul, 2014.
<https://cds.cern.ch/record/1741021>.
- [25] ATLAS Collaboration, G. Aad et al., *Electron and photon energy calibration with the ATLAS detector using LHC Run 1 data*, *Eur. Phys. J. C* **74** (2014) no. 10, 3071, [arXiv:1407.5063](https://arxiv.org/abs/1407.5063) [hep-ex].
- [26] W. Lampl, S. Laplace, D. Lelas, P. Loch, H. Ma, S. Menke, S. Rajagopalan, D. Rousseau, S. Snyder, and G. Unal, *Calorimeter Clustering Algorithms: Description and Performance*, Tech. Rep. ATL-LARG-PUB-2008-002. ATL-COM-LARG-2008-003, CERN, Geneva, Apr, 2008. <http://cds.cern.ch/record/1099735>.
- [27] ATLAS Collaboration Collaboration, G. Aad et al., *Electron performance measurements with the ATLAS detector using the 2010 LHC proton-proton collision data*, *Eur. Phys. J. C* **72** (2011) no. arXiv:1110.3174. CERN-PH-EP-2011-117, 1909. 45 p.
<https://cds.cern.ch/record/1390775>.
- [28] S. Heim, K. Lohwasser, L. Iconomidou-Fayard, G. Pasztor, J. Kretzschmar, and M. Delmastro, *Update of Electron Efficiency Plots*, Tech. Rep. ATL-COM-PHYS-2013-1287, CERN, Geneva, Sep, 2013.
<https://cds.cern.ch/record/1598869>. ATLAS Internal Only.
- [29] J. Mitrevski, *Electron and Photon Reconstruction with the ATLAS Detector*, Tech. Rep. ATL-PHYS-PROC-2014-189, CERN, Geneva, Oct, 2014.
<https://cds.cern.ch/record/1954310>.
- [30] ATLAS Collaboration, *Electron efficiency measurements with the ATLAS detector using the 2012 LHC proton-proton collision data*, Tech. Rep. ATLAS-CONF-2014-032, CERN, Geneva, Jun, 2014. <https://cds.cern.ch/record/1706245>.
- [31] ATLAS Collaboration, *Improved electron reconstruction in ATLAS using the Gaussian Sum Filter-based model for bremsstrahlung*, Tech. Rep. ATLAS-CONF-2012-047, CERN, Geneva, May, 2012. <https://cds.cern.ch/record/1449796>.
- [32] ATLAS Collaboration, *Expected electron performance in the ATLAS experiment*, Tech. Rep. ATL-PHYS-PUB-2011-006, CERN, 2011. <https://cds.cern.ch/record/1345327>.
- [33] M. Aharrouche, C. Anastopoulos, V. Dao, F. Derue, F. Dudziak, O. Fedin, D. Fournier, D. Froidevaux, J. Hartert, L. Iconomidou-Fayard, K. Kerschen, S. Koenig, T. Koffas, V. Maleev, E. Paganis, G. Psztor, J. Poveda, A. Robichaud-Vronneau, A. Schaffer,

- T. Sarangi, E. Sedykh, V. Solovyev, K. Tackmann, T. Theveneaux-Pelzer, P. Urquijo, M. Wielers, and S. L. Wu, *Expected electron performance in the ATLAS experiment*, Tech. Rep. ATL-PHYS-INT-2010-126, CERN, Geneva, Nov, 2010. <https://cds.cern.ch/record/1309907>. ATLAS Internal Access Only.
- [34] S. Menke, *Introduction to Local Hadron Calibration*, <https://indico.cern.ch/event/132005/session/16/contribution/12/attachments/97724/139535/hcw11-19092011.pdf>, September, 2011. ATLAS Internal Access Only.
- [35] B. Lenzi and R. Turra, *Monte Carlo calibration update for electrons and photons using multivariate techniques*, Tech. Rep. ATL-COM-PHYS-2013-1426, CERN, Geneva, Oct, 2013. <https://cds.cern.ch/record/1609589>. ATLAS Internal Access Only.
- [36] L. Chytka, *MVA techniques in MC calibration of the EM calorimeter of ATLAS*, http://indico.cern.ch/event/203712/attachments/308077/430161/MCcalib_Ladislav_Chytka.pdf, August, 2012.
- [37] A. Hcker, J. Stelzer, F. Tegenfeldt, H. Voss, K. Voss, A. Christov, S. Henrot-Versill, M. Jachowski, A. Krasznahorkay, Y. Mahalalel, X. Prudent, and P. Speckmayer, *TMVA - Toolkit for Multivariate Data Analysis*, Tech. Rep. physics/0703039. CERN-OPEN-2007-007, Mar, 2007. <https://cds.cern.ch/record/1023102>.
- [38] ATLAS Collaboration, *egamma MVA Calibration*, <https://twiki.cern.ch/twiki/bin/viewauth/AtlasProtected/EgammaMVACalibration>, December, 2015. ATLAS Internal Access Only.
- [39] CDF, D0 Collaboration, Tevatron New Physics Higgs Working Group, *Updated Combination of CDF and D0 Searches for Standard Model Higgs Boson Production with up to 10.0 fb⁻¹ of Data*, 2012. [arXiv:1207.0449 \[hep-ex\]](https://arxiv.org/abs/1207.0449). http://lss.fnal.gov/cgi-bin/find_paper.pl?conf-12-318.
- [40] S. H. Abidi et al., *Mass and signal strength measurement of the Higgs particle in the four leptons decay channel with the ATLAS detector*, Tech. Rep. ATL-COM-PHYS-2014-007, CERN, Geneva, Jan, 2014. <http://cdsweb.cern.ch/record/1641921>. ATLAS Internal Access Only.
- [41] S. H. Abidi et al., *Study of the SM-like Higgs particle at 125 GeV properties using production mechanisms specific signatures in the $H \rightarrow ZZ^{(*)}l^+l^-l^+l^-$ channel.*, Tech. Rep. ATL-COM-PHYS-2013-1663, CERN, Geneva, Dec, 2013. <https://cds.cern.ch/record/1639131>. ATLAS Internal Access Only.

- [42] ATLAS Collaboration, HSG2, *Measurement of the Higgs boson spin, parity, and HZZ tensor structure in the four-lepton decay channel with the ATLAS detector*, Tech. Rep. ATL-COM-PHYS-2014-174, CERN, Geneva, Mar, 2014.
<https://cds.cern.ch/record/1666722>. ATLAS Internal Supporting note for paper.
- [43] ATLAS Collaboration, *Measurement of inclusive and differential fiducial cross-sections of the Higgs boson in the $H \rightarrow ZZ^* \rightarrow 4l$ decay channel using 20.3 fb¹ of pp collision data at $\sqrt{s}=8$ TeV with the ATLAS detector*, Tech. Rep. ATLAS-CONF-2014-044, CERN, Geneva, Jul, 2014. <https://cds.cern.ch/record/1741017>.
- [44] LHC, *LHC Higgs Cross-Section Working Group*,
<https://twiki.cern.ch/twiki/bin/view/LHCPhysics/LHCHXSWG>. Accessed: 2016-01-28.
- [45] ATLAS Collaboration, G. Aad et al., *Search for an additional, heavy Higgs boson in the $H \rightarrow ZZ$ decay channel at $\sqrt{s} = 8$ TeV in pp collision data with the ATLAS detector*, Tech. Rep. arXiv:1507.05930. CERN-PH-EP-2015-154, CERN, Geneva, Jul, 2015.
<https://cds.cern.ch/record/2036291>.
- [46] A. L. Read, *Presentation of search results: The CL(s) technique*, *J. Phys. G* **28** (2002) 2693–2704.
- [47] S. H. Abidi et al., *Event selection and background estimation for the measurement of the properties of the Higgs particle in the four lepton decay channel with the ATLAS detector*, Tech. Rep. ATL-COM-PHYS-2013-1599, CERN, Geneva, Dec, 2013.
<https://cds.cern.ch/record/1634096>. ATLAS Internal Access Only.
- [48] M. Cacciari, G. P. Salam, and G. Soyez, *Anti-KT jet clustering Algorithm*, *JHEP* **04** (2008) 063, [arXiv:0802.1189](https://arxiv.org/abs/0802.1189) [hep-ph].
- [49] S. H. Abidi, C. Anastopoulos, G. Artoni, M. Baak, P. J. Clark, T. Cuhadar Donszelmann, N. C. Edwards, F. Garay Walls, R. Harrington, M. Dano Hoffmann, L. S. Kaplan, D. Kyriazopoulos, R. Nicolaidou, S. Oda, K. A. Parker, S. L. Wu, E. Mountricha, L. Aperio Bella, X. Ju, and R. Di Nardo, *Heavy Higgs boson searches in the four-lepton channel with the ATLAS detector using $\sqrt{s} = 8$ TeV data.*, Tech. Rep. ATL-COM-PHYS-2014-272, CERN, Geneva, Apr, 2014.
<https://cds.cern.ch/record/1693487>. ATLAS Internal Access Only.
- [50] G. Cowan, K. Cranmer, E. Gross, and O. Vitells, *Asymptotic formulae for likelihood-based tests of new physics*, *Eur. Phys. J.* **C71** (2011) 1554, [arXiv:1007.1727](https://arxiv.org/abs/1007.1727) [physics.data-an]. [Erratum: *Eur. Phys. J.*C73,2501(2013)].

- [51] ATLAS Collaboration, CMS Collaboration and The LHC Higgs Combination Group, *Procedure for the LHC Higgs boson search combination in Summer 2011*, Tech. Rep. CMS-NOTE-2011-005. ATL-PHYS-PUB-2011-11, CERN, Geneva, Aug, 2011. <https://cds.cern.ch/record/1379837>.
- [52] ATLAS Collaboration, M. Leyton, *Minimum Bias and Underlying Event Measurements with ATLAS*, in *Proceedings, 3rd International Workshop on Multiple Partonic Interactions at the LHC (MPI@LHC 2011)*, pp. 11–19. 2012. [arXiv:1202.2090](https://arxiv.org/abs/1202.2090) [hep-ex]. <http://inspirehep.net/record/1088609/files/arXiv:1202.2090.pdf>.
- [53] T. Sjostrand, S. Mrenna, and P. Z. Skands, *A Brief Introduction to PYTHIA 8.1*, *Comput.Phys.Commun.* **178** (2008) 852–867, [arXiv:0710.3820](https://arxiv.org/abs/0710.3820) [hep-ph].
- [54] ATLAS Collaboration, *Performance of the ATLAS electromagnetic calorimeter for $\pi^0 \rightarrow \gamma\gamma$ and $\eta \rightarrow \gamma\gamma$ events*, Tech. Rep. ATLAS-CONF-2010-006, CERN, Geneva, Jun, 2010. <https://cds.cern.ch/record/1273999>.
- [55] Particle Data Group Collaboration, K. A. Olive et al., *Review of Particle Physics*, *Chin. Phys.* **C38** (2014) 090001.
- [56] N. Kerschen and A. Schaffer, *Electron performance of the ATLAS detector using the $J/\psi \rightarrow ee$ decays*, Tech. Rep. ATL-PHYS-INT-2010-124, CERN, Geneva, Nov, 2010. <https://cds.cern.ch/record/1308401>. ATLAS Internal Only.
- [57] M. Pivk and F. R. Le Diberder, *SPlot: A Statistical tool to unfold data distributions*, tech. rep., 2005. [arXiv:physics/0402083](https://arxiv.org/abs/physics/0402083) [physics.data-an].
- [58] M. Pivk, *sPLOT: A Quick introduction*, tech. rep., 2006. [arXiv:physics/0602023](https://arxiv.org/abs/physics/0602023) [physics]. http://inspirehep.net/record/710479/files/arXiv:physics_0602023.pdf.
- [59] ATLAS Collaboration, *Letter of Intent for the Phase-II Upgrade of the ATLAS Experiment*, Tech. Rep. CERN-LHCC-2012-022. LHCC-I-023, CERN, Geneva, Dec, 2012. <https://cds.cern.ch/record/1502664>.
- [60] ATLAS Collaboration, *ATLAS Phase-II Upgrade Scoping Document*, Tech. Rep. CERN-LHCC-2015-020. LHCC-G-166, CERN, Geneva, Sep, 2015. <http://cds.cern.ch/record/2055248>.

- [61] Y. Unno et al., *Development of n^+ -in-p large-area silicon microstrip sensors for very high radiation environments - ATLAS12 design and initial results*, Nucl. Instrum. Methods Phys. Res., A **765** (2014) 80–90. 11 p. <https://cds.cern.ch/record/2025835>.
- [62] RD50 Collaboration, S. Kuehn, *Silicon Sensors for High-Luminosity Trackers - RD50 Collaboration Status Report*, PoS **TIPP2014** (2014) 041. <http://cds.cern.ch/record/2025928>.
- [63] W. J. Stirling, *Parton Luminosity and Cross-Section Plots*, <http://www.hep.ph.ic.ac.uk/~wstirlin/plots/plots.html>. Accessed: 2015-11-25.
- [64] A. D. Martin, W. J. Stirling, R. S. Thorne, and G. Watt, *Parton distributions for the LHC*, *Eur. Phys. J.* **C63** (2009) 189–285, [arXiv:0901.0002](https://arxiv.org/abs/0901.0002) [hep-ph].
- [65] M. Capeans, G. Darbo, K. Einsweiler, M. Elsing, T. Flick, M. Garcia-Sciveres, C. Gemme, H. Pernegger, O. Rohne, and R. Vuillemet, *ATLAS Insertable B-Layer Technical Design Report*, Tech. Rep. CERN-LHCC-2010-013. ATLAS-TDR-19, CERN, Geneva, Sep, 2010. <http://cds.cern.ch/record/1291633>.
- [66] *Track Reconstruction Performance of the ATLAS Inner Detector at $\sqrt{s} = 13$ TeV*, Tech. Rep. ATL-PHYS-PUB-2015-018, CERN, Geneva, Jul, 2015. <https://cds.cern.ch/record/2037683>.
- [67] ATLAS Collaboration, *Luminosity Public Results Run2*, <https://twiki.cern.ch/twiki/bin/view/AtlasPublic/LuminosityPublicResultsRun2>. Accessed: 2015-11-25.
- [68] ATLAS Collaboration, *Letter of Intent for the Phase-I Upgrade of the ATLAS Experiment*, Tech. Rep. CERN-LHCC-2011-012. LHCC-I-020, CERN, Geneva, Nov, 2011. <http://cds.cern.ch/record/1402470>.
- [69] S. McMahon, P. Allport, H. Hayward, and B. Di Girolamo, *Initial Design Report of the ITk: Initial Design Report of the ITk*, Tech. Rep. ATL-COM-UPGRADE-2014-029, CERN, Geneva, Oct, 2014. <https://cds.cern.ch/record/1952548>. ATLAS Internal Only.
- [70] A. Ferrari, P. R. Sala, A. Fass, and J. Ranft, *FLUKA: A multi-particle transport code (program version 2005)*. CERN, Geneva, 2005. <http://cds.cern.ch/record/898301>.
- [71] T. Jones, *Measurements of the Bending Stiffness and Failure in 3-Point Bending of Irradiated and Non-irradiated Sandwich Beams*, tech. rep., University of Liverpool, January, 2012.

- http://indico.cern.ch/event/169643/contribution/17/attachments/210037/294483/Irradiation_3pt_Bend.pdf.
- [72] T. Jones, *Measurements of the Flat-wise Tensile Strength of Irradiated and Non-irradiated Sandwich Test Tokens*, tech. rep., University of Liverpool, January, 2012.
http://indico.cern.ch/event/169643/contribution/17/attachments/210037/294482/Irradiation_FWT.pdf.
- [73] Z. Liang, *ATLAS strip detector upgrade for the HL-LHC*, Tech. Rep. ATL-INDET-PROC-2015-010, CERN, Geneva, Aug, 2015.
<http://cds.cern.ch/record/2046943>.
- [74] M. Moll, *Radiation damage in silicon particle detectors: Microscopic defects and macroscopic properties*. PhD thesis, Hamburg University, 1999.
<https://mmoll.web.cern.ch/mmoll/thesis/>.
- [75] W. R. Leo, *Techniques for Nuclear and Particle Physics Experiments*. Springer, 1994.
- [76] C. Kittel, *Introduction to Solid State Physics*. Wiley, 2004.
- [77] B. Streetman and S. Banerjee, *Solid State Electronic Devices*. Prentice-Hall series in solid state physical electronics. Pearson Prentice Hall, 2006.
- [78] Y. Unno, *Development of n-in-p large-area silicon microstrip sensors for very high radiation environments*,
<https://indico.cern.ch/event/228876/session/16/contribution/53/attachments/378028/525836/UnnoATLAS12siliconMicrostripSensors.pdf>,
September, 2013. 9th International "Hiroshima" Symposium on the Development and Application of Semiconductor Tracking Detectors, Hiroshima, Japan.
- [79] A. Dierlamm, *Studies on the Radiation Hardness of Silicon Sensors*. PhD thesis, KIT - Karlsruhe Institute of Technology (DE), 2003.
www-ekp.physik.uni-karlsruhe.de/~thesis/data/iekp-ka2003-23.pdf.
- [80] A. Kramida, Yu. Ralchenko, J. Reader, and NIST ASD Team. NIST Atomic Spectra Database (ver. 5.3), [Online]. Available: <http://physics.nist.gov/asd> [2016, March 28]. National Institute of Standards and Technology, Gaithersburg, MD., 2015.
- [81] Y. Unno et al., *Development of n-on-p silicon sensors for very high radiation environments*, *Nucl. Instrum. Meth.* **A636** (2011) S24–S30.

- [82] D. Forshaw, *Development of radiation hard planar silicon tracking detectors for the ATLAS Experiment at the HL-LHC*. PhD thesis, University of Liverpool, 2014.
<http://repository.liv.ac.uk/id/eprint/2002859>.
- [83] A. Affolder et al., *Silicon detectors for the sLHC*, *Nuclear Instruments and Methods in Physics Research Section A: Accelerators, Spectrometers, Detectors and Associated Equipment* **658** (2011) no. 1, 11 – 16.
<http://www.sciencedirect.com/science/article/pii/S0168900211008163>.
- [84] G. Casse, *The effect of hadron irradiation on the electrical properties of particle detectors made from various silicon materials*. PhD thesis, University of Joseph Fourier, Grenoble, 1998. <http://hep.ph.liv.ac.uk/~gcasse/>.
- [85] P. Dervan, C. Wigglesworth, J. Vosseveld, G. Casse, A. Affolder, and A. Greenall, *Update of the annealing scenario for irradiated silicon p-in-n microstrip sensors*, *Nuclear Instruments and Methods in Physics Research Section A: Accelerators, Spectrometers, Detectors and Associated Equipment* **658** (2011) no. 1, 17 – 19.
<http://www.sciencedirect.com/science/article/pii/S0168900211008308>.
- [86] M. Moll, *Radiation Damage in Silicon Particle Detectors*, <https://indico.cern.ch/event/412722/attachments/842148/1171314/01-09-14-CERN-Seminar.pdf>, September, 2001. CERN Detector Seminar.
- [87] A. Vasilescu and G. Lindstroem, *Displacement damage in silicon, on-line compilation*, <http://rd50.web.cern.ch/RD50/NIEL/default.html>. Accessed: 2015-11-25.
- [88] S. Wonsak. Personal communication.
- [89] R. Marco-Hernandez, J. Bernabeu, G. Casse, C. Garca, A. Greenall, C. Lacasta, M. Lozano, S. Mart i Garca, R. Martnez, M. Miano, G. Pellegrini, N. A. Smith, and M. Ulln, *ALIBAVA: A portable readout system for silicon microstrip sensors*, .
<https://cds.cern.ch/record/1091739>.
- [90] AliBaVa systems. <http://www.alibavasystems.com/>.
- [91] I. Mandic, V. Cindro, G. Kramberger, and M. Mikus, *Annealing effects in n+-p strip detectors irradiated with high neutron fluences*, *Nucl. Instrum. Meth.* **A629** (2011) 101–105.
- [92] University of Birmingham, *MC40 Cyclotron*,
<http://www.np.ph.bham.ac.uk/pic/cyclotron>.

- [93] D. Parker, *The Birmingham MC40 Cyclotron*,
https://www.hep.shef.ac.uk/seminars/DParker_Nov14.pdf.
- [94] K. Strijckmans, *The isochronous cyclotron: principles and recent developments*,
Computerized Medical Imaging and Graphics **25** (2001) no. 2, 69 – 78.
<http://www.sciencedirect.com/science/article/pii/S0895611100000562>.
- [95] P. Dervan, R. French, P. Hodgson, H. Marin-Reyes, and J. Wilson, *The Birmingham Irradiation Facility*, *Nuclear Instruments and Methods in Physics Research Section A: Accelerators, Spectrometers, Detectors and Associated Equipment* **730** (2013) no. 0, 101 – 104. <http://www.sciencedirect.com/science/article/pii/S0168900213007675>.
- [96] H. Marin-Reyes, R. French, P. Hodgson, K. Parker, J. Wilson, and P. Dervan, *Pre-configured xy-axis Cartesian robot system for a new ATLAS scanning facility*, *Mobile Service Robotics: Proceedings of CLAWAR 2014, Poznan, Poland, 21 July - 23 July 2014*, World Scientific Publishing Co. (2014) 477483.
http://www.worldscientific.com/doi/abs/10.1142/9789814623353_0056.
- [97] National Instruments, *LabVIEW System Design Software*,
<http://www.ni.com/labview/>.
- [98] P. Dervan, R. French, P. Hodgson, H. Marin-Reyes, K. Parker, J. Wilson, and M. Baca, *Upgrade to the Birmingham Irradiation Facility*, *Nuclear Instruments and Methods in Physics Research Section A: Accelerators, Spectrometers, Detectors and Associated Equipment* (2015) .
<http://www.sciencedirect.com/science/article/pii/S0168900215001734>.
- [99] Ist Innovative Sensor Technology, *PT1000 sensor*,
[http://uk.farnell.com/ist-innovative-sensor-technology/
plk0-232-6w-a-010/sensor-pt1000-600-c-class-a/dp/1266941?ost=1K0.232.
6W+A.010&selectedCategoryId=&categoryName=All+
Categories&categoryNameResp=All%2BCategories](http://uk.farnell.com/ist-innovative-sensor-technology/plk0-232-6w-a-010/sensor-pt1000-600-c-class-a/dp/1266941?ost=1K0.232.6W+A.010&selectedCategoryId=&categoryName=All+Categories&categoryNameResp=All%2BCategories).
- [100] P. Bonneau, *Evaporative cooling system for Pixel/SCT*, Tech. Rep. ATC-TL-EP-0001, CERN, Geneva, 2006. <https://edms.cern.ch/document/391168/5>.
- [101] Ashland, *Gafchromic radiotherapy films*, .
<http://www.ashland.com/products/gafchromic-radiotherapy-films>.
- [102] V. Cindro, *World Irradiation Facilities for Silicon detectors*,
<https://indico.cern.ch/event/300851/session/4/contribution/27/>

- [attachments/567104/781154/Presentation.pdf](#), Sept, 2014.
- [103] JSI, *AIDA2020 Transnational Access - Triga Mark-III Reactor*,
<http://aida2020.web.cern.ch/content/jsi>.
- [104] K. Hara, *Charge collection and field profile studies in heavily irradiated silicon strip sensors for the ATLAS Inner Tracker Upgrade*,
https://indico.cern.ch/event/340417/session/4/contribution/52/attachments/1160524/1670628/Hiroshima_CCE_hara_final.pdf, Sept, 2015.
- [105] CERN, *AIDA2020 Transnational Access - CERN*,
<http://aida2020.web.cern.ch/content/cern>.
- [106] KIT, *AIDA2020 Transnational Access - KIT*,
<http://aida2020.web.cern.ch/content/kit>.
- [107] Los Alamos National Laboratory, *LANSCE user guide*, .
<http://lansce.lanl.gov/media/WNRUserGuide.pdf>.
- [108] CYRIC, *AVF Cyclotron*, .
<http://www.cyric.tohoku.ac.jp/english/facilities/guide/cyclotron.html>.
- [109] F. Ravotti, *IRRAD and GIF++ Facilities Infrastructure Upgrade*, https://indico.cern.ch/event/382133/session/12/contribution/23/attachments/761539/1044706/2015_06_04_AIDA-2020_WP15_CERN_contribution_Ravotti.pdf, June, 2015.
- [110] P. Dervan, R. French, P. Hodgson, H. Marin-Reyes, K. Parker, J. Wilson, and M. Baca, *Scanning facility to irradiate mechanical structures for the LHC upgrade programme*, *Proceedings of Science* **419** (2014) no. AIDA-CONF-2015-021, .
<https://cds.cern.ch/record/1999159>.
- [111] Norhof, *LN2 microdosing system*, . <http://www.norhof.com/>.
- [112] M. Baca, *Heating of ATLAS Silicon Sensors at the Birmingham Irradiation Facility*,
<http://indico.hep.manchester.ac.uk/getFile.py/access?contribId=52&sessionId=6&resId=0&materialId=slides&confId=4534>, April, 2015. IOP HEPP Annual Meeting 2015.
- [113] P. Dervan. Personal communication.
- [114] D. Briglin, *Update of irradiation at Birmingham cyclotron*,
<https://indico.cern.ch/event/461382/session/0/contribution/55/>

[attachments/1228086/1799170/ITKFeb16_Birmingham_Irrad_Update.pdf](#),
February, 2016. ATLAS Internal Access Only.